Imagerie géoradar (GPR) en milieu hétérogène : application aux failles actives en Mongolie et aux dépôts pyroclastiques du Tungurahua (Equateur)

Jean-Rémi Dujardin

▶ To cite this version:

Jean-Rémi Dujardin. Imagerie géoradar (GPR) en milieu hétérogène : application aux failles actives en Mongolie et aux dépôts pyroclastiques du Tungurahua (Equateur). Sciences de la Terre. Université de Strasbourg, 2014. Français. NNT : 2014STRAH008 . tel-01145058

HAL Id: tel-01145058
https://theses.hal.science/tel-01145058

Submitted on 23 Apr 2015

UNIVERSITÉ DE STRASBOURG

ÉCOLE DOCTORALE DES SCIENCES DE LA TERRE DE L'UNIVERS ET DE L'ENVIRONNEMENT

Institut de Physique du Globe de Strasbourg (UMR7516)

THÈSE

présentée par :

Jean-Rémi DUJARDIN

soutenue le 22 septembre 2014

pour obtenir le grade de : **Docteur de l'université de Strasbourg**

Discipline/ Spécialité : Géophysique

Imagerie géoradar (GPR) en milieu hétérogène

Application aux failles actives en Mongolie et aux dépôts pyroclastiques du Tungurahua (Equateur)

THÈSE dirigée par :	
Maksim BANO	Directeur de thèse, Université de Strasbourg/EOST
RAPPORTEURS :	
Roger GUERIN	Université Pierre et Marie Curie
Xavier DEROBERT	IFSTTAR
AUTRES MEMBRES DU JURY :	
Jean-Michel MARTHELOT	Université de Strasbourg/EOST
MEMBRES INVITES :	
Antoine SCHLUPP	Université de Strasbourg/EOST

UNIVERSITÉ DE STRASBOURG

ÉCOLE DOCTORALE DES SCIENCES DE LA TERRE DE L'UNIVERS ET DE L'ENVIRONNEMENT

Institut de Physique du Globe de Strasbourg (UMR7516)

THÈSE

présentée par :

Jean-Rémi DUJARDIN

soutenue le 22 septembre 2014

pour obtenir le grade de : **Docteur de l'université de Strasbourg**

Discipline/ Spécialité : Géophysique

Imagerie géoradar (GPR) en milieu hétérogène

Application aux failles actives en Mongolie et aux dépôts pyroclastiques du Tungurahua (Equateur)

THÈSE dirigée par :

Maksim BANO	Directeur de thèse, Université de Strasbourg/EOST

RAPPORTEURS :

Roger GUERIN	Université Pierre et Marie Curie
Xavier DEROBERT	IFSTTAR

AUTRES MEMBRES DU JURY :

Jean-Michel MARTHELOT	Université de Strasbourg/EOST

MEMBRES INVITES :

Antoine SCHLUPP	Université de Strasbourg/EOST

Résumé

Le géoradar est une méthode électromagnétique haute fréquence (>10 MHz) utilisé pour caractériser les premiers mètres du sous-sol.

Lors de la présence d'une topographie, les données géoradar sont déformées en conséquence. Afin de retrouver la vraie géométrie des réflecteurs, nous avons codés un algorithme de migration prenant en compte la topographie. La méthode est démontrée grâce à un modèle synthétique simple, puis testée avec succès sur des données réelles.

Les algorithmes de migration apportent cependant du bruit dans les données. Pour pallier à ce problème, deux méthodes ont été mises en place : la première, inhérente à la migration, permet de réduire l'aliasing dit sur l'opérateur. La deuxième est un filtre ré-interpolant les traces en se basant sur un profil de pendage. Les deux méthodes suppriment un bruit incohérent des données mais dégradent les profils lorsqu'ils sont utilisées abusivement.

Dans un deuxième chapitre, nous avons appliqué avec succès le géoradar dans un contexte de paléo-sismologie en Mongolie. L'utilisation conjointe de deux fréquences (50 et 500 MHz) ainsi que des comparaisons avec des tranchées a permis d'obtenir des informations complémentaires sur les géométries et les déplacements potentiels le long de deux failles.

Dans un dernier chapitre, nous avons appliqué les mesures géoradar sur les dépôts pyroclastiques du volcan Tungurahua en Equateur. A nouveau, l'utilisation jointe de différentes fréquences (250, 500 et 800 MHz) nous permet d'imager efficacement les dépôts. Les unités principales sont mises en évidence avec l'antenne de 250 MHz et les architectures des dépôts sont observables avec les antennes de 500 et 800 MHz.

Mots clés : géoradar, migration topographique, paléo-sismologie, dépôts pyroclastiques

Abstract

Georadar is a high frequency (>10MHz) electromagnetic method used to prospect near surface.

When a topography is present, GPR images are distorted. To restore the true geometry of reflexions, we coded a migration algorithm which takes the topography into account. The method is first demonstrate on a simple synthetic model, and then succesfully applied on real data.

However, migration algorithms bring noise to the data. Two methods have then been tested to avoid and remove it. The first one is inherent to the migration algorithm and reduce what is called operator's aliasing. The second one is a filter re-interpolating traces based on a profile containing the slope. Both methods remove inconsistent noise when used with caution, but decrease their quality when used with excess: reflexions presenting dip are the first to be deteriorated, as well as reflexions below strong topography.

In a second chapter, we successfully used GPR in a paleo-sismology context in Mongolia. The use of two frequencies (50 and 500 MHz) as well as comparison with trenches bring complementaries informations on the geometry and possible offset along two faults.

In the last chapter, GPR was tested over pyroclastic deposits from the Tungurahua volcano in Ecuador. Again, the combination of several frequencies (250, 500 and 800 MHz) has proven its efficiency. Main units were obvious with the 250 MHz antenna while the inner architecture of deposits was visible with the 500 and 800 MHz antenna.

Keywords: georadar, topographic migration, paleosismology, pyroclastic deposits

TABLE DES MATIÈRES

La migration topographique, le filtre anti-aliasing, les profils de pendages

Application du géoradar dans un contexte de faible déformation. Exemple des failles d'Emeelt et d'Hustaï en Mongolie

Application du Géoradar sur les dépôts pyroclastiques du Tungurahua, Equateur

INTRODUCTION

Le géoradar est une méthode d'investigation basée sur la propagation des ondes électromagnétiques hautes fréquence (10 MHz à 2 GHz) dans le sous-sol. Existant depuis les années 60, son utilisation s'est intensifiée au cours des 20 dernières années (Annan, 2002). L'historique de la méthode est disponible dans Neal (2004) et Annan (2002).

De part son faible coût, sa facilité de mise en œuvre et sa nature non destructrice, le géoradar a été adopté et a prouvé son efficacité dans une grande variété de domaines tels que la sédimentologie, la paléo-sismologie, l'archéologie, ou l'hydrologie. Cette liste est non-exhaustive.

La propagation des ondes électromagnétiques est décrite par les équations de Maxwell, qui pour un milieu isotrope linéaire, nous amène aux équations de diffusion-propagation, données ci-dessous pour un champ électrique :

$$\Delta\vec{E} = \mu\sigma\frac{\partial\vec{E}}{\partial t} + \mu\varepsilon\frac{\partial^2\vec{E}}{\partial t^2}$$

Avec μ la perméabilité magnétique, σ la conductivité électrique et ε la permittivité diélectrique. Cette équation comporte deux termes dont le premier est un terme de diffusion et le deuxième un terme de propagation. Lorsque la conductivité du milieu est faible et la fréquence des ondes élevées (comme c'est le cas en géoradar), le terme de diffusion devient négligeable devant le terme de propagation. Les courants de déplacement dominent et l'énergie se transmet sur un mode de propagation. Dans ce mode de mesure, les ondes électromagnétiques sont principalement sensibles aux contrastes de permittivité diélectrique.

Le géoradar émet un signal impulsionnel comprenant une largeur de fréquence dont la fréquence centrale est connue. Obéissant aux lois de la propagation, les ondes suivent le principe de réflexion, réfraction et transmission de Snell-Descartes lors de leur trajet dans le sous-sol. Le signal enregistré correspond donc aux ondes réfléchies sur les contrastes de permittivité diélectrique rencontrés dans le sous-sol. Leur vitesse de propagation est en moyenne comprise entre 0.07 et 0.18 m/ns, mais atteint 0.3 m/ns dans l'air. La vitesse peut être reliée à la permittivité diélectrique et la perméabilité magnétique par l'équation :

$$v = \frac{1}{\sqrt{\mu\varepsilon}}$$

La profondeur de pénétration quand à elle dépend principalement de la conductivité électrique du milieu et de la fréquence. Plus la fréquence augmente, plus la profondeur de pénétration décroit, mais meilleure sera la résolution. Dans la gamme de fréquences utilisées dans le cadre de cette thèse (50 MHz à 800 MHz), elle varie (théoriquement) de 2 à 50 m environ.

Afin d'obtenir des images interprétables et d'être exploités au mieux, les profils géoradar nécessitent des techniques d'imagerie qui, pour la plupart, sont similaires à celles rencontrées en sismique. Un traitement de base permet de faire ressortir les informations pertinentes des données. Des traitements plus avancés peuvent alors avoir des objectifs particuliers. Une des problématiques concerne la prise en compte de la topographie, et notamment lors de l'étape de migration quand celle-ci est nécessaire. Dans un premier chapitre, nous présentons la migration topographique, basée sur la migration de Kirchhoff, tel que présentée par Lehmann and Green (2000). A travers un modèle synthétique simpliste, nous montrons les effets de la topographie sur les données, puis redémontrons les équations de la migration de Kirchhoff. Cet algorithme est alors utilisé sur des données réelles pour observer les améliorations et les limites de la méthode.

Malgré les améliorations obtenues (disparition des hyperboles, prise en compte correct de la topographie), la migration apporte toujours du bruit dans les données. Une partie du bruit provient d'un aliasing dit sur l'opérateur. Une technique inhérente à la migration topographique a été rajoutée pour examiner les améliorations sur les données.

Enfin, encore une fois inspirée de la sismique, un algorithme de ré-interpolation des traces basé sur le calcul automatique des pendages présent dans les profils radar a été investigué. Il permet de réduire le bruit aléatoire dans les données et, utilisé en conjonction avec la migration topographique, réduit significativement les artefacts de la méthode.

La suite de mon travail de thèse présente deux terrains d'application distincts dans lesquels le géoradar a prouvé son efficacité. En premier lieu, le deuxième chapitre se focalise sur les résultats de deux campagnes géoradar (2010 et 2011) dont le but est la caractérisation de deux failles actives (Emeelt et Hustaï, dont la faille d'Emeelt a été découverte en 2008) dans la région d'Ulaanbaatar, capitale de la Mongolie. Cette étude s'inscrit dans un contexte plus vaste d'estimation du risque sismique de la région.

Deux antennes de fréquences 500 MHz et 50 MHz, ainsi que des tranchées, ont été utilisées conjointement. L'antenne de 500 MHz, de par sa haute résolution, mais une profondeur de pénétration modérée, est adaptée aux investigations des petits dépôts sédimentaires de quelques mètres d'épaisseur (paléo-chenaux comblés, petits cônes alluviaux), et potentiellement affectées par la faille. La haute résolution est adaptée à la comparaison des données géoradar avec les observations de tranchée, et permet de relier faciès géoradar et lithologie. Une méthodologie pseudo-3D (réseau dense de profils parallèles) a été mis en place sur la faille d'Emeelt, pour cartographier la base d'un paléo-chennal, et un décalage dextre de 2 m environ est mis en évidence.

L'antenne de 50 MHz est utilisée en complément sous la forme de longs profils 2D, perpendiculaires à la faille. Une forte réflexion avec un fort pendage, observée dans un grand nombre de profils, est interprétée comme le plan de faille. Ces profils nous donnent accès à la direction et la valeur du pendage de la faille entre 3 et 12 m de profondeur et sur une zone plus étendue qu'avec la première antenne.

Le troisième chapitre concerne une campagne de mesure effectuée sur les dépôts pyroclastique du volcan Tungurahua en Equateur. En effet, le volcan Tungurahua a débuté un cycle éruptif en 1999 et a atteint sa phase maximale lors de l'éruption d'août 2006. Le volcan est encore en activité au jour d'aujourd'hui. L'éruption a déclenchée des coulées pyroclastiques qui peuvent être séparées en deux phases : une phase composée de matériel dense, dont la trajectoire est confinée dans les vallées, et une phase de matériel léger diluée dans l'air, pouvant s'extraire des pièges topographiques et former localement des dépôts de taille réduite (de la dizaine à la centaine de mètre). Ces dépôts exposent très souvent des stratifications entrecroisées ainsi que des dunes présentant une signature sédimentaire particulière.

Dans ce chapitre, nous présentons la méthodologie employée et les résultats obtenus lors de la campagne géoradar effectuée en 2012. Nous montrons l'intérêt de l'utilisation conjointe de plusieurs antennes de fréquence différente (ici 250, 500 et 800 MHz) qui permettent d'imager les structures internes des dépôts à différentes échelles et profondeurs. Les principales unités de dépôts sont reconnues dans les données, ainsi que les motifs de sédimentation à petite échelle. L'utilisation d'une méthodologie pseudo-3D à l'échelle d'une dune permet de suivre l'évolution latérale des dépôts.

Chapitre 1 : L'imagerie en Géoradar

LA MIGRATION TOPOGRAPHIQUE, LE FILTRE ANTI-ALIASING, LES PROFILS DE PENDAGES

1. Introduction

Ce chapitre présente une méthode de migration des données géoradar permettant la prise en compte de la topographie ainsi que deux méthodes de réduction du bruit. La première, inhérente à la migration topographique, permet de réduire les artefacts de migration. La deuxième est basée sur le calcul automatique des pentes d'un profil. Ces trois méthodes ont été investiguées dans une optique d'amélioration de l'imagerie géoradar afin d'en faciliter la lecture et les interprétations.

Migration topographique

Dans cette partie, nous présentons d'abord la migration de Kirchhoff en nous appuyant sur un modèle synthétique simple : un point diffractant. Le principe de la méthode réside dans le calcul de l'hyperbole de diffraction (template) le long de laquelle les échantillons sont sommés puis replacés à son sommet. Une surface plane est considérée dans ce cas. La surface plane est ensuite modifiée (en prenant comme topographie un arc de cercle de centre le point diffractant) afin d'évaluer les effets de la topogrpahie dans les données. Le résultat est alors une hyperbole tronquée en son sommet (sommet horizontal). Le template initial n'est donc plus adapté à la migration des données. Nous nous basons sur ce modèle pour démontrer les équations de la migration topographique dont le principe est la correction du template.

Les données synthétiques sont alors reprises pour permettre la comparaison entre la migration topographique et les techniques classiques de prise en compte de la topographie (i.e. correction statique appliquée avant ou après une migration classique). Dans l'exemple synthétique, la topographie étant importante, les différences entre les différentes méthodes sont marquées et la migration topographique exprime clairement sa supériorité.

Dans une dernière partie, la méthode est utilisée sur des données réelles et à nouveau comparée avec un schéma classique de migration précédé ou suivi d'une correction statique. Les différences sont plus subtiles qu'avec les données synthétiques. Mais plusieurs points sont à retenir. En présence d'une pente constante, les réflexions pentées afficheront leur vrai pendage et leur vraie localisation uniquement après migration topographique. Dans les zones de fortes variations de la topographie, une détérioration significative de signal est observée, mais pas dans la migration topographique.

Cette partie a été publiée dans la revu CRAS sous la référence suivante :

Dujardin, J. R., & Bano, M. (2013). Topographic migration of GPR data: Examples from Chad and Mongolia. Comptes Rendus Geoscience, 345(2), 73-80.

(la version publiée est disponible en annexe).

Filtre anti-aliasing

Lors de la migration de Kirchhoff et donc de la migration topographique, trois types d'aliasing peuvent être observés. Le premier sur l'image de départ, lorsque le théorème d'échantillonnage de Nyquist n'est pas respecté, le deuxième sur l'image d'arrivée, pour les mêmes raisons que précédemment et le dernier est l'aliasing sur l'opérateur, lorsque la pente de la trajectoire de migration devient trop importante pour un contenu fréquentiel et un pas inter-trace donné.

Dans ce chapitre, nous présentons un filtre inhérent à la migration de Kirchhoff (et à la migration topographique), ainsi que son implémentation dans l'algorithme de migration. Le filtre repose sur plusieurs versions du profil initial. Chaque version est filtrée par un filtre passe bas dont la fréquence de coupure est de plus en plus basse d'une version à l'autre. Lorsque la pente de l'opérateur (i.e. trajectoire de migration) devient trop pentue pour un contenu fréquentiel et un pas inter-trace donné, l'échantillon choisi lors de la sommation le long du template est sélectionné dans la version du profil filtré pour la fréquence basse suivante. Un coefficient est ajouté dans l'algorithme afin d'appliquer le filtre avec plus ou moins d'intensité.

Dans un deuxième temps, le profil de la dune de sable (utilisé précédemment) est repris et migré avec différentes intensités du filtre pour observer les résultats. Dans notre exemple, le profil de la dune est relativement bien échantillonné. Par conséquent, il est nécessaire d'augmenter l'intensité du filtre pour en voir les effets. En première observation, les artefacts de migration sont atténués voire supprimés, puis, lorsque l'intensité augmente, du signal utile commence également à être supprimé, notamment dans les zones à l'aplomb des fortes variations de topographie. En dernier lieu, le profil a été sous-échantillonné (une trace sur deux) afin d'observer les effets dans un contexte où l'aliasing est beaucoup plus présent. L'aliasing, alors très marqué dans les données initiales, masque clairement des réflexions après la migration topographique. Lors de l'utilisation du filtre anti-aliasing, une partie du signal peut être récupérée, améliorant nettement la qualité des données.

Filtre basé sur les profils de pendages

Dans cette dernière partie, nous présentons un filtre basé sur le calcul automatique des pendages présents dans les profils. Le but de ce filtre est la suppression du bruit aléatoire présent dans les données.

Deux algorithmes ont été codés à cet effet. L'un en domaine temporel et le second dans le domaine fréquentiel. Dans les deux cas, une première fenêtre glissante parcourt les traces et les échantillons en tant que fenêtre de référence. Une seconde fenêtre glissante parcourt les traces précédentes et suivantes afin de comparer les données. Les comparaisons entre les deux fenêtres glissantes sont effectuées à l'aide des coefficients de corrélation (domaine temporel), ou dans le domaine de Fourier (domaine fréquentiel). Deux profils de pendages, vers les traces suivantes et vers les traces précédentes, sont déduits de ces calculs, puis regroupés en prenant la moyenne entre les deux, la pente pour laquelle le coefficient de corrélation est le plus fort, ou la pente la plus proche de zéro. Dans les deux cas (domaine temporel et fréquentiel), la prise en compte de la pente la plus proche de zéro donne les résultats les plus stables. Les différences entre la méthode temporelle et la méthode fréquentielle sont minimes, mais le profil dans le domaine fréquentiel reste supérieur en qualité. Les profils de pendages nécessitent alors un filtrage (via un filtre médian) pour ne garder que les tendances observées avant d'être utilisées pour la ré-interpolation des traces.

Le profil filtré est calculé par ré-interpolation de chaque trace. Pour une trace donnée, l'échantillon considéré est recalculé par moyenne pondérée entre lui-même et les échantillons des traces précédentes et suivantes, choisis en fonction du profil de pendages. Un coefficient permet de donner plus ou moins de poids à l'échantillon central, pour appliquer le filtre avec plus ou moins d'intensité. Les résultats, à nouveau présentés sur une portion du profil de la dune, montrent deux séries de résultats. La première permet de voir les effets du filtre médian sur les profils de pendages, et le second, permet de tester les paramètres de ré-interpolation des données. En dernier lieu, le filtre est utilisé sur un exemple impliquant une migration topographique. Le filtre est appliqué avant et/ou après migration pour en observer les effets. L'amélioration est particulièrement visible lorsque le filtre est utilisé avant migration. Bon nombre d'artefacts de migration sont supprimés. Les profils paraissent « lissés » et l'interprétation en est facilitée. Lors de son application après la migration uniquement, des artefacts tendent à apparaitre, dégradant légèrement la qualité du profil.

2. Migration topographique des données géoradar : exemples du Tchad et de la Mongolie

Résumé

La plupart des mesures géoradar sont effectuées sur des zones relativement planes. Lorsque des réflexions à fort pendage et/ou des diffractions sont présentes dans les données, un algorithme de migration classique est nécessaire pour retrouver les géométries des structures souterraines. Cependant une migration standard n'est pas adaptée aux données géoradar enregistrées sur des zones présentant de fortes variations du relief. Pour prendre en compte les variations de la topographie, une correction statique est généralement appliquée aux données géoradar. Une migration topographique serait plus appropriée pour replacer les réflecteurs à leur vraie position, avec leur vrai pendage. Dans cet article, nous présentons une vue d'ensemble de la migration de Kirchhoff et montrons l'importance de la migration topographique dans le cas où la profondeur des structures et les variations du relief sont du même ordre de grandeur. Des exemples, basés sur des données radar synthétiques et réelles, permettent d'illustrer l'efficacité de la méthode.

2.1. Introduction

The ground penetrating radar reflection (GPR) technique, a geophysical method based on high frequency (10-2300 MHz) electromagnetic (EM) wave propagation, can provide very detailed and continuous images of the subsurface. One of the goals of GPR measurements is to determine the geometries of fine structures by imaging the shallow subsurface. In general, the GPR measurements are performed on nearly flat surfaces and in this case, if highly dipping reflections and/or diffractions are present in the data, a standard migration is needed in order to precisely determine the geometries of shallow structures (Feng et al., 2009; Zeng et al., 2004).

For a variable topographic relief, a standard processing procedure includes the application of static shifts (Sheriff and Geldart, 1995; Annan, 1991) followed by a classical migration commonly performed with a flat datum plane. Nevertheless, this processing technique does not give good results for large topographic variations. In addition, the inadequacy of conventional elevation static corrections in accounting for a gentle to rugged topographic relief was shown to be a particular problem (Lehmann and Green, 2000). To obtain reliable images from GPR data acquired on areas showing irregular topography, a special processing which accounts for the topography may be required. Although the relief variation, in seismic acquisition, is small compared to the investigation depth, various migration methods with topography have been developed for seismic data (Berryhill, 1979; Wiggins, 1984; Shtivelman and Canning, 1988; and Bevc, 1997). These migration techniques could be of a more important use in GPR data than in seismic, as the target structures have often the same order of depth as the topographic relief variations.

Lehmann and Green (2000) adapted a topographic migration for GPR data based on the

Kirchhoff algorithm proposed by Wiggins (1984) for the seismic data collected in mountainous areas. According to these authors, the topographic migration should be considered when the surface slope exceeds 10%.This migration method has been successfully used, in 3D, by e.g. McClymont et al. (2008) for the GPR data acquired on active fault areas showing a rugged topography.

In this article, we first present an overview of the Kirchhoff topographic migration algorithm and demonstrate the diffraction equation used in this method as presented by Lehmann et al. (1998). To show the efficiency of the method, we first use synthetic data from a single diffraction point model, and compare the migration results with flat datum and topography, respectively. Then, we present two different examples of real GPR data recorded in areas presenting local and large topographic variations as well as a mean slope of less than 10%. The first example is from a dry sand dune of the Chadian desert, presenting a high velocity medium with local topographic variations, while the second one is from Mongolia presenting a topographic slope of 10 %. Finally, we show and compare the results of GPR profiles processed with static shift followed by migration, migration followed by static shift and topographic migration, and discuss the superiority of the later one even in the cases where the topographic slope is lower than 10%.

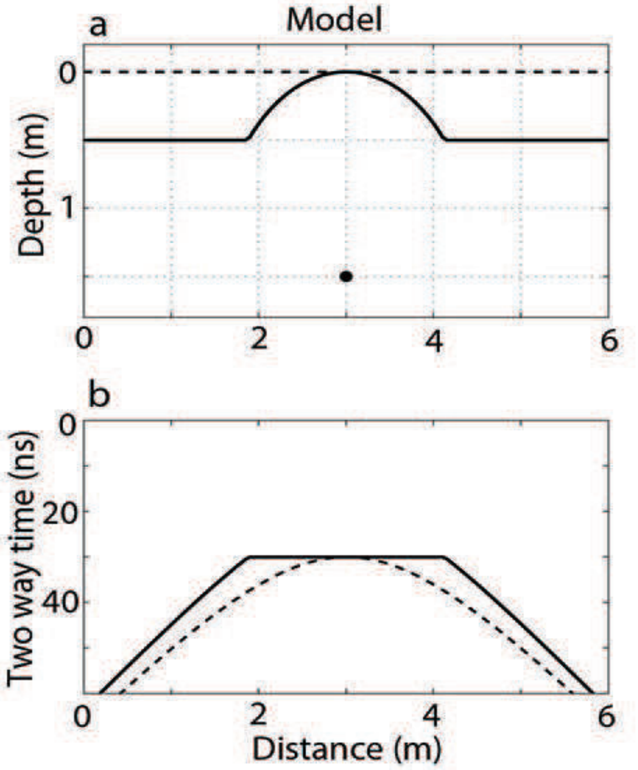

Figure 1 : a) A geological model composed of a diffraction point (black dot) placed on (x_d, z_d). The dashed line represents the flat datum plane located at z = 0, while the thick line shows the acquisition surface with topography. b) Zero offset GPR profiles obtained by moving the antennas on both surfaces. The dashed line (a diffraction hyperbola) corresponds to the acquisition on the flat datum plane (dashed line in Fig. 1a), while the thick line represents the case where the acquisition is performed on the surface with topography (thick line in Fig. 1a). Note the difference between the two observed curves.

2.2. The Kirchhoff topographic migration

2.2.1. The Kirchhoff migration

Let us consider a simple 2D geological model (x-z plane) composed of a diffraction point (diffractor) placed on a perfectly resistive medium with a constant electromagnetic (EM) velocity. The coordinates of this diffractor are x_d and z_d, respectively (Figure 1a). We assume a zero offset survey with transmitting and receiving antennas which move on a flat horizontal surface at z = 0 (dashed line in Figure 1a). In this case, the result of the zero offset GPR profile in time (x-t plane) will be a diffraction hyperbola (shown by the dashed line in Figure 1b) and the electric field variation can be described by a scalar wave propagation equation, which is similar to the acoustic wave equation (Leparoux et al., 2001).

The goal of the migration is to find the geological model (in the x-z plane) from the zero offset GPR profile (in the x-t plane). For a resistive medium (high frequency approximation) we can use the Kirchhoff method which gives the wave field at the location of the diffractor (x_d, z_d) from the zero-offset wave field measured at the surface z = 0 (Schneider, 1978; Feng et al., 2009). Practically, the Kirchhoff migration will calculate the diffraction hyperbola (migration template) for each point of the GPR profile and, by adding the amplitudes along the template, will place it at the top of the template in the migrated profile (Claerbout, 1985; Yilmaz, 2001). Migrating each of these points for a given velocity will focus the amplitudes at their correct positions and the reflector is imaged with its true position and dip angle.

2.2.2. Effect of the topography

When GPR measurements are performed over a surface with a topography, the migration template is no longer a diffraction hyperbola, instead it will be a distorted diffraction curve. This is shown in Figure 1 where the topography is chosen to be a circle whose centre is on the diffraction point (x_d, z_d), and on both sides of which the topography is flat (see the thick line in Figure 1a). Be aware that de x-axis and y-axis do not have the same sacle. The distance between the diffraction point and the antennas (in zero offset), moving on the surface along the circle, is constant. Therefore the migration template, shown by the thick line in Figure 1b, will be flat on the top, and on both sides it will be represented by two flanks of a diffraction hyperbola. In this case the imaging result of the classical Kirchhoff migration with a flat datum plane will be spurious (see Figure 4 below). For this reason we absolutely need to take into account the topography of the GPR acquisition surface.

2.2.3. Migration with topography

For the standard Kirchhoff migration, at a location x on the surface z = 0 (i.e. the antennas move on the flat datum plane), the two-way travel time t(x) along the gray line path in Figure 2 is given by:

$$t(x) = \sqrt{{t_0}^2 + \frac{4(x - x_d)^2}{V^2}} \tag{1}$$

where $t_0 = 2z_d/V$ is the two-way travel time above the diffraction point (black dot in Figure 2), x_d is the horizontal position of the diffraction point, z_d is the depth of the diffraction point from the flat datum surface (see Figure 2) and V is the EM wave velocity. This is the equation of a diffraction hyperbola (or migration template) which is used in the standard Kirchhoff migration scheme with a flat datum plane.

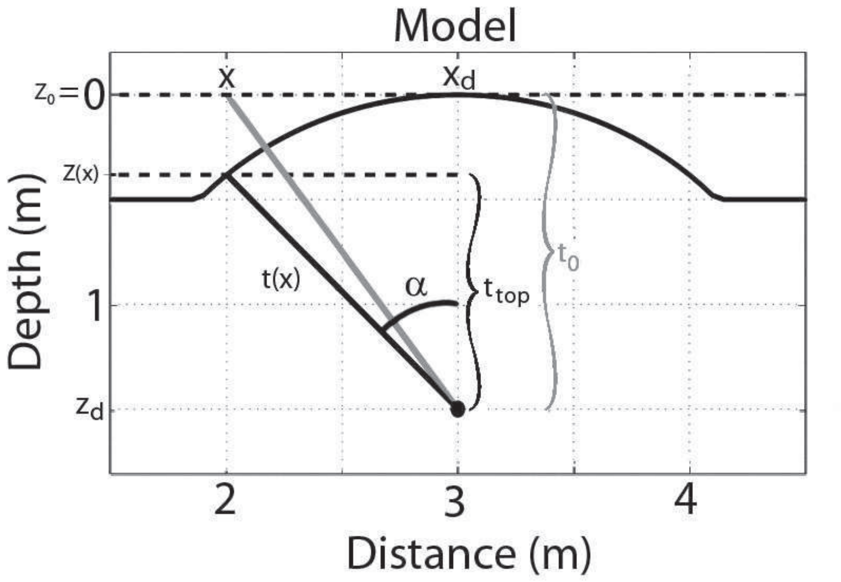

Figure 2 : Schematic presentation showing the topographic correction for the Kirchhoff migration. For a given position x at the surface $z = z_0 = 0$, we take into account the topography z(x) instead of considering the flat datum plane (dashed line at z_0). The travel time t(x) is now calculated along the black line path rather than along the gray line one.

Correcting for the topography means to choose for the migration template the thick line of Figure 1b, instead of using the dashed one, which is exactly a diffraction hyperbola. This will allow the template to follow exactly the real travel path of the GPR data. Indeed, for the same x location (Figure 2), the z position of the antennas (moving on the rugged surface) has been changed and the two-way travel time t(x) is now calculated along the thick line path in Figure 2 to obtain:

$$t(x) = \sqrt{{t_{top}}^2 + \frac{4(x - x_d)^2}{V^2}} \tag{2}$$

with:

$$t_{top} = t_0 - \frac{2(z(x) - z_0)}{V} \tag{3}$$

where z(x) is the topography of the acquisition surface shown by the thick line in Figure 2.

Substituting equation (3) into equation (2) we obtain:

$$t(x)=\sqrt{{t_0}^2+4\frac{(x-x_d)^2+(z(x)-z_0)^2}{V^2}-4\frac{t_0(z(x)-z_0)}{V}} \tag{4}$$

This equation is the same as the one given without any demonstration by Lehmann et al. (1998) in the case of a 2D migration. Figure 3 presents an overview of the different steps to compute the topographic migration. We have used the same notations as in equations (1) to (4).

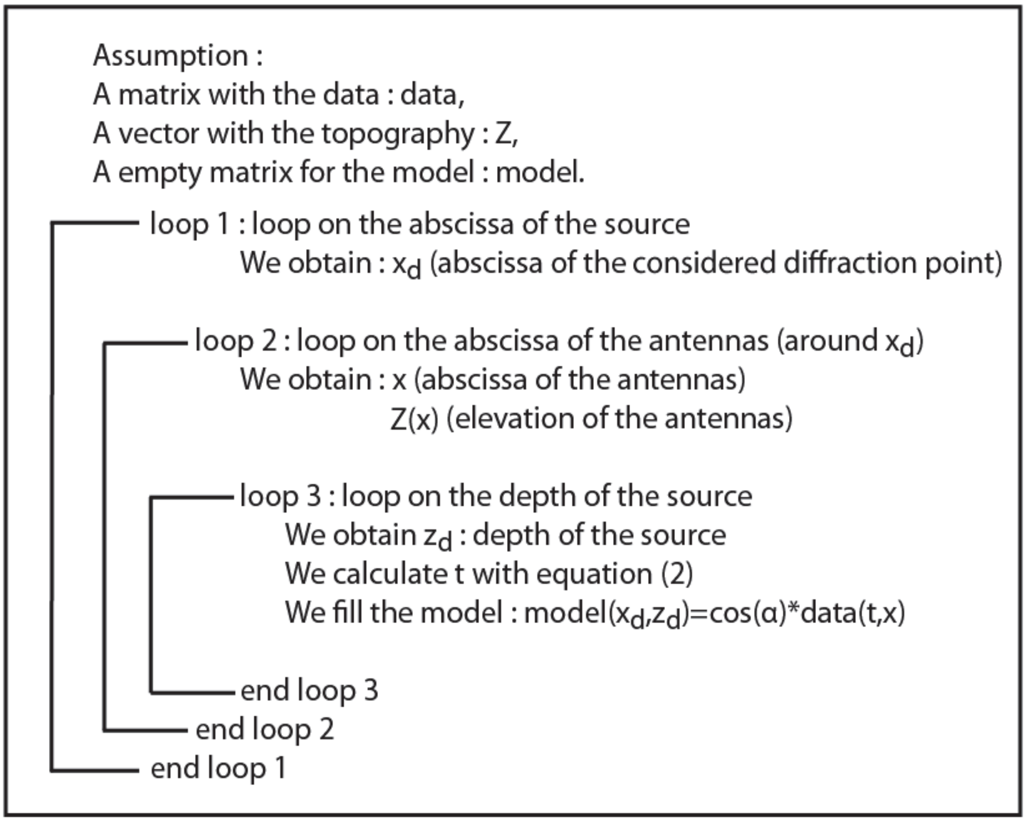

```
Assumption :
A matrix with the data : data,
A vector with the topography : Z,
A empty matrix for the model : model.

loop 1 : loop on the abscissa of the source
        We obtain : $x_d$ (abscissa of the considered diffraction point)

    loop 2 : loop on the abscissa of the antennas (around $x_d$)
        We obtain : x (abscissa of the antennas)
                    Z(x) (elevation of the antennas)

        loop 3 : loop on the depth of the source
            We obtain $z_d$ : depth of the source
            We calculate t with equation (2)
            We fill the model : $model(x_d,z_d)=cos(\alpha)*data(t,x)$

        end loop 3
    end loop 2
end loop 1
```

Figure 3 : Diagram showing the different steps of the Kirchhoff topographic algorithm. The names of the variables are the same as the ones used in equations (1) to (4) and Figure 2. A first matrix with the data (data), a vector Z with the topography, and an empty matrix for the model (model) are required. The algorithm starts with a first loop on the x position of the diffraction point (x_d). We move around the x_d position to get x and z(x) (position of the antenna) in a second loop. The third loop is running on the depth location of the diffraction point (z_d). Finally we calculate the two-way travel-time between the antennas location [x, z(x)] and the diffraction location (x_d,z_d) using equation (2) to fill the model.

In figure 4 we compare the results of the classical migration with flat datum plane, the classical migration after static shift and the topographic Kirchhoff migration. Figure 4b displays the synthetic radargram computed with the model of figure 4a. This radargram is obtained by using a second order Ricker source having a dominant frequency of 500 MHz, located over a homogeneous medium with a velocity of 0.1 m/ns. The distance between traces is 2 cm.

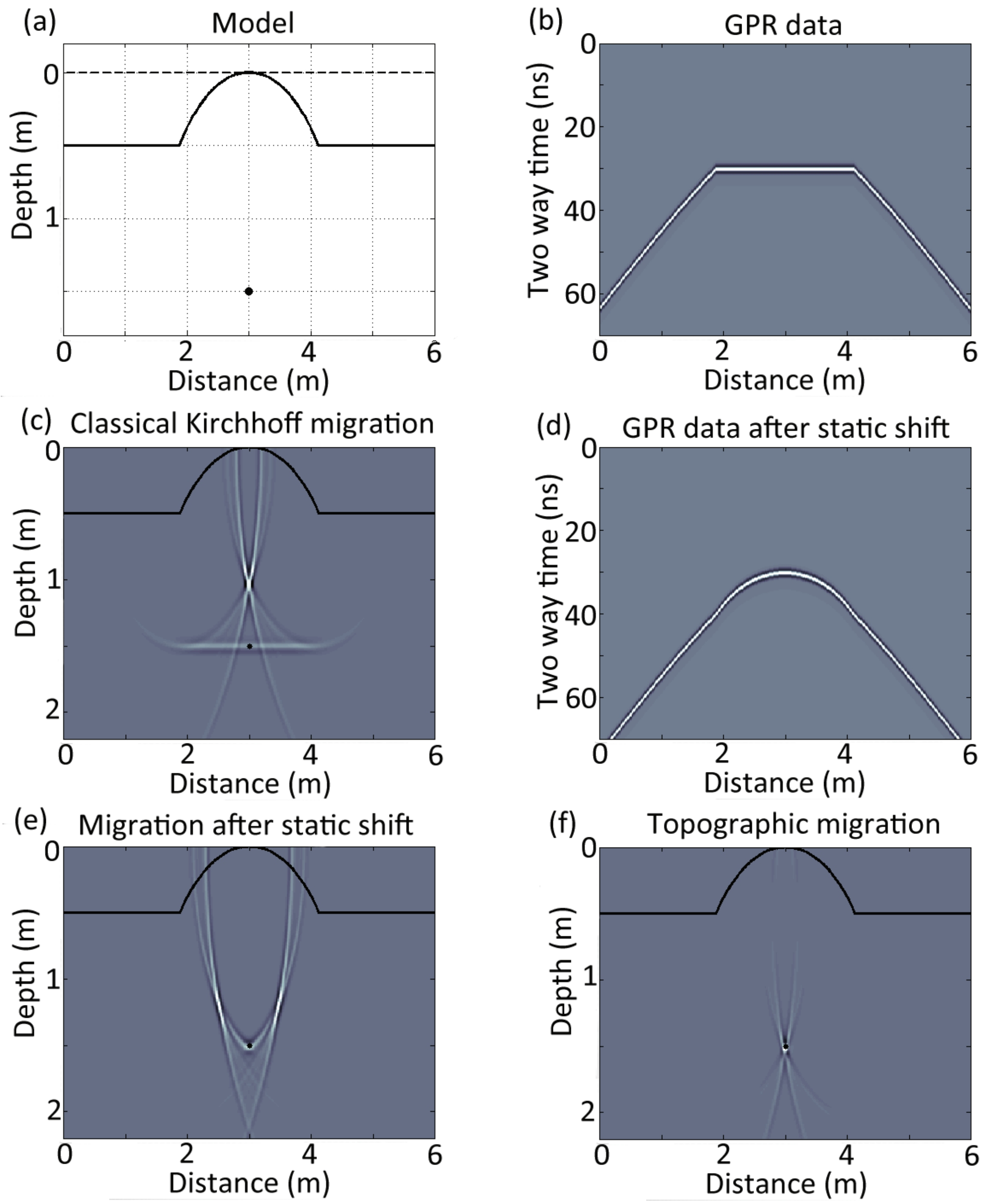

Figure 4 : a) The diffraction point model, with topography (thick line); b) Zero offset GPR data corresponding to a survey over this area. Note the distorted diffraction curve (migration template); c) Classical Kirchhoff migration with a flat surface at z = 0; d) GPR data after the static shift; e) Classical Kirchhoff migration after static shift; f) The result of the topographic migration; The thick line on figure c, e and f corresponds to the real topography.

Figure 4c shows the classical migration of the zero offset GPR synthetic data of Figure 4b. One can see a flat horizontal 2 m wide layer located at a depth of 1.5 m, as well as a bright spot in the middle of the section at a depth of around 1 m (Figure 4c). The imaging result is very poor and might lead to a misinterpretation of the data. The actual classical procedure is a static shift followed by a classical migration. Figure 4d shows the synthetic data after the static shift, and Figure 4e displays the migration after the static shift. The result seems to be better than the one of Figure 4c. In Figure 4e we observe not only a bright spot at the correct depth of 1.5 m, but also two strong spots located on both sides of the diffraction point (around a depth of 1.2 m). In Figure 4f we present the result of the topographic migration appropriately weighted by an amplitude factor proportional to cos(a) = $t_{top}/t(x)$ which also depends on the topography (see Figure 2). The amplitude factor is added to take into account the directivity factor which describes the angle dependence of amplitudes and is given by the cosine of the angle between the propagation direction and the vertical axis (Yilmaz, 2001; Claerbout, 1985). The data are well imaged and, as expected, are focused on a single bright spot located at its real depth of 1.5 m (Figure 4f).

2.3. Real GPR data examples

2.3.1. The Chad Dunes

The first example is a GPR profile collected over an aeolian dry dune in the Chadian desert (Bano et al., 1999). The goal of this survey was to image the interior and the base of the dunes to better understand the sedimentological processes. The GPR profile has been obtained using a 450 MHz shielded antenna. The acquisition mode was a constant offset of 0.25 m, the antennas were moved by 0.125 m steps with a stack of 64 to improve the signal-to-noise ratio.

A standard processing (with in-house interactive GPR software) has been applied and the resulting profile is displayed in Figure 5a. The following processing sequence was used: constant shift to adjust the time zero followed by normal move-out corrections; running average (DC) filter to remove the low frequency; flat reflections filter to remove some clutter noise (continuous flat reflections) caused by multiple reflections between shielded antennas and the ground surface; a band-pass filter and finally a time-varying gain function. The same standard processing is applied to all GPR data presented in this section.

The GPR profile of Figure 5a shows complex geometries, with imbricate reflections corresponding to different deposit phases. The undulating reflection indicated by four white arrows in this figure represents the base of the dune, which in fact is nearly flat and consists of pebbles (>2.0 mm in diameter). This reflection is from the contact between the aeolian sands near the surface and deeper lake deposits consisting of an unconsolidated silty sandstone layer of very fine to medium grain-size. In order to apply the topographic static shift and/or migration, we need to know the velocity of the GPR waves. In Figure 5a we also observe a nice 10 m wide (80 traces) diffraction hyperbola situated just under the base of the dune (see black circle). After analyzing this diffraction, with different velocities, we found that it can be fitted very well with a constant velocity model of 0.18 m/ns. This value represents an average velocity from the surface of the dune to the diffraction point and it is in good agreement with values found in the literature for dry sands (Gómez et al., 2009; Guillemoteau et al., 2012).

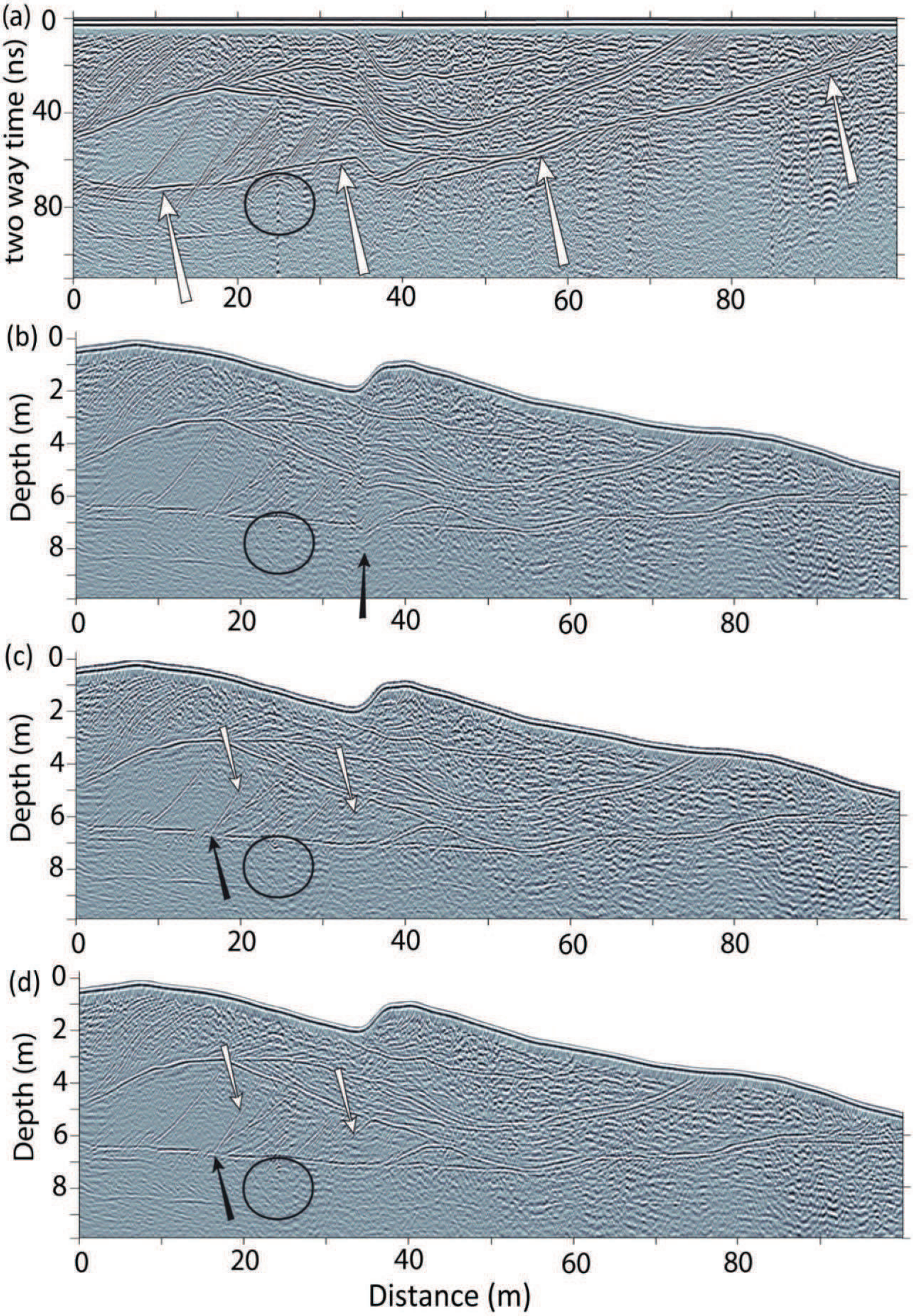

Figure 5 : GPR profile acquired over a Chadian dry dune with a 450 MHz antenna. a) After the standard processing described in the text. b) After a standard migration followed by a static shift, with a velocity of 0.18 m/ns. This same velocity has been used for all the following migrations and topographic corrections. c) After static shift followed by standard migration and d) After Kirchhoff's topographic migration.

Figure 5b shows the same GPR profile as in Figure 5a, but when a standard migration followed by topographic corrections are performed, using a velocity of 0.18 m/ns. The topography shows a local variation of about 30% (at profile coordinate 38 m, black arrow on figure 5b) and its global variation of about 5 m (5%) is comparable to the investigation depth. The diffraction hyperbola is well collapsed (at profile coordinate 25 m, black circle) and the reflection from the base of the dune is roughly flattened. Below the area of high topographic gradient (38 m horizontally) we observe a very bad feature (black arrow). The whole area looks blurred, and reflectors are losing consistency. The results of the standard migration followed by topographic corrections are bad.

Figure 5c presents the profile after a static shift followed by a standard migration. The migration hyperbola (black circle) is slightly over-migrated. The bad feature indicated by the black arrow in figure 5b is corrected. The reflectors are now consistent and the dipping reflector shown by the black arrow (Figure 5c) has been moved up-dip.

Figure 5d presents the topographic migration with the same velocity (0.18 m/ns, as in both previous cases) and a specific migration template 13 m wide (100 traces) has been chosen, which is slightly larger than the width of the observed hyperbola (10 m) on the profile. The base of the dune is flattened and the diffraction at 25 m is now correctly focused on a single point inside the black circle, which justifies our choice of 0.18 m/ns for the GPR velocity. The dipping reflector shown by the black arrow has undergone a vertical and horizontal shift of 1.1 and 3.8 m, respectively. It starts at the base of the dune and goes up-dip rightwards as expected (on the non-migrated section of Figure 5a, these reflections were crossing the base of the dune).

The measured dips on the topographic migrated section of the same reflectors (shown by white arrows) are slightly larger than the dips measured on Figure 5c (static shift followed by standard migration). Their values are now 26.5° and 19.5° on the topographic migrated section, instead of 25° and 17.7° in Figure 5c. Although the global topographic variation of the profile does not exceed 5%, the result of the topographic migration is slightly better than the result of the static shift followed by the standard migration. Remember here that the later routine over-migrates the data at large depth (case of the diffraction under the base of the dune).

Figure 6 shows a portion of the profile of Figure 5d with topographic migration for different velocities ranging from 0.16 m/ns (left) to 0.20 m/ns (right) with a 0.1 m/ns increment. The hyperbola is not collapsed for the two first figures, while it is over-migrated for the last two. The middle figure shows the migrated image with the correct velocity of 0.18 m/ns. The depths and the dips of the reflectors are also changed. The depth of the diffracting point is ranging from 6.5 m (for a velocity of 0.16 m/ns) to 7.8 m (for a velocity of 0.20 m/ns). Therefore, a change of around 5% in the velocity causes a change in depth of nearly 0.3 m (for a depth of around 7 m). The dip of the reflector indicated by white arrows (Fig. 6) is ranging from 22.6° (velocity of 0.16 m/ns) to 29.9° (velocity of 0.20 m/ns). The dip increases by roughly 2° per 0.01 m/ns velocity increase. To have a correct migration, we conclude that the precision in the estimation of the velocity should be better than 5% of the true velocity.

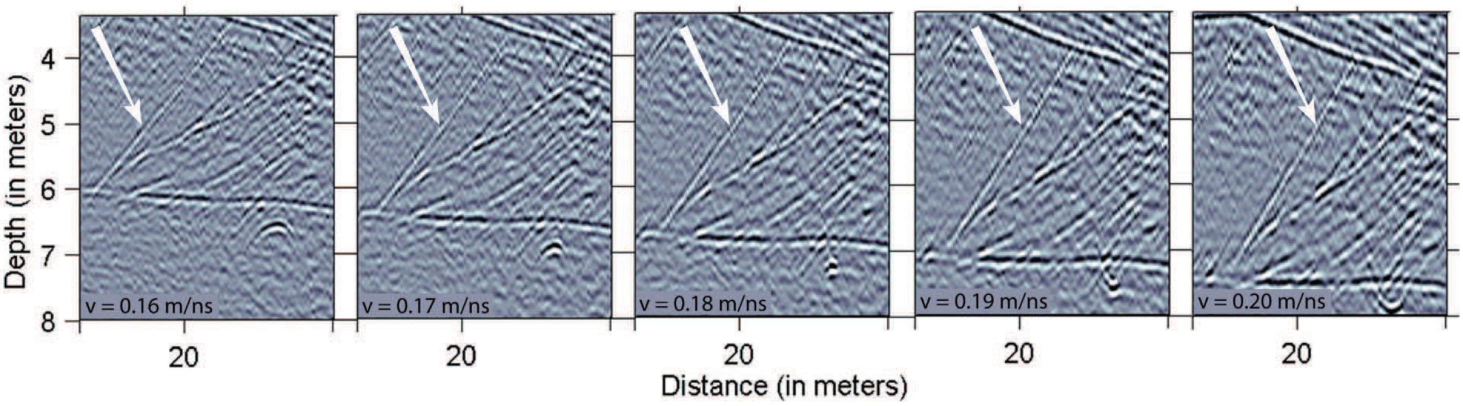

Figure 6 : Detailed area of the base of the dune showing the diffraction topographic migration (under the base of the dune) for different velocities ranging from 0.16 m/ns (on the left) to 0.20 m/ns (on the right) with a 0.01 m/ns increment. The Figure in the middle shows the correct topographic migration with V = 0.18 m/ns.

2.3.2. Example of a fault in Mongolia

In 2010 we conducted a GPR campaign in Mongolia, 80 km to the west of the capital Ulaanbaatar. The context of this study was seismic hazard. Figure 7 shows a GPR profile obtained with an unshielded 50 MHz Rough Terrain Antenna (RTA). The profile is more than 200 m long and is perpendicular to the Hustaï Fault. This is in a context of a very low slip rate (most likely less than 1 mm per year), and the fault geomorphology has been smoothed during a long period of erosion. Therefore displacements in the topography are not observable. However, in the field, evidences of the fault plane are still visible. Most of the profiles acquired in this area display a strong reflection, which corresponds to the fault plane. These profiles give complementary information such as the dip of the structure and the exact location of the fault near the surface to help design the layout of future paleoseismic campaigns. The acquisition mode was a constant offset of 4.1 m, traces have been recorded every 0.2 m with a stack of 16 to improve the signal-to-noise ratio.

The processing used to obtain Figure 7a is similar to the one used in the case of the Chadian GPR data. A velocity analysis, which is not presented here, has been done over the surveying area by analysing diffraction hyperbola present in the GPR data. A mean velocity of 0.12 m/ns has been determined for the whole area. As in the previous example, the topographic variation of 20 m (slope less than 10%) is comparable to the investigation depth. Figures 7b, 7c and 7d respectively display the data after standard migration followed by static shift, static shift followed by standard migration, and topographic migration. The diffraction hyperbola indicated by the black circle is well focused in Figures 7b and 7d, and appears slightly over-migrated in Figure 7c (as in the case of the Chad dune). The dipping reflector (fault plane) indicated by the white arrow now displays a constant slope down to a depth of 24 m in Figures 7b and 7d. However, on the section of Figure 7c, the reflector is attenuated at a depth of 17 m and has lost its continuity. Its dip angle is changing from 32.2° (migration and static shift) to 34° (static shift and migration and migration with topography). The main observation is the location of the reflector, which is very similar in the case of Figures 7b and 7d, while in Figure 7c the reflector has been shifted (5.5 m horizontally and 2.6 m vertically) and is reaching the surface. In this case, the migration followed by static shift seems to give more convincing results than the static shift followed by migration (which is the opposite of what was observed in the Chadian dune example). From this result, we conclude that topographic migration should be considered at any location where the subsurface shows steep dip angle structures (exceeding 30°), even in the case where the surface slope is less than 10%.

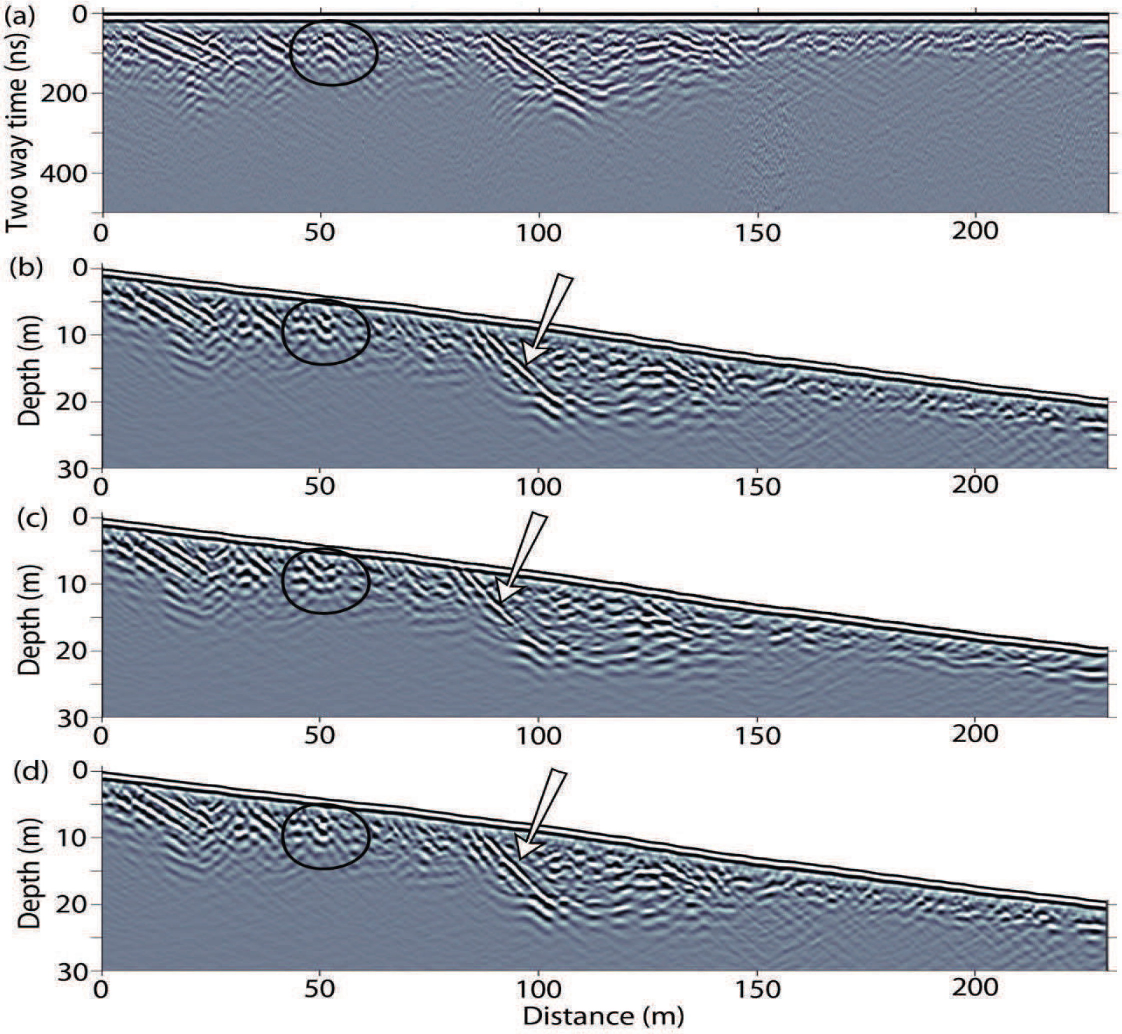

Figure 7 : GPR profile obtained in Mongolia with an unshielded 50 MHz Rough Terrain Antenna. a) Standard processing (see the text). b) With standard migration followed by static shift. c) With static shift followed by standard migration and d) With topographic migration. Static corrections and migrations are performed with a constant velocity of 0.12 m/ns.

As in the previous case, we performed a velocity sensitivity analysis by using a topographic migration of the fault plane reflection with different velocities ranging from 0.1to 0.14 m/ns with a 0.01 m/ns step. After topographic migrations, the slope of this reflector is varying from 28.9° to 39.5° and increases by roughly 2.65° for a 0.01 m/ns increase in the velocity. In this case, for a correct topographic migration, the estimation of the velocity should be better than 8%.

2.4. Conclusion

In the presence of relief variations of the same order as the investigation depth of GPR data, a topographic migration is necessary to correctly locate the dipping reflectors and focus the diffractions. The topographic migration, presented in this article, is based on Kirchhoff's algorithm similar to the method proposed by Lehmann and Green (2000). The application may be more useful for GPR data than for seismic data, as the topographic variations are comparable to the depth of the target structures. We demonstrate the template migration equation, as a function of the topography, along which the amplitudes are added together to give a single point on the migrated section.

By comparing processed sections obtained from GPR data measured over media of high EM velocity (dry sand) having large local topographic variations within a global topographic slope of 5%, we show that reflectors obtained by standard processing (static shift corrections followed by migration) have dip angles that deviate from the angles in a topographically migrated profile by 1 to 2°. Their locations are also changing by a few meters even for reflectors close to the surface. Thus, for high velocity media with large local topographic variations, even in the case where the global surface slope does not exceed 5%, the application of the topographic migration is necessary and efficient. We also show that topographic migration should be considered at any location where the subsurface shows steeply dipping structures (>30°), even for surface topographic slopes of less than 10%. Finally, we have shown that the precision in the velocity estimation should be from 5 to 10% of the true velocity, in order to have a correct topographic migration.

3. Le filtre anti-aliasing sur l'opérateur

3.1. Introduction et travaux antérieurs

L'aliasing est un problème bien connu en géophysique et plus généralement dans tous les domaines impliquant un signal échantillonné. Il a été décrit et quantifié par Nyquist. Son théorème énonce que la composante fréquentielle maximum enregistrée dans un signal est égale à la moitié de la fréquence d'échantillonnage. Les fréquences plus élevées subiront un sous-échantillonnage conduisant au phénomène d'aliasing.

En sismique, lors de la migration de Kirchhoff (basée sur la sommation du signal le long d'hyperboles), trois types d'aliasing sont observés :

1. Sur l'image de départ, dû au sous-échantillonnage du signal. Si le théorème de Nyquist est respecté, le signal final est libre d'aliasing.

2. Sur l'image d'arrivée (après migration), si l'image est sous-échantillonnée. Si l'image de départ est correctement échantillonnée et que l'image d'arrivée conserve le même échantillonnage, aucun aliasing n'est observé (sous condition de ne pas observer l'aliasing de troisième type).

3. L'aliasing sur l'opérateur. Il apparait lorsque la pente de la trajectoire de migration devient trop importante pour un contenu fréquentiel et un pas inter-trace (dx) donné. Mathématiquement, il intervient lorsque pour le passage de x à $x+\Delta x$, t(x) saute plus qu'un seul Δt. L'aliasing peut se présenter dans les données finales comme un bruit aléatoire ou cohérent.

Ce troisième type d'aliasing est bien connu en sismique. De ce fait, plusieurs méthodes (trois principales) ont été développées pour en réduire voire en supprimer les effets :

1. Ouverture de l'opérateur : consiste à limiter la largeur de l'hyperbole de sommation. Cette méthode est la plus simple à mettre en œuvre mais les réflexions montrant un fort pendage sont largement atténuées, voire supprimées. De plus un aliasing sur les faibles pentes à haute fréquence peut subsister.

2. Interpolation des traces : l'augmentation du nombre de traces par interpolation augmente l'échantillonnage et réduit les risques d'aliasing. Néanmoins les algorithmes d'interpolation des données sont très couteux en mémoire et en temps de calcul.

3. Filtres basés sur la pente de l'opérateur. C'est une méthode implémentée directement dans le processus de migration et celle qui sera développée dans la suite.

Gray (1992) propose une méthode où au moins trois copies des données sont filtrées via des filtres passe basse-fréquences dont la fréquence de coupure choisie est de plus en plus basse d'un jeu de données à un autre. Les données lors de la migration sont utilisées en fonction de la fréquence maximum non aliasée. Lorsque la pente devient trop abrupte et que la condition de la fréquence maximum utilisée n'est plus respectée, on utilise le jeu de données filtrées à la fréquence basse suivante. Le critère de la fréquence maximum utilisée est le critère d'échantillonnage de Nyquist pour une pente, soit :

$$f_{\max} \leq \frac{1}{2(\partial t_k / \partial \rho)\Delta\rho}$$

où $\partial t_k/\partial \rho$ est la dérivée spatiale de l'opérateur de migration au point d'intersection avec la trace sismique, et $\Delta\rho$ est l'espacement inter-trace le long de la surface d'enregistrement (soit Δx en 2D). Il est à noter que la présence d'une topographie peut localement limiter ou amplifier le phénomène d'aliasing.

Claerbout (1992) et Lumley et al. (1994) présentent une méthode basée sur le même principe, mais le filtrage passe-bas s'effectue avec un filtre triangulaire. La méthode de Gray semble bénéficier d'une vitesse de calcul bien plus rapide que la méthode de Lumley mais nécessite une capacité de mémoire plus importante. Selon Lumley, dans le cas de mesure 3D, $\Delta\rho$ devient

$$\Delta\rho = \max(\Delta x \cos\theta, \Delta y \sin\theta)$$

avec Δx l'espacement inter-trace le long des profils in-line, Δy l'espacement entre les profils et θ l'azimuth de l'opérateur gradient.

D'autres auteurs ont travaillé sur l'amélioration de la méthode. Abma et al. (1999) ont amélioré la fréquence de coupure et dans le cas de données 3D, $\Delta\rho$ devient :

$$\Delta\rho = \sqrt{(\Delta x \cos\theta)^2 + (\Delta y \sin\theta)^2}$$

Cette modification montre une amélioration significative des réflexions pentées dans les données.

Biondi (2001) montre la possibilité de récupérer du signal dans des données où l'aliasing est déjà présent. Cette méthode nécessite une information a priori sur les pendages. Toutes les études précédentes se basent sur une migration en temps. Baina et al. (2003) adaptent la méthode pour la migration en profondeur et pour finir, Wang et al. (2003) restreignent encore la fréquence de coupure pour conserver encore plus de signal et garder des amplitudes plus fortes dans les réflexions pentées.

3.2. Le principe retenu

Bien que les ondes soient différentes entre les données sismiques (ondes acoustiques) et les données géoradar (ondes électromagnétiques), le système de propagation est le même (propagatif) et le mode de présentation des données est également similaire. Une série de traces juxtaposées constitue le profil et par conséquent, un certain nombre de traitements en géoradar sont issus d'adaptation de traitement en sismique. C'est le cas de la migration de Kirchhoff ainsi que des problèmes inhérents à la méthode.

En nous basant sur l'approche de Gray, nous allons adapter la méthode de l'anti-aliasing pour la migration avec topographie et en investiguer les effets sur les données GPR. Comme présenté précédemment, plusieurs auteurs ont démontré les améliorations sur les données en réajustant la fréquence de coupure. Dans notre cas, nous nous limitons à évaluer les effets de la méthode en ne prenant pour fréquence de coupure que celle présentée initialement (eq. F_{max}, p. 37). Un coefficient sera cependant ajouté à ce calcul pour augmenter ou diminuer les fréquences retenues et ainsi en apprécier les effets. Ce coefficient sera par la suite appelé coefficient de restriction (Cr).

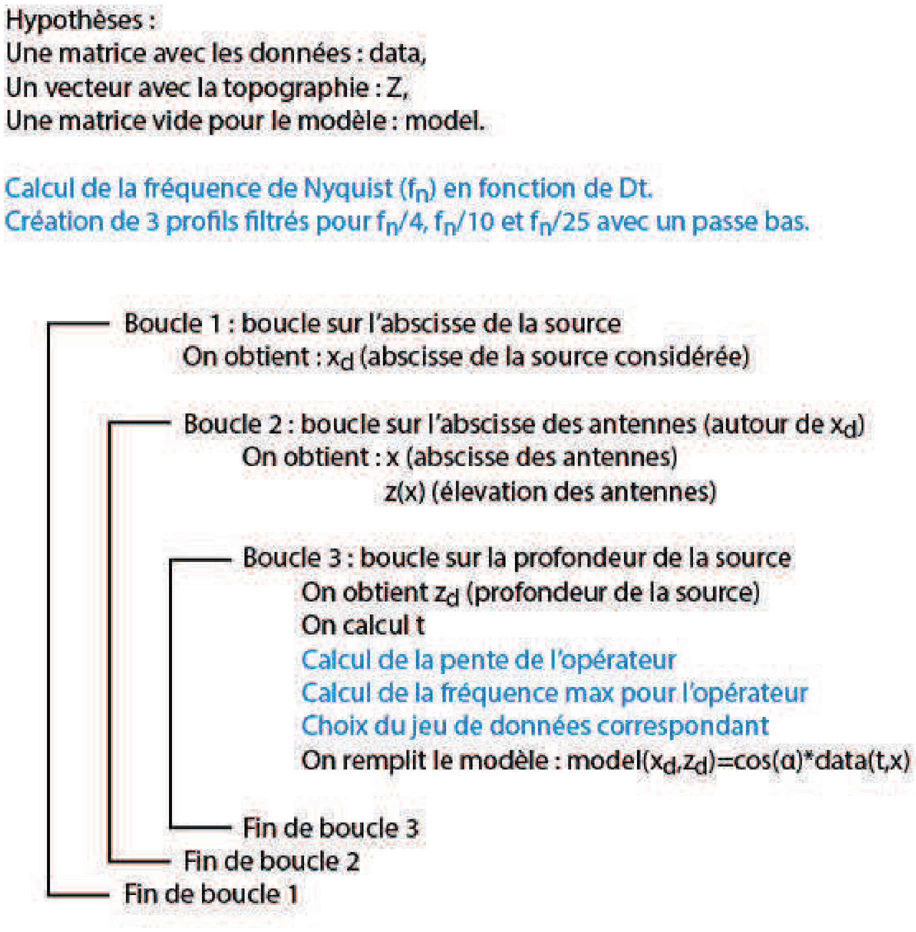

```
Hypothèses :
Une matrice avec les données : data,
Un vecteur avec la topographie : Z,
Une matrice vide pour le modèle : model.

Calcul de la fréquence de Nyquist ($f_n$) en fonction de Dt.
Création de 3 profils filtrés pour $f_n/4$, $f_n/10$ et $f_n/25$ avec un passe bas.

Boucle 1 : boucle sur l'abscisse de la source
        On obtient : $x_d$ (abscisse de la source considérée)

    Boucle 2 : boucle sur l'abscisse des antennes (autour de $x_d$)
            On obtient : x (abscisse des antennes)
                         z(x) (élevation des antennes)

        Boucle 3 : boucle sur la profondeur de la source
                On obtient $z_d$ (profondeur de la source)
                On calcul t
                Calcul de la pente de l'opérateur
                Calcul de la fréquence max pour l'opérateur
                Choix du jeu de données correspondant
                On remplit le modèle : $model(x_d,z_d)=cos(\alpha)*data(t,x)$

        Fin de boucle 3
    Fin de boucle 2
Fin de boucle 1
```

Figure 8 : Schéma présentant les différentes étapes de l'algorithme de migration topographique avec prise en compte du filtre anti-aliasing. Les lignes en noir sont les mêmes que dans la partie précédente (i.e. la migration topographique). Les lignes en bleu sont spécifiques au filtre anti-aliasing. Avant d'entamer les trois boucles successives, la fréquence de Nyquist est calculée en fonction de Dt, puis trois copies du profil à migrer sont filtrées via un filtre passe-bas pour $f_n/4$, $f_n/10$ et $f_n/25$. Au sein de la troisième boucle, la fréquence maximum non aliasée de l'opérateur est calculée en fonction de sa pente, puis le jeu de données approprié est sélectionné pour la sommation de long de l'hyperbole.

3.3. Algorithme

Le schéma de la figure 8, similaire à celui présenté pour la migration topographique, présente les différentes étapes de la migration avec topographie en prenant en compte le filtre anti-aliasing. Ainsi, les notations et les hypothèses préliminaires sont les mêmes que dans le schéma précédent et ne seront pas redéfinies. Les instructions relatives au filtre anti-aliasing sont en bleu. En premier lieu, la fréquence de Nyquist est calculée :

$$f_n = \frac{1}{2 * Dt}$$

et trois sous profils filtrés via des filtres passe-bas sont calculés (avec des fréquences de coupures de plus en plus basses : $f_n/4$, $f_n/10$ et $f_n/25$).

A l'intérieur de la troisième boucle (sur la profondeur de la source), la pente de l'opérateur est calculée (slo) en prenant en compte la topographie, puis la fréquence maximum non aliasée le long de l'opérateur et donné par l'équation : $F_{\max} = \frac{1}{2 * slo * Dx}$

avec slo la pente de l'opérateur et Dx la distance inter-trace. F_{max} est divisée par le coefficient de restriction (Cr) dans le cas où celui-ci est donné. Ainsi, pour un coefficient supérieur à 1, l'algorithme est plus restrictif. Dans le cas d'un coefficient compris entre 0 et 1, plus de signal est conservé. Le jeu de données filtrées approprié est alors choisi pour la sommation de Kirchhoff.

Il est à noter que l'utilisation du filtre anti-aliasing augmente le temps de calcul. Pour le jeu de données utilisé dans tous nos tests (i.e. la dune de sable comprenant 681 échantillons et 800 traces), le temps de calcul passe de 11 à 50 secondes, ce qui reste inférieur à la minute, et largement utilisable pour la plupart des jeux de données si nécessaire.

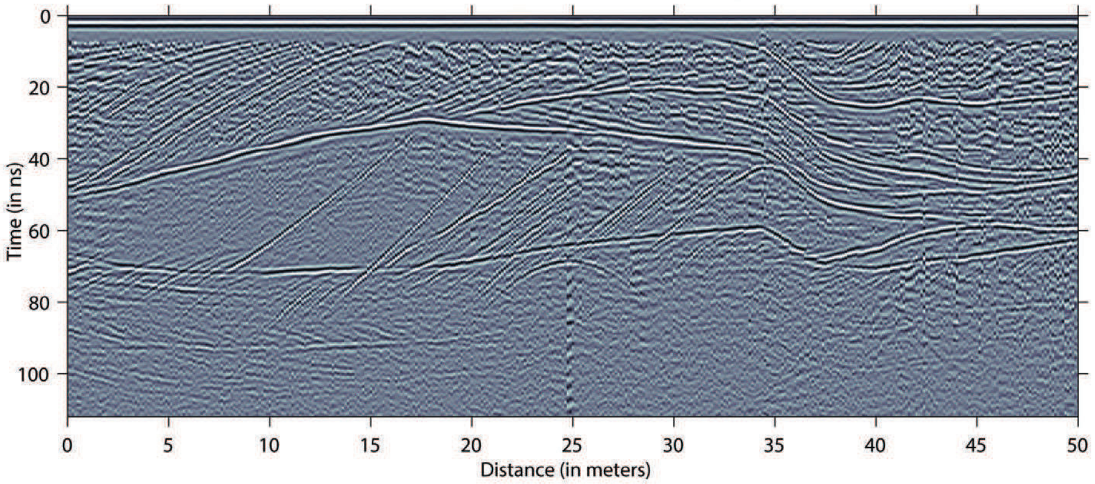

Figure 9 : Profil utilisé pour la démonstration du filtre anti-aliasing. Ce profil est le même que celui utilisé pour la démonstration de la migration topographique (Fig. 5a). Seuls les 50 premiers mètres ont été utilisés.

3.4. Résultats

Une portion du profil utilisé dans le chapitre précédent (dune éolienne du Tchad) est réutilisée ici pour investiguer les effets du filtre. La version non migrée de la section radar est présentée sur la figure 9. Les trois profils de la figure 10 montrent la même section après migration topographique (Fig. 10a), après migration topographique et filtre anti-aliasing avec un coefficient de restriction de 1 (Fig. 10b) et avec un coefficient de restriction de 3 (Fig. 10c). Pour faciliter les comparaisons, les différences entre le profil migré sans filtre anti-aliasing et les profils avec anti-aliasing sont montrés sur la figure 11 (a et b respectivement).

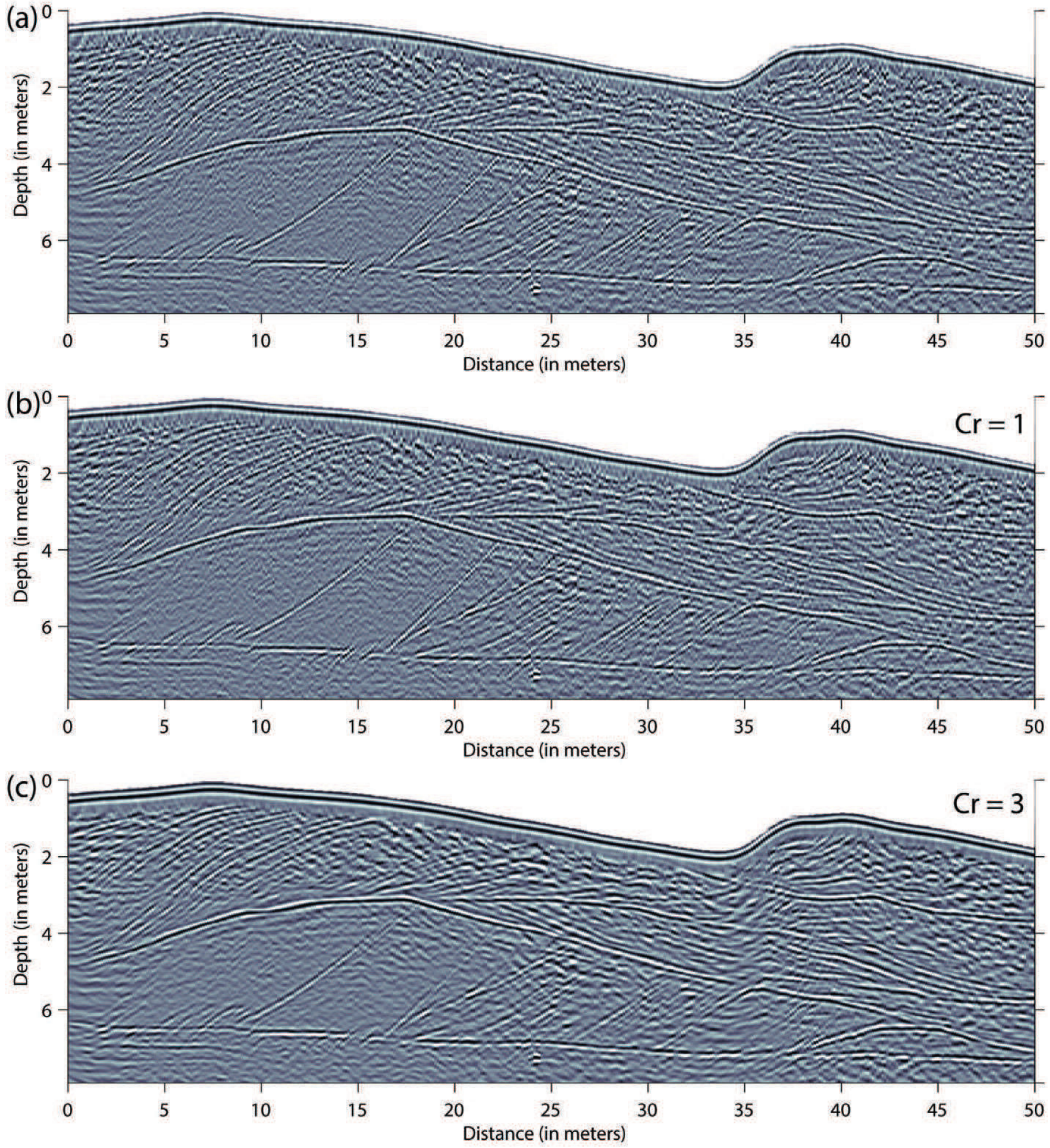

Figure 10 : (a) Section de la figure 9 après migration topographique sans filtre anti-aliasing ; (b) avec filtre anti-aliasing et Cr = 1 ; (c) avec filtre anti-aliasing et Cr = 3.

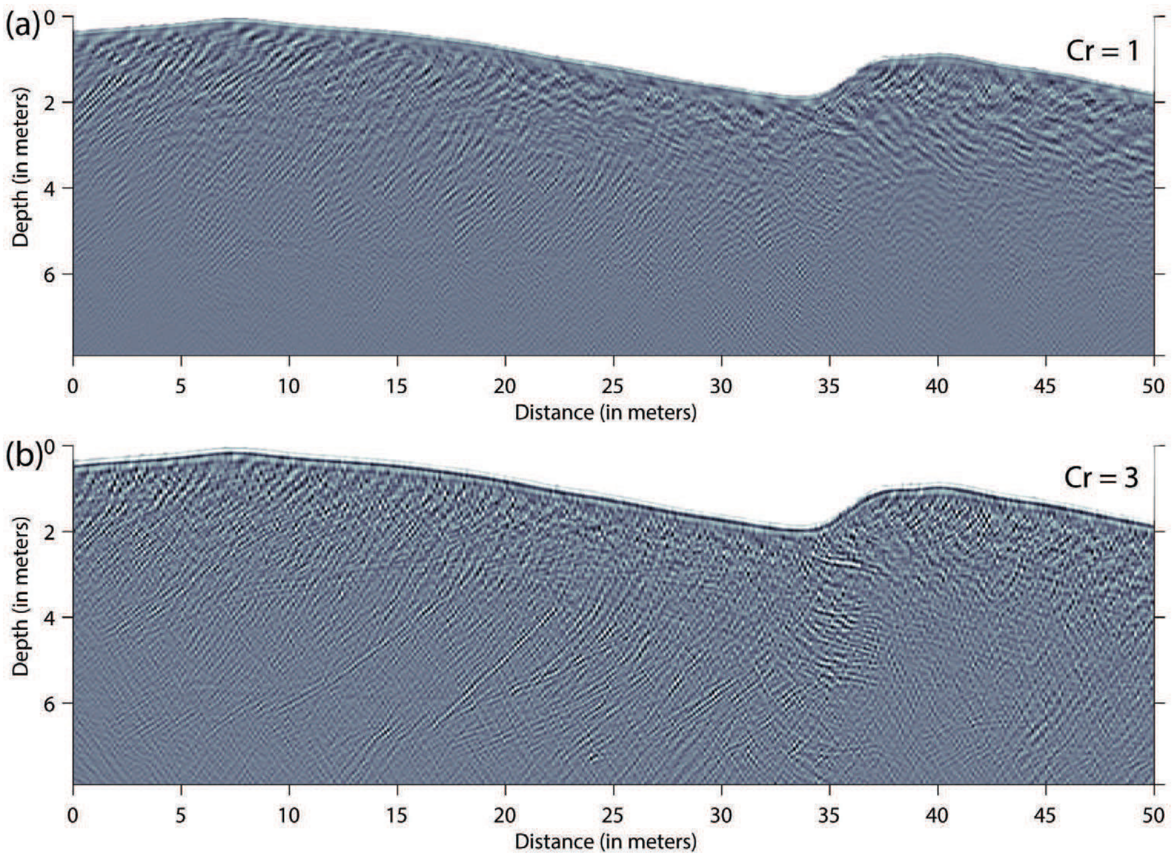

Figure 11 : Différences entre la section migrée sans filtre anti-aliasing et les sections migrées avec filtre anti-aliasing et (a) Cr = 1 et (b) Cr = 3.

Les variations sur la section avec un coefficient de restriction de 1 (Fig. 10b) sont quasiment invisibles à l'œil nu. Seule la différence avec la section migrée (Fig. 11a) nous permet de voir les variations. Lorsque le coefficient de restriction augmente (Fig. 10c), les changements deviennent évidents. Le troisième profil est « lissé » par rapport aux deux premiers. La « granulosité » observée dans les deux premiers profils disparait, ainsi que les arcs de cercle montant vers la surface (artefacts de la migration de Kirchhoff), observables presque partout dans les données et très marqués dans la zone d'ombre juste sous la première arrivée. Cependant, l'amplitude des réflexions montrant un pendage (et d'autant plus que le contenu fréquentiel est élevé) est fortement atténuée (réflexion montrant un pendage entre 4 et 6 m de profondeur). Le signal est également fortement atténué dans la zone à fort gradient topographique (à 35 m de distance).

Les profils de la figure 11 confirment les observations précédentes. Dans le premier cas (Fig. 11a), le signal supprimé est totalement découplé des réflexions observées sur le profil (Fig. 10b). Les amplitudes du signal éliminé étant faibles, les effets sur le profil sont quasiment imperceptibles. Ce signal supprimé est retrouvé dans la figure 11b, mais noyé parmi un signal plus fort. Un grand nombre de signaux observés dans ce dernier est indépendant des réflexions (les artefacts de migration notamment), mais on commence cependant à retrouver des réflexions pentées ainsi que le signal autour de 35 m (à l'aplomb de la forte variation de topographie), preuve d'un filtrage trop intense.

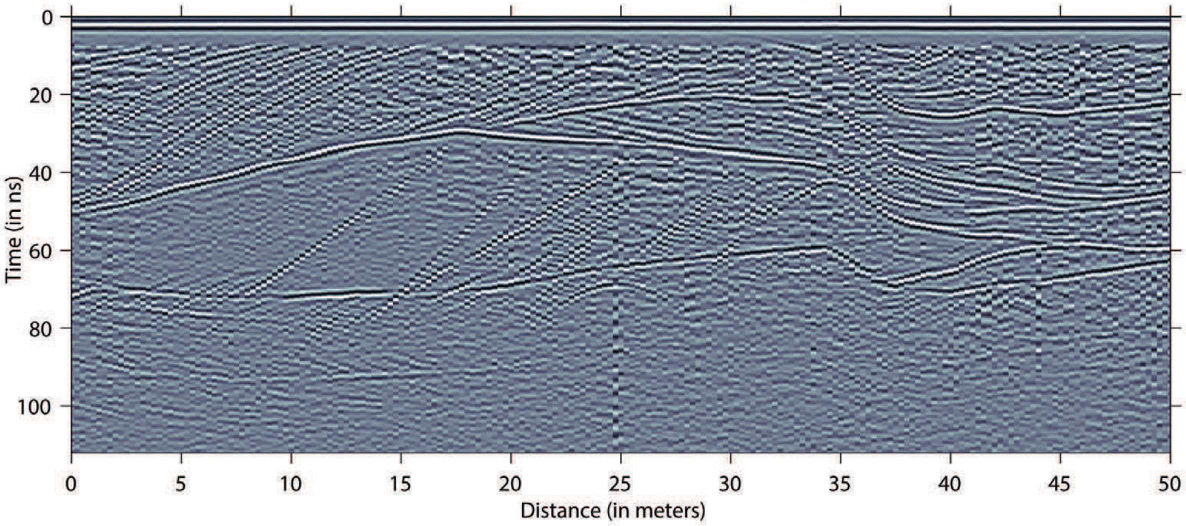

Figure 12 : Section de la figure 9 après ré-échantillonnage. Une trace sur deux est conservée.

Ce premier essai de l'utilisation d'un filtre anti-aliasing dans l'algorithme de migration topographique montre des résultats intéressants. Le filtre, avec un coefficient de restriction de 1, supprime bien un signal indépendant des réflexions observées, mais dont les amplitudes sont faibles (environ 3 fois inférieures au signal). Les différences observées entre les deux profils sont par conséquent minimes. Il faut augmenter le coefficient de restriction pour évaluer les effets du filtre. Une « granulosité » dans le profil ainsi que les artefacts de migration sont alors supprimés. Cependant, un coefficient de restriction trop élevé se traduit également par une perte des hautes fréquences, ainsi que par l'atténuation des réflexions pentées et des réflexions présentes sous les zones de fort gradient topographique. Dans le cas de la dune, un coefficient de restriction intermédiaire entre 1 et 3 serait le mieux adapté. Néanmoins, dans cet exemple, le signal étant bien échantillonné et de bonne qualité, l'aliasing sur l'opérateur n'est pas flagrant et le filtre n'est pas d'une absolue nécessité.

Pour tester le filtre sur des données de moins bonne qualité, le profil précédent (Fig. 9) a été ré-échantillonné en ne gardant qu'une trace sur deux. Le résultat est affiché sur la figure 12 et l'aliasing dans les données devient évident dans les réflexions avec pendage. Comme précédemment, les sections migrées sans anti-aliasing, avec anti-aliasing et un coefficient de restriction de 1 et avec un coefficient de restriction de 2 sont présentées sur la figure 13 (a, b et c respectivement).

Dans la première section (Fig. 13a), les données sont fortement dégradées. Les réflexions principales correspondant aux limites des dunes sont retrouvées mais beaucoup moins claires. Les réflexions pentées correspondant aux litages sont très difficilement observables car noyées dans le bruit (cercles noirs, fig. 13a). Après utilisation du filtre anti-aliasing (Fig. 13b), on observe directement qu'une grande quantité de bruit est retirée des données. La figure 14, affichant les différences entre la section sans filtre et les sections avec filtre anti-aliasing (coefficient de restriction de 1 et 2 pour respectivement les figures 14a et 14b) montre bien une grande quantité de signaux indépendant des réflexions. Les réflexions provenant des litages, difficilement interprétables dans la section précédente, font leur apparition (voir cercles noirs). La dernière section montre le profil avec un coefficient de restriction de deux. Une part supplémentaire de signal a été ôtée, s'exprimant par une impression de lissage des données. La lisibilité en est facilitée. Cependant, l'amplitude des réflexions pentées est largement atténuée et une perte significative de signal apparait dans la zone à fort gradient topographique. La section de la figure 14b illustre bien le problème. Parmi un bruit incohérent, des réflexions provenant du profil apparaissent et sont autant de signal utile supprimé. Il en résulte les pertes d'amplitude constatées sur la figure précédente.

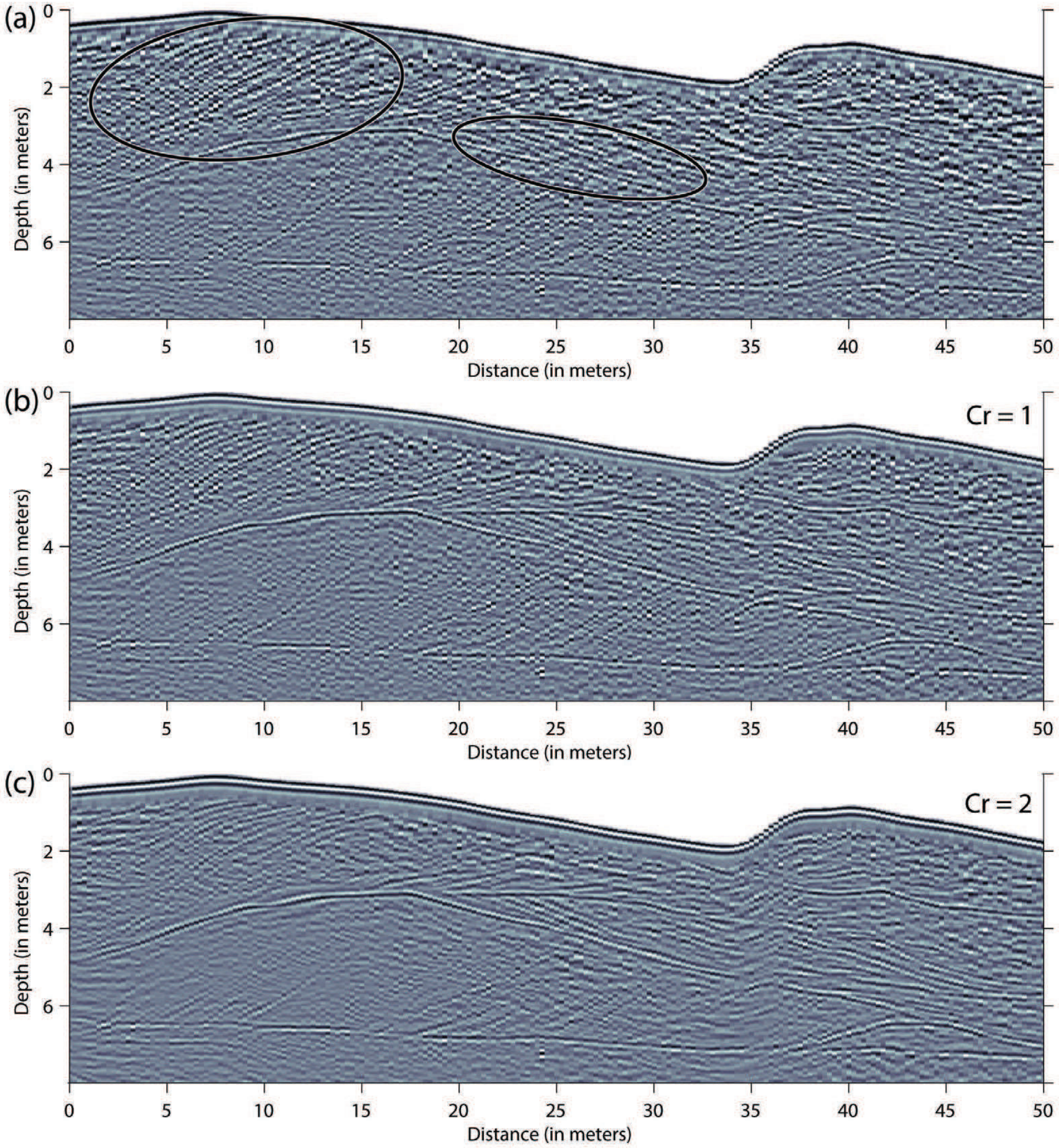

Figure 13 : (a) Section de la figure 12 après migration topographique sans filtre anti-aliasing. Les cercles noirs indiquent les réflexions pentées masquées dans le bruit. (b) Avec filtre anti-aliasing et Cr = 1 ; (c) avec filtre anti-aliasing et Cr = 2.

En conclusion, l'algorithme de prise en compte de l'aliasing sur l'opérateur est efficace. Il améliore significativement les données dans les cas où l'aliasing sur l'opérateur est marqué (et dans les cas où un aliasing sur les données est présent). Le temps de calcul en est considérablement augmenté (multiplié par 5 dans notre exemple), mais la migration restant inférieure à une minute, son utilisation reste tout à fait adaptée pour de larges jeux de données. Dans les données radar actuelles, le signal est généralement sur-échantillonné. Les profils non migrés sont donc libres de tout aliasing et l'aliasing sur l'opérateur n'apparait que très rarement. L'utilisation de cet outil peut donc être négligeable dans le cas de données 2D. En revanche, pour des raisons de temps de mesure, les conditions d'aliasing sont plus rarement respectées dans le cas de mesures 3D. Une vraie migration 3D pourrait grandement bénéficier de cet outil. Malheureusement, n'ayant pas à notre disposition un jeu de données adapté, nous ne pouvons présenter ici de résultats sur la 3D.

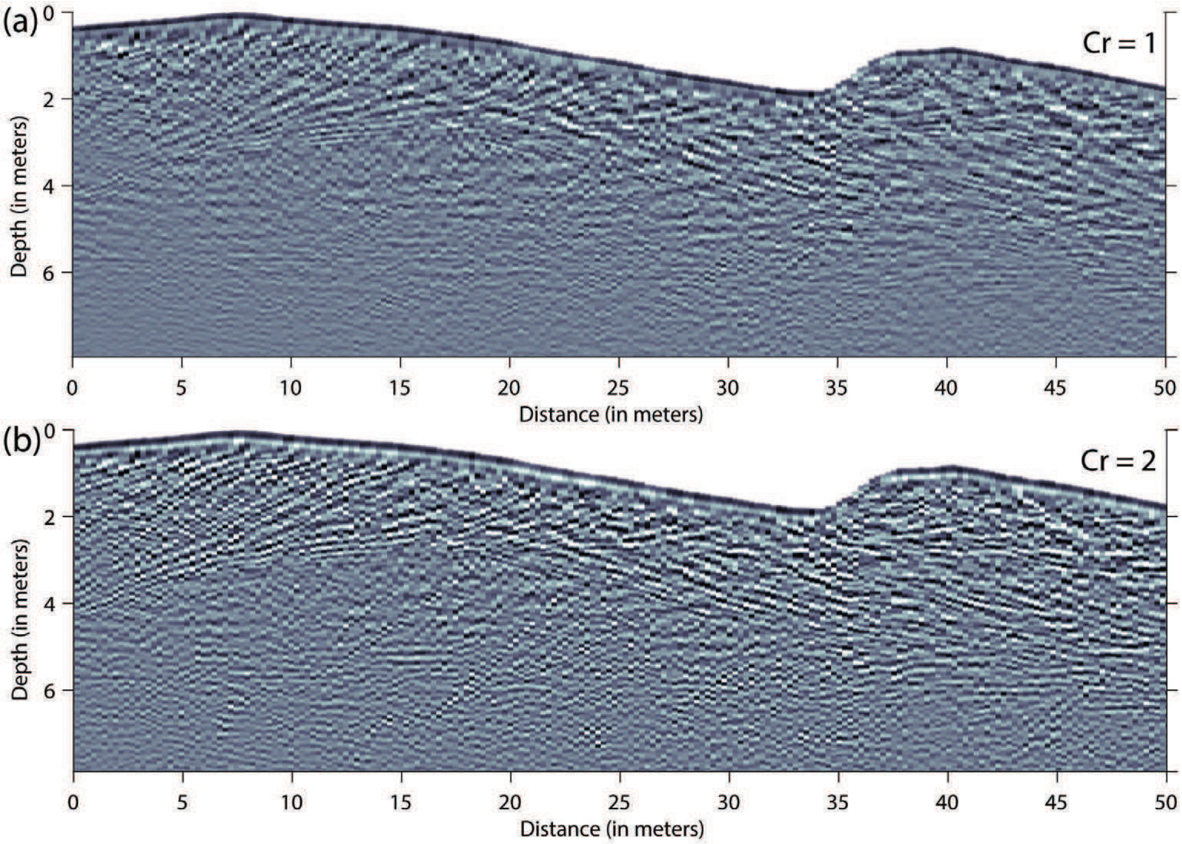

Figure 14 : Différence entre la section migrée sans filtre anti-aliasing et les sections migrées avec filtre anti-aliasing et (a) Cr = 1 et (b) Cr = 2.

4. Le calcul de pentes automatiques

4.1. Introduction

Le bruit est un problème récurrent en géophysique et plus largement dans tous les domaines impliquant un enregistrement. La qualité des données en est altérée, ainsi que les interprétations qui en découlent. En géoradar, le bruit a tendance à réduire la continuité des réflexions et dans les cas les plus extrêmes, à les masquer. Sa réduction, voir sa suppression, peut être cruciale pour une interprétation correcte des données.

Le bruit est constamment présent dans les données géophysiques et peut apparaitre lors de deux stades. Pendant l'enregistrement des données, lorsque le rapport signal/bruit est trop faible, mais également pendant les étapes de traitement de données, par amplification du bruit existant au détriment du signal ou par introduction d'un bruit supplémentaire lors de l'utilisation d'un filtre (artefacts). En géoradar, la première source de bruit est contrée par augmentation du nombre de mesures pour une trace. Dans le deuxième cas, beaucoup de filtres ont été imaginés, créés et améliorés pour le diminuer. Parmi les plus fréquents, on retrouve les filtres fréquentiels (passe-bande, filtre f-k, filtre prédictif spatial). Tous ces filtres contribuent à améliorer les données lorsque leur utilisation est modérée. Lors d'une utilisation poussée, une partie du signal utile est supprimée, réduisant du même coup la résolution des données. Dans la majorité des cas, les réflexions montrant un pendage et les réflexions à haute fréquence sont les premières à être dégradée par les filtres.

Pour pallier à ce problème, nous avons, dans ce chapitre, investigué un nouveau type de filtre basé sur une information a priori sur les pendages. Ce filtre, développé originellement pour les données sismiques, s'effectue en deux étapes : le calcul des pendages présents dans les profils, dont le résultat sera appelé profil de pendages, et le filtrage des données utilisant cette information a priori. Ce chapitre est donc présenté comme suit : la présentation des algorithmes de calcul des pendages (en domaine fréquentiel et temporel), avec les résultats ; le filtrage des profils de pendages ; application du filtre sur les données et présentation des résultats ; un exemple complet impliquant une migration topographique.

4.2. Les profils de pendages

4.2.1. Algorithmes

Deux algorithmes ont été codés et comparés pour calculer les profils de pendages. L'un dans le domaine temporel et le second dans le domaine fréquentiel. Le principe de base est similaire pour les deux algorithmes. Une double boucle permet de parcourir le profil le long des traces et des échantillons. Une fenêtre avec une longueur donnée est centrée, pour une trace donnée (de référence), sur un échantillon dit de référence. Une fenêtre glissante, de même longueur que la fenêtre de référence, parcourt la trace précédant et la trace suivant la trace de référence. La fenêtre montrant la plus grande corrélation avec la fenêtre de référence permet de déduire la pente.

Les pentes sont enregistrées en nombre d'échantillons pour une distance d'une trace. Ainsi une pente de zéro est une réflexion horizontale. Les figures 15 et 16 sont des schémas détaillant les algorithmes dans le domaine respectivement temporel et fréquentiel.

- Le domaine temporel :

L'algorithme dans le domaine temporel est présenté schématiquement sur la figure 15. Les pré-requis sont les données, enregistrées dans une variable *data*, et une variable *len* contenant la longueur de la fenêtre glissante (en nombre d'échantillons). Le profil est ensuite parcouru le long des traces et des échantillons à l'aide d'une double boucle. Une sous-trace, de la longueur de la fenêtre glissante et centrée sur l'échantillon considéré est enregistrée dans une variable *ref*. Cette variable sera l'échantillon de référence pour les comparaisons et la valeur de la pente déduite sera affectée à l'échantillon central de cette variable.

Une troisième boucle parcourt les échantillons des traces précédentes et suivantes, confinés autour de l'échantillon de référence. A chaque itération, une sous-trace de chacune des traces précédentes et suivantes est enregistrée dans une variable temporaire. Les coefficients de corrélation entre ces sous-traces et la sous-trace de référence (*ref*) sont calculés et les résultats enregistrés dans une nouvelle variable (*Corcofneg* et *Corcofpos* respectivement pour la trace précédente et la trace suivante) avec l'écart d'échantillon avec la sous-trace de référence.

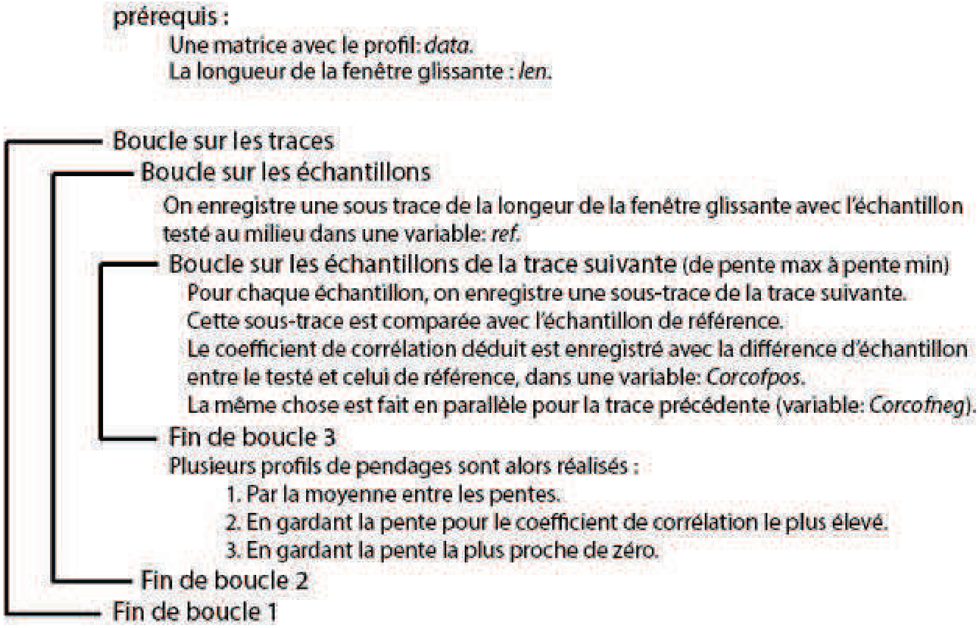

```
prérequis :
    Une matrice avec le profil: data.
    La longueur de la fenêtre glissante : len.

Boucle sur les traces
  Boucle sur les échantillons
    On enregistre une sous trace de la longeur de la fenêtre glissante avec l'échantillon
    testé au milieu dans une variable: ref.
    Boucle sur les échantillons de la trace suivante (de pente max à pente min)
      Pour chaque échantillon, on enregistre une sous-trace de la trace suivante.
      Cette sous-trace est comparée avec l'échantillon de référence.
      Le coefficient de corrélation déduit est enregistré avec la différence d'échantillon
      entre le testé et celui de référence, dans une variable: Corcofpos.
      La même chose est fait en parallèle pour la trace précédente (variable: Corcofneg).
    Fin de boucle 3
    Plusieurs profils de pendages sont alors réalisés :
        1. Par la moyenne entre les pentes.
        2. En gardant la pente pour le coefficient de corrélation le plus élevé.
        3. En gardant la pente la plus proche de zéro.
  Fin de boucle 2
Fin de boucle 1
```

Figure 15 : Schéma présentant l'algorithme de calcul des pendages dans le domaine temporel.

En fin de troisième boucle, la différence d'échantillon correspondant au coefficient de corrélation le plus élevé dans chacune des variables *Corcofneg* et *Corcofpos* est enregistrée dans les profils de pendages. On obtient alors deux profils de pendages : l'un pour les pentes vers les traces suivantes et l'autre pour les pentes vers les traces précédentes. On parlera dans la suite de pente positive lorsqu'il s'agit de la pente vers la trace suivante, et de pente négative lorsque qu'il s'agit de la pente vers la trace précédente. Les pentes positives et les pentes négatives peuvent alors se combiner de trois manières différentes pour obtenir le profil de pendages final :

1. Par la moyenne entre les deux profils de pendages.
2. En gardant la pente associée au coefficient de corrélation le plus élevé entre la pente positive et la pente négative.
3. En gardant la pente la plus proche de zéro (i.e. réflexion horizontale) entre la pente positive et la pente négative.

- Le domaine fréquentiel :

Comme précédemment, l'algorithme dans le domaine fréquentiel est présenté schématiquement sur la figure 16. Les pré-requis sont une matrice avec le profil (*data*) et une variable *len* contenant la longueur de la fenêtre glissante. Dans cet algorithme, les comparaisons sont effectuées dans le domaine de Fourier plutôt que par un coefficient de corrélation.

Dans un premier temps, pour éviter de répéter les calculs des transformées de Fourier et pour limiter les temps de calcul, on parcourt le profil par l'intermédiaire d'une double boucle (sur les traces et les échantillons). A chaque itération, les transformées de Fourier sont calculées sur la longueur de fenêtre *len* et sont stockées dans une matrice *fft_data*. Cette matrice sera donc à trois dimensions : la première pour les traces, la deuxième pour les échantillons et la troisième de la longueur de la transformée de Fourier.

La série de boucles suivantes sert au calcul des pentes. A nouveau, une double boucle permet de parcourir le profil le long des traces et des échantillons. Pour une trace et un échantillon donné, la transformée de Fourier correspondante (pré-calculée lors de la double boucle précédente) est chargée dans une variable *fft_ref.* Une troisième boucle permet de parcourir la trace suivante et la trace précédente autour de l'échantillon de référence. Les transformées de Fourier associées sont chargées dans les variables *fft_pos* et *fft_neg* respectivement, puis comparées à *fft_ref.* Pour les comparaisons, la somme des valeurs absolues de la différence des parties réelles et des parties imaginaires est calculée. Le résultat de la somme et l'échantillon associé sont enregistrés dans les variables *diff_fft_pos* et *diff_fft_neg.* A la fin de la troisième boucle, la trace de référence, l'échantillon de référence, l'échantillon correspondant à la somme minimum de *diff_fft_pos* (*diff_fft_neg*) et la valeur de la somme minimum de *diff_fft_pos* (*diff_fft_neg*) sont enregistrés dans une variable *info_pente_pos* (*info_pente_neg*).

Les profils de pendage vers les traces suivantes (*pente_pos*) et vers les traces précédentes (*pente_neg*) seront alors calculés en sortie des boucles, puis combinés de trois manières différentes comme précédemment :

1. Par la moyenne entre *pente_neg* et *pente_pos*.
2. En gardant la pente associée à la valeur de la différence la plus faible.
3. En gardant la valeur de pente la plus proche de zéro.

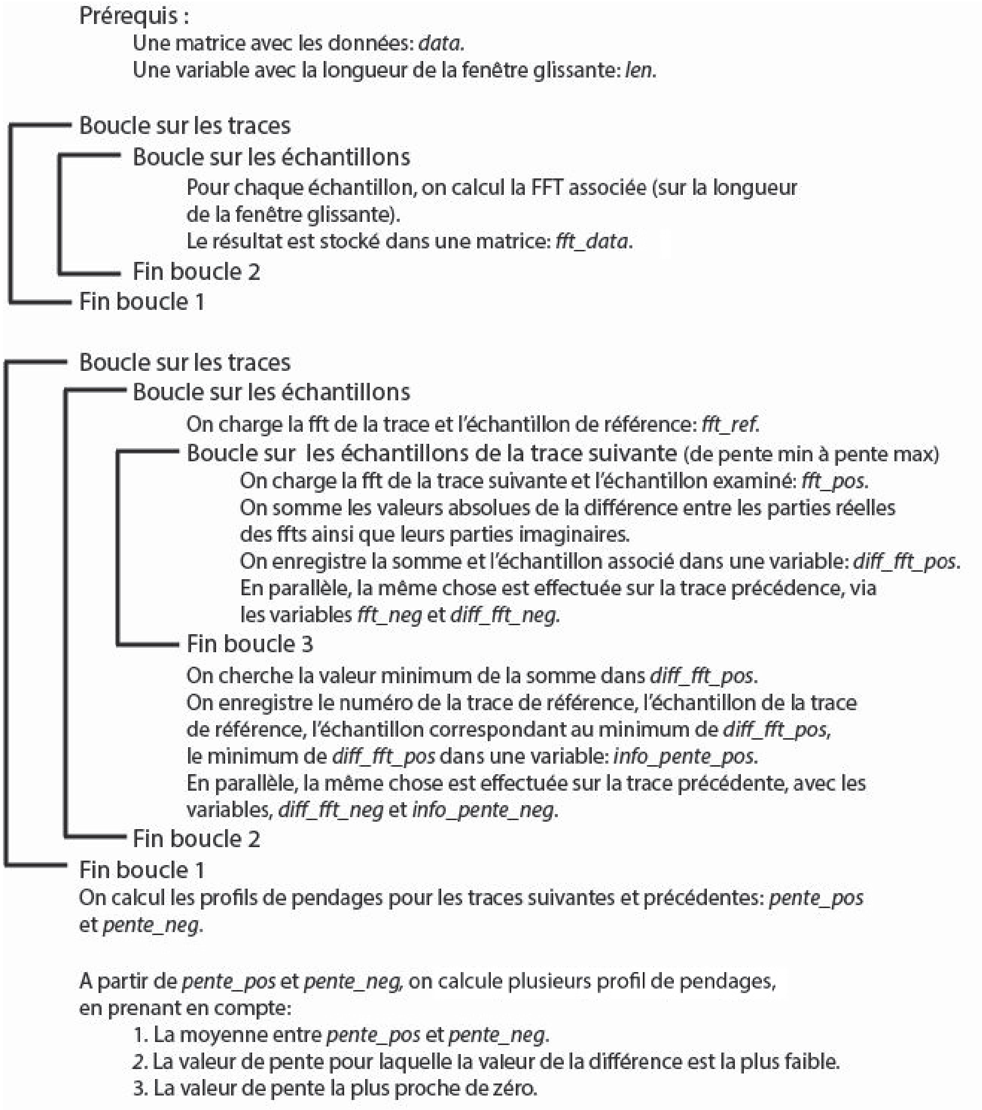

```
Prérequis :
    Une matrice avec les données: data.
    Une variable avec la longueur de la fenêtre glissante: len.

Boucle sur les traces
    Boucle sur les échantillons
        Pour chaque échantillon, on calcul la FFT associée (sur la longueur
        de la fenêtre glissante).
        Le résultat est stocké dans une matrice: fft_data.
    Fin boucle 2
Fin boucle 1

Boucle sur les traces
    Boucle sur les échantillons
        On charge la fft de la trace et l'échantillon de référence: fft_ref.
        Boucle sur les échantillons de la trace suivante (de pente min à pente max)
            On charge la fft de la trace suivante et l'échantillon examiné: fft_pos.
            On somme les valeurs absolues de la différence entre les parties réelles
            des ffts ainsi que leurs parties imaginaires.
            On enregistre la somme et l'échantillon associé dans une variable: diff_fft_pos.
            En parallèle, la même chose est effectuée sur la trace précédence, via
            les variables fft_neg et diff_fft_neg.
        Fin boucle 3
        On cherche la valeur minimum de la somme dans diff_fft_pos.
        On enregistre le numéro de la trace de référence, l'échantillon de la trace
        de référence, l'échantillon correspondant au minimum de diff_fft_pos,
        le minimum de diff_fft_pos dans une variable: info_pente_pos.
        En parallèle, la même chose est effectuée sur la trace précédente, avec les
        variables, diff_fft_neg et info_pente_neg.
    Fin boucle 2
Fin boucle 1
On calcul les profils de pendages pour les traces suivantes et précédentes: pente_pos
et pente_neg.

A partir de pente_pos et pente_neg, on calcule plusieurs profil de pendages,
en prenant en compte:
    1. La moyenne entre pente_pos et pente_neg.
    2. La valeur de pente pour laquelle la valeur de la différence est la plus faible.
    3. La valeur de pente la plus proche de zéro.
```

Figure 16 : Schéma explicatif de l'algorithme de calcul des pendages en domaine de Fourier.

4.2.2. Résultats

Les essais et les comparaisons de calcul des profils de pendages ont été réalisés sur le profil de la dune de sable éolien enregistré au Tchad (Fig. 17). La présence de nombreuses réflexions pentées, dont certaines à haute fréquence, ainsi que la présence d'une topographie localement importante en font un profil très intéressant pour l'essai de nouvelles méthodes. De plus, le profil étant bien échantillonné et les données étant de bonne qualité, les conditions sont optimales pour le test de nouvelles méthodes.

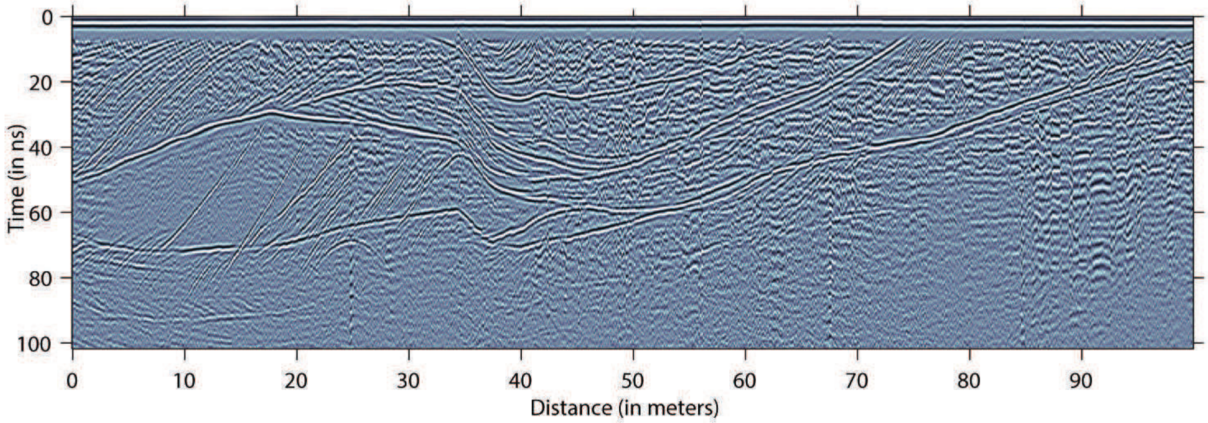

Figure 17 : Profil géoradar effectué sur une dune de sable éolien, au Tchad (Fig. 5a). Le profil est présenté après un traitement classique des données géoradar.

Les profils de pendages calculés en domaine temporel et fréquentiel sont présentés sur les figures 18 et 19 respectivement. Dans les deux cas, la largeur de la fenêtre glissante est la même, fixée à 36 échantillons. Une fenêtre d'échantillonnage trop petite affichera plus de corrélations entre les traces mais sans qu'elles ne soient pour autant reliées à de réelles continuités entre les réflexions. Au contraire, une fenêtre d'échantillonnage trop grande ne trouvera plus de corrélation d'une trace à l'autre. Pour chacune des figures 18 et 19, le profil (a) est obtenu par la moyenne entre les *pente_pos* et *pente_neg*, le profil (b) correspond à la pente pour le coefficient de corrélation le plus élevé (en temporel) ou la différence la plus faible (en fréquentiel) et le profil (c) correspond à la pente la plus proche de zéro. Les pentes négatives (positives) correspondent à un pendage vers la gauche (vers la droite) et un pendage nul, à une réflexion plane. Les valeurs des pentes sont données en échantillon (pour un espacement d'une trace).

Dans les six profils présentés, on retrouve aisément les principales réflexions, dont les valeurs correspondent bien aux pendages du profil initial. Dans les zones où peu de réflexions sont visibles, de forts pendages incohérents d'une trace à l'autre (et d'un échantillon à l'autre) sont observés. Ils sont considérés comme du bruit et donc de moins bonne qualité. Dans les deux algorithmes (temporel et fréquentiel), les mêmes tendances sont retrouvées : la quantité de bruit diminue du profil (a) vers le profil (c) (i.e. de la moyenne, à la corrélation la plus forte, à la pente la plus proche de zéro). Pour une méthode donnée de mélange de *pente_neg* et *pente_pos*, l'algorithme en fréquentiel est celui affichant la meilleure qualité. Ceci est particulièrement visible sur les profils (c) des figures 18 et 19. Dans la suite de ce chapitre, le profil de la figure 19c est donc utilisé.

Les temps de calcul de ces deux algorithmes ont été comparés et ne sont malheureusement pas négligeables. Dans le cas de notre profil composé de 800 traces, 681 échantillons et d'une fenêtre glissante de 36 échantillons, les algorithmes ont mis environ 2h20 et 3h30 en domaine temporel et fréquentiel respectivement. Ces temps de calcul relativement longs peuvent malheureusement décourager l'utilisation de cette méthode, notamment dans le cas d'un large jeu de données comprenant plusieurs profils.

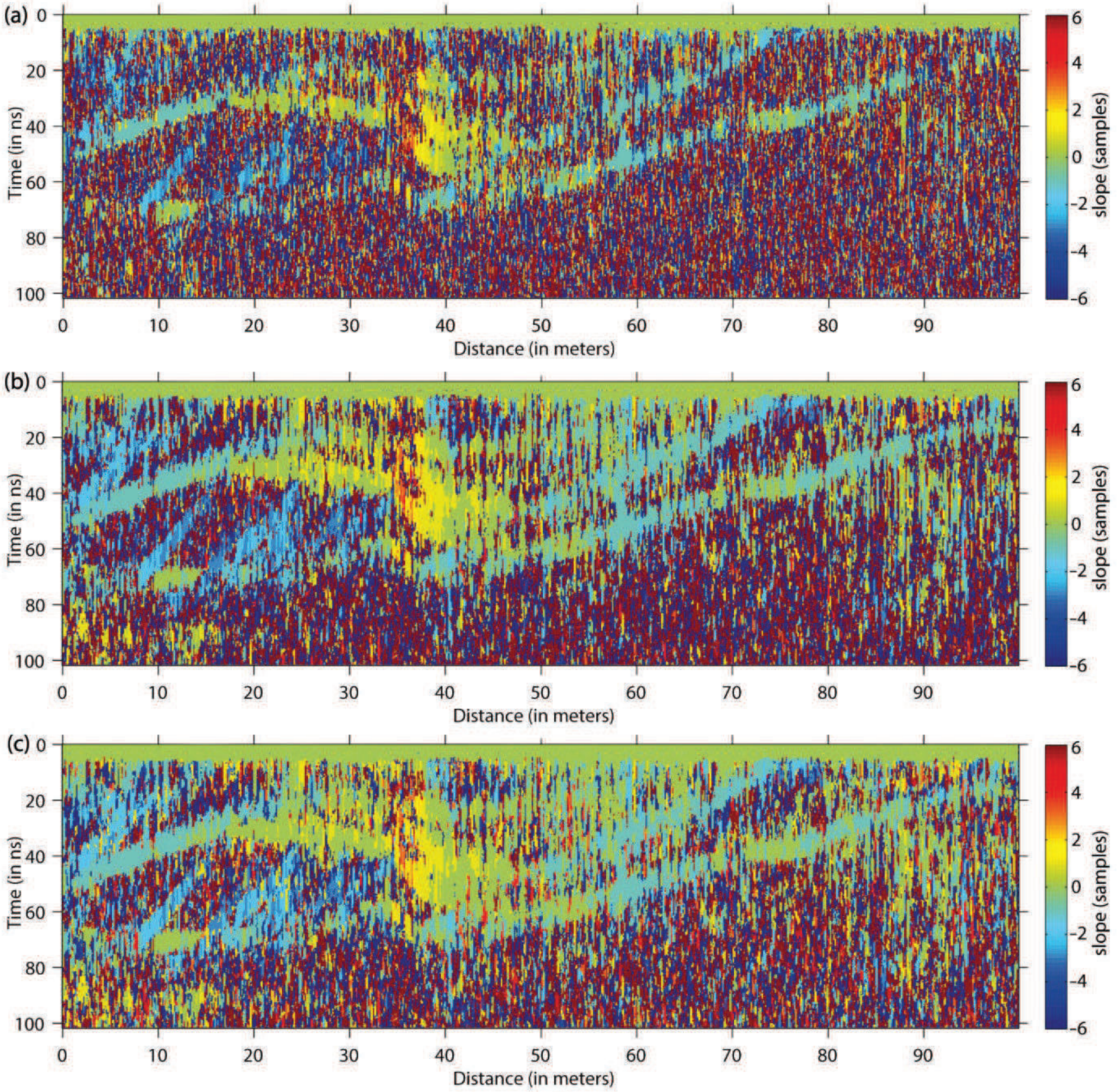

Figure 18 : Profils de pendages calculés en domaine temporel. L'algorithme calcule deux profils de pendages, l'un vers la trace suivante (pentes positives) et l'autre vers la trace précédente (pentes négatives). Les profils sont ensuite mélangés en prenant (a) la moyenne entre les pentes positives et les pentes négatives ; (b) la pente avec le coefficient de corrélation associé le plus élevé et (c) la pente la plus faible entre la pente positive et la pente négative.

4.2.3. Filtrage des profils de pendages

Avant d'utiliser les profils de pendages comme information a priori pour traiter les données, il est nécessaire de les filtrer afin de réduire les pentes incohérentes et de ne garder que les tendances (à plus ou moins grande échelle) des pendages. Pour ce faire, un filtre médian à deux dimensions est utilisé. Ce filtre est défini comme un rectangle positionné sur le profil, dont la taille est connue (m traces et p échantillons) et est centré sur un échantillon. La valeur médiane des valeurs des échantillons comprises dans le rectangle est alors extraite, puis affectée à l'échantillon considéré. Ce procédé est appliqué à l'ensemble des échantillons du profil de pendages.

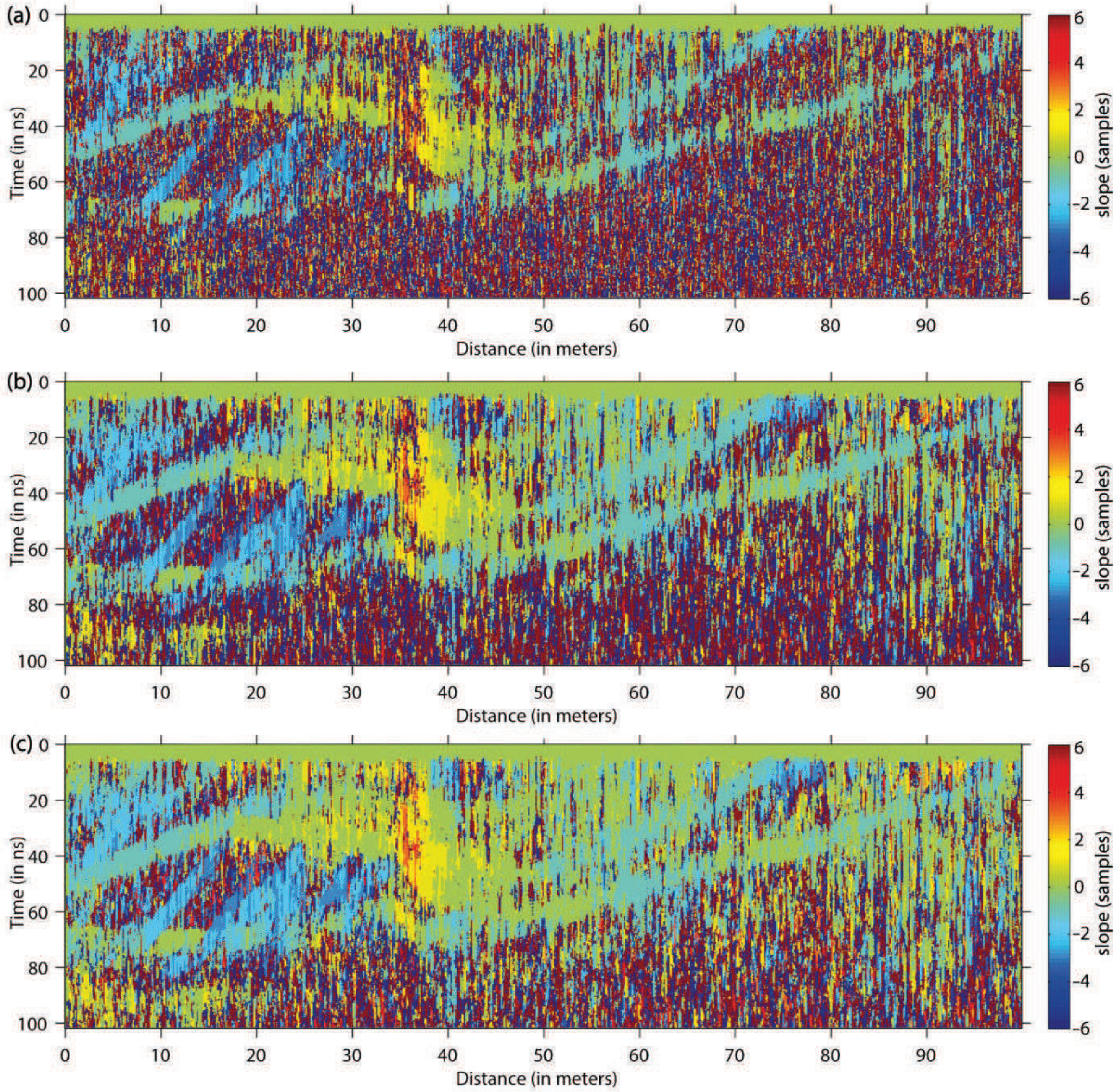

Figure 19 : Profils de pendages calculés en domaine fréquentiel. L'algorithme calcule deux profils de pendages, l'un vers la trace suivante (pentes positives) et l'autre vers la trace précédente (pentes négatives). Les profils sont ensuite mélangés en prenant (a) la moyenne entre les pentes positives et les pentes négatives ; (b) la pente avec la différence associée la plus faible et (c) la pente la plus faible entre la pente positive et la pente négative.

Le profil de pendages initial utilisé est présenté sur la figure 19c. Les profils de pendages filtrés pour des tailles de rectangle allant de 2 traces et 6 échantillons, 4 traces et 12 échantillons et 8 traces et 24 échantillons sont présentés sur la figure 20. Du profil (a) vers le profil (c), le bruit s'atténue, et ce d'autant plus vite que des pendages cohérents entourent les zones de bruit. Dans les zones où beaucoup de bruit est observé (i.e. en dessous de 80 ns) celui-ci reste très présent après filtrage des données. Cependant, cette suppression du bruit se fait au détriment de la précision des pendages calculés. Plus le filtre est important, plus de finesse est perdue et seules les tendances principales sont conservées.

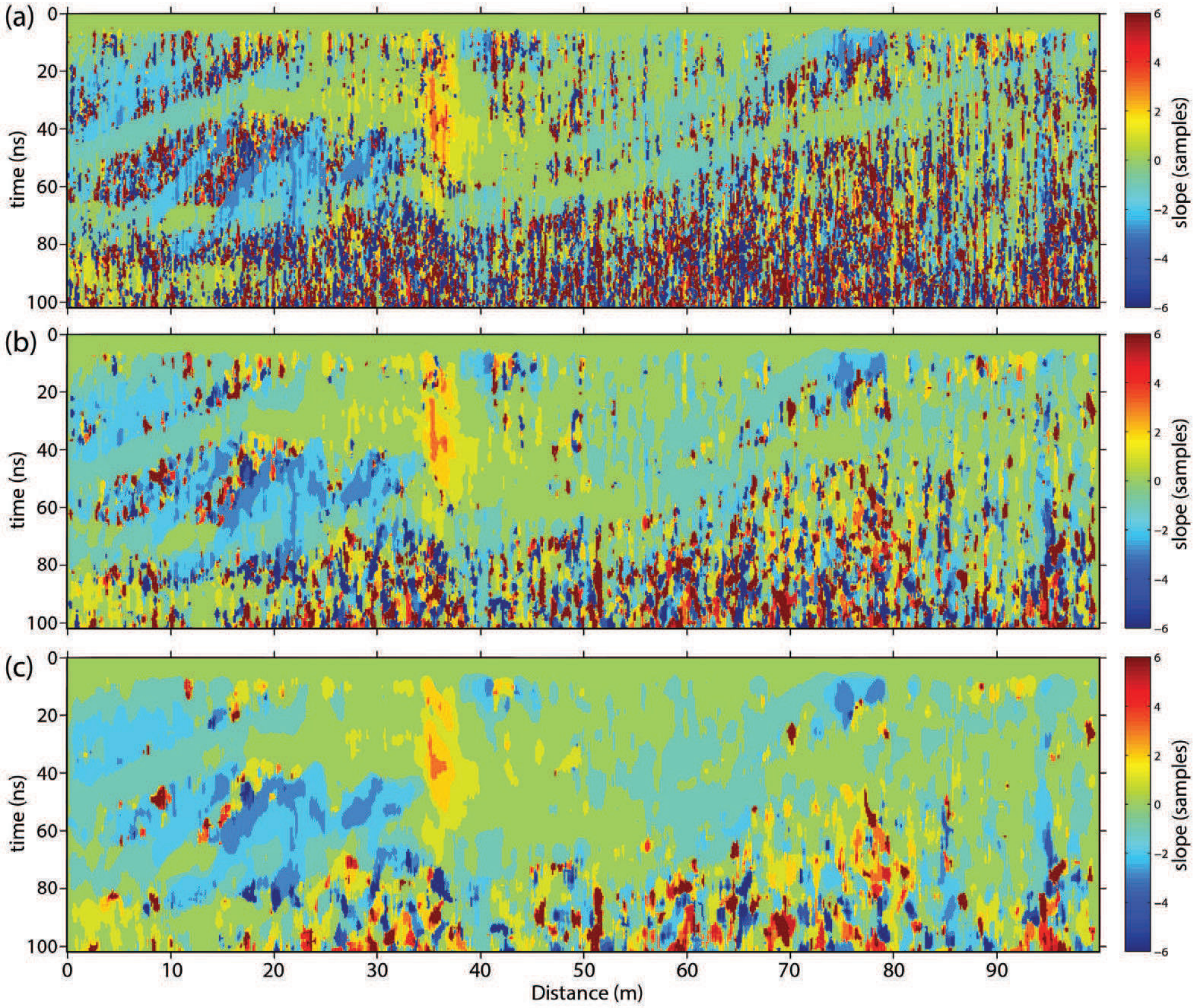

Figure 20 : Profils de pendages après application d'un filtre médian. Le profil initial est présenté sur la figure 19c. Le filtre médian est appliqué sur une fenêtre rectangulaire de dimension (a) 2 traces et 6 échantillons, (b) 4 traces et 12 échantillons et (c) 8 traces et 24 échantillons.

4.3. Filtre sur les données

4.3.1. Algorithme

Les profils de pendages étant réalisés, nous pouvons les utiliser pour le filtrage des données. Le principe est relativement simple. Il s'agit de ré-interpoler les données en prenant, pour un échantillon donné, les informations des traces précédentes et suivantes, en fonction de l'information a priori donnée par le profil de pendages.

Le schéma de calcul est présenté sur la figure 21. Les informations requises pour l'algorithme de calcul sont : le profil de données (*data*), le profil de pendages associé (*pente*), la largeur de la fenêtre d'interpolation donnée en nombre de traces (*l_tr*) et un coefficient d'application du filtre (*cof*), représenté par un scalaire prenant les valeurs de 0.5 à 3. Ce coefficient permet d'appliquer le filtre avec plus ou moins d'intensité.

```
Pré-requis:
    data : matrice contenant le profil à filtrer
    pente : profil de pendages
    l_tr : largeur de la fenêtre d'interpolation (de 1 à 3)
    cof : coefficient pour l'application du filtre (de 0,5 à 3)

Calcul du poids des échantillons pour l'interpolation (rangé dans wint)

Boucle 1 : sur les traces (indice tr)

    Boucle 2 : sur les échantillons (indice spl)
        sp_p=spl (échantillon de la trace suivante initialisé à l'échantillon actuel)
        sp_n=spl (échantillon de la trace précédente initialisé à l'échantillon actuel)
        temp=data(spl,tr) (variable temp initialisé à data(spl,tr))

        Boucle 3 : sur la largeur de la fenêtre d'interpolation (indice k)
            sp_p=sp_p+pente(sp_p,tr+k-1) calcul de l'échantillon pour la trace suivante
            temp=[ temp data(sp_p,tr+k) ] valeur de la trace suivante rangée à la fin de temp
            sp_n=sp_n-pente(sp_n,tr-k+1) calcul de l'échantillon pour la trace précédente
            temp=[ data(sp_n,tr-k) temp ] valeur de la trace précédente rangée au début de temp
        Fin boucle 3

        data_filt(spl,tr)=convolution de temp avec wint
    Fin boucle 2

Fin boucle 1
```

Figure 21 : Schéma de calcul utilisé pour la ré-interpolation des données en utilisant l'information a priori sur les pendages.

Le poids de chaque échantillon dans la ré-interpolation des données est ensuite calculé et stocké dans un vecteur *wint*. Ce dernier a une dimension de : *2*l_tr+1*, avec *l_tr* le nombre d'échantillons de chaque côté de l'échantillon considéré pour le calcul à venir. Ainsi, l'échantillon considéré est au centre de la série de mesures.

Dans la suite, deux boucles permettent de parcourir le profil de données le long des traces (*tr*) et des échantillons (*spl*). Les variables *sp_p* et *sp_n* prennent initialement la valeur de *spl* (i.e. l'échantillon considéré). Une variable *temp* est initialisée à la donnée considérée : *temp=data(tr,spl).*

La troisième boucle permet de parcourir les traces précédentes et suivantes (indice *k*). A chaque itération, *sp_p* prend la valeur de l'échantillon de la trace suivante en accord avec le profil de pendage et *sp_n* occupe la même fonction mais pour la trace précédente. On obtient donc les équations :

$$sp\_p=sp\_p+pente(sp\_p,tr+k-1)$$

et

$$sp\_n=sp\_n-pente(sp\_n,tr-k+1)$$

Les données correspondantes (dans *data*) sont concaténées dans la variable *temp*, puis convoluées avec *wint*. On obtient ainsi la moyenne des termes de la variable *temp* pondérée par les coefficients contenus dans *wint*. Cette moyenne est alors affectée à l'échantillon et à la trace considérée dans le profil filtré : *data_filt(spl,tr).*

Il est à noter l'importance du coefficient *cof*, comme les exemples futurs le montreront. En effet, pour une valeur de 0.5, les coefficients de *wint* prennent la valeur de 1. La moyenne des éléments de *temp* est donc prise en compte pour l'affecter au profil filtré. Lorsque *cof* prend les valeurs de 1 et plus, la valeur centrale de *temp* prend de plus en plus d'importance, donnant plus de poids à la valeur initiale du profil dans le profil filtré. Le filtre perd de son intensité. Lorsque le coefficient dépasse 3, la valeur du coefficient central devient beaucoup plus importante que les valeurs latérales et le profil filtré est quasiment identique au profil initial.

4.3.2. Résultats

Seule une portion du profil (présentée sur la figure 22) est utilisée pour tester les effets du filtre. De nombreuses réflexions d'intensité, de pendage et de longueurs d'onde variées sont observées, dont certaines sont mélangées avec un bruit ambiant (réflexions présentent entre 0 et 40 ns).

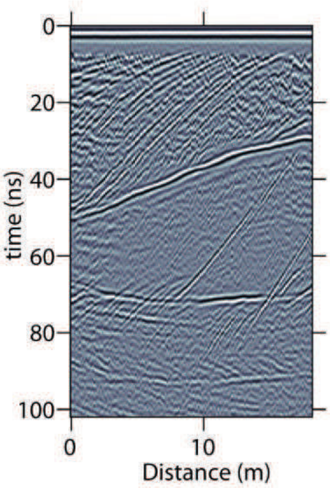

Figure 22 : Section du profil de la figure 9 pour montrer les effets du filtre basé sur les profils de pendages.

4.3.2.1. Un profil de pendages, plusieurs filtres médians

Le but de cette section est de montrer les effets du filtre pour les différents profils de pendages (i.e. le profil de pendages non filtré, puis avec les filtres médians présentés sur la figure 20). La figure 23 présente les résultats avec sur la première ligne les quatre profils filtrés, sur la deuxième ligne les différences entre le profil initial et les profils filtrés et sur la troisième ligne, les profils de pendages utilisés. Les paramètres de filtrage sont constant dans les quatre cas (i.e. largeur de trace : 2, coefficient : 2).

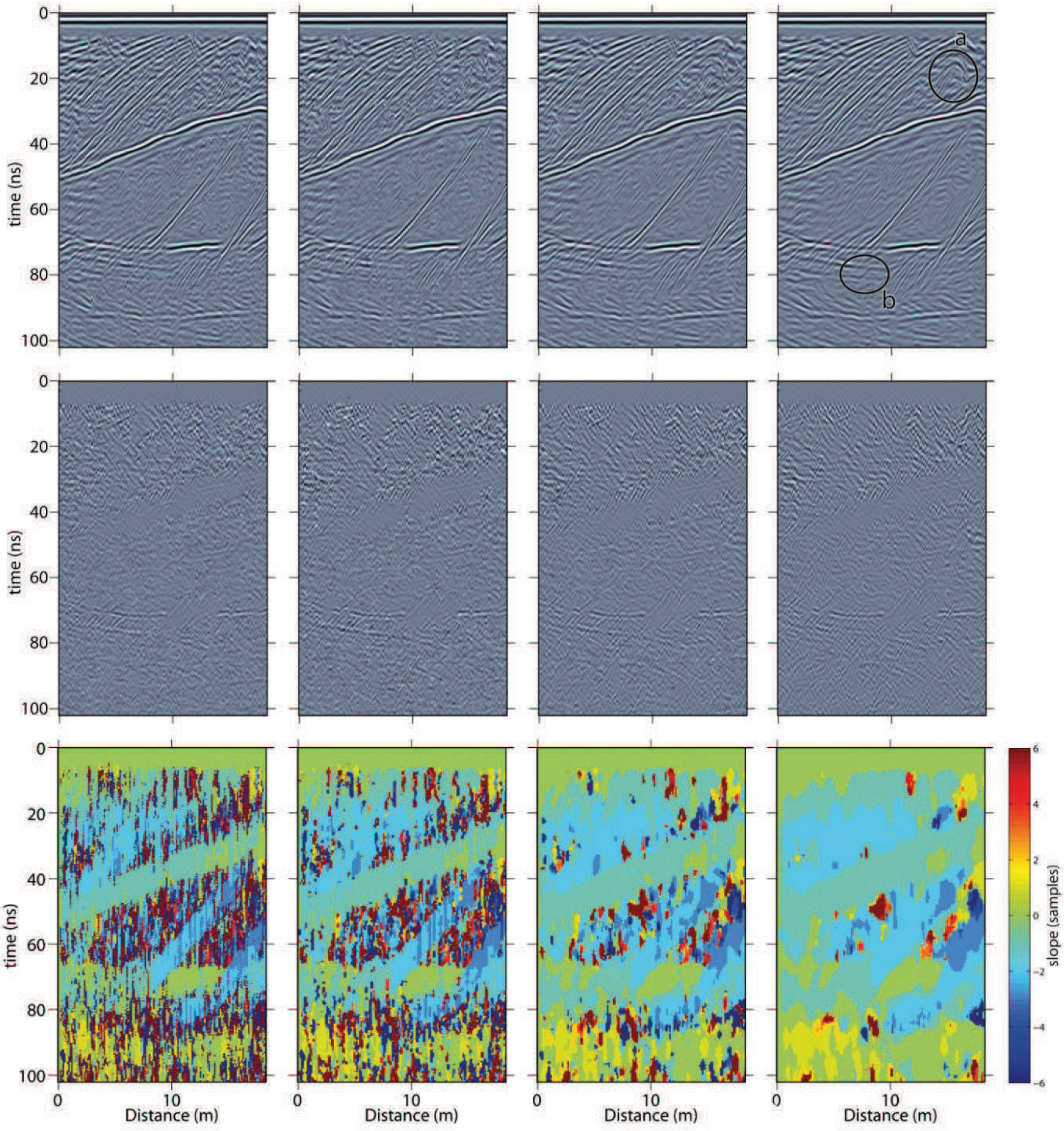

Figure 23 : Présentations des résultats pour des profils de pendages ayant différents filtres médians. De gauche à droite : sans filtre médian, 2 traces et 6 échantillons, 4 traces et 12 échantillons et 8 traces et 24 échantillons. De haut en bas : la section de profil filtré, la différence entre le profil initial et le profil filtré et les profils de pendages associés. Les cercles noirs (en haut à droite) mettent en évidence des caractéristiques décrites dans le texte. Le profil en haut à gauche est repris de la figure 22.

Au niveau des profils de pendages, on retrouve les profils présentés précédemment (Fig. 20). De gauche à droite (Fig. 23, ligne du bas), le bruit est de plus en plus atténué et nous obtenons des profils de plus en plus représentatifs des variations globales. Au niveau des profils filtrés (Fig. 23, première ligne), on observe en premier lieu une forte diminution d’une « granulosité » présente dans le profil initial. Les profils des différences (Fig. 23, ligne centrale) confirment cette observation : la majorité du signal présent dans les différences est un bruit incohérent. De gauche à droite, cette tendance s’accentue et les réflexions gagnent en cohérence (comparer les réflexions entre 0 et 40 ns). Dans un même temps, les réflexions pentées (même fortement) sont très bien conservées et ce, peu importe leur pendage et leur fréquence. Ce point est une excellente nouvelle, puisque c'est là l'un des buts de la méthode. Cependant, malgré les améliorations évidentes, certains artefacts sont à noter. Premièrement, une hyperbole fait son apparition sur le profil le plus à droite (à environ 20 ns, cercle (a)). Aucun indice ne laisse supposer son existence dans le profil initial. Un deuxième exemple est mis en évidence par le cercle (b). Deux réflexions sont parallèles mais non connectées. Sur le profil le plus à droite, une continuité à été créée entre ces deux réflexions (cercle (b)). Il est à noter que dans cette zone, des réflexions horizontales croisent des réflexions pentées. L'algorithme ne pouvant prendre en compte deux pentes différentes, il en résulte des artefacts tels que celui-ci. Dans les profils des différences, on s'aperçoit qu'une partie des réflexions cohérentes est supprimée dans ces zones de croisement de réflexions, confirmant les difficultés de l'algorithme à s'occuper de deux pentes. Ces réflexions restent cependant très marquées dans les profils finaux.

Un compromis devant être choisi entre présence d'artefacts, suppression de bruit et amélioration de la cohérence des réflexions, le troisième profil de pendages est conservé pour la suite de l'exposé (i.e. 4 traces et 12 échantillons).

4.3.2.2. Test des paramètres d'interpolation

Deux paramètres sont nécessaires pour l'application de notre filtre. Le premier est la largeur de la fenêtre pour ré-interpoler la donnée et le deuxième est un coefficient donnant plus ou moins de poids à la valeur initiale. Pour un coefficient de 0.5, la moyenne des traces est prise en compte lors de la ré-interpolation. Pour un coefficient supérieur à 3, le profil final est quasiment identique au profil initial. Le but de cette section est d'investiguer les effets de ces deux paramètres.

Pour ce faire, une batterie de tests est effectuée (Fig. 24) en incrémentant d'une part la largeur de la fenêtre (de 1 à 3, de haut en bas) et d'autre part le coefficient d'application (3, 2, 1 et 0.5 de gauche à droite). Les différences avec le profil initial sont affichées sur la figure 25 pour faciliter les comparaisons. Les profils ont à nouveau la même dimension que le profil initial (Fig. 22), le profil de pendages est identique dans chaque cas (i.e. troisième profil de la figure 23, obtenu après filtre médian de 4 traces et 12 échantillons) et l'échelle de couleur est la même sur chacun des profils.

Comme précédemment, la première observation est la diminution de la granulosité de l'arrière plan. Cet effet s'intensifie lorsque la largeur de la fenêtre augmente et lorsque le coefficient d'application diminue (se rapproche de 0.5). Ainsi l'effet du filtre est minimum sur le profil en haut à gauche et maximum en bas à droite, comme attendu. Les différences présentées sur la figure 25 soulignent bien ce comportement. Présentées avec la même échelle de couleur, on observe bien que de plus en plus de signal est soustrait au profil initial. De manière générale, la majorité des réflexions sont bien conservées, qu'elles soient horizontales ou avec un pendage. Dans la zone des réflexions courbées (entre 0 et 40 ns), zone présentant le plus de bruit, elles deviennent plus lissées et plus claires. Des réflexions pentées, de faible amplitudes et difficilement observables dans les données d'origine ont tendance à ressortir après utilisation du filtre, et ce particulièrement à l'intérieur de la dune inférieure (entre 50 et 70 ns). A nouveau, les profils des différences affichent principalement un signal indépendant des réflexions dans ces zones, confirmant son efficacité.

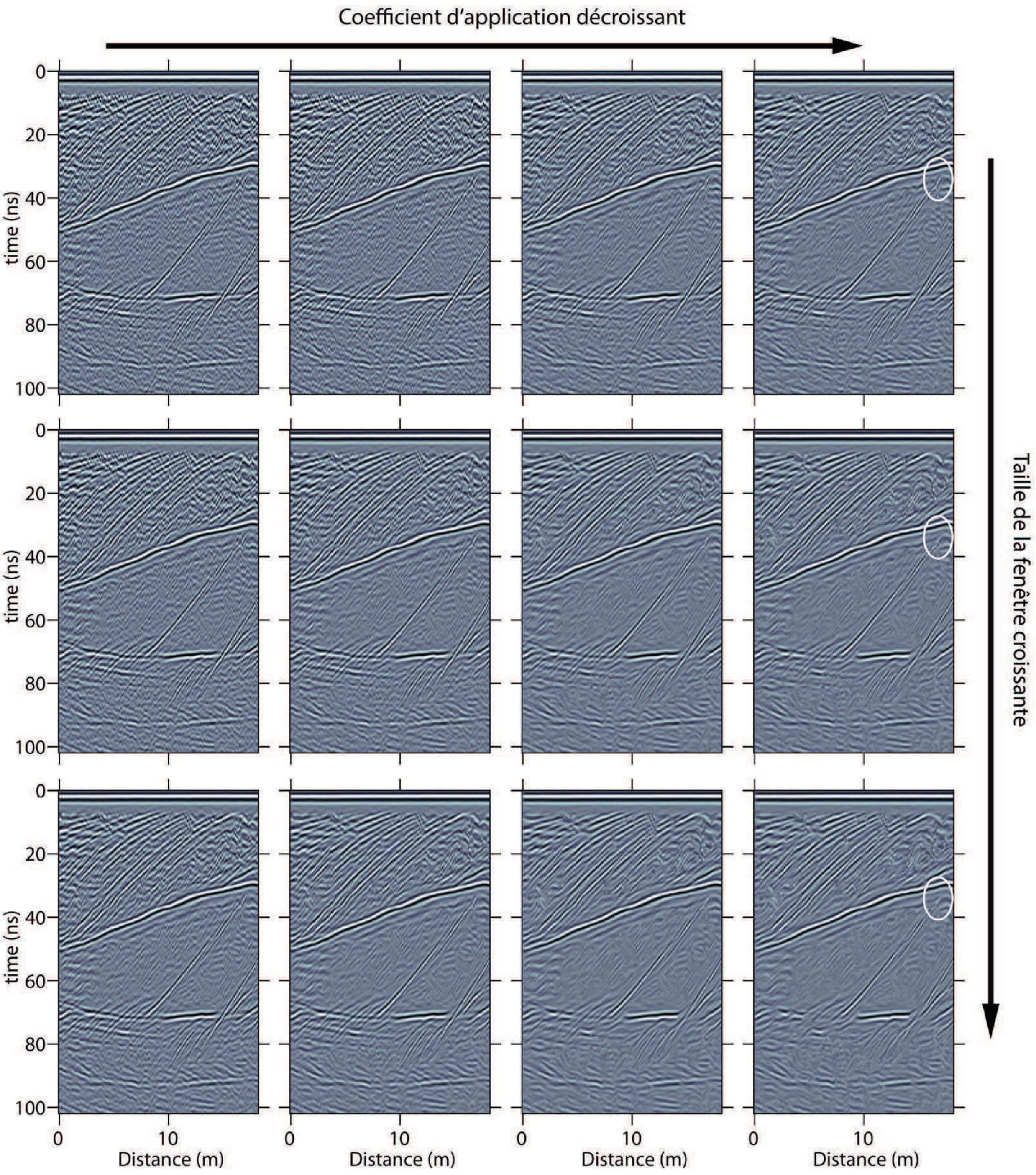

Figure 24 : Présentation des résultats des tests de paramètres du filtre. De haut en bas : augmentation de la taille de la fenêtre (1,2 et 3 traces de part et d'autres de l'échantillon ré-interpolé). De gauche à droite : diminution du coefficient d'application (i.e. augmentation de l'intensité du filtre). Le coefficient prenant les valeurs de 3, 2, 1 et 0.5. La description de la figure est effectuée dans le texte.

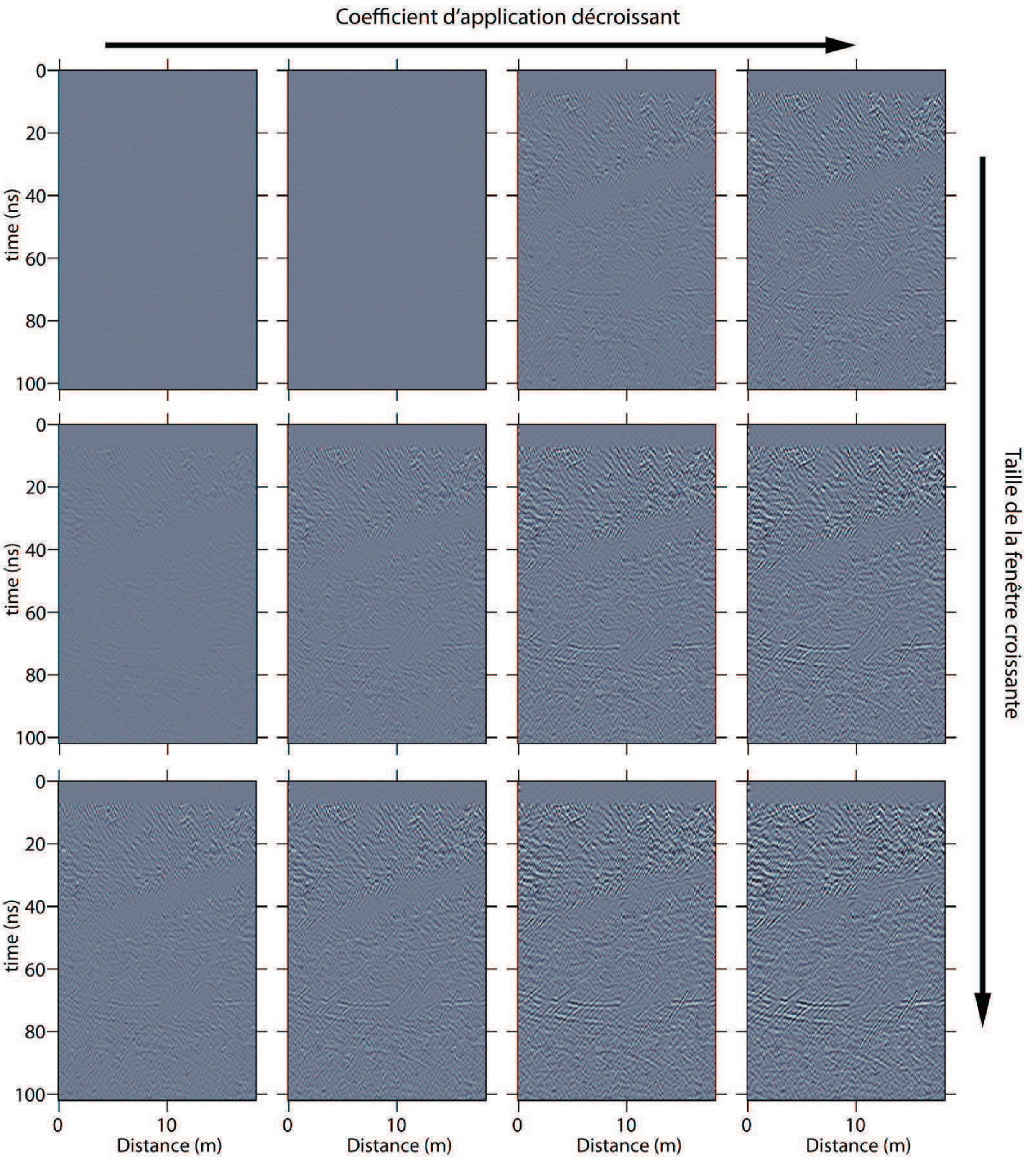

Figure 25 : Différences entre le profil initial (Fig. 22) et les profils filtrés (Fig. 24). La description est effectuée dans le texte.

Cependant, ce filtre a ses inconvénients et ses limites. Lorsque le coefficient devient trop faible (application plus intense du filtre), la part de signal utile supprimée est de plus en plus importante et ce d'autant plus que la largeur de la fenêtre est grande. Pour illustrer ces propos, deux zones sont particulièrement intéressantes. La première se trouve dans les réflexions horizontales entre 70 et 80 ns et la deuxième se trouve dans les réflexions courbées (au dessus de 40 ns). Au sein de la première zone, on voit clairement la disparition du signal dans les zones de croisement lorsque l'on se dirige vers les profils du bas ou de la droite. L'incapacité du filtre à prendre en compte deux pendages simultanément est à nouveau mise en cause. Dans la zone des réflexions courbées, le filtre supprime en priorité le bruit incohérent, lissant les réflexions. Au fur et à mesure de l'augmentation de la largeur de fenêtre et de l'intensification du filtre, des morceaux de réflexions sont peu à peu effacées. Le bruit peut localement entraîner une erreur sur le calcul des pentes, ainsi qu'une mauvaise ré-interpolation, supprimant du signal utile des données. Ces observations sont encore plus flagrantes dans les profils de différences où des réflexions apparaissent petit à petit dans les données. Un dernier exemple de limitation du filtre est observable sur la fine réflexion en milieu de profil. Sur les profils faiblement filtrés, cette réflexion se termine presque en contact de la forte réflexion à son aplomb (cercles blancs, colonne de droite). Lorsque l'intensité du filtre augmente, la distance entre ces réflexions a tendance à augmenter. Les données n'étant plus cohérentes en fin de réflexion, la ré-interpolation atténue les extrémités des réflexions.

Le filtrage par les profils de pendages est efficace pour la suppression du bruit incohérent et dans la conservation des réflexions pentées, même lorsque celles-ci montrent de hautes fréquences. Dans les meilleurs cas, la continuité des réflexions est améliorée et certaines petites réflexions, quasiment invisibles avant, ont tendance à ressortir. Cependant, ce filtre nécessite une utilisation modérée afin d'éviter les risques de dégradation du signal dans les zones sensibles (terminaison et croisement de réflecteurs).

4.4. Exemple avec migration

Dans cette dernière section, nous montrons les améliorations obtenues avec ce filtre dans le cas d'un traitement impliquant une migration topographique. Le profil initial est à nouveau une sous-section (les 35 premiers mètres) du profil enregistré sur la dune Tchadienne. Les résultats présentés (Fig. 26) le sont après migration topographique avec une vitesse de 0.18 m/ns. Ils présentent le profil après migration (a), le profil filtré puis migré (b), le profil migré puis filtré (c), le profil filtré, migré puis filtré à nouveau (d). Les profils de pendages ont été recalculés avant chaque étape d'application du filtre. Un filtre médian de 4 traces et 12 échantillons est utilisé sur chacun des profils de pendages. Les paramètres d'application du filtre (2 traces et coefficient de 2) ont été gardés constant dans toutes les étapes. Les deux derniers profils (Fig. 26e et 26f) sont respectivement la différence entre le profil migré initial (a) et les profils (c) et (d).

L'utilisation du filtre avant migration (Fig. 26b) montre déjà une nette amélioration des données. Bon nombre d'artefacts dus à la migration sont réduits et ce particulièrement dans la zone juste sous la première arrivée. De manière générale, la granulosité observée dans les profils est réduite. Le profil migré puis filtré (Fig. 26c) montre des résultats quelque peu différents. A nouveau, la granulosité est atténuée comme il est facilement observable juste sous la première arrivée et dans la zone des réflexions courbées entre 0 et 4 m. La différence entre le profil (a) et celui-ci (Fig. 26e) corrobore nos observations. Cependant, de très petites réflexions font leur apparition dans tout le profil. Celles-ci sont principalement visibles dans les zones où peu de signal est présent (entre 5 et 6 m de profondeur). Dans les zones où du signal existe, ces minis réflexions ont tendance à couper les réflexions préexistantes et à interrompre localement leur continuité. Le quatrième profil (d) représente le profil (b) après ré-application du filtre. Le résultat est une version très épurée de la section migrée. Les observations faites sur le profil (b) sont toujours d'actualité, mais plus poussées encore. La différence entre le profil initial (a) et le profil (d) (Fig.

26f) montre bien un signal indépendant des réflexions. On retrouve principalement la granulosité du profil initial, ainsi que les artefacts dus à la migration topographique (i.e. les arcs de cercles tournés vers la surface). On retrouve tout de même, avec une très faible amplitude, les réflexions horizontales entre 6 et 7 m, où les réflexions se croisent. L'amplitude de ce signal est très faible dans la différence et le profil (d) n'est donc quasiment pas affecté par ce retrait.

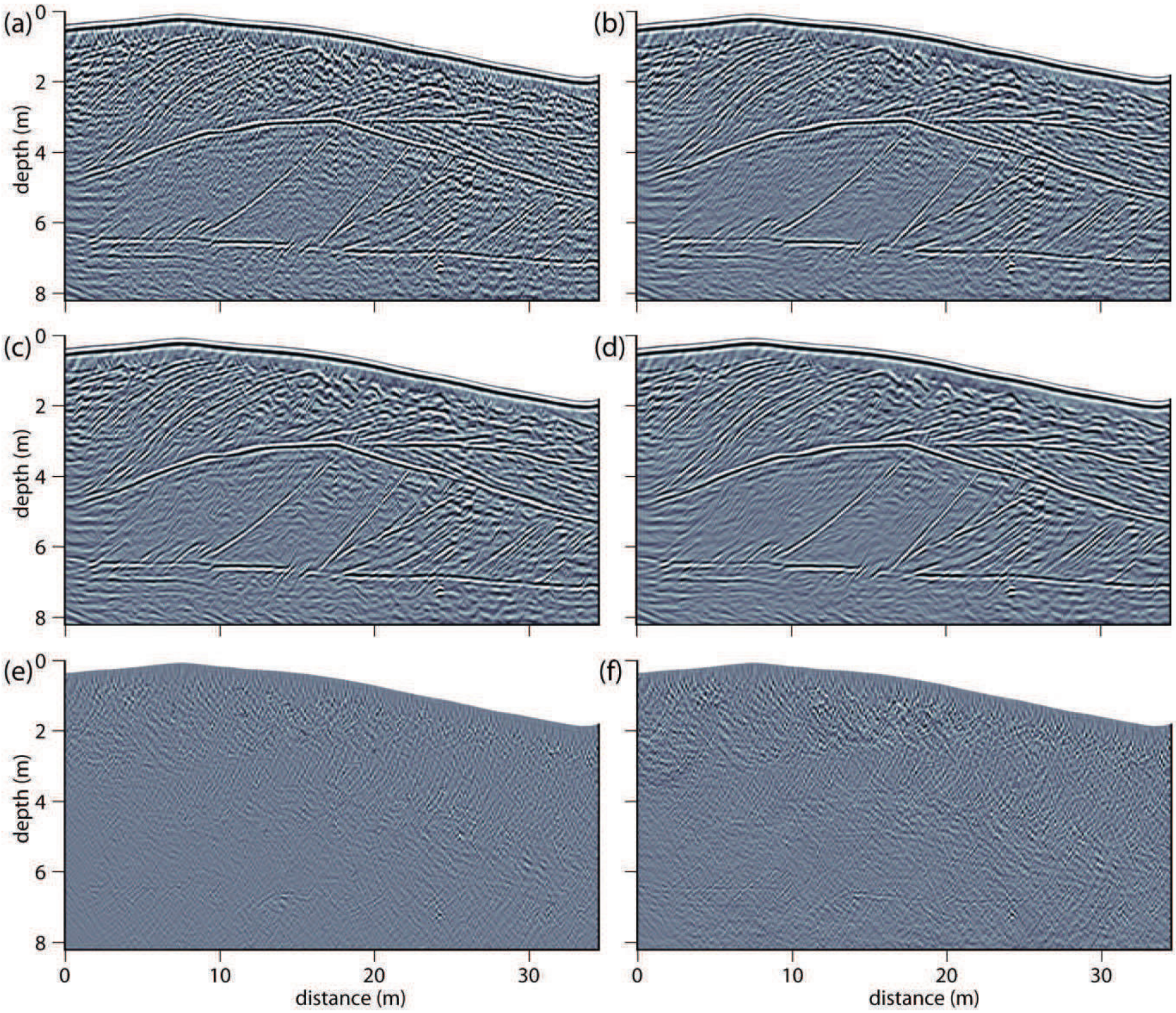

Figure 26 : Exemple d'utilisation du filtre lors de la migration topographique. (a) Profil migré sans filtre de pendages ; (b) Profil filtré puis migré ; (c) Profil migré puis filtré ; (d) Profil filtré, migré, puis filtré à nouveau. (e) Différence entre les profils (a) et (c) ; (f) Différence entre les profils (a) et (d). La description des profils est faite dans le texte.

4.5. Conclusion

Deux algorithmes, l'un en domaine temporel, l'autre en domaine fréquentiel ont été écrit pour calculer les profils de pendages. Le résultat de chacun de ces algorithmes est deux profils de pendages, l'un vers les traces suivantes et l'autre vers les traces précédentes, qui à leur tour sont combinés pour obtenir le profil de pendages final. Leur combinaison se fait selon trois méthodes : la moyenne entre les deux, en prenant le profil montrant le coefficient de corrélation le plus élevé, en prenant le profil dont la pente est la plus faible. Dans les deux cas (temporel et fréquentiel), la combinaison basée sur la pente la plus faible est celle donnant les résultats les plus propres (i.e. les moins bruités). De même, l'algorithme codé en domaine de Fourier donne des résultats légèrement moins bruités que son homologue temporel. Avant utilisation, le profil de pendages est filtré par un filtre médian sur une fenêtre glissante à deux dimensions, afin de ne garder que les tendances du profil, ainsi qu'à supprimer une partie du bruit contenu dans les données. Un échantillon donné sera donc ré-interpolé en prenant en compte les valeurs des traces alentour, basées sur le profil de pendages.

Deux paramètres sont nécessaires pour faire tourner le filtre : la largeur du filtre (i.e. le nombre de traces à prendre en compte de part et d'autre de l'échantillon à interpoler) et l'intensité du filtre. Lorsque le filtre est utilisé judicieusement, il réduit significativement le bruit incohérent dans les données et améliore la continuité des réflexions. Les réflexions pentées sont toutes aussi bien conservées que les réflexions horizontales et ce même lorsqu'elles présentent de hautes fréquences. C'est là l'un des problèmes des filtres classiques. Utilisé en combinaison avec la migration, il permet d'en réduire significativement les artefacts, améliorant sensiblement les résultats.

Il est cependant important de noter quelques limitations. Les algorithmes de calcul des pendages sont incapables de considérer deux pentes en même temps. Ainsi, les zones affichant des croisements de réflexions sont sujettes à détérioration, particulièrement lorsque les paramètres d'application du filtre sont élevés (largeur de traces et coefficient d'application importants). En combinaison avec la migration, les meilleurs résultats seront observés lorsque le filtre est appliqué avant la migration. Appliqué uniquement après migration, des micro-réflexions perturbant la continuité des réflexions existantes font leur apparition. Une utilisation avant et après migration donnera une version très épurée du profil, conservant très bien le signal utile. Ce filtre remplit donc correctement nos exigences, mais son application est rendue difficile par le temps de calcul. En effet, pour un profil de 800 traces et 680 échantillons, environ 3h30 sont nécessaires pour calculer le profil de pendage sur un ordinateur « classique ». Heureusement, le calcul des profils de pendages ne nécessite aucun paramètre. Le temps de calcul du reste du filtre est négligeable.

Chapitre 2 : Le géoradar en tectonique active

Application du géoradar dans un contexte de faible déformation. exemple des failles d'Emeelt et d'Hustaï en Mongolie

1. Introduction

Ce chapitre présente les résultats de deux investigations GPR menées sur deux failles actives dans la région d'Ulaanbaatar (UB), capitale de la Mongolie. Cette étude s'inscrit dans une étude plus vaste, dont l'objectif est l'estimation du risque sismique dans la région. En effet, UB, capitale économique et politique du pays, regroupe 1,2 millions d'habitants sur les 3 millions que compte la Mongolie. Depuis 2005, la sismicité n'a cessé d'augmenter et se localise principalement le long de deux directions perpendiculaires, délimitant deux failles actives : la faille d'Emeelt, découverte en 2008, et la faille de Hustaï. Ces failles se situent respectivement à moins de 10 et 20 km d'UB. L'étude du risque sismique est donc de première importance pour le pays.

La région est caractérisée par un contexte tectonique intracontinental associé à de faibles déformations, très probablement inférieures à 1 mm par an. Pendant les périodes de retour (quelques milliers d'années), les marqueurs géomorphologiques ont été largement érodés. Par conséquent, une première reconnaissance géomorphologique a été effectuée sur le terrain en 2009, suite à laquelle deux sites d'études ont été choisis pour mener des investigations GPR dans le but de caractériser les failles d'Emeelt et de Hustaï. Leur dimension et leur géomorphologie indiquent qu'elles pourraient produire des séismes de magnitude 6.5 à 7.5.

Emeelt :

La faille d'Emeelt a été découverte en 2008 par les observations géomorphologiques et les enregistrements de sismicité. Elle est située à environ 10 km à l'ouest d'UB. Les images satellites et les marqueurs géomorphologiques permettent de la suivre sur une distance de 25 km environ avec une direction NNO-SSE. Suite aux observations préliminaires de 2009 (observations géomorphologiques et ouverture d'une tranchée sur le bord d'un cône alluvial), nous avons décidé d'utiliser le GPR pour investiguer plus en détails les dépôts de subsurface potentiellement affectés par la faille.

Deux campagnes GPR (en 2010 et 2011) ont été réalisées afin d'imager deux structures sédimentaires (un cône alluvial et un paléo-chenal) avec une antenne de 500 MHz. Sur le cône alluvial, 25 profils de 40 m de long avec un espacement d'1 m entre les profils ont été enregistrés parallèlement à la tranchée (dans l'axe du cône). Pour le paléo-chenal, nous avons opté pour des mesures pseudo 3D, avec un espacement de 25 cm entre les profils. Trois tranchées ont été ouvertes simultanément pour permettre une comparaison directe entre la géologie et les données radar. De longues lignes 2D ont été effectuées en complément avec une antenne de 50 MHz, pour voir l'extension en profondeur et latéralement.

Les profils ont été interprétés en combinant reconnaissance de faciès et pointage de réflexions. Une forte réflexion interprétée comme le plan de faille dans les données de 50 MHz nous donne un accès direct à sa géométrie entre 3 et 12 m de profondeur (les pendages varient de 23° à 35° vers le NNE). Sur les deux zones, la comparaison entre les profils GPR et les tranchées est concordante et nous a permis de relier les faciès GPR à une lithologie. Sur le cône alluvial, un faciès chaotique, cohérent avec les réflexions de profils de 50 MHz, est interprété comme une zone de matériel désorganisé par les mouvements de la faille. L'imagerie du fond du paléo-chenal sur la deuxième zone a mis en évidence un décalage dextre de 2 m environ. Aucun déplacement vertical n'a été observé, mais la base du paléo-chenal étant délicate à suivre, rien ne prouve son inexistence.

Cette partie a été publiée dans la revu GJI sous la référence suivante :

Dujardin, J. R., Bano, M., Schlupp, A., Ferry, M., Munkhuu, U., Tsend-Ayush, N., & Enkhee, B. (2014). GPR measurements to assess the Emeelt active fault's characteristics in a highly smooth topographic context, Mongolia. Geophysical Journal International, ggu130.

(la version publiée est disponible en annexe).

Hustaï :

L'extrémité est de la faille de Hustaï se situe à moins de 20 km à l'ouest de UB. Elle s'étend avec une direction OSO sur près de 80 km. La sismicité enregistrée depuis 2005 est principalement focalisée sur deux grappes. La première correspond à l'extrémité est de la faille et la deuxième se situe à environ 70 km de la zone urbaine de UB. C'est au sein de cette deuxième grappe que nos mesures GPR ont été effectuées.

Un total de 9 profils avec une antenne de 50 MHz, et 7 profils avec l'antenne de 500 MHz ont été effectués sur deux sites. Le premier site correspond à des alluvions déposées à l'entrée d'une petite vallée, et le deuxième site est directement sur les contreforts des collines environnantes.

La même méthodologie d'interprétation que précédemment a été utilisée. Les informations pertinentes se retrouvent principalement sur les profils effectués à l'antenne de 50 MHz. Trois profils affichent une forte réflexion qui est interprétée comme le plan de faille. De part la localisation des profils et par analogie avec la zone d'Emeelt, les faciès GPR ont pu être reliés avec une lithologie, mais aucune géométrie de faille n'a pu être mise en évidence pour autant. Les profils avec l'antenne de 500 MHz ne montrant pas de variations notables de faciès, les dépôts sur les 2 à 3 premiers mètres du sous-sol sont considérés postérieurs aux derniers grands séismes sur cette faille. Les derniers grands séismes sont donc considérés relativement vieux sur ce site.

2. Emeelt

Abstract

To estimate the seismic hazard, the geometry (dip, length, orientation) and the dynamics (type of displacements and amplitude) of the faults in the area of interest need to be understood. In this paper, in addition to geomorphologic observations, we present the results of two Ground Penetrating Radar (GPR) campaigns conducted in 2010 and 2011 along the Emeelt fault in the vicinity of Ulaanbaatar, capital of Mongolia, located in an intra-continental region with low deformation rate that induces long recurrence time between large earthquakes. As the geomorphology induced by the fault activity has been highly smoothed by erosion processes since the last event, the fault location and geometry is difficult to determine precisely. However, by using GPR first, a non-destructive and fast investigation, the fault and the sedimentary deposits near the surface can be characterized and the results can be used for the choice of trench location. GPR was performed with a 50 MHz antenna over 2D lines and with a 500 MHz antenna for pseudo-3D surveys. The 500 MHz GPR profiles show a good consistency with the trench observations, dug next to the pseudo-3D surveys. The 3D 500 MHz GPR imaging of a paleo-channel crossed by the fault allowed us to estimate its lateral displacement to be about 2 m. This is consistent with a right lateral strike-slip displacement induced by an earthquake around magnitude 7 or several around magnitude 6. The 2D 50 MHz profiles, recorded perpendicular to the fault, show a strong reflection dipping to the NE, which corresponds to the fault plane. Those profiles provided complementary information on the fault such as its location at shallow depth, its dip angle (from 23° to 35°) and define its lateral extension.

2.1. Introduction

Central Asia is known for its high level of seismic hazards, especially Mongolia, which has been one of the most seismically active intra-continental regions in the world with four large earthquakes (Magnitude around 8) along its active faults in the western part of the country during the last century (Khilko et al., 1985). The deformation in Mongolia is located between compressive structures related to the collision and penetration of the Indian plate into the Eurasian plate and extensive structures in the North of the country related with the Baykal rift (Tapponnier and Molnar, 1979; Baljinnyam et al., 1993; Schlupp, 1996; Bayasgalan et al., 1999a).

The seismic activity observed in the vicinity of Ulaanbaatar (UB), capital of Mongolia, is relatively low compared to the activity observed in western Mongolia. Nevertheless since 2005, the seismic activity around UB not only has increased, but is also organized (see Fig. 1) at the west of UB along two perpendicular directions, which determine two active faults: Emeelt fault, discovered in 2008 (NNW-SSE direction, 25 km long minimum and situated about 10 km west of UB) and Hustai fault (WSW-ENE direction, 80 km long, with its NE tip at less than 20 km west of UB); their length and morphology indicate they can produce earthquakes of magnitude 6.5 to 7.5 (Schlupp et al., 2012). Most of the Mongolian population (1.2 million over 3 million) is concentrated at UB, which is the main political and economical centre of the country. Hence, the study of seismic hazard and the estimation of the probability of future destructive earthquakes are of primary importance for the country (Dugarmaa et al., 2006). Since the last large earthquake, the faults geomorphology has been highly smoothed by erosional processes and the exact location of the fault plane surface rupture is thus hidden within a several metre wide strip.

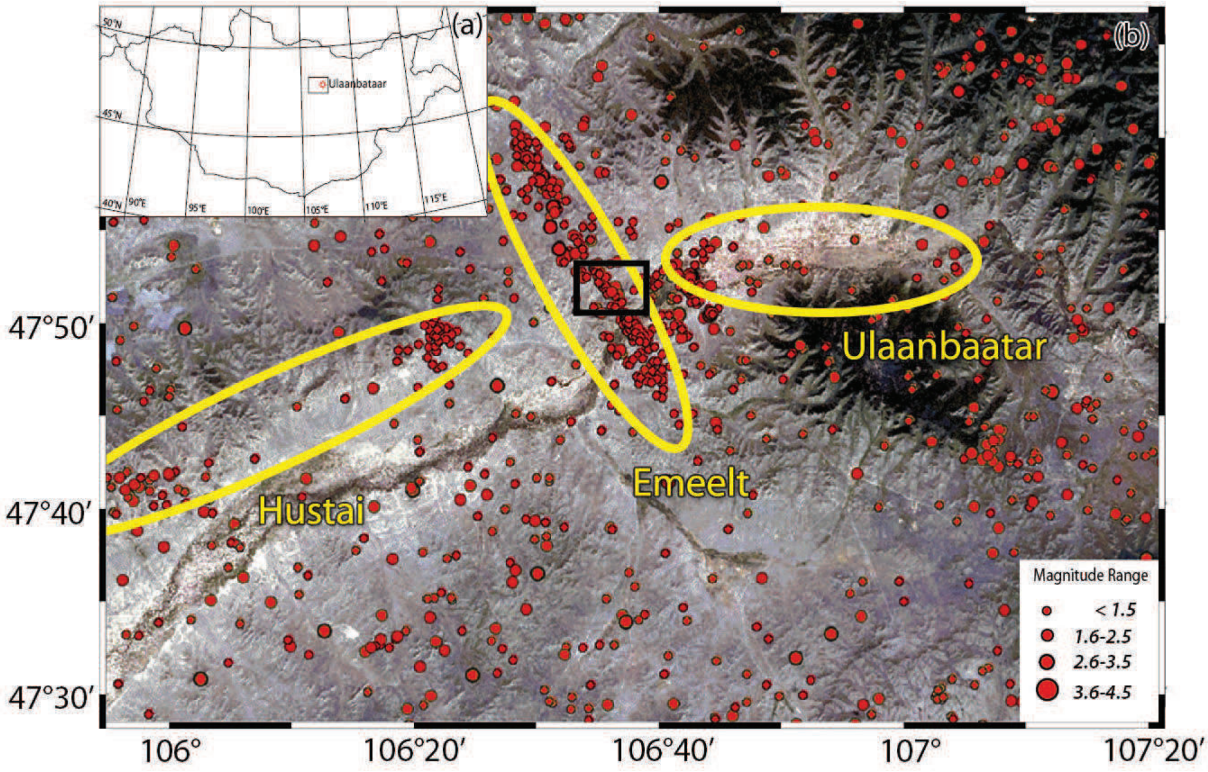

Figure 1 : (a) Map of Mongolia with location of the capital, Ulaanbaatar. (b) Zoom over the area of Ulaanbaatar. Yellow lines surround the two main active faults (Emeelt and Hustaï) and Ulaanbaatar urban area. Red dots represent the seismicity since 2005 (after NDC data, RCAG). Note the strong alignment of the seismicity defining the Emeelt fault.

The Ground Penetrating Radar (GPR) method has been proven to give good and useful results to characterize faults by identifying offsets of radar reflections (Malik et al., 2007; Christie et al., 2009; Yalçiner et al., 2012) and buried fluvial channel deposits (Ferry et al., 2004). Many studies have shown that pseudo-3D and 3D GPR allow a better and reliable interpretation than 2D GPR profiles (e.g. Gross et al., 2000, 2002, 2003, 2004; Tronicke et al., 2004; McClymont et al., 2008b). Beauprêtre et al. (2012) used a pseudo-3D survey in order to image a buried channel network, which allows the reconstruction of the past slip history. McClymont et al. (2008a) have used geometric attributes of 3D GPR data to improve the visualization of active faults. Dentith et al. (2010) compared GPR data with trench results in order to study paleo-fault scarps in the case of deeply weathered terrains. The concept of radar facies developed and mainly used in sedimentology (Neal, 2004; Pellicer and Gibson, 2011) is now widely considered in active tectonic context (e.g. McClymont et al., 2008a, 2010).

Nevertheless none of these studies were performed on active fault zones showing low slip rate. It is the first time that we use GPR to explore and reveal the buried traces of an active fault in such a context. Our study is focused on the Emeelt fault (Fig. 1), which is associated to an intracontinental context, with moderate deformation very likely much less than 1 mm/year (Calais et al., 2003, 2006; Vergnolle et al., 2007). After some preliminary geomorphologic observations and a trench dug in 2009, two GPR campaigns were conducted in 2010 and 2011. Pseudo-3D profiles were recorded with a 500 MHz antenna over an alluvial fan and a paleo-channel crossed by the fault, to look for the displacement and/or the deformation of reflections and horizons. In addition, several long 50 MHz 2D lines (about 200 m long) were realized perpendicular to the fault in a much wider area. The objective of these profiles was to look for the geometry and lateral extension of the fault at greater depth and to verify the presence of other branches.

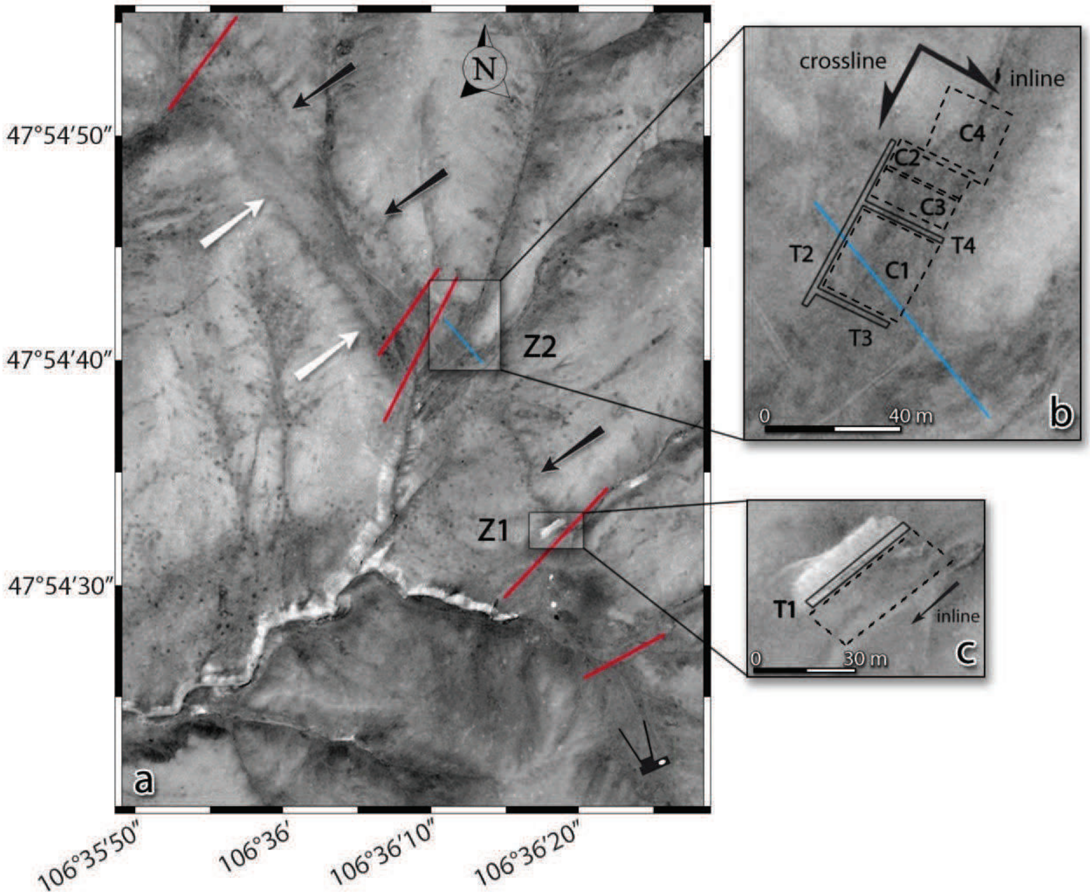

Figure 2 : (a) Aerial view of the studied area (satellite image digital globe, google earth 2009). Red lines indicate the location of the 50 MHz profiles (RTA). Black arrows highlight the fault trace and white arrows highlight a morphological scarp at the opposite side of the basin. Camera pictogram indicates the viewpoint of the Fig. 3. Figures 2.b and 2.c: zoom of areas Z1 and Z2. Trench locations are in black and the border of pseudo-3D 500 MHz GPR cubes are with black dashed lines. The C1 and C2 cubes were recorded in 2010 while the C3 and C4 cubes were recorded in 2011 (see the text for more details). The blue line in Z2 area represents the 500 MHz profile shown in Fig. 6.

2.2. Context and purpose

The geomorphologic features shown by the picture in Fig. 3 are clearly visible on the satellite view (Fig. 2). The scarp generated by the fault is clearly seen. The trace left by the fault on the surface (black arrows, Fig. 2) is a couple of metre wide. It has a N143° direction and can be followed about 10 km on the satellite image (Fig. 2, from google earth). If we include the seismic activity, we can consider its length to be 25 km minimum. From the picture (Fig. 3), we observe a valley in the center that is surrounded by two hills on both sides. The scarps separate those hills and the valley. This specific geometry recalls a collapsed basin such as a normal graben system (in an extensional tectonic context) or a reverse graben (in a compressional tectonic context) or even in a transtensional context. However, due to the low slip rate (less than 1 mm/y) and the long recurrence time, the fault scarp has been heavily smoothed by erosional processes, hiding the precise location of the fault on the surface. In addition, no clues on the direction of the fault dip are yet observed. However, recent deposits recognized in the area allow possible dating in paleo-seismology. Thus a first trench (referred to as trench T1) was dug in 2009 on the edge of an actual alluvial fan (Fig. 2c). GPR surveys were performed only in 2010 near the trench to, on one hand, compare both datasets and connect GPR facies with geological units and, on the other hand, identify the fault rupture at depth. Furthermore, we investigated a paleo-channel, by combining the trenches and GPR results, to estimate the cumulative displacement along the fault. A second trace, parallel to the first one, is observed on a smaller area (white arrows, Fig. 2 and 3). Both traces show a similar signature on the surface, and raise the question of a possible second branch.

Figure 3 : Picture of the survey area (see Fig 2 for location). Black arrows highlight the Emeelt fault scarp and white arrows show another morphological scarp. The trenches are visible on the right side.

2.3. Data acquisition and processing

2.3.1. Methodology of GPR acquisition

GPR is a geophysical method based on the propagation, reflection and scattering of high frequency (from 10 MHz to 2 GHz) electromagnetic (EM) waves in the earth (Daniels et al., 1988; Jol, 2009). For non-magnetic rocks, it allows imaging of the electric and dielectric contrasts of the shallow subsurface. The depth of investigation depends on the EM attenuation of the medium and the frequency used. The lower the frequency, the greater the penetration depth, which varies from a few centimeters in conductive materials up to 50 m for low conductivity (less than 1 mS/m) media (Davis and Annan, 1989; Jol, 2009). The vertical resolution depends on the velocity of EM waves and the frequency of the antennae used. Following the λ/4 criterion (Widess, 1973; Jol, 1995; Zeng, 2009), it varies from 70 to 5 cm for frequencies of 50–500 MHz and velocities of 0.1–0.14 m/ns. In general, features such as sedimentary structures, lithological boundaries, fractures and/or faults are clearly visible with GPR (Neal, 2004; Deparis et al., 2007; Gross et al., 2004;

McClymont et al., 2010), even when these features differ only by small changes in the nature, size, shape, orientation and packing of grains (Guillemoteau et al., 2012).

After the geomorphologic recognition of the Emeelt fault and a preliminary trench (T1) realized in 2009 (Fig. 2), we decided to use GPR measurements to investigate subsurface deposits potentially affected by the fault on a wider area. The GPR observations should help us to decide location of future trenches. Our first objective was to study an alluvial fan situated close to the trench T1 (referred to as Z1 area) for three reasons. First, the sedimentary deposits provide a stratigraphy that, if offset by the fault, can give us information on the geometry and dynamic of the fault, such as the dip, amplitude and direction of displacement with a non-destructive method. Second, sediments are usually favorable to EM propagation and third, the proximity of the trench will allow us to perform a direct comparison of both datasets (geology and GPR). In this survey we used a 500 MHz antenna to get detailed features at shallow depth and to have a depth of penetration and a wavelength consistent with the trench observations. We recorded 25 profiles of 40 m long on both sides of the trench T1 and parallel to it with the aim to cut through the fault. The space between profiles was 1 m and the recoding step was 0.03 m. Only fifteen profiles situated south of the trench show interesting results and are displayed on Fig. 2c. Two of them are presented and discussed later on (Fig. 4).

About 300 m north of Z1 area, the morphology shows two small streams crossing the fault and evidence of recent sedimentary deposits (Fig. 2b). To check for the presence of hidden paleo-channels filled by sediments and cut by the fault, we recorded eleven profiles across and perpendicular to both streams using the 500 MHz antenna. The profiles were 80 m long with a recording step of 0.03 m. The profiles show a clear paleo-channel under the northernmost stream, well imaged by GPR (blue line on Fig. 2b and Fig. 6). Consequently, we decided to perform the pseudo-3D GPR survey in this area crossed by the fault (Z2 area). We opened simultaneously, due to field constraints, three trenches (T2, T3 and T4) in Z2 area; one across the fault (T2) and two parallel to it (T3 and T4). Their location and geometry are shown in Fig. 2b. The GPR survey was separated in four distinct pseudo-cubes, denoted 1 to 4. Cubes C1 and C2 were recorded in 2010 while complementary cubes C3 and C4 were recorded in 2011. An overlap of five profiles was performed between the cubes C2 and C3 in order to assess the reliability of GPR data recorded at two different periods (2010 and 2011). The main objective of this survey was to image the paleo-channel in 3D in order to characterize any horizontal/vertical displacement caused by the fault. The pseudo-3D approach has become a common procedure and has successfully been used in the case of active fault studies (e.g. Malik et al., 2007; Beauprêtre et al., 2012). A full 3D acquisition schema requires an interval of a quarter wavelength grid spacing (Grasmueck et al., 2005) in both in-line and cross-line directions of the 3D cube. This would require one profile every five centimeters (for a mean velocity of 0.1 m/ns) with a 500 MHz antenna. The number of profiles would then be multiplied by five compared to our current survey. As a result, and due to time constraints on the field, we have chosen the pseudo-3D approach rather than a full 3D schema.

The profiles were parallel to the fault direction and spaced each 25 cm. (see Table 1 for more details about the acquisition geometry). In addition, long 2D lines were recorded with a 50 MHz RTA (Rough Terrain Antenna) antenna. The acquisition geometry is shown in Table

2. The purpose of those lines was to provide additional information such as the geometry and behavior of the fault at greater depth, the lateral extension of the fault and to test the hypothesis of a second branch in the area of investigation, which could take place along the second scarp.

	C1 (2010)	C2 (2010)	C2 (2011)	C3 (2011)
Size (inline x crossline)	25 m x 26.5 m	24 m x 10 m	24 m x 9.5 m	20 m x22 m
Number of inlines	107	41	38	45
Space between inlines	25 cm	25 cm	25 cm	50 cm
Number of crosslines	26	25	9	
Space between crosslines	1 m	1 m	3 m	

Table 1 : Details of the pseudo-3D surveys.

Frequency (MHz)	50	500 (Z1)	500 (Z2)
Antenna separation	4.2 m	0.18 m	0.18 m
Step interval	0.2 m	0.02 m	0.03 m
Samples	512	528	528
Stacks	16	16	16
Time window (ns)	535	82	82

Table 2 : Details of the acquisition parameters.

The topography of all GPR profiles was recorded using differential GPS. The GPS antenna was mounted on a backpack carried by an operator who was following GPR paths. The recording step of the GPS was set to 20 cm. Saw-tooth effects were observed on the topographic profiles due to the small movements of the operator while he was walking. In order to get rid of these undesirable effects, a high degree polynomial curve fitting for the data was used, instead of using raw topographic profiles.

2.3.2. Methodology of GPR processing

The processing of all GPR profiles has been performed with in-house software (Girard, 2002) written in Matlab. We used a common flow procedure involving a constant shift to adjust the time zero; a DC filter to remove the low frequencies; a flat reflections filter to remove some clutter noise (ringing caused by multiple reflections between shielded antennae and the ground surface); a time varying gain function and finally a band-pass filter (elliptic tapered filter). The time varying gain function is a smoothed version of the trace envelope calculated by Hilbert transform. Band-pass filters are of 20-150 MHz and 100-800 MHz for the 50 and 500 MHz antennae, respectively. A velocity analysis, which is not presented here, has been done over the surveying area by analyzing diffraction hyperbolae present in the GPR data. It gives a mean velocity of 0.135 and 0.095 m/ns for the data collected in 2010 and 2011, respectively. These values are constant and consistent for both frequencies (500 and 50 MHz antennae). The difference in velocity is explained by the unusual humid period during the survey in 2011 compared to the 2010 dry summer. Afterwards a Kirchhoff migration, which accounts for the topography (Lehmann and Green, 2000; Heincke et al., 2005 and Dujardin and Bano, 2013), has been applied before loading the data into seismic interpretation software (OpendTect). The topographic migration of each profile has been performed with a constant velocity.

2.4. GPR imaging results and interpretation

2.4.1. 500 MHz antenna, Z1 area, description of the profiles

The filtered radar sections were visually analyzed for data interpretation, and two of them are presented in Fig. 4. They are equally scaled and are presented with a vertical exaggeration of 1.9. Their locations are shown in Fig. 4a. The investigated alluvial fan is highlighted in yellow on Fig. 4a. The beginning of the profiles is on the NE to be in agreement with the map. The x-axis is also from NE to SW to stay consistent with the recording path of the GPR. For the interpretation, we used a combination of reflections picking with radar facies recognition. Four facies, used in the interpretation, are presented in Fig. 5. Despite the very low penetration depth of the profiles (up to 1.5 m), special features are observed and are related to the local geology. They give us information that helps to understand the fault behavior. The first facies is visible on both the profiles, it is either horizontal (pointed by black arrows) or with a slight dip in the direction of the topographic slope (grey arrow). Horizontal ones are related to the inner stratigraphy of the alluvial fan and were slowly deposited probably during rainfall or snow thaw. The dipping one is only observed in the first profile and is aligned with the uphill topography. This reflection is interpreted as paleo-topography before being wrapped up by the recent alluvial fan. Looking at the location of the profiles (Figs. 2 and 4a), we notice that profile (c) is on the edge of the fan, whereas profile (d) is much more on its central part. The sediment cover, undoubtedly greater in the central part of the alluvial fan (combined with the low penetration depth), results in the disappearance in the GPR profiles of the dipping reflection, which are either deeper or eroded. The third facies, the discontinuous-chaotic background, is observed on profile (d) at the beginning and the end. It also appears in-between the horizontal reflections (profile-c: from 23 m to the end; profile-d: from 20 to 25 m). On profile (d), a special feature has to be noticed: at the meeting point of facies 1 and 3, horizontal reflections are bent upward (circle on Fig. 4d). This curvature can be due to the warping of the reflectors during the last fault rupture.

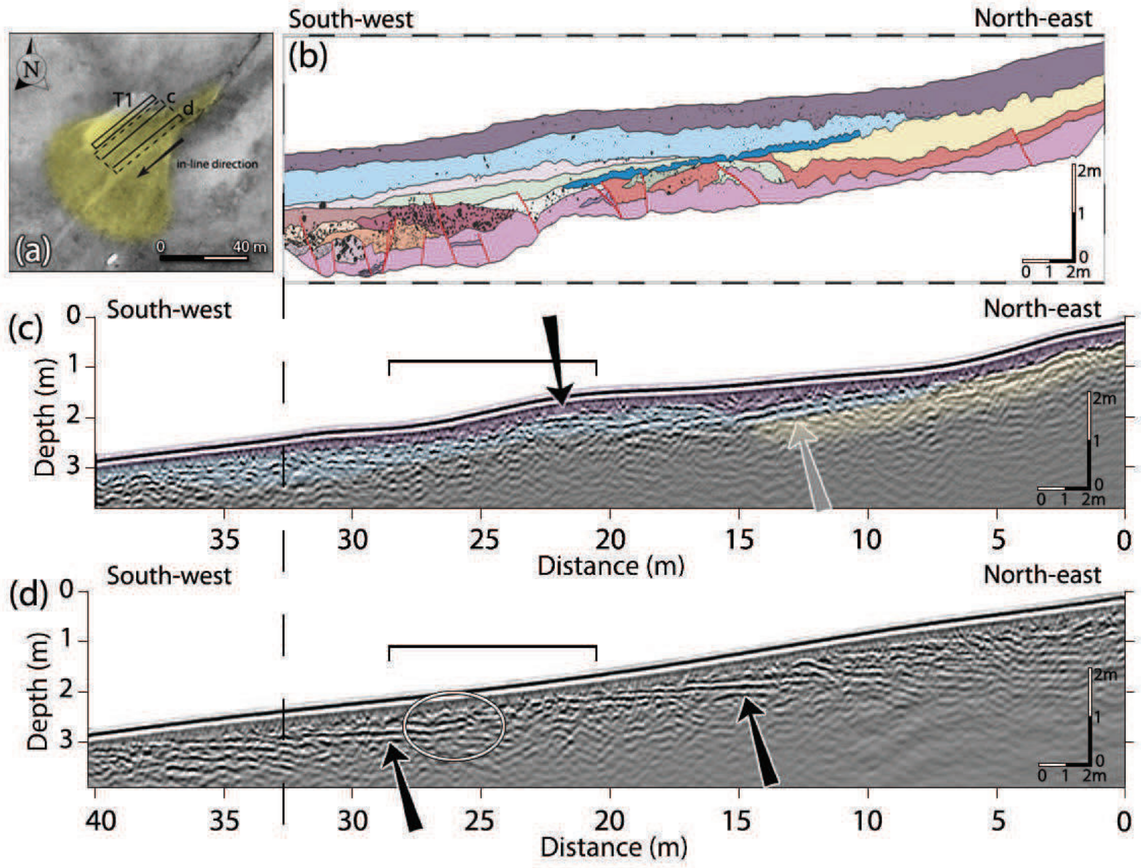

Figure 4 : a) Same as fig. 2c with the location of the GPR profiles (c and d) and the alluvial fan in yellow. b) Log of the southern wall of trench T1 situated in Z1 area and dug in 2009. c and d) 500 MHz GPR profiles. The profiles and the log are equally scaled; the vertical exaggeration is 1.9. Red lines in the log represent ruptures dipping mostly to the north-east from 20° to sub-vertical. The three first units, purple, blue and yellow in (b) are superimposed on the profile (c) for comparison. Black arrows show horizontal reflections and grey arrow shows dipping reflection (contact between blue and yellow units). The white circle highlights the bending of a reflection. Horizontal black brackets show the position of the fault scarp at the surface.

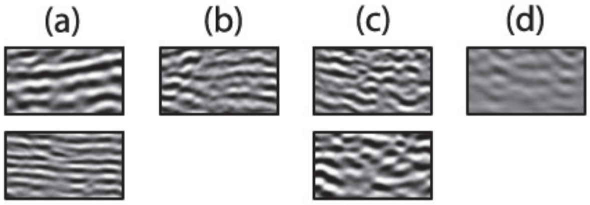

Figure 5 : Facies used in the interpretation of the 500 MHz data. (a) Facies having sub-horizontal to slightly dipping reflections with a clear lateral continuity. (b) Sub-horizontal to slightly dipping reflections with a moderate lateral continuity. (c) Chaotic background with no lateral continuity. (d) Strongly attenuated signal.

2.4.2. Comparison with the trench

Trench T1 was dug in 2009 on the edge of an actual alluvial fan (Fig. 2c), just before the GPR survey. It is around 2 m deep and displays mainly typical alteration from dry and cold climate. In the first metre, we find clay and silty material, which can be responsible for the low depth of penetration the GPR signal. On the south wall of the trench, a network of synthetic and antithetic ruptures and displacing deposits has been mapped (see red lines). The dip of these ruptures ranges from 20° to sub-vertical and most of them are dipping toward the north-east. The upper units of the trench (purple, blue and yellow) have been reported on profile (c) to allow comparison. Although the profile is 5.5 m away from the trench, interfaces between units are relatable to particular reflections in the GPR profile. The dipping reflection (grey arrow) is then well aligned with the top of the yellow unit and on the left is following the bottom of the light blue one. The interface between the purple and the blue units is rather flat and fits the observed horizontal reflections (from 16 to 13 m). This is relatable to both reflections indicated by black arrows on profile (d) of Fig. 4. The chaotic background in the middle of the profiles (24 to 29 m on profile (c) and 20 to 25 m on profile (d)) corresponds to the location where the purple-blue interface is dipping. However, due to the low penetration of the 500 MHz antenna, it is not possible to link the deeper units and ruptures with the GPR data.

To sum up, two different types of reflections were observed (the dipping one and the horizontal ones), and a chaotic facies is breaking off their continuity. The dipping reflection observed on the first profile is related with a previous paleo-surface, wrapped up by the alluvial fan sediments. The horizontal reflections, overlapping the dipping one on the right are related to the inner sedimentation of the fan. However, in the middle, a chaotic facies is observed and interpreted in terms of crushed or disorganized material destroying the continuity of the layers. The location of it, in the fault zone (black brackets, Fig. 4c and 4d), is considered to be the result of the movement of the fault underneath. The horizontal reflections are bent where they meet the chaotic facies. As the fault seems to have an important strike-slip component, we cannot use these observations as a measure of displacement but only as a deformation zone.

2.4.3. 500 MHz antenna, Z2 area, pseudo-3D cubes

2.4.3.1. Description of the profiles

On the north of the Z1 area we recorded eleven profiles of 80 m long across the two streams to verify the presence of the paleo-channel in the GPR data and to help choose a location for the precise 3D work. One of these profiles is presented in Fig. 6. The dipping reflections showing moderate continuity are indicated by black arrows. The middle and the right ones clearly define the flanks of a paleo-channel. Sub-horizontal reflections with moderate continuity and many diffraction hyperbolas lie in-between and are related to the sedimentary filling of the channel and the presence of many rocks. On the left side, another dipping reflection is observed. It is related to the edge of a second paleo-channel crossed by the profile. From those results, we decided to investigate the first channel in depth with the pseudo-3D surveys (Dujardin et al,. 2012). The acquisition geometry is presented in table 2.

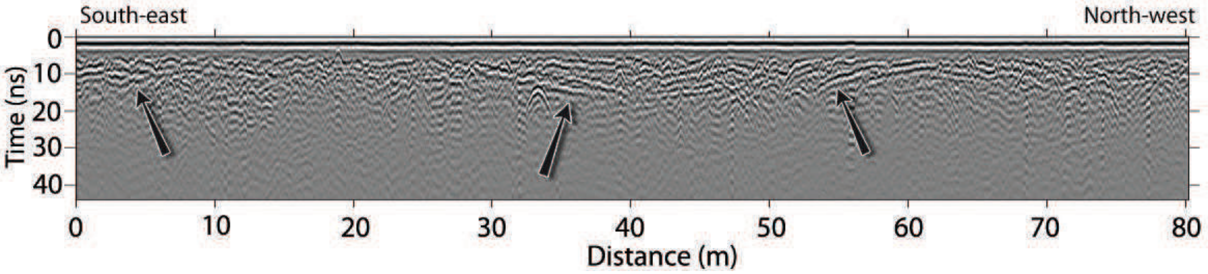

Figure 6 : Example of a 500 MHz profile crossing paleo-channels and recorded in 2010 to verify the presence of the paleo-channel in the GPR data before the precise work on "cubes". Its location is displayed in Fig. 2 (blue line). Black arrows highlight dipping reflections (with facies a, Fig. 5), which are related to the flanks of the channels.

A selection of five profiles, extracted from the pseudo-3D cubes, equally scaled and with a vertical exaggeration of 1.4 is displayed on Fig. 7. The depth axes of the profiles are related to the most elevated point for the four GPR cubes, thus, the zero does not appear in the presented profiles. As observed in the map (Fig. 7f), profiles (a) to (d) are in-line profiles (from downstream to upstream). Profile (e) is a cross-line profile. Profiles (a) and (b) were recorded in 2010, and profiles (c), (d) and (e) in 2011. GPR sections (c) and (b) are both presenting the same profile, but recorded at different periods (2010 and 2011, respectively). They allow a comparison between the 2010 and the 2011 surveys. The location of the actual stream is at the lowest point of the topography in the profiles (between 6 and 10 m in profiles (a) to (c)). Once again, for the interpretation, we use the combination of reflection picking with facies recognition as presented in Fig. 5. The first facies (having sub-horizontal to slightly dipping reflections) show strong continuity and are observed in the central part of each profile. Their edges are highlighted by dipping reflections (black arrows) toward the center of the profiles except for profile (a). The dipping reflections are the signature of the flanks of the channel. On profile (b), a second, deeper reflection is observed (white arrow). This feature is probably due to interlocked channels. Horizontal reflections are related to the sedimentation within the channel. Facies having sub-horizontal reflections with moderate continuity and facies showing chaotic background with no lateral continuity are interlocked in between (profile a: 14 to 18 m; profile b: 11 to 14 m; profile c: 13 to 15 m) and on the extremities of the profiles (profile a: before 9 m and after 21 m; profile b: before 8 m; profile c: before 7 m). On profile (d), the extremities are characterized by a strong attenuation of the GPR signal corresponding to the bedrock in which the channel has been incised and filled. EM waves are then attenuated by a different lithology. The last profile (e) presents a cross-line from north to south; it shows many continuous reflections sub-parallel to the topography and consistent with the first facies. They are the GPR response of the sedimentary deposition in the direction of the flow. Cross-line profiles are of great importance in the later interpretation as they allow a strong connection with in-line profiles.

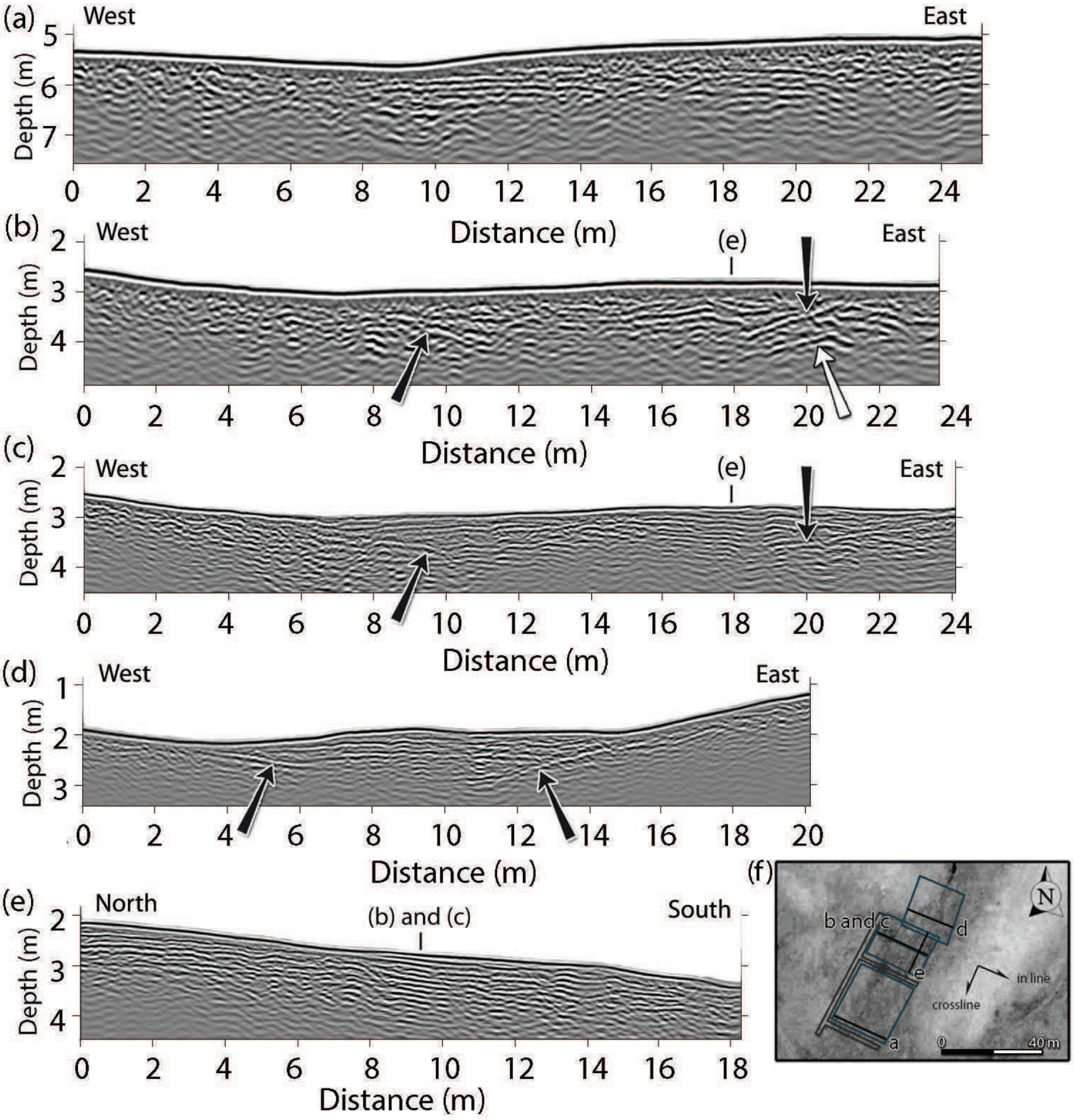

Figure 7 : Selection of 500 MHz profiles from the pseudo-3D cubes in Z2 area (profiles (a), to (e) in Fig. 7f), respectively. They are equally scaled and the vertical exaggeration is 1.4. Although the depth of penetration is low (from 1 to 1.5 m), many reflections, organized in two groups, are observed. The dipping reflections are related to the flanks of the channel (black arrows), while the horizontal reflections, confined between the flanks are related to the sedimentary filling of the channel. Note on profile (b) a second deeper flank (white arrow) probably due to interlocked channels. Profiles (b) and (c) are the same (b was recorded in 2010 and c in 2011), and display very consistent image. Note the much smaller wavelength in (c) due to the lower velocity in 2011 (soil more humid). Profile (e) is a cross-line showing only sub-horizontal reflections dipping slightly downstream, which are related to the sedimentary filling.

2.4.3.2. Comparison of the 2010 and 2011 data

The 2010 and 2011 profiles were then compared to check for their consistency. In 2011, the weather was very wet with heavy rainfall. This translated into a soil much more humid and a decrease in the EM wave velocity from 0.135 m/ns in 2010 to 0.095 m/ns in 2011. Profile (c) is the repetition of profile (b) (Fig. 7). The most striking feature is the difference in the wavelength, a direct consequence of the change in the velocity. The first facies is recognized in both profiles.

In profile (b), it is restricted between 14 to 20 m, with the chaotic facies lying from 9 to 14 m. In profile (c), the first facies is observed in the whole channel and the dipping reflection on the left, related to the flank of the channel, is better resolved until the surface. On the right, the deeper flank is not observed on profile (c). The electrical conductivity of the ground is higher due to the increased water content and the depth of penetration has decreased, masking the deeper flank on the 2011 data. It is not possible to connect specific reflection in both profiles, but the location of the facies is in good agreement and the channel flanks are very similar in both the profiles.

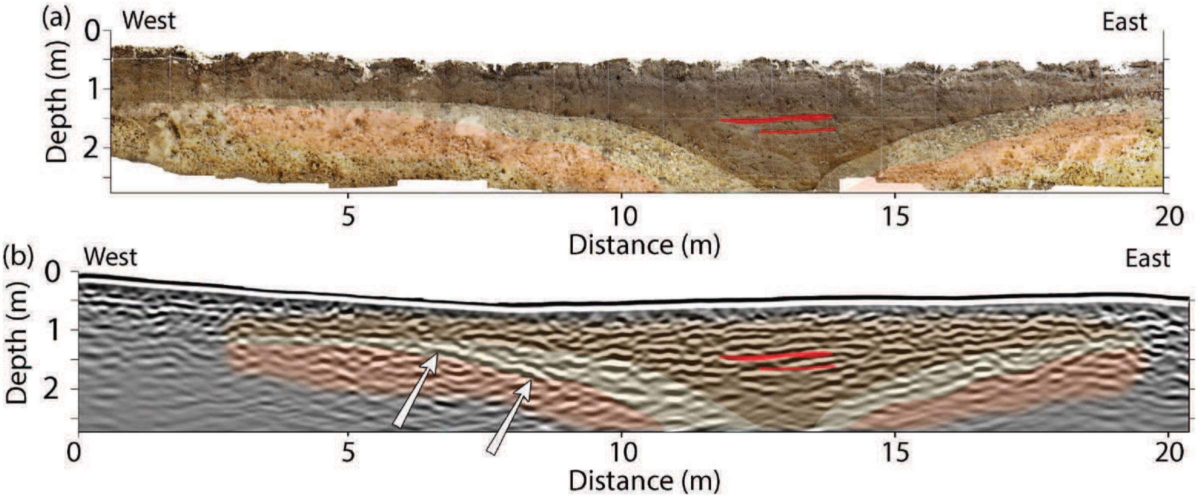

Figure 8 : a) Photomosaic of the north wall of T4 trench and (b) northernmost profile of cube C1, 2.5 m away from the trench wall (see location at fig. 2). Three main different units were identified in the trench highlighted here by brown, yellow and orange colors. They are superimposed on the trench and the profile for comparison. The brown is a thin brownish unit filling the channel, the yellow is a yellowish coarse deposits unit (centimetric sized) and the orange is a yellowish unit with fine material. Within the brown unit, a gravel lens is observed and highlighted by the red lines. A good consistency is observed between the GPR data and the trench. The gravel lens (red lines) is almost perfectly aligned with a reflection in the GPR profile. The left flank of the channel (limit between the yellow and the orange unit) is as well matching a reflection (arrows) and the yellow unit corresponds to an attenuated signal. On the east side, the units interfaces seems to match with dipping reflections but with a lateral offset that can be explained by the distance between the trench and the GPR profile (2.5 m).

2.4.3.3. Comparison between profiles and trenches

Fig. 8a presents a photomosaic from the north wall of trench T4. White wires in vertical and horizontal directions highlight the 1 m spacing gridding of the trench. The profile shown in Fig. 8b is the northern most profile of the cube C1 and is 2.5 m away from the trench T4 wall. The photomosaic and the GPR profile have the same scale, and there is no vertical exaggeration. Three main units were identified in the trench and highlighted here by brown, yellow and orange colors. The brown unit is characterized by a silty-sandy material with some gravel scattered inside it. Locally, gravels are gathered in thin horizontal layers, highlighted by red lines. It corresponds to the filling of the channel. The two next units are characterized by yellowish coarser material. The first one (the yellow unit) is a layer of around 50 cm thick with centimetric stones. The last unit (orange one) is very similar to the yellow unit, but with many scattered centimetric stones. The consistency between the GPR profile and the photomosaic becomes evident when we superimposed the interpretation of the trench on the profile. Boundaries of the units match reflections observed in the GPR profiles. The gravel lens (red lines) is almost perfectly aligned with a reflection in the GPR profile. The left flank of the channel (limit between the yellow and the orange unit) is as well matching a reflection and the yellow unit corresponds to an attenuated signal. On the east side, the units interfaces seems to match with dipping reflections but with a lateral offset that can be explained by the distance between the trench and the GPR profile (2.5 m). It is worthwhile to do the comparison for two reasons: firstly, it confirms our interpretation and secondly, it allows the connection of GPR facies with a specific lithology. Thus, first and second facies (Fig. 5) are linked to the brownish, massive unit of silty sands where gravel-sized lenses are found sporadically. Third facies is linked to a coarser-grained material (centimetric size stones) showing no evidence of layering.

2.4.3.4. Picking of the paleo-channel

After processing, all the profiles were merged in one single survey and loaded into seismic interpretation software (Opendtect) which allows 3D representations, depth slices and horizon picking. We tried depth slices representation and attribute analysis to improve the quality of the interpretation, but the results were disappointing due to the space between the profiles. Horizon picking was much more time consuming but gave much more interesting results. Owing to the strong disparity of the reflections, which did not allow a semi automatic picking, we picked the channel's flanks manually. During this step, cross-line profiles were of great importance as they permit a strong correlation of the reflections from one profile to the next one. The result of the manual picking is the 3D surface presented in Fig. 9 in relation with GPR profiles (three in-lines and one cross-line). The depth (from the most elevated point in the topography) is presented by color scale. Green lines on the profiles represent the picking, thus the intersection between the surface and the profiles. The red arrow indicates the flow direction. The displayed surface is obtained by interpolating the picked profiles taken from cubes C2, C3 and C4. Afterwards, the main slope of the channel was subtracted to provide a better interpretability of the data. The removal of the main slope straightens the channel, and the geometry of the flanks is greatly enhanced. The result is superimposed on the aerial view (Fig. 13). The channel appears very heterogeneous and many bumps are observed at its bottom. The penetration depth, from 1.5 to 2 m, is often lower than the depth of the channel. Thus, the bumps are related either to a mispicking of the base of the channel or to the collapse of a flank during storm weather. The SE flank is fairly straight on its upper part and starts enlarging at around 27 m distance from the SE corner of cube C1 (scale on Fig. 13a). This enlargement is linked to the arrival in the sedimentary basin. The NW flank is as well fairly straight in its deepest part except for the shift at around 49 m distance with right lateral amplitude of about 2 m (black arrow, Fig. 13).

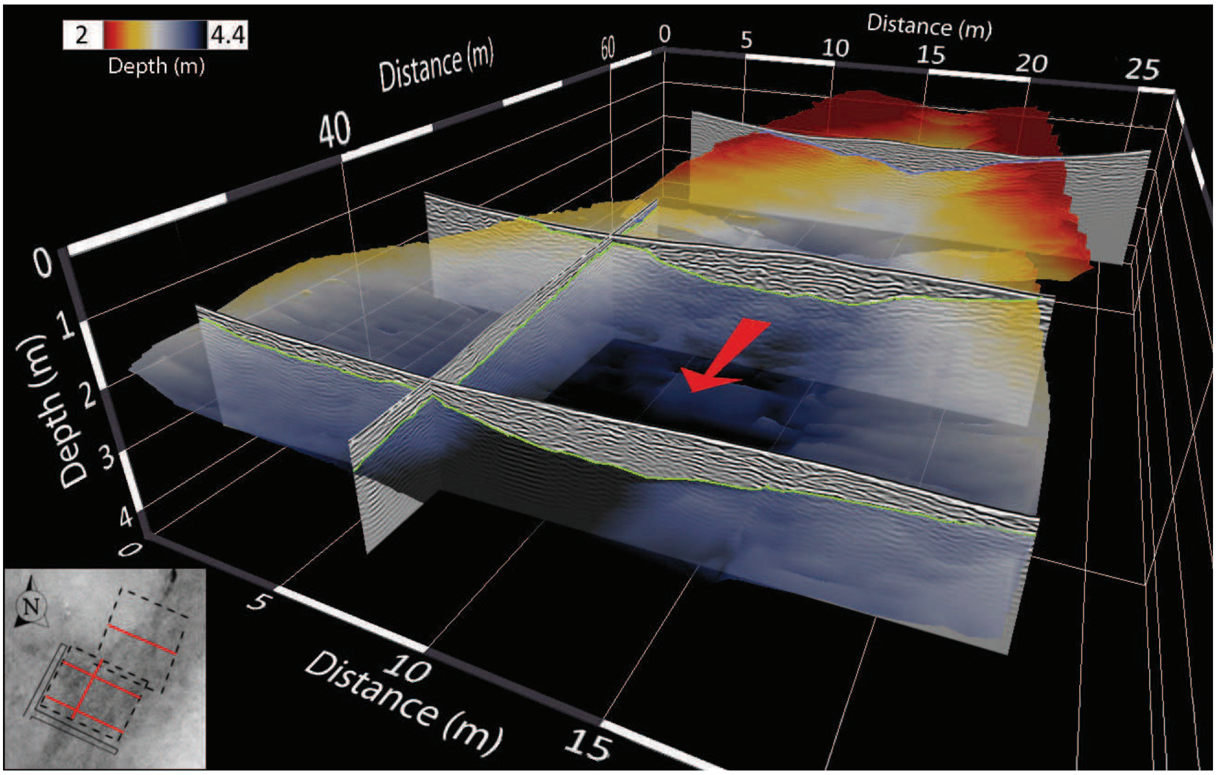

Figure 9 : Four GPR profiles with the paleo-channel picked in green. The 3D surface (in colors) of the paleo-channel was deduced from the picking on all the profiles of the cube C2, C3 and C4. The red arrow shows the paleo-flow direction. The map on the down-left corner show the relative position of the profiles.

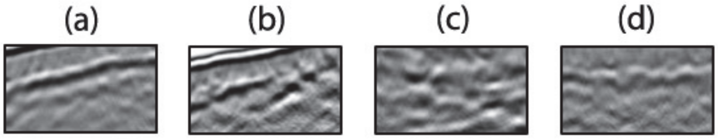

Figure 10 : Four facies (extracted from the GPR images) used in the interpretation of the 50 MHz GPR profiles. (a) Reflections showing clear lateral continuity; (b) Reflections showing moderate lateral continuity; (c) chaotic background; (d) strongly attenuated signals.

2.4.4. RTA (50 MHz antenna)

RTA profiles (50 MHz) were interpreted in a similar way as the 500 MHz profiles. They were visually analyzed and interpreted using a combination of GPR facies with reflection picking. The four facies used in the interpretation are shown in Fig. 10. They represent reflections parallel to the topography with strong and moderate continuity, facies with chaotic reflections, and, finally, facies strongly attenuated. All the RTA profiles presented in Fig. 11 were equally scaled with a vertical exaggeration of 1.8. The x-axis is from right to left to match the direction of the profiles on the map (Fig. 2 and 11f). Black lines on the map are the intersection of the fault scarps with the profiles. Their locations are reported on the profiles with the brackets. Despite the low penetration depth (10 m in the best case), much information is recovered from those profiles. First, a strong north-east dipping reflection was observed in almost every profile (indicated by black arrows). This feature is interpreted as a direct reflection from the fault plane, it gives access to the dipping direction (north-east), its dip and the exact location of the fault (from near the surface up to ten metres depth). The dip ranges from 27° in the north (profiles b and c), to 23° (profile d) increasing up to 35° in the south (profile e). Those reflections are exactly located under the brackets, which mean that the rupture reaches the surface. On profile (a), the reflection is not observed. However a strong separation (white arrow) between the chaotic facies (at NE) and the reflection with clear continuity (at SW) is observed at the base of the scarp. Discontinuities in the reflections (pointed by grey arrows) are the results of the collapse of diffraction hyperbolae after migration. Reflections, showing a clear continuity, are also present in other profiles, especially in their central part (in the valley) and in profiles (c) and (d), in their upper part as well. Around the fault reflections, a chaotic facies is always observed on a width of around 30 to 40 m.

On the other side of the valley, neither reflections nor a change in facies are observed on profiles (a) and (b) where they cross the second scarps. However, profile (c) displays an abrupt variation as well with a change in the penetration depth (white arrow). Reflections with lateral continuity on the right are contrasting with a chaotic background on the left. This sharp contact is in good agreement with the location of the geomorphologic scarp but is not enough to conclude on its origin.

2.5. Discussion

In addition to geomorphology and trench observations, the GPR images obtained by using 500 and 50 MHz antennae give us important information about the Emeelt fault, which was discovered in 2008 (Schlupp et al., 2012).

The GPR profiles across the fault with the 50 MHz antenna show the structure between 3 and 12 m depth. The location of the fault is consistent with the surface observations. The strong reflection, observed on all the profiles and related to the fault plane, confirmed the stability of the fault geometry in depth along the structure over about 2 km. This reflection is probably due to the contact between base rock on top and sedimentary deposits underneath. It gives us a good estimation of the near surface slope of the fault (23° to 35° to the NNE) in addition to the observations done at the bottom of the trench T1 (in area Z1) at depth between 1.5 and 2.5 m but showing steeper angle, mainly from 30 to 45° (fig 4b and 12b). The picture in Fig. 13b has been taken inside the trench T2 (area Z2), at the position of the pink asterisk. It shows evidence of the fault within a gravel layer with a dip toward the NNE. This dip direction was also determined at the surface as the fault trace moves upstream when crossing a local valley.

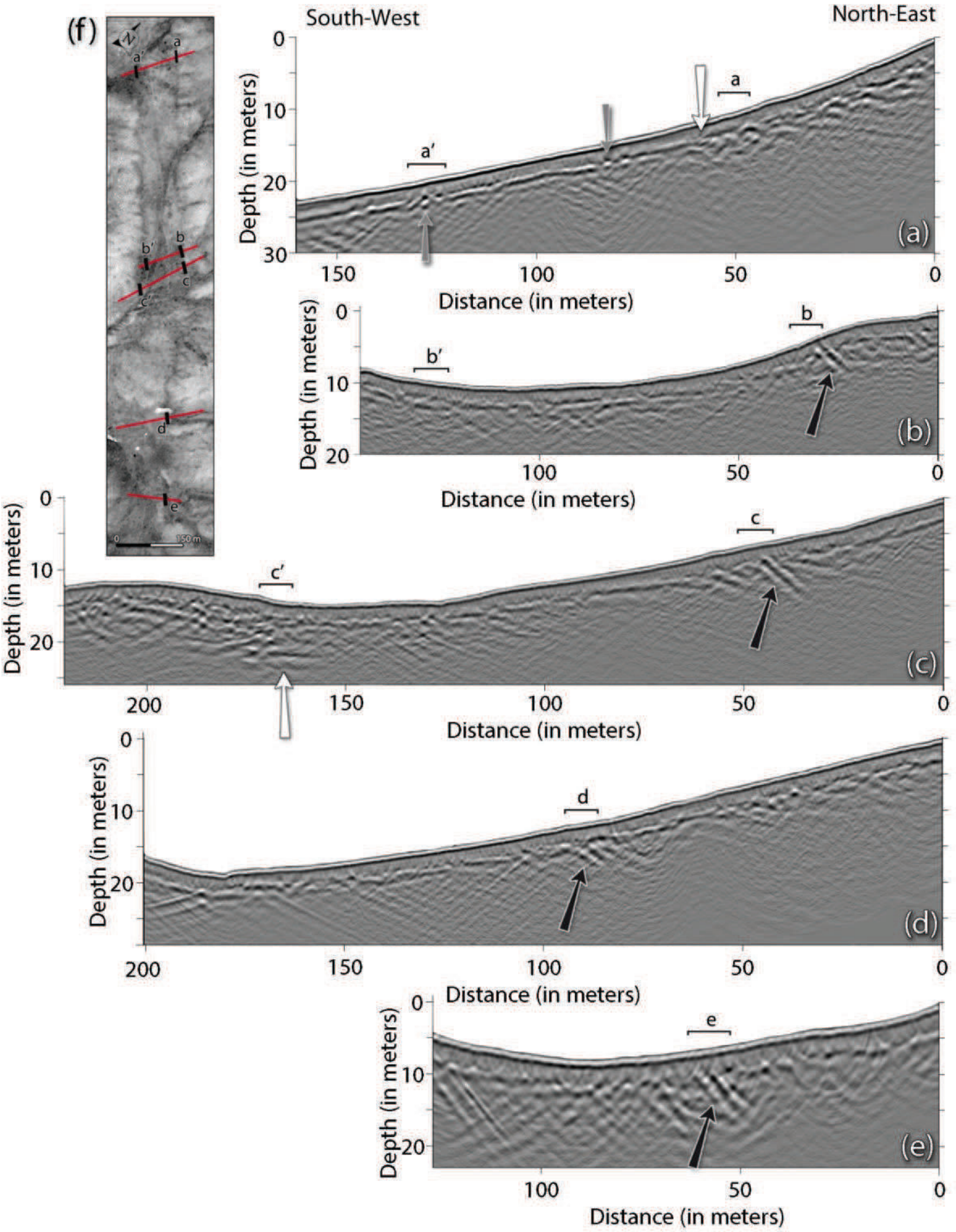

Figure 11 : 50 MHz GPR profiles (RTA). All the profiles are equally scaled with a vertical exaggeration of 1.8. Location of profiles (from top to bottom) is shown by red lines on the map (fig 11f). Letters (a) to (e) show the place where morphological scarps are observed on the surface. Black arrows show the reflections from the fault plane and the change in the GPR facies that highlight the location and geometry of the fault (see the text for more details).

The 500 MHz profiles across the fault, imaging a small alluvial fan (Z1 area), highlight a chaotic facies, interpreted in terms of crushed or disorganized material destroying the continuity of the layers, and located in the fault zone but no “fault reflection” has been observed with this antenna (Fig 4b and 4d). However, the “fault reflection” observed in the 50 MHz profile crossing the area is totally consistent with the location of this chaotic facies (Fig. 12c and 12d). The locally apparent vertical offsets of reflections on some of these profiles cannot be directly related to a vertical component of the slip. Firstly, it is impossible to associate the reflections observed on each side of the fault zone because of the shallow penetration of 500 MHz signal and the very few sub-horizontal reflections. On the other hand, the right lateral component can bring itself apparent vertical offsets in a context of interlocked alluvial deposits. However, a vertical component is suspected by the morphology and the dip of the fault near the surface but its amplitude cannot be quantified by our data.

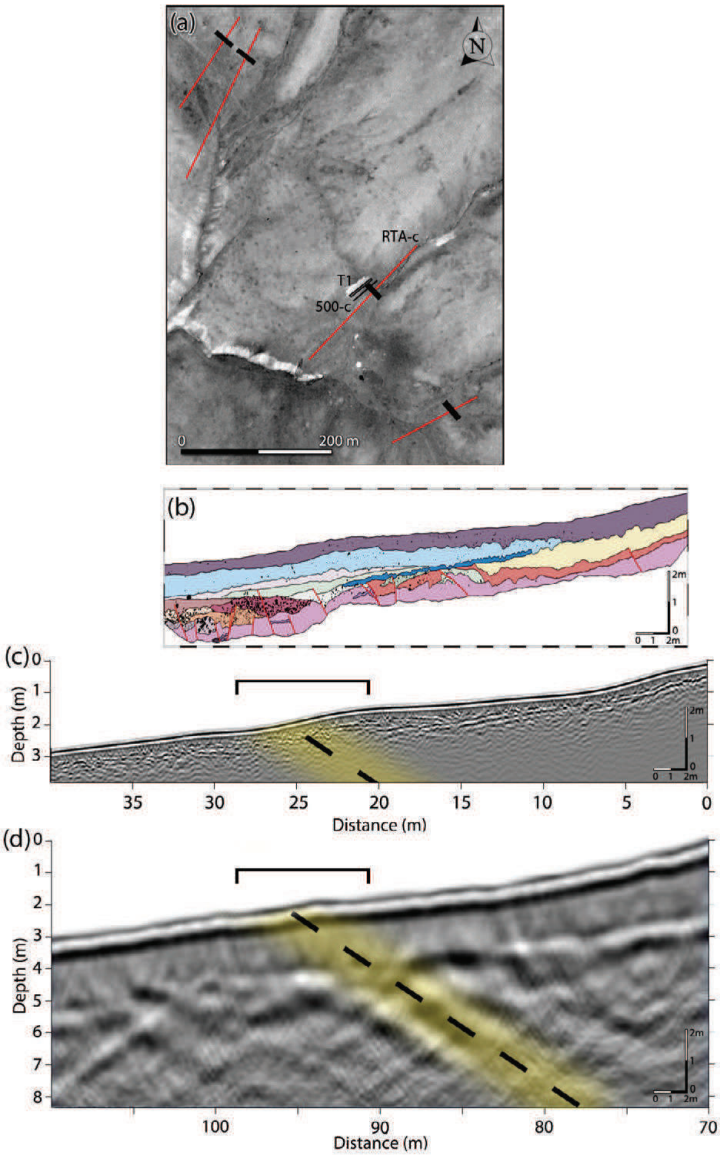

Figure 12 : Synthesis figure of area Z1. (a) Map, displaying the RTA profiles (red lines) with the location of the fault at surface (black lines perpendicular to the profiles). Trench T1 and the 500 MHz profile are drawn in black. (b) Trench T1, (c) 500 MHz profile from Z1 (Fig. 4c) and (d) 50 MHz RTA profile (Fig. 11d). They are all equally scaled and the vertical exaggeration is 1.9. Black brackets at the top of the profiles show the location of the scarp as observed on the field and satellite image. The dashed line, surrounded by yellow zone, highlights the fault as observed in the RTA profile. It is reported as well on the 500 MHz profile and corresponds to a chaotic facies between clear horizontal reflections.

On Z2 area, we observed a deep paleo-channel with a few 500 MHz profiles (down to about 2.5 m depth) fossilized by the filling material and crossing the fault. As we suspected a horizontal slip component from the linearity of the seismicity and the fault morphology, we decided to map the channel flanks across the fault by a pseudo-3D approach with numerous 500 MHz in-line and cross-line profiles that were acquired during 2010 and 2011 summers. A right lateral offset of about 2 m was imaged on the right downstream flank; it was preserved on the downstream right flank while it has been eroded on the downstream left flank (schema, Fig. 13c). Afterwards, the filling of the paleo-channel fossilizes the paleo-morphology.

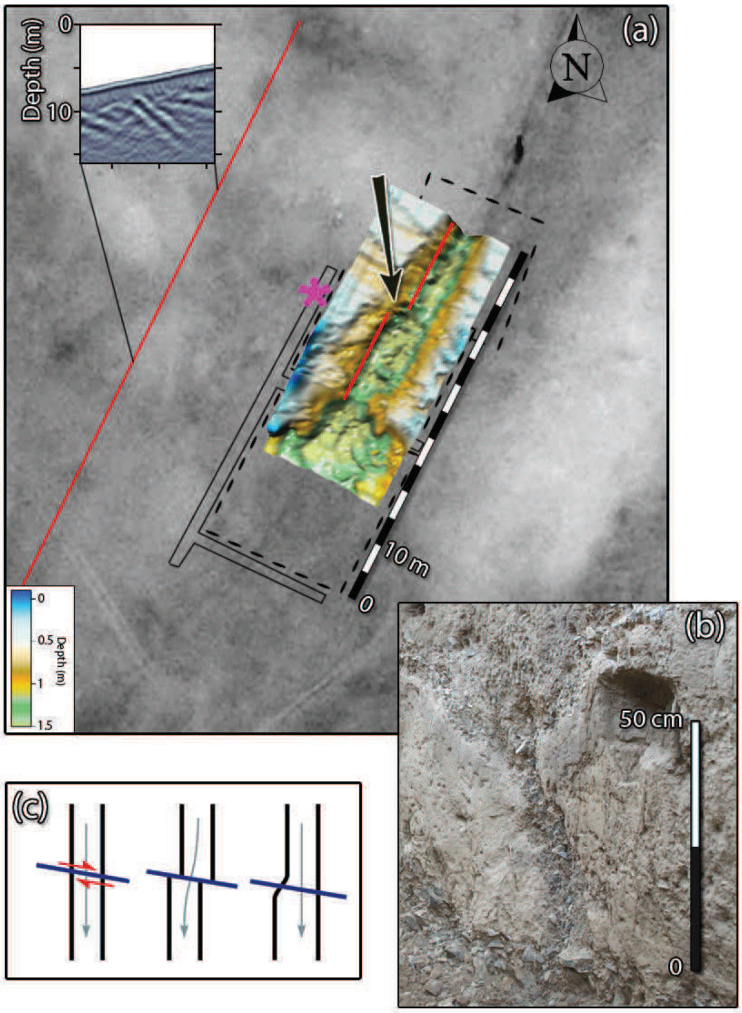

Figure 13 : (a) Interpretation map of Z2 area. The interpolated 3D surface of the channel (after subtraction of its main slope) is superimposed on the satellite image. An offset of 2 m horizontally is observed on the NW flank of the channel (highlighted by the red lines and the black arrow), which is consistent with a right lateral strike-slip. The pink asterisk shows the location of picture (b) in the trench where an evidence of the fault is observed. The closest RTA profile (upper left corner) shows the record and the location of the fault plane in depth. (c) Illustration of the evolution of the channel flanks due to the right lateral strike slip. The down left flank is preserved while the down right flank is eroded after the shift. The filling of the paleo-channel fossilizes the paleo-morphology.

This horizontal displacement could have been produced by one event (at least of Mw = 7) as it is observed for the Mogod earthquake (in 1967, about 280 km west of UB) of Mw=7.1 with a mean horizontal slip of 1.5 m (Baljinnyam et al., 1993; Bayasgalan et al., 1999b) or by several of Mw ≥ 6. In the 3D channel reconstruction, we did not observe any clear vertical offset. Nevertheless, it does not prove its absence as the bottom of the channel was locally difficult to follow due the low penetration depth, which was more or less of same depth as the bottom of the channel.

2.6. Conclusion

This work is a part of numerous studies on the characterization of active faults near the capital of Mongolia, UB. For the first time we used GPR to explore and reveal the buried traces of a newly discovered active fault in area showing low slip rate. It is a challenge as we are in a context where the geomorphologic features have been heavily smoothed since the last event due to erosion processes combined with a very long return period probably of several thousands of years. Despite the low penetration depth of the GPR (up to 12 m for the 50 MHz antenna and 1.5 m for the 500 MHz antenna), it clearly provided several important pieces of information that improve our understanding of the Emeelt fault geometry and horizontal displacement. The combination of 500 with 50 MHz antennae produces two complementary and consistent datasets as they allow the imaging of different structures.

A good consistency is observed between the 500 MHz GPR profiles and trench results. Pseudo-3D profiles, recorded with a 500 MHz antenna over a paleo-channel crossing the fault, provided information about the lateral displacement of 2 m caused by the fault. It could be associated to an earthquake with magnitude Mw of about 7 or several with magnitude Mw≥ 6.

The 50 MHz GPR profiles show a direct reflection, coming from the fault plane, giving access to the location, the dip angle and direction of the fault. The dip is toward NNE and it ranges from 23° in the north to 35° in the south part of fault segment investigated. In contrast, the linearity of the actual seismicity indicates a near vertical fault plane. To clarify that point, we need to investigate more in depth the active structure, by combining GPR with high resolution seismic profiles and very precise 3D relocation of the seismicity.

3. Hustaï

3.1. Introduction

L'extrémité est de la faille de Hustaï se situe à moins de 20 km à l'ouest de Ulaanbaatar. Elle s'étend sur près de 80 km vers l'ouest-sud-ouest (Fig. 14). La sismicité, dont la fréquence s'est intensifiée depuis 2005, est principalement localisée sur deux grappes distinctes (Fig. 15). La première se situe sur son extrémité est, tandis que la seconde se concentre sur la limite ouest de la figure 15, à environ 70 km de la zone urbaine de Ulaanbaatar. C'est au sein de cette deuxième zone que les investigations géoradar ont été réalisées. Les mesures géoradar représentent un travail préliminaire dans la zone, dont l'objectif est la caractérisation de la faille de Hustaï.

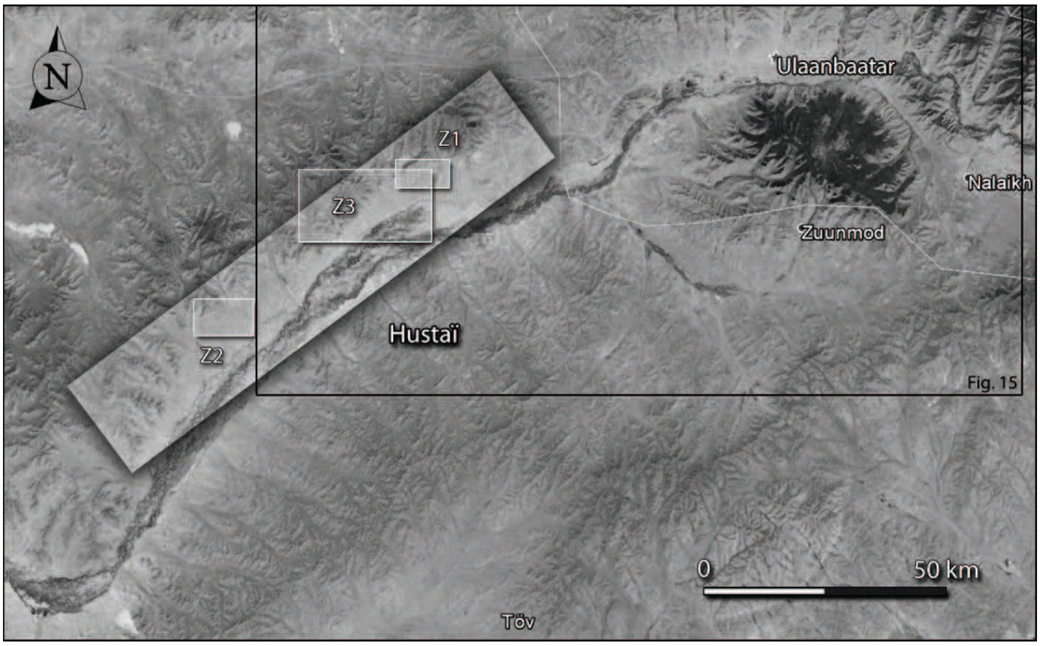

Figure 14 : Image satellite (google earth) de la région d'Ulaanbaatar. La zone de la faille d'Hustai est représentée par le grand rectangle en biais. Elle commence à moins de 20 km à l'ouest d'Ulaanbaatar. Les rectangles intitulés Z1, Z2 et Z3 représentent les zones agrandies de la figure 16. Les investigations géoradar présentées ultérieurement ont été faites dans la zone Z2. Le cadre noir localise la figure 15.

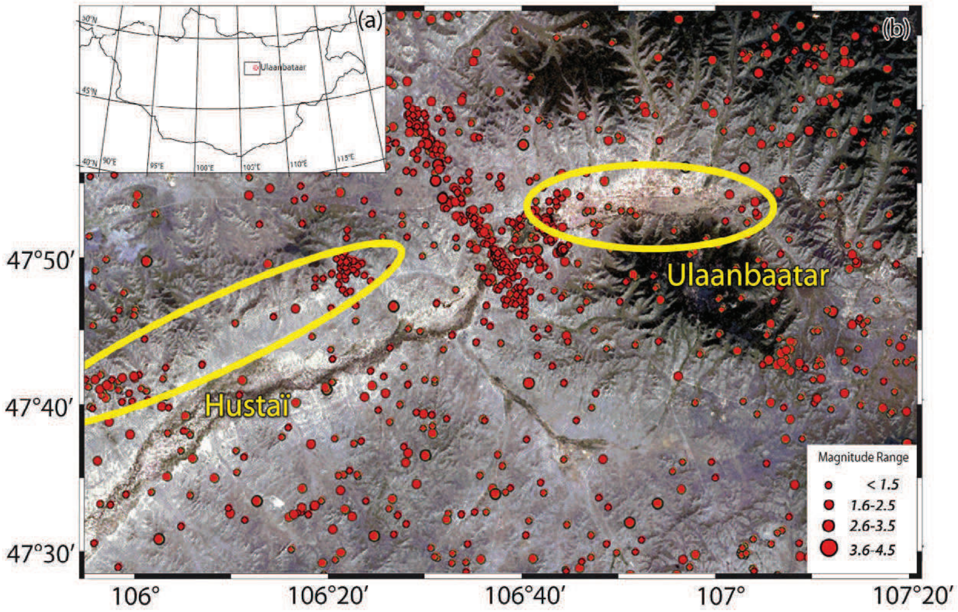

Figure 15 : (a) Carte de la Mongolie avec la localisation de la capitale, Ulaanbaatar. (b) Zoom sur la région d'Ulaanbaatar. Les points rouges représentent la sismicité depuis 2005 (d'après les données NDC, RCAG). Deux grappes de sismicité sont observées le long de la faille d'Hustai.

3.2. Géomorphologie

Des traces, associées aux anciennes ruptures de surface de la faille sont observées sur les images satellites. Trois zones ont été agrandies (Fig. 16, et localisation sur la Fig. 14) sur lesquelles plusieurs structures intrigantes ont été reconnues. Les flèches noires de la Fig. 16a et 16b indiquent une linéation continue observée sur une grande partie des figures, à la limite entre les collines et le départ des cônes alluviaux. A environ 800 m au sud de cette première empreinte (Fig. 16a), un alignement de patches verts (flèches blanches, Fig. 16a) est assimilé à une végétation plus dense que le terrain alentour, et donc une humidité plus importante en sous-sol. Ces îlots de végétation sont globalement linéaires et subparallèles à la première empreinte. Ils sont interprétés comme la marque d'une possible seconde branche de la faille. Les mouvements de la faille peuvent avoir bloqué localement le drainage naturel, ou au contraire, par désorganisation du matériel, augmenté localement la porosité du milieu. Dans les deux cas, le résultat est une plus grande concentration d'eau en sous-sol, créant ces petits îlots de végétation, marqueur du passage de la faille. Ces deux alignements se poursuivent sur environ 5 km, puis disparaissent à l'ouest et à l'est au contact de grands cônes alluviaux plus récent, évacuant les sédiments des vallées principales. Des indices supplémentaires sont observés sur la figure 16b malgré la moins bonne définition de l'image satellite. Dans l'alignement de la linéation mise en évidence par les flèches noires, un chenal, perpendiculaire à la faille, semble avoir subi un décalage (cercle 2). Ce même chenal, environ 1 km en aval est marqué par un coude (cercle 3) similaire à la première déformation. Le cercle 1, quand à lui, entoure une zone plus blanche en forme de lentille. Cette structure est interprétée comme un petit glissement de terrain d'environ 300 m de long et 120 m dans sa plus grande largeur. La limite aval de ce glissement est linéaire et alignée avec le coude du cercle 3. Ces marqueurs géomorphologiques semblent être un signe de la présence d'une autre branche de la faille dans cette zone. La figure 16c est une image aérienne à plus grande échelle. Elle correspond à la zone Z3 (Fig. 14). Sur cette figure, les marqueurs géomorphologiques, potentiellement reliés à d'anciennes ruptures de surface, ont été surlignés en noir. La partie en pointillé est une supposition sur la continuité de la faille (non visible) entre les parties est et ouest relativement bien alignées. Les distances entre ces segments sont de 900 m et 1,6 km au niveau des accolades, au sud et au nord respectivement. Sur cette image, on voit nettement que la faille de Hustaï n'est pas un simple plan de faille traversant l'intégralité du massif, mais plutôt la succession de nombreux segments de plusieurs kilomètres de long chacun.

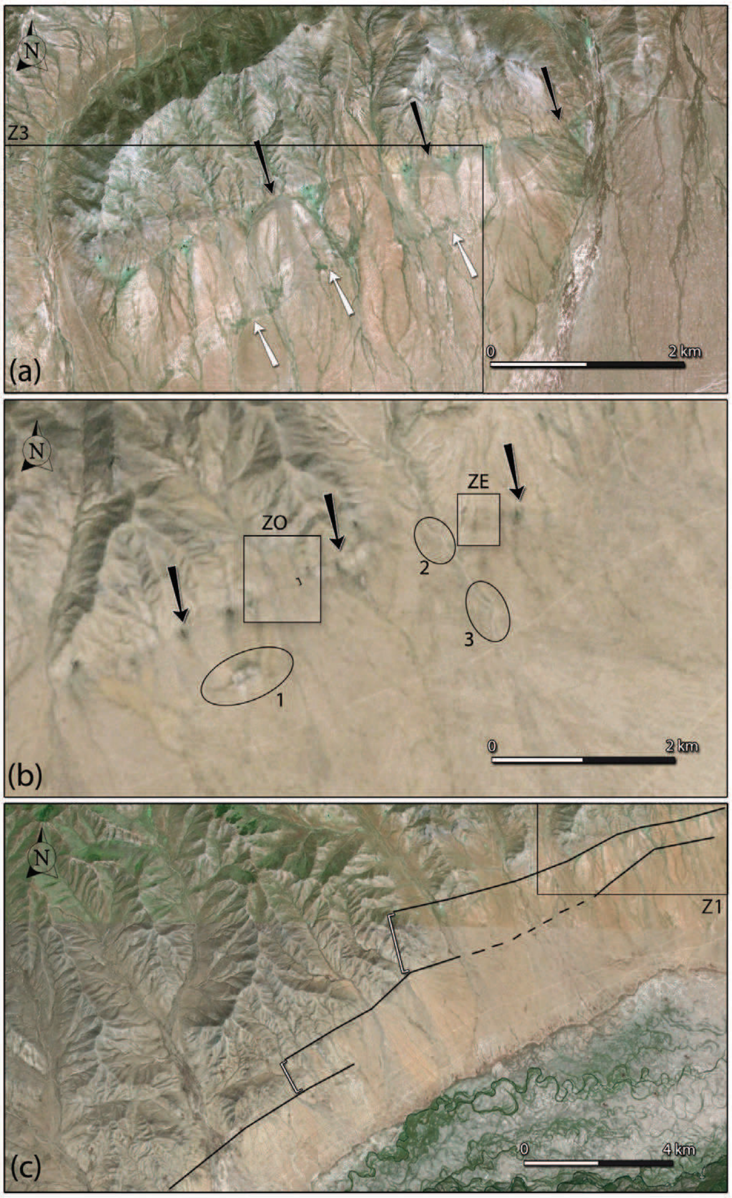

Figure 16 : Image satellite (google earth) des zones Z1 (a), Z2 (b) et Z3 (c). Les localisations sont montrées sur la figure 14. Les cadres noirs montrent les intersections entre les zones Z1 et Z3. (a) Les flèches noires pointent une linéation au pied des montagnes reliée à la trace de la faille en surface. Les flèches blanches indiquent des patches verts assimilés à une végétation plus dense. (b) Flèches noires : idem que (a). Le cercle 1 montre un probable glissement de terrain. Les cercles 2 et 3 indiquent des coudes dans un chenal. A noter : le possible alignement entre le glissement de terrain (cercle 1) et le coude du cercle 3. Les cadres ZO et ZE indiquent les zones d'investigations présentées sur la figure 17. L'accolade à l'intérieur du cadre ZO est reporté sur les figures 17a et 19a. (c) Les lignes noires sont superposées sur les marqueurs de la faille en surface. La partie en pointillé est une supposition sur la continuité du segment intermédiaire, masquée par les grands cônes alluviaux. Les segments sont espacés de 1,6 km et 900 m au niveau des accolades nord et sud respectivement.

3.3. Géoradar

3.3.1. Mesures et traitements

Nous avons retenu deux secteurs situés dans la zone de la figure 16b (cadres noirs) pour nos investigations géoradar. La zone ZO, à l'ouest (Fig. 16b et 17a), dont les profils ont été effectués sur des dépôts alluviaux, en sortie d'une petite vallée, et la zone ZE, à l'est (Fig. 16b et 17b), sur les contreforts des collines (en amont des dépôts alluviaux). Les données ont été acquises (comme précédemment sur Emeelt) avec deux antennes de fréquences différentes. Premièrement, de longs profils avec une antenne RTA (50 MHz) ont été effectués perpendiculairement à la faille dont le but est la localisation précise du plan de faille en surface et en profondeur et si possible (cf. chapitre sur Emeelt) la détermination de son pendage ainsi que de sa direction. En complément, des mesures avec une antenne de 500 MHz ont été effectuées pour préciser sa géométrie en proche surface. Les données radar ont été enregistrées en 2010.

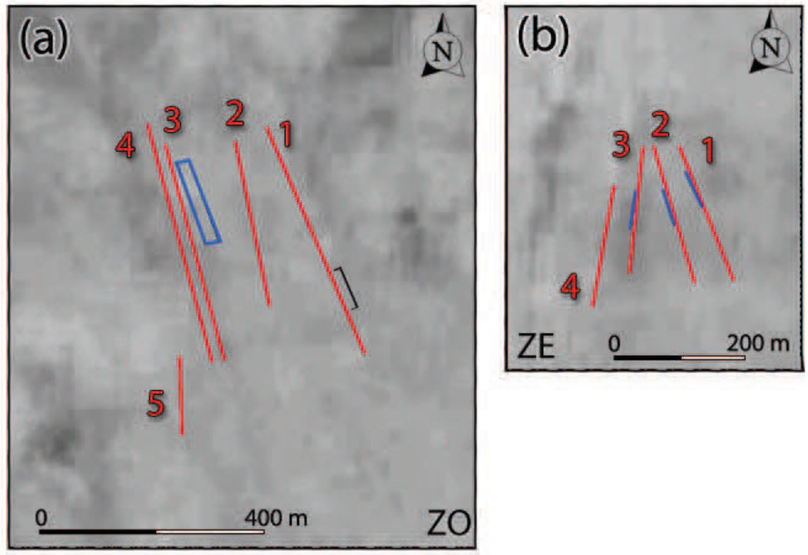

Figure 17 : Localisation des profils géoradar sur les zones ZO (a) et ZE (b). Tous les profils ont été enregistrés du nord au sud. Les zones sont localisées sur la figure 16b. Les lignes rouges indiquent les profils à l'antenne 50 MHz (RTA). Les lignes bleues indiquent les profils à l'antenne 500 MHz. Sur (a), le rectangle bleu représente 5 profils de 500 MHz, distants de 5m, le premier étant à l'est.

Dans la zone ZO, 5 profils RTA ont été effectués, mesurés du nord vers le sud (de l'amont vers l'aval) et perpendiculaires à la faille (lignes rouges, Fig. 17a). Ils sont complétés par 5 profils avec l'antenne de 500 MHz, également du nord au sud, et parallèles entre eux (lignes bleues, Fig. 17a). L'espacement entre les profils est de 5 m, et le premier se situe à l'est.

Dans la zone ZE, 4 profils RTA, suivant la même logique et les mêmes orientations que précédemment ont été enregistrés (lignes rouges, Fig. 17b). Les profils 500 MHz effectués sont une répétition d'une portion des trois premiers RTA (lignes bleues, Fig. 17b), afin de préciser les premiers mètres du sous-sol, invisibles dans les données de 50 MHz.

Les paramètres d'acquisition étant similaires entre les deux zones, ils sont résumés dans la table 3. De même, le traitement des données étant similaire à celui de la zone d'Emeelt, il ne sera pas détaillé ici (cf. partie Emeelt).

Frequency (MHz)	50	500
Antenna separation	4.2 m	0.18 m
Step interval	0.2 m	0.05 m (ZO); 0.02 m (ZE)
Samples	512	528
Stacks	16	16
Time window	535	81

Table 3 : Paramètres d'acquisition des profils.

3.3.2. Description et interprétation

La visualisation des profils RTA (50 MHz) indique une grande hétérogénéité du sous-sol, malgré une profondeur d'investigation modérée (de 10 à 15 m). La méthodologie d'interprétation suivie dans le chapitre précédent (combinaison de reconnaissance de faciès et de pointage de réflexions) a également été choisie ici. Les faciès utilisés et extraits des profils RTA sont affichés sur la figure 18.

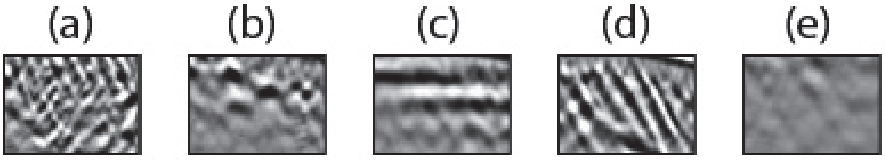

Figure 18 : Faciès géoradar extraits des profils de 50 MHz. (a) Faciès chaotique hachuré ; (b) Faciès chaotique ; (c) Faciès à réflexion continue subhorizontale ou subparallèle à la topographie ; (d) Faciès à réflexion pentée ; (e) Faciès fortement atténué.

3.3.2.1. zone ZO

- RTA

Les trois profils RTA les plus représentatifs de la zone ZO (1, 3 et 4, Fig. 17a) sont affichés sur la figure 19. Les profils sont présentés avec la même échelle et une exagération verticale de 1.8. Les profils 3 (b) et 4 (c) sont parallèles et espacés de 20 m. Le profil 3 (b) est décalé sur la figure pour correspondre au profil 4 (c).

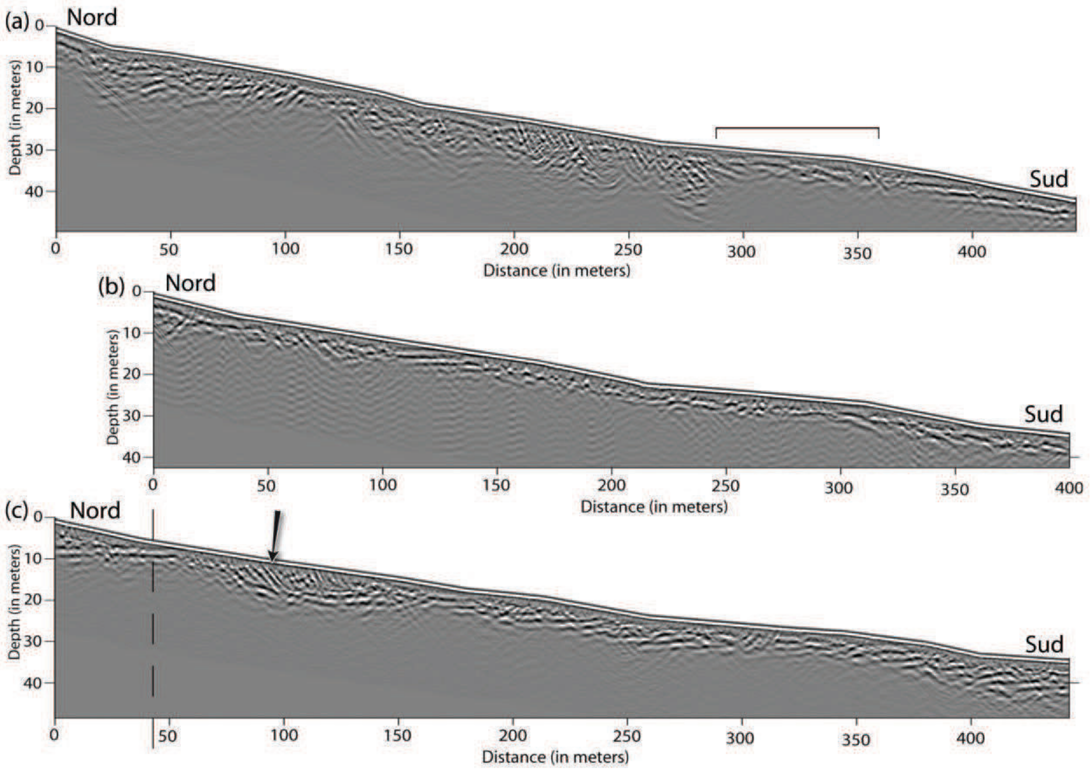

Figure 19 : Profils 1, 3 et 4 de la zone ZO mesurés avec l'antenne 50 MHz (respectivement a, b et c). Les profils ont la même échelle et une exagération verticale de 1.8. Le profil (b) est décalé pour être en accord avec le (c). L'accolade noire (a), correspondant à un faciès atténué, est reportée sur les figures 16b et 17a. La description détaillée des profils est dans le texte.

Le profil 1 (a) présente trois faciès principaux. Un faciès principalement chaotique de 0 à 280 m avec une profondeur d'investigation d'environ 12 m et montrant des variations secondaires. Un second faciès, de 280 à 360 m, chaotique mais beaucoup plus atténué (profondeur d'investigation de seulement 5 m) précède un faciès à réflexions horizontales légèrement inclinées vers l'aval, avec une profondeur de pénétration d'environ 5 m. Au sein du faciès chaotique (de 0 à 280 m), des variations de profondeur de pénétration sont observées sur des zones relativement localisées (à 120 m, 190 m et 240 m). Deux patches de faciès chaotiques hachurés sont observés entre 200 et 280 m.

Les profils 3 (b) et 4 (c) sont très similaires, avec cependant moins d'informations sur le 3 (b). Dans les deux cas, une réflexion horizontale (profil 4 (c)) ou subparallèle à la topographie (profil 3 (b)) est observée sur les 50 premiers mètres. Sur le profil 4 (c), une forte réflexion inclinée, d'un pendage de 34° (flèche noire à 95 m), est précédée et suivie d'un faciès chaotique. A la base de cette réflexion et du faciès chaotique en aval, une réflexion subhorizontale, moyennement continue est observée sur une distance de 60 m (de 90 à 150 m). L'intégralité de cette zone se présente sous forme d'un faciès chaotique sur le profil 3 (b). Le reste du profil 4 (c) est plus homogène et présente des réflexions subhorizontales moyennement définies (à la limite du faciès chaotique). Sur le profil 3 (b), une réflexion subhorizontale est observée de 110 à 140 m de distance, puis le reste du profil présente un faciès chaotique. Les profils 2 et 5 (Fig. 17a) ne sont pas présentés car ils ne présentent aucune structure particulière. Un faciès chaotique est observé sur la totalité des profils, sans variations notables.

Le profil 1 (a) est localisé sur le bord de la vallée, à proximité des collines. Les faciès chaotiques sont interprétés comme un signal représentatif de la géologie environnante (i.e. socle altéré). Les variations au sein des faciès chaotiques sont reliées à des hétérogénéités dans les profils d'altération du socle sous-jacent. Certaines zones, plus altérées, et permettant une circulation d'eau plus importante peuvent avoir une conductivité électrique plus importante, d'où une diminution de la profondeur de pénétration. La partie fortement atténuée (de 280 à 360 m) est cohérente avec la zone de linéation observée dans les images satellites (accolades, Fig. 16b, 17a et 19a). Elle est considérée comme une zone de déformation due à la faille. L'épaisseur des sédiments étant plus importante au milieu de la vallée, et la profondeur de pénétration des ondes géoradar étant relativement faible, cette zone de déformation n'est pas retrouvée dans les autres profils. La faille est donc considérée antérieure aux sédiments. La fin du profil se trouve dans les dépôts sédimentaires charriés par la vallée. Les réflexions subhorizontales sont donc interprétées comme du dépôt sédimentaire. Les deux profils suivant (Fig. 19b et 19c) se situent plus au centre de la vallée, où le faciès à réflexion subhorizontale est plus marqué, ce qui est cohérent avec une augmentation de l'épaisseur des sédiments vers le centre de la vallée. Les faibles profondeurs de pénétration sont interprétées comme des zones à plus forte concentration en argile. Bien qu'aucune tranchée ne permette d'étayer cette hypothèse, la similarité du climat avec la zone d'Emeelt (partie précédente) nous permet de supposer que l'on trouvera le même type d'altération. Le profil 4 (c) présente une structure particulière entre 80 et 150 m. Deux hypothèses peuvent expliquer la structure observée. Dans la première, la réflexion pointée par la flèche noire est interprétée comme un plan de faille et la zone chaotique en aval (environ 50 m de long), délimitée dans sa partie inférieure par une réflexion horizontale, comme un coin colluvial associé. Cependant, le coin colluvial est relativement grand (50 m de long pour 8 m de profondeur environ) et la réflexion horizontale semble couper le plan de faille. De plus, le plan de faille serait bien plus en amont qu'attendu au vu des traces de surface. Dans la deuxième hypothèse, la structure est interprétée comme un glissement de terrain. Les réflexions horizontales et inclinées étant à mettre en relation avec la surface de glissement. Cette deuxième hypothèse nous parait plus plausible. Aucune information ne nous permet cependant de mettre en relation le glissement de terrain avec la faille.

- 500 MHz

Les profils effectués à l'antenne de 500 MHz ont été enregistrés dans le but d'imager les premiers mètres de profondeur, invisibles avec l'antenne de 50 MHz. Au vue des résultats, ces profils n'ont été ni migrés, ni corrigés pour la topographie. La profondeur de pénétration atteint en moyenne 20 ns, localement 30 ns, ce qui correspond à une profondeur de 1.2 à 1.8 m pour une vitesse de 0.12 m/ns.

Un de ces profils est présenté sur la figure 20. Un faciès unique est observé, défini comme présentant des réflexions à continuité modérée à discontinue et affichant une configuration chaotique, localement subparallèle. Aucune évidence de faille, ni de déformation n'est observée, nous amenant à conclure que la partie superficielle du sous sol (les deux premiers mètres) ne semble pas avoir été endommagé par les séismes. La période de retour estimée étant relativement élevée dans la région (quelques milliers d'années), les sédiments observés sont considérés postérieurs au dernier grand séisme.

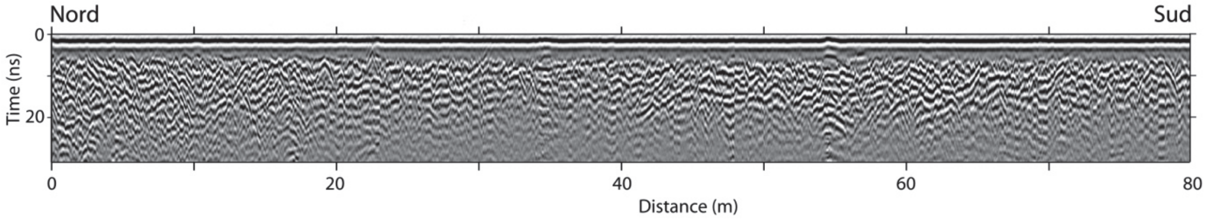

Figure 20 : Exemple d'un profil réalisé avec l'antenne de 500 MHz sur la zone ZO. Seuls les 80 premiers mètres sont affichés. Un unique faciès, présentant des réflexions à continuité modérée à discontinue, et affichant une configuration chaotique, localement subparallèle est observé.

3.3.2.2. zone ZE

- RTA

Les trois premiers profils de la deuxième zone sont représentés sur la figure 21 avec la même échelle et une exagération verticale de 1.3. Leur localisation est affichée sur la figure 17 et les rectangles noirs sont la localisation des profils 500 MHz (présentés plus loin). Ils présentent de grandes similarités entre eux. Au premier abord et sur les trois profils, une forte réflexion avec un pendage vers le sud (vers l'aval) est observée jusqu'à 12 m de profondeur environ. Ces réflexions, de part leur répétition, sont interprétées comme le plan de faille. Les pendages mesurés sont de 36°, 39° et 41° de l'est vers l'ouest (profils 1 (a) vers 3 (c)). Il est à noter que les profils sont distants d'environ 50 m, et que le troisième ne présente pas le même azimut. La trace de surface de la faille n'étant pas visible dans cette zone, nous ne connaissons pas son orientation exacte. De ce fait, les profils n'étant pas perpendiculaires à la faille, les pendages ne sont pas représentatifs de son vrai pendage. La partie en amont du plan de faille est caractérisée sur l'ensemble des profils par un faciès chaotique. En aval, un faciès chaotique est retrouvé juste en dessous du plan de faille. Il s'étend sur une distance d'environ 40 et 50 m sur les profils 1 (a) et 2 (b) respectivement, et jusqu'en fin de profil sur le 3 (c). Sur le profil 1 (a), il est suivi par une réflexion subparallèle à la topographie (de 120 à 180 m), puis par un faciès chaotique à très faible profondeur de pénétration jusqu'à la fin. Sur le profil 2 (b), on ne retrouve qu'un faciès fortement atténué de 140 m à la fin. Ces faciès de bout de profils sont interprétés comme du dépôt sédimentaire sur les contreforts des collines.

La partie en aval du plan de faille sur le profil 2 (b) présente également une réflexion subhorizontale à environ 15 m de profondeur sous la zone chaotique superficielle. Cette structure rappelle les observations faites sur le profil 4 (c) de la zone ZO. Cependant, la réflexion inclinée est interprétée ici comme le plan de faille. Le faciès chaotique et la réflexion horizontale associée peuvent être considérée comme un coin colluvial ou un glissement de terrain ayant eu lieu contre la faille, et probablement déclenché par le séisme.

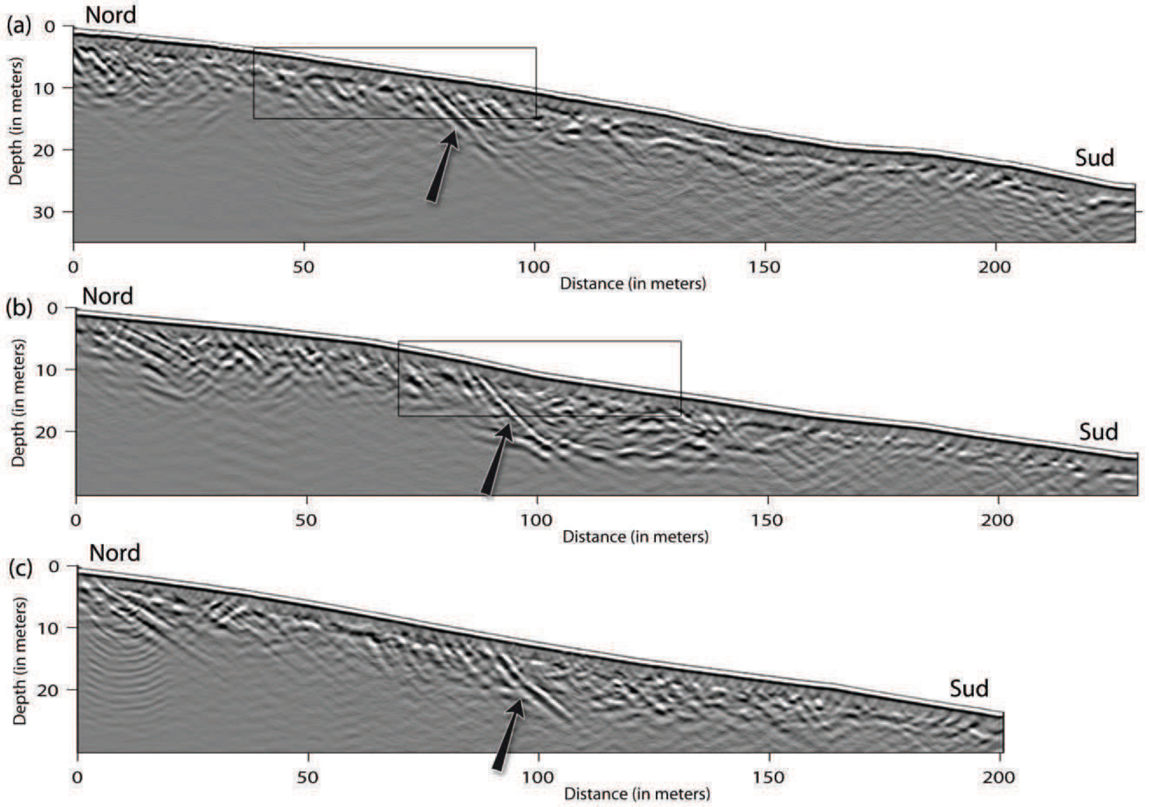

Figure 21 : Profils 1, 2 et 3 de la zone ZE, mesurés avec l'antenne 50 MHz. Les profils ont la même échelle et une exagération verticale de 1.3. Les flèches noires pointent une réflexion pentée interprétée comme le plan de faille. Les cadres noirs correspondent aux profils 500 MHz. La description détaillée des profils est dans le texte.

- 500 MHz

En complément des profils RTA, la partie à l'aplomb du plan de faille a été répétée avec l'antenne de 500 MHz pour préciser la géométrie dans les premiers mètres du sous-sol. Les profils 1 et 2 sont présentés sur la figure 22, avec la même échelle et une exagération verticale de 1.25. Au premier ordre, on observe un faciès présentant des réflexions à continuité modérée à discontinue. La configuration de ces réflexions est chaotique et localement, subparallèle. En détail, des réflexions inclinées (flèches blanches, Fig. 22) s'horizontalisent en profondeur avant de remonter vers la surface plus en aval. Ils délimitent des petits bassins d'1 à 1,5 m de profondeur pour 5 à 10 m de longueur (en rouge). Ces bassins rappellent, à petite échelle, les structures observées avec l'antenne RTA. Ils sont interprétés comme des zones de glissement dont la surface de décollement nous offre une réflexion. Bien que les derniers séismes aient pu déclencher ces glissements ou être un des facteurs déclencheurs, il n'est en aucun cas possible de conclure sur leur origine.

3.4. Conclusion

La sismicité et les images satellites ont permis de reconnaitre la faille de Hustaï et d'y choisir un site d'étude pour le géoradar. Les données géoradar ont été effectuées à la limite ouest d'une des grappes de sismicité, à environ 70 km de la limite ouest d'UB. Deux structures ont été prises pour cible. La première concerne des dépôts alluviaux en sortie d'une petite vallée, et la deuxième les contreforts des collines alentour.

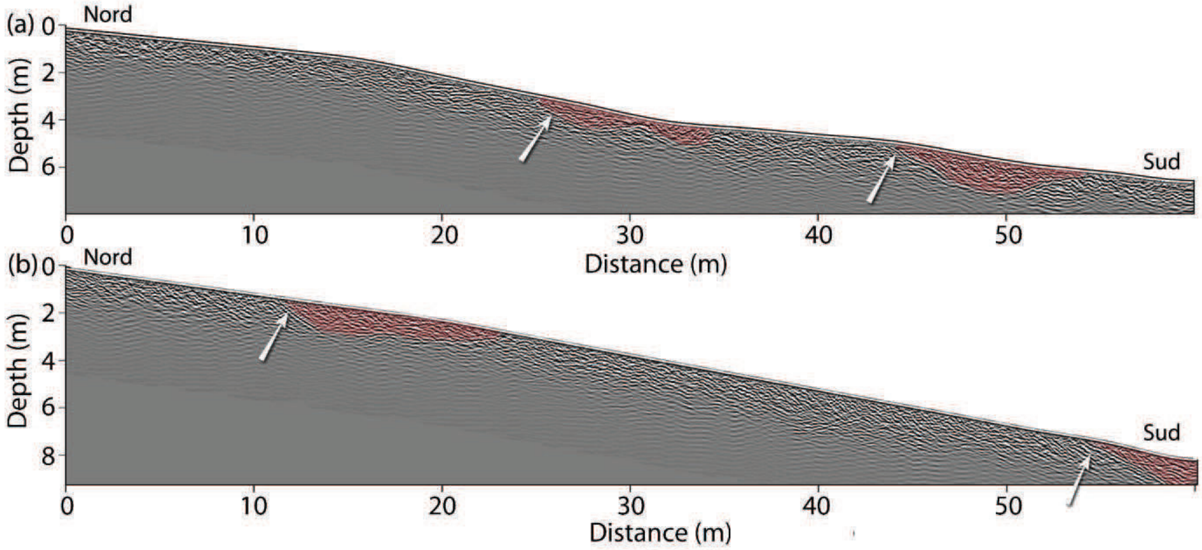

Figure 22 : Profils 1 et 2 de la zone ZE, mesurés avec l’antenne 500 MHz. Les profils ont la même échelle avec une exagération verticale de 1.25. Les flèches blanches pointent des réflexions inclinées, s’horizontalisant en profondeur, et délimitant des petits bassins (en rouge).

Sur la première zone (ZO), deux types de faciès, caractéristiques du socle (faciès chaotique) et des sédiments (faciès à réflexions horizontales), sont reconnus. La zone de faille, observée sur les images satellites est reconnue comme une zone à forte atténuation dans le profil sur le socle, mais n’est pas observée dans les autres profils. Cependant, une structure particulière est observée sur le profil 4 (c) mais l’hypothèse d’un glissement de terrain est plus plausible que celle d’une faille et d’un coin colluvial associé. Cette structure correspond à un faciès chaotique sur le profil 3 (b), mais reste très localisée. Les profils effectués avec l’antenne de 500 MHz ne montrent qu’un faciès chaotique et n’indiquent aucune perturbation notable dans les deux premiers mètres du sous-sol.

Sur la deuxième zone (ZE), une forte réflexion inclinée vers le sud, et correspondant à un pendage de 36 à 41° est retrouvée sur trois des quatre profils RTA. La répétition de l’observation nous permet de l’interpréter comme un plan de faille. A nouveau, une réflexion horizontale et un faciès chaotique sont observés et reliés à un glissement de terrain. Cette fois ci, son lien avec le plan de faille, et donc le dernier séisme semble évident. Les profils 500 MHz présentent des petits bassins interprétés comme des petits glissements de quelques dizaines de mètres maximum, mais leur origine ne peut pas être déterminée par nos données.

Grâce aux données géoradar, nous avons pu mettre en évidence une grande hétérogénéité du sous-sol. Les différents faciès observés avec les antennes de 50 MHz sont reliés aux différents milieux rencontrés (sédimentation en sortie de vallée, socle altéré) et localement nous donne des indications sur la faille jusqu’à 10 m de profondeur. Les données mesurées avec l’antenne de 500 MHz, à l’opposé, ne montrent que très peu de variations dans les premiers mètres du sous-sol.

Chapitre 3 : Le géoradar sur les dépôts pyroclastiques

APPLICATION DU GÉORADAR SUR LES DÉPÔTS PYROCLASTIQUES DU TUNGURAHUA, EQUATEUR

1. Introduction

Le Tungurahua est un stratovolcan andésitique situé dans les Andes équatoriennes. Une cycle éruptif a débuté en 1999 et est toujours d'actualité. Le paroxysme de l'éruption, atteint les 16 et 17 août 2006, a conduit à la formation de courant de densité pyroclastiques (coulées pyroclastiques).

Les coulées pyroclastiques sont des phénomènes pouvant se produire lors d'éruption volcaniques explosives. Ils sont composés d'un mélange de particules et de fluides (air ambiant, gaz) qui, dans leur ensemble, se comportent de manière similaire à un fluide homogène. Ces coulées, hautement mobiles et extrêmement dangereuses, sont souvent constituées de deux phases. La première, relativement dense, reste confinée dans les bas topographiques (vallées). La deuxième quant à elle, beaucoup plus diluée en particules, surnage la première et peu déborder des vallées lors de variations brusques (virage, falaise), formant des dépôts de cendres de dimensions variables. Sur le Tungurahua, ces dépôts de cendres sont couverts de dunes présentant des stratifications entrecroisées. La compréhension de la genèse et de la croissance des dunes peuvent apporter des informations sur la dynamique des flux pyroclastiques.

Dans cette optique, une campagne géoradar a été réalisée en mai 2012 sur les dépôts très bien conservés du Tungurahua. Trois antennes, de fréquences 250, 500 et 800 MHz ont été utilisées afin d'imager les structures internes des dépôts à différentes échelles et profondeur. Des longs profils avec l'antenne de 250 MHz ont été effectués sur une dune à grande échelle (environ 15 m de long pour 5 m de hauteur), délimitant la limite amont du dépôt de cendres. Certains profils ont été répétés avec les antennes plus hautes fréquence pour comparaison. Les antennes de 500 et 800 MHz ont par ailleurs été utilisées sur des dunes individuelles (6 à 10 m de long pour 0,4 à 1 m de haut) afin d'observer les structures internes et de voir les évolutions latérales. Une méthodologie pseudo-3D a été utilisée, et des traitements et visualisation 3D ont été essayés.

Ce travail a été effectué en collaboration avec l'université Ludwig Maximilians de Munich (LMU) et principalement avec Guilhem Douillet, doctorant en sédimentologie appliquée aux dépôts pyroclastiques. La campagne de mesure a été financée par le LMU.

Dans la première partie de ce chapitre, à vocation méthodologique, nous présentons en premier lieu une revue bibliographique des études GPR sur des dépôts volcaniques. Le potentiel de la méthode est clairement démontré, mais les traitements et méthodologies utilisés restent bien souvent simplistes. Nous présentons ensuite notre méthodologie d'acquisition et détaillons nos traitements, avec les avantages et limitations de chacun. Les mesures pseudo-3D ont montré des résultats très positifs, mais les traitements 3D (time slice, migration 3D, attributs) n'ont pas permis d'améliorer la qualité des données. Les raisons et améliorations possibles sont discutées.

Cette partie est actuellement en cours de publication dans la revue Solid Earth sous le titre:

Dujardin, J. R., Douillet, G. A., Kueppers, U., Abolghasem, A., Hall, J., Ramon, P., Mothes, P., Bano, M., Dingwell, D. B. The 3D structure of pyroclastic dune bedforms from the August 2006 deposits of Tungurahua volcano, (Ecuador): Part 1, ground penetrating radar methods.

La deuxième partie, quand à elle, est axée sur l'interprétation des données. Il s'agit ici de résultats préliminaires sur les différents objets investigués.

Ces résultats sont actuellement repris et approfondis pour la rédaction d'un second article qui sera publiée également dans la revue Solid Earth, sous le titre :

Douillet, G. A., Dujardin, J. R., Kueppers, U., Abolghasem, A., Hall, J., Ramon, P., Mothes, P., Bano, M., Dingwell, D. B. The 3D structure of pyroclastic dune bedforms from the August 2006 deposits of Tungurahua volcano, (Ecuador): Part 2, ground penetrating radar results.

2. The 3D structure of pyroclastic dune bedforms from the august 2006 deposits of Tungurahua volcano, Ecuador : Part 1, ground penetrating radar methodology

Abstract

Ground Penetrating Radar (GPR) has proven its efficiency in various contexts from the volcanic environment. Besides simple 2D imaging, this easy-to-use and non-destructive method is well suited to unravel the 3D architecture of deposits. Here, a GPR survey was carried out on the overbank, cross-stratified deposits resulting from dilute pyroclastic density currents generated during the August 2006 eruption of Tungurahua volcano (Ecuador). Three antennae (250, 500 and 800 MHz) yield imaging of structures to depths of 9, 4 and 3 m, respectively. The electromagnetic wave velocity is in the range typical of pyroclastic materials (0.09-0.12 m/ns). Several methods of acquisition and processing that can be useful for investigating pyroclastic deposits are tested. Migration is demonstrably efficient, as it enables the discrimination of real reflectors from diffraction hyperbolas produced by blocks. Results from pseudo-3D surveys can be interpolated to produce fictive cross lines and depth slices, helping to unravel the 3D nature of the deposits. Full 3D migration is attempted, but the results of that procedure are however blurred due to insufficiently constrained antenna position and the lack of a vertical profile of velocity structure. The sedimentary interpretation of the data can be found in the part 3 of this chapter.

2.1. Introduction

2.1.1. Ground penetrating radar

Ground Penetrating Radar (GPR) is a high-resolution, near surface, geophysical method based on the propagation, reflection and scattering of high frequency (from 10 MHz to 2 GHz) electromagnetic (EM) waves in the Earth (Daniels et al., 1988; Jol, 2009; Van Dam, 2012). EM waves sent into the ground are reflected at interfaces of electric and dielectric contrast and the reflected signals are recorded. Those discontinuities can result from changes in the water content, the chemical composition or the texture of the deposits. In sedimentary deposits, variations in grain size and water saturation are the main factors triggering reflections. GPR has proven its efficiency in many fields of geosciences but seems generally most efficient in sedimentary deposits, marked lithological boundaries, fractures and/or faults (Gross et al., 2004; Deparis et al., 2007; McClymont et al., 2010), even for subtle changes in the nature, size, shape, orientation and packing of grains (Guillemoteau et al., 2012). In the sedimentological context, interpretation generally uses GPR-facies analysis, analogous to their use in seismic studies (Jol and Bristow, 2003; Neal, 2004). 3D approaches have become a common GPR procedure in various environments with one of two alternative strategies typically having been employed (e.g. Beres et al., 1999; Corbeanu et al., 2001; Grasmueck and Weger, 2002; Malik et al., 2007; Munroe et al., 2007; Nielsen et al., 2009; Beauprêtre et al., 2012): 1) pseudo-3D surveys consist of dense arrays of profiles treated individually as 2D profiles, but with a small enough separation that they can be interpolated in

Paper	Type of study	Type of deposits	Frequencies (MHz)	EM wave velocity (m/ns) & method
LAVA FLOWS, FALLOUT, PDC				
Stasiuk and Russel 1994	test profiles, image stratigraphic units	LF, fall, blocks to ash PDC	100	0.1 assumed
Russel and Stasiuk 1997	major stratigraphic units - lab K'	LF, fall, blocks to ash PDC	100 (Field profiles); 10Hz-10MHz (lab K')	0.09 (LF); 0.7 (pumice fall); 0.1 (PF); (match exposure)
Rust et al. 1999	lab K' 8 poro	various samples	0.01 - 10	-
Russel and Stasiuk 2000	image stratigraphic units	pyroclasts	50 & 100 tested	0.09-0.11 CMP
Rust and Russel 2000	profiles and lab K' and waveforms	welded and unwelded and fall - poro	50	0.09 assumed
Rust and Russel 2001	profiles & velocities	welded and unwelded and fall - poro	50	0.08-0.11 CMP logs
Gómez-Ortiz et al. 2006	tests volcanic material	LF, fall, dikes	100	0.075 (fall); 0.099 (phonolitic LF); 0.097 (basanitic–phonolitic LF); 0.12 (Old LF); 0.070 (Aa and pahoehoe LF); (match exposures and hyperbolae)
Grimm et al. 2006	profiles and attenuation measurements	welded and non welded tuff	12.5-80	0.12-0.14
Heggy et al. 2006b	attenuation & dielectric properties, profiles	scoria cone	20, 40, 80	0.075
Abrams and Sigurdsson 2007	deposit boundaries	PF, fall	100, 200	0.088-0.11 (outcrop calibration) 0.091–0.105 (CMP)
Gómez-Ortiz et al. 2007	tests volcanic material -combined with ERI	LF, fall, hydromagmatic PF	100	0.075 (loose pyroclasts) to 0.1 (lava flows); (match exposures and hyperbolae)
Khan et al. 2007	profiles imaging	cinder cone & lava tube	100-400	0.03-0.0625 (inferred in figures from depth-time conversion)
DENSE PYROCLASTIC FLOWS				
Cassidy 2008	PF lobe contact	PF lobe	225	0.15 (in figure scale)
Gomez et al. 2008	Longitudinal architecture	PF	100	0.11 to 0.14 in text
Cassidy et al. 2009	stratigraphic units & block characterization	PF /pumice	225, 450	0.14 (CMP & hyperbolae)
Gomez et al. 2009	BAF architecture	BAF lobe	100	0.15 (in figure scale)
Gertisser et al. 2012	BAF architecture	BAF overflow and pre eruptive contact	200	0.1 to 0.12 (CMP & hyperbolae)
DILUTE PDCS				
Cagnoli and Russel 2000	soil contact, stratigraphy, bedforms	phreatomagmatic cross bedded tuff ring	50, 100, 200	0.095 to 0.1 (CMP)
Cagnoli and Ulrych 2001a	amplitude and waveform evolution	phreatomagmatic cross bedded tuff ring	900	0.12 (CMP)
Cagnoli and Ulrych 2001b	cross stratification imaging, pseudo 3D	phreatomagmatic cross bedded tuff ring	900	0.12 (CMP)
Cagnoli and Ulrych 2001c	soil contact, stratigraphy, amplitude evolution, cross stratification, pseudo 3D,	phreatomagmatic cross bedded tuff ring	50, 100, 200, 900	0.095 to 0.12 (CMP)
Kruse et al. 2010	stratigraphy tests	tephra fall & dilute PDC deposits	100, 200	0.043-0.047 - Poás; 0.065-0.09 - Irazú (CMP)
Nobes et al. 2012	long profiles units	phreatomagmatic cross bedded tuff ring	100, 200	0.70 CMP & 0.16 diffractions
FALL AND BALLISTICS				
Koralay et al. 2007	determination of zonation boundaries	welded ignimbrite	250	0.14 (hyperbolae)
Courtland et al. 2012	fallout architecture	tephra fallout on cinder cone	50, 100, 200	0.13-0.15 - dry season; 0.095-0.13 - rain season; (CMP)
Courtland et al. 2013	architecture / fallout vs ballistic deposition	cinder cone	100	0.06 -0.13 (CMP & hyperbolae)
LAHARS & DEBRIS FLOWS				
Cassidy et al 2003	architecture & large scale supercritical bedforms	jökulhlaup	50, 100	0.06 to 0.08 (CMP)
Carrivick et al. 2007	architecture and stratigraphy	Outburst flood	50, 100	0.05-0.1 (sediments); 0.09-0.12 (Igneous); CMP
Gomez and Lavigne 2010	preliminary architecture	Fresh lahar	500	?
Gomez et al. 2012	large scale bedding	volcaniclastic flood and ignimbrite	50	0.04 to 0.075 (hyperbolae)
Starheim 2013	architecture	debris flow	500	approx 0.09 to 0.11 (hyperbolae)

3D; 2) full 3D surveys treat every data point independently of the profile they belong to, before the reconstruction of 2D slices. A full 3D acquisition schema, although time-consuming, usually brings much higher quality results (Grasmueck et al., 2005; Heincke et al., 2005; McClymont et al., 2009a; McClymont et al., 2009b; Carpentier et al., 2012). It allows for advanced analysis by means of attributes (McClymont et al., 2008a; McClymont et al., 2008b) and even composite imaging of multiple methods (Böniger and Tronicke, 2010).

2.1.2. Pyroclastic density currents

Pyroclastic Density Currents (PDCs) are highly mobile and hazardous mass flows that are common products of certain types of explosive volcanic eruptions (Branney and Kokelaar, 2002). They belong to the class of particulate density currents (i.e. mixtures of particles and ambient fluid that behave, on a whole, in a manner similar to a homogenous liquid flow). The excess weight of particles induces a higher flow density compared to the surrounding fluid and thereby drives the momentum. The specificities of PDCs are their particulate phase, which is composed of variable amounts of juvenile erupted clasts, so-called pyroclasts. The high temperatures of the gas and/or pyroclasts possibly influence the flow dynamics by acting as a source of buoyancy (Andrews and Manga, 2012).

From the study of their deposits, PDCs are thought to enclose a broad range of flow characteristics, in grain size and sorting (from m- to µm scale), particle concentration (from dense granular flows to colloidal mixtures), and temperature (ambient to several 100s of °C). PDCs often consist of a dense basal pyroclastic flow (i.e. granular dominated boundary with characteristics of granular flows) confined by topography, and an overriding dilute flow (i.e., traction dominated boundary with low particle concentration) which can overflow topography but which also depends on the basal flow for its energy and particle supply (Douillet et al., 2013a and references therein). Dilute PDC deposits often exhibit cross-stratification and dune bedforms with characteristic sedimentary signatures (Douillet et al., 2013b and references therein). The genesis and growth of such bedforms have the potential to illuminate much towards our understanding of dilute PDC dynamics, although inaccuracies and controversy have hampered their description and use in interpretation of flow conditions (Cole 1991; Douillet et al., 2013b). In light of this opportunity, we have conducted a GPR campaign on the well preserved dilute-PDC deposits of the August 2006 eruption of Tungurahua (Ecuador) in order to constrain the sedimentary signatures of such flows.

2.1.3. GPR in the volcanic context

A number of studies have demonstrated the efficiency of GPR as an imaging technique within volcanic deposits (Table 1), though no signal is obtainable in the presence of active fluid circulation (Olhoeft et al., 2000; Pettinelli et al., 2008; Finizola et al., 2010). Two strategies have been employed to date.

In the first, the GPR signal has been used itself to characterize different types of deposits from the reflection parameters (Russell and Stasiuk, 1997, 2000; Rust et al., 1999; Rust and Russell, 2000). Such studies may then be complemented with laboratory measurements (see review in Rust et al., 1999; Heggy et al., 2006a) and/or numerical modelling (e.g. Cagnoli and Ulrych, 2001a).

GPR is also a powerful resource in profiles to image the continuous reflectors that represent stratigraphic limits, deposit bases and the internal flow deposit architecture. GPR studies on dense pyroclastic flows, lahars and other types of debris flows show that dense granular flow deposits are well suited for the method though highly susceptible to signal perturbation due to the presence of large blocks (e.g. Carrivick et al., 2007; Kruse et al., 2010; Gertisser et al., 2012). Migration techniques that enable correction of such effects are more and more exploited (Chow et al., 2006; Gómez-Ortiz et al., 2006, 2007; Khan et al., 2007; Kruse et al., 2010; Rowell et al., 2010). Some studies have elucidated the 3D architecture of deposits with 2D profiles with different orientations (Cagnoli and Ulrych, 2001b; Gomez and Lavigne, 2010; Starheim et al., 2013, Gertisser et al., 2012; Ettinger et al., 2014); but pseudo-3D strategies (i.e. dense arrays of profiles) are few (Cagnoli and Ulrych, 2001b; Cassidy et al., 2003; Chow et al., 2006; Koralay et al., 2007) and no full-3D data are yet available. Due to their fine-grained nature, coupled with their tendency to exhibit large grain-size variations between individual laminae, deposits of dilute PDCs are generally good GPR reflectors (Cagnoli and Russell, 2000; Cagnoli and Ulrych, 2001a; 2001b; 2001c). In light of this opportunity, provided here by very recent deposits from the August 2006 eruption of Tungurahua, a GPR survey was conducted with pseudo- and full-3D acquisition schemes in order to investigate the efficacy of topographic migration efficiency and 3D migration methods on pyroclastic dune bedforms. The sedimentary interpretation of the results is presented in part 3 of this chapter.

2.1.4. Dilute PDC deposits from the August 2006 eruption of Tungurahua

Tungurahua is an andesitic stratovolcano located on the eastern belt of the Ecuadorian Andes (Hall et al., 1999; 2008). The current eruption cycle began in 1999 is ongoing at the time of writing (June 2014). The climactic phase of the eruption led to the formation of PDCs on 14th of July and the night from 16th to 17th of August 2006 (Hall et al., 2013). A series of studies on the deposits enables a retracing of the eruptive conditions. Dense pyroclastic flows, with front velocities estimated at around 30 m/s (Kelfoun et al., 2009) and clasts temperatures of several 100s C in a colder gas phase (Benage et al., 2014; Rader et al., 2014-submitted) were confined to valleys on the flanks of the volcano. Dilute PDCs emanated from the dense flows by flow stripping at cliffs and were able to overflow the drainage network to eventually sediment as isolated, cross-stratified, “ash bodies” (Douillet et al., 2013a) with dominant grain modes in the range of ash (i.e. pyroclasts with diam. < 2 mm) at ca. 125 µm with spam in lapilli (i.e. > 2 & < 64 mm) and volcanic dust (i.e. < 0.63 mm). The juvenile fraction has an andesitic composition with 58-59 weight. % SiO2 (Samaniego et al., 2010). The surfaces of these ash bodies are covered with fields of dune bedforms that can be grouped into four types, each with distinctive surface morphologies and internal structures (Douillet et al., 2013b). Our GPR survey was carried on the four dune bedforms types detailed in Douillet et al., 2013b. It permits to investigate their 3D construction phases and shed light on the onset of growth, which is developed in part 3 of this chapter.

2.2. Field acquisition

2.2.1. Material

The GPR survey was performed with shielded antennas (Ramac system, from Mala Geoscience) with constant offset mode (constant antenna separation). The trigger for trace measurements was controlled by a measuring wheel (odometer). Three antennas of frequencies 250, 500 and 800 MHz were employed in order to access internal structures at differing resolutions and depths (Fig. 1, Table 2). The investigation depth depends on the EM attenuation of the medium and lower frequencies penetrate deeper. Field data generally exhibit penetration depths from a few cm up to 5 m for low conductivity (less than 1 mS/m) media (Davis and Annan, 1989; Jol, 2009). In contrast, for vertical resolution, which depends primarily on the wavelength of EM waves, lower frequencies yield a lower resolution. Following the "quarter-wavelength" (λ/4) criterion (Widess, 1973; Jol, 1995; Zeng, 2009), at a velocity of 0.1 m/ns, resolutions of 10, 5 and 3.1 cm should theoretically be attainable for frequencies of 250, 500 and 800 MHz, respectively (Davis and Annan, 1989). The configurations for each antenna were chosen in order to have the best compromise between data quality, signal-to-noise ratio and recording time (Table 2).

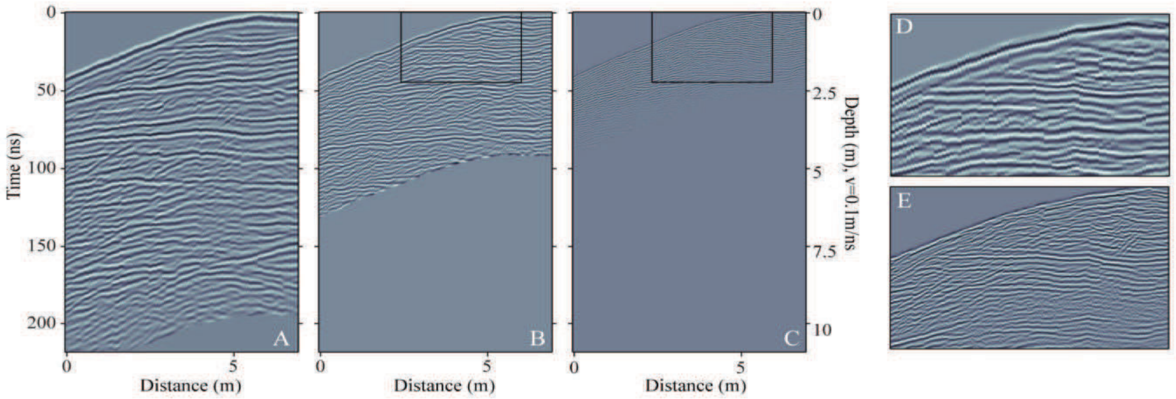

Figure 1 : Comparison of the results achieved on the same profile for each of the three antennas used in the study for the same profile. A) 250, B) 500 and C) 800 MHz; D) and E) Zoom into the structure in inlet in figure B and C) respectively. The vertical scale is in two-way time and the conversion to depth is made assuming a constant velocity of 0.1 m/ns (ca. no vertical exaggeration is displayed)

Antenna frequency (MHz)	250	500	800
Antennas separation (m)	0.36	0.18	0.14
Interval between traces (m)	0.05	0.05	0.02
Samples per trace	564	528	512
Time window (ns)	205	75	50
Stacks per traces	16	16	16

Table 2 : Parameters for the three different antennas used in this survey.

2.2.2. Survey

The field campaign was conducted six years after the eruption, in May 2012 and a thin (0.5 cm), consolidated, ash crust draped the 2006 pristine surface. Intermittent rain occurred daily and the investigated areas were in a fairly moist state. Data collection followed three acquisition schemes, depending on the object investigated (Table 3). Most profiles were acquired parallel to the inferred flow direction (i.e., perpendicular to a bedform's mean crest line), with some cross-profiles used for correlation. For individual small-scale bedforms (6 – 10 m length, 0.4 – 1 m thickness), only the 500 and 800 MHz antennas were used, in pseudo- and full-3D acquisition schemes. Over one particularly large bedform (ca. 15 m length, 5 m thickness) marking the upstream limit of an ash deposition zone ("quarter pipe shape of Chontal ash body" in Douillet et al., 2013a), long profiles (ca. 50 m) were acquired with the 250 MHz antenna and several meter steps between the profiles for imaging of its architecture together with some redundant profiles with the 500 and 800 MHz antennas for comparison (Table 3). Unfortunately, more than 150 profiles with the 250 MHz antenna, representing several kms of data over several ash deposition zones, could not be processed due to problems with GPS data that prevented any localisation and topographic constraints.

	Elongate		Trans		Lunate A	Lunate C		Quarter pipe Chontal				
Frequency (MHz)	500	800	500	800	800	500	800	250			500	800
Nb profiles	35	35	71	8	32	5	59	01-18	18-23	23-32	11	24
Space between profiles (m)	0.1	0.1	0.1	1	0.2	1	0.1	5	10	20	4	2
Size (inl*crl) (m*m)	12.5*3.4		9*7		6.6*6.2	10.75*5.8		~50*200			~40*40	~40*40

Table 3 : Details of surveys on individual zones and bedforms. Inl*crl is the area covered by the profiles in the direction of the profiles (inl) and in the cross direction (crl).

2.2.3. Topography acquisition

The topography of the whole survey areas was recorded with a terrestrial laser scanner coupled with differential GPS, but due to acquisition problems, only the GPS data alone could be used for some long 2D lines. For those, heavy manual processing was necessary to correct for anomalous offsets in the data. After those corrections, saw-tooth effects were still visible. They consist of slight random vertical shift of individual GPS measurements that are related to the precision of the GPS measurements (GPS data were here of bad quality due to unknown acquisition problems). A high-order (degree 10) polynomial curve was fitted to the data to get rid of those remaining effects (Fig. 2A). In zones of dense profiles over small dune beds, photographs obtained with a hand-held camera were used for photogrammetric reconstruction with a free online software autodesk (123D catch: http://www.123dapp.com/catch). Scaling was then achieved by fitting markers measured in the field with a tape (Fig. 2B & 2C).

2.3. Processing

2.3.1. Standard processing

All profiles were processed with an in-house software written in Matlab (“RadLab”; Girard, 2002). The high quality of the data allows a very light workflow in four standard steps, which are described in great detail elsewhere (Fisher et al., 1992; Yilmaz, 2001; Annan, 2001; 2002; Jol and Bristow, 2003; Neal, 2004; Annan, 2009; Cassidy et al., 2009).

2.3.1.1. Time zero correction

The first arrival in the data is recorded with a short delay to prevent changes in its position from trace to trace. This causes misalignment of the first arrival, as well as the first reflections beneath. Drifts commonly result from temperature differences between console electronics and ambient air, or due to damaged cables or low battery charge state. Such discrepancies are corrected for each trace by applying a time shift of the signal in order to achieve alignment of the first arriving reflection with time zero.

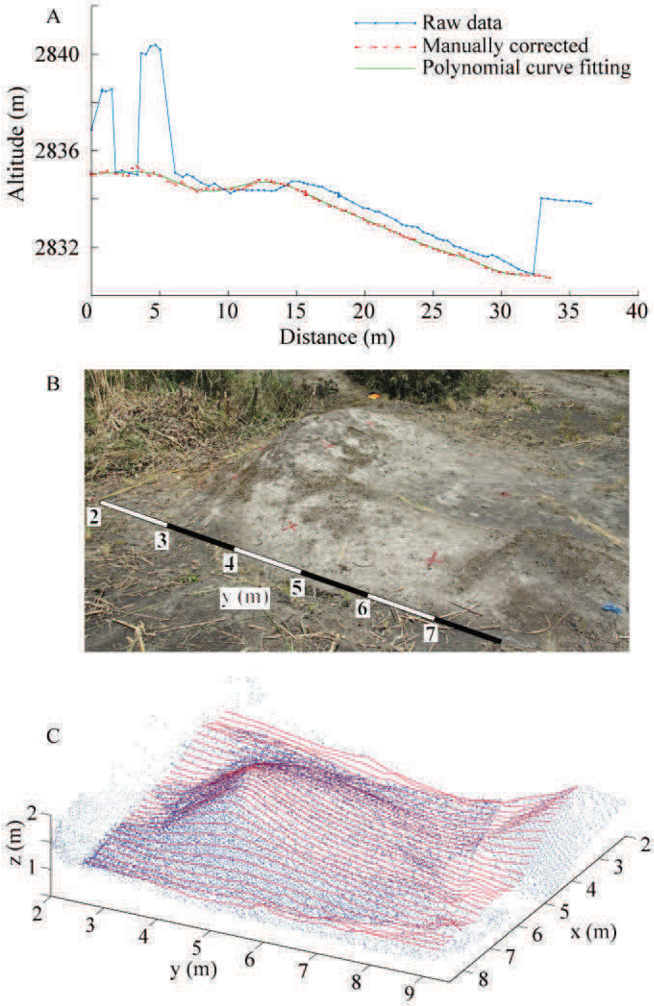

Figure 2 : Topography acquisition. A) GPS topography profiles for a long 250 MHz survey: comparison between raw (blue continuous line with dot), manually corrected (red dashed line with dot) and polynomial curve fitting (green continuous line). B) Photography of a small-scale dune bedform (Lunate A), note sprayed markers (red crosses). C) 3D topography cloud (blue dot) of the same dune bedform from photogrammetric reconstruction. Red lines represent GPR profiles.

2.3.1.2. Dewow filter

Due to the short time interval during acquisition between transmitter shots, receivers become saturated. This induces a slowly decaying low frequency noise (wow) on traces, superimposed on the high frequency signal. The dewow filter removes this low frequency by subtracting the mean value of a short filter window (same length as the GPR pulse wavelet) to each sample.

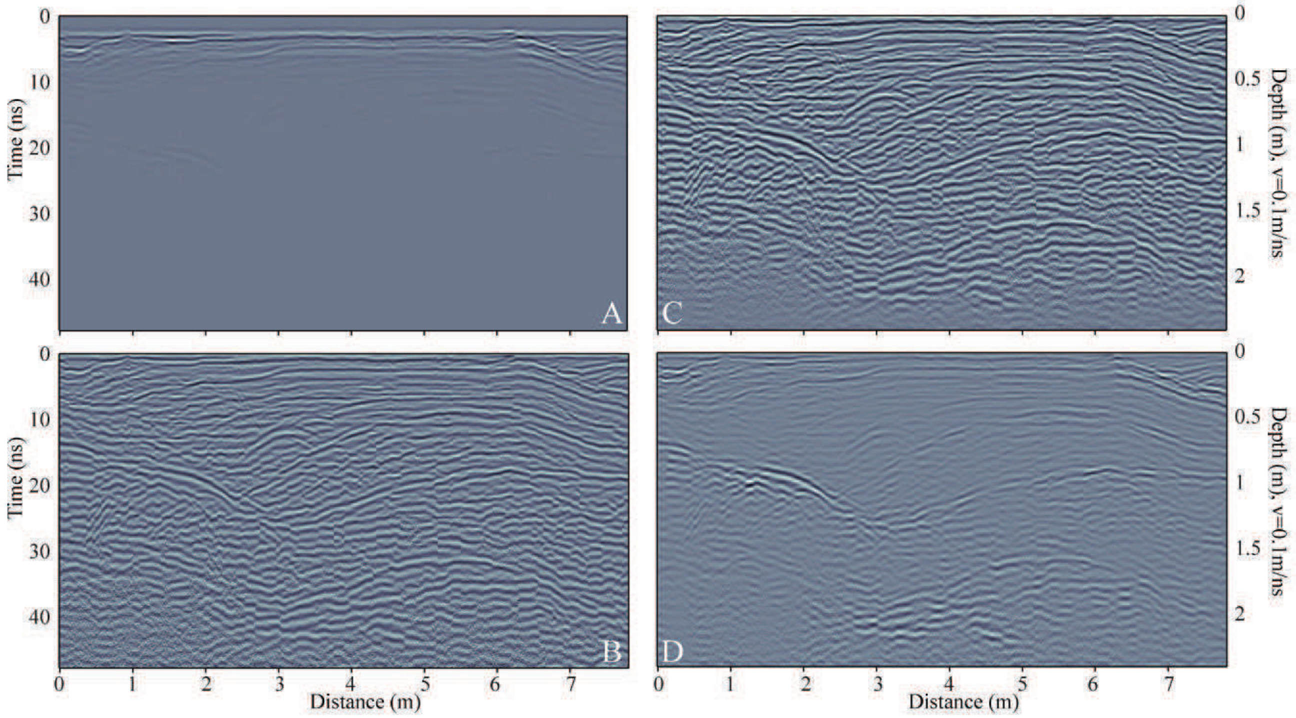

Figure 3 : Comparison of gain functions on a 800 MHz profile (see text). A) Raw profile. B) AGC gain with a 3 ns time window. C) WET gain. D) SEC gain.

2.3.1.3. Time gain

EM waves are highly attenuated during propagation through the deposits, which results in a decay of signal amplitude with depth (Grimm et al., 2006; Fig. 3A). We equalize amplitudes by applying a time varying gain function in order to compensate for the attenuation of the signal. Gain functions work on individual traces separately. Several types exist depending on the imaging purpose and three gain functions were used and combined in this study.

- Automatic Gain Control (AGC) is amongst the most common of amplification methods. It is a mathematical amplification, with no physical background. First, the average amplitude of a trace is calculated. Then, the average is calculated on a given sliding time window. The sample in the middle of this window is scaled by the ratio of average of the trace over the average of the window. With a small sliding window (EM wavelength scale), every reflections will be amplified, without preserving their relative amplitudes whereas with a larger window, relative amplitudes become clearer. A 3 ns sliding window was used for the 800 MHz antennas (Fig. 3B).

- WET gain (Wave Envelope from Hilbert Transform). For each trace, the envelope of the signal is computed using a smoothed version of the Hilbert transform. Data are then multiplied by the inverse of the envelope. It does not maintain the relative amplitudes of the signal and highlight all reflections (Fig. 3C).

- SEC gain (Spherical and Exponential Compensation). A linear time gain and an exponential time gain are combined to account for the spherical spreading losses and the exponential dissipation of the energy, respectively. This filter keeps the relative amplitude (Fig. 3D).

2.3.1.4. Energy equalizer

The total energy of each trace may vary between traces due to, e.g., coupling problems between the antenna and the ground. This translates into attenuation of some traces in the profile (lack of continuity). The energy equalizer correction calculates the energy of each trace (sum of absolute value of every sample) and equalizes it over the whole profile.

2.3.2. Topography correction

In order to avoid distortion of reflections and thereby correctly depicting the subsurface geometries, topography has to be taken into account. EM wave velocity is a prerequisite for the conversion of the time-scale into a depth-scale and for the topography correction. Velocities were measured by diffraction hyperbolae modelling (Fig 4). Here, three different methods for including topography in the data were tested: 1) static shift, 2) topographic migration, and 3) for surveys satisfying the full-3D requirements, 3D migration (Fig. 5).

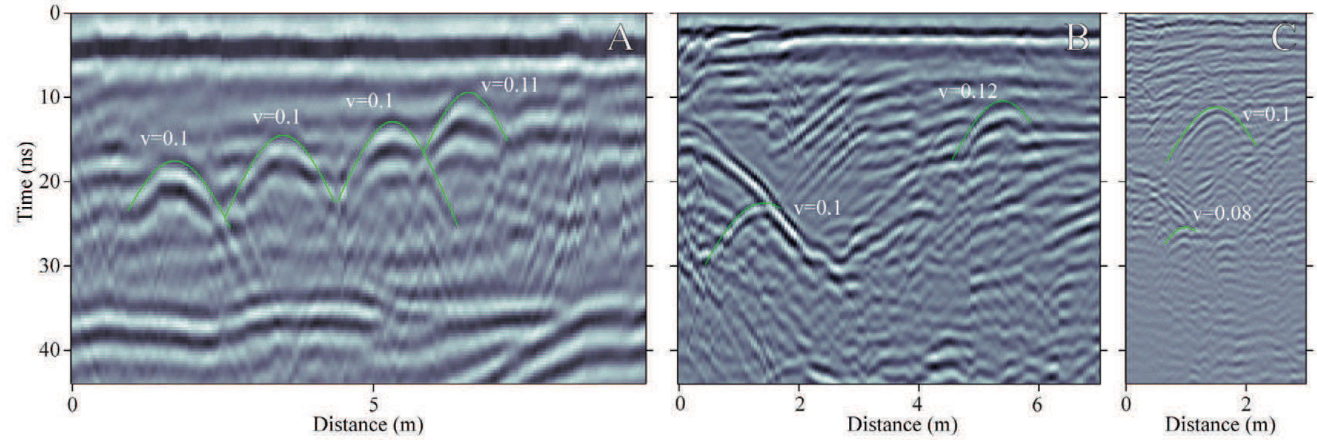

Figure 4 : Example of velocity analysis by hyperbolae fitting over the three frequencies. A) 250; B) 500; and C) 800 MHz.

2.3.2.1. Topographic static shift

With knowledge of the EM velocity, topography is converted into two-way travel time, and each trace is shifted in depth according to its position. This procedure is commonly used in GPR studies, although it may lead to distortion of reflections (e.g. Lehmann and Green, 2000).

2.3.2.2. Topographic migration

Migration is a process that attempts to correctly reconstruct the geometry of reflections at depth (Yilmaz, 2001). Again, EM wave velocity is needed during this step. The topographic migration used here is an algorithm based on the Kirchhoff migration and corrected to account for topography (Lehmann and Green, 2000; Dujardin and Bano, 2013). It relocates the energy of the recorded signal (i.e. reflections) at its correct position, yielding thereby a view of the true geometry (location, dip) of the reflections. This method is particularly useful for retrieving the real dip angle of inclined reflectors as well as for collapsing diffraction hyperbolae to their points of origin (Fig. 6).

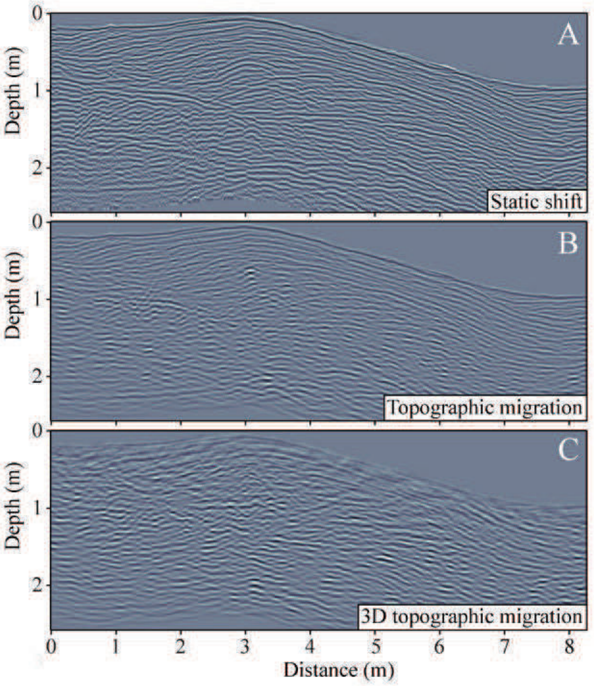

Figure 5 : Topography correction for the 800 MHz profile from figure 3. A) Static shift. B) Topographic migration. C) 3D topographic migration.

2.3.2.3. 3D topographic migration

3D topographic migration is similar to the 2D topographic migration, except for the fact that the information is treated as a 3D cloud of traces rather than a set of 2D profiles. In this manner information from neighbouring profiles is taken into account during the process (Grasmueck et al., 2005; Heincke et al., 2005). Generally, a 3D outcrop is better reconstructed from a 3D dataset, such that 3D topographic migration type should greatly improve the results.

2.3.3. 3D visualization

After corrections, profiles from the 3D surveys were loaded into a seismic interpretation software (Opendtect) which allows for 3D representation (Fig. 7). A post process using the Dip Steering Median Filter method (DSMF) was applied. This filter consists in computing a dip steering volume (volume containing the dips of the reflections through the 3D data) and then re-interpolates the traces relative to the dip-steering volume. It removes inconsistent noise with respect to the data that appears smoother and with more continuous reflections. Here, depth slices and virtual cross-lines were produced by interpolation of the 2D profiles.

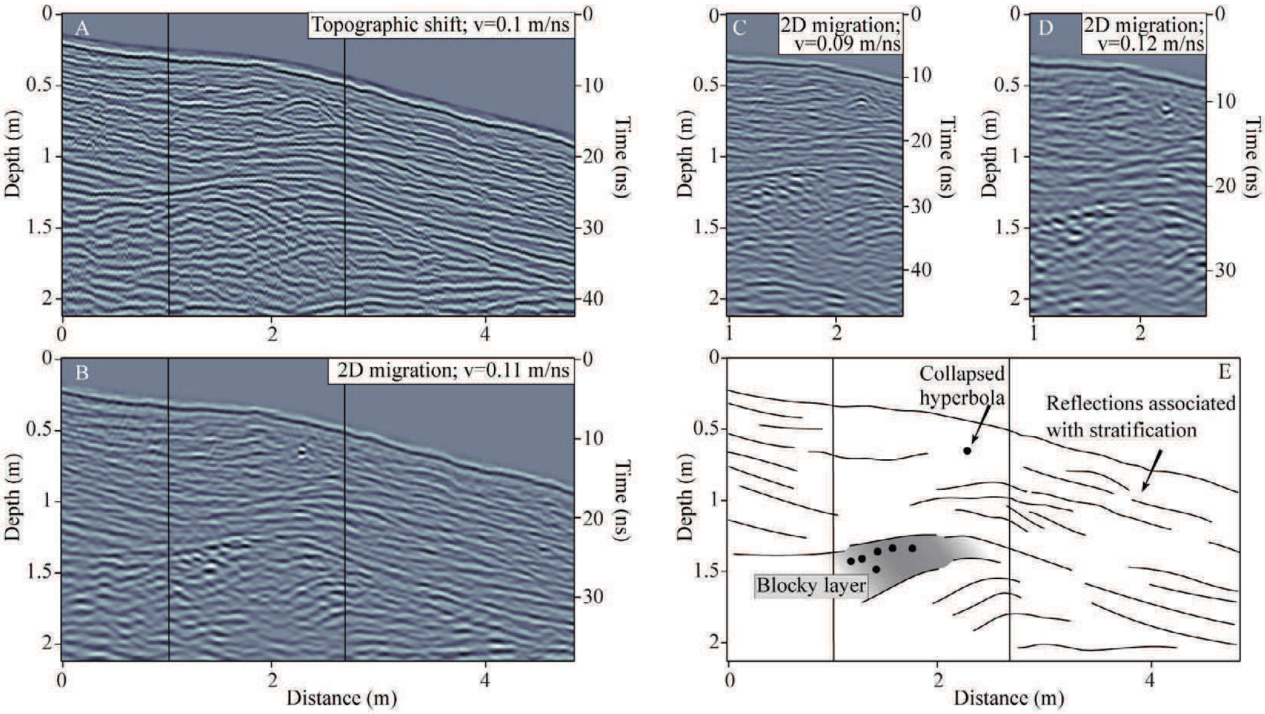

Figure 6 : Collapse of diffraction hyperbolae with topographic migration. A) static shift; note the hyperbola at distance of 2.5 m and 0.5 m depth as well as unresolved reflections between 1.2 and 1.8 m depth. B) Hyperbolae are collapsed to single points and reflections resolved after topographic migration with a correct velocity of 0.11 m/ns. C) Migration with a too slow velocity, the hyperbola has not collapsed. D) Migration with a too fast velocity, the hyperbola resembles a “smiley”. E) Interpretative sketch of profile B.

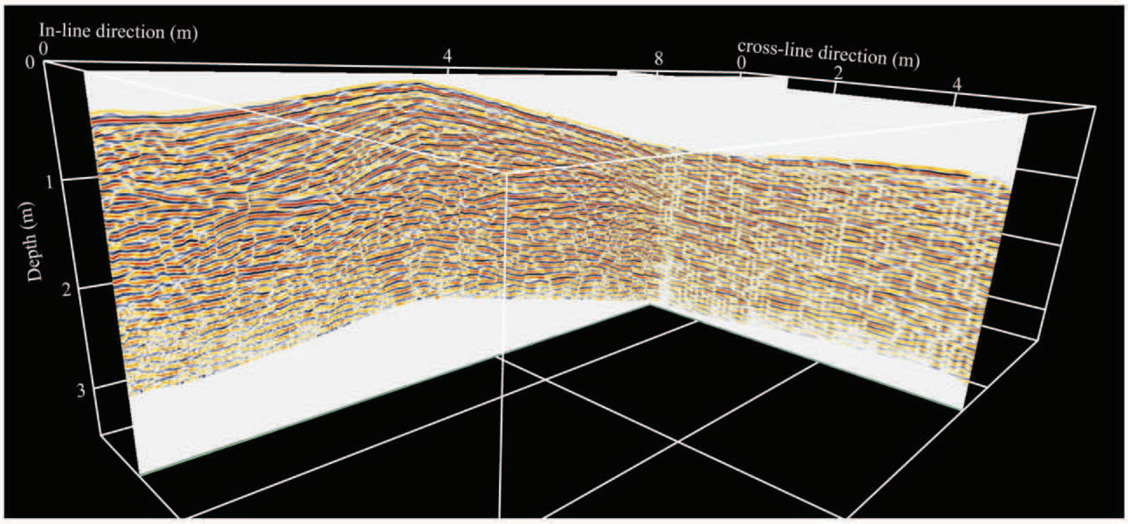

Figure 7 : 3D view of a GPR volume with the 800 MHz antenna in Opendtect.

2.4. Results and Discussion

The dataset appears to be of good quality, and requires little to yield a meaningful analysis of the sedimentary structure of the bedforms, developed part 3 of this chapter. Whereas the application of both time-shift and DC filters are standard and necessary steps linked to the intrinsic functioning of the GPR, gain functions, topography corrections and migrations can take several forms depending on the imaging purpose and different types were tested.

2.4.1. Wave velocity

EM wave velocity is a crucial parameter for migration and depth analysis. The literature generally agrees on a value around 0.09-0.12 m/ns for pyroclastic sediments (see Table 1). In this study, the velocity analysis was performed by fitting diffraction hyperbolae contained in the profiles with ones modelled for a given velocity (Jol, 2009, p. 159). Modelled velocities ranged from 0.09 to 0.12 m/ns for the different frequencies and profiles and a 0.1 m/ns was used as it was the most highly represented velocity throughout the profiles (Fig. 4). Daily rain and associated soil moisture changes appear not to have affected velocity, consistent with observations from a GPR study in a nearby area (Cotopaxi, ca. 100 km distant; Ettinger et al., 2014).

2.4.2. Gain

The WET gain is a robust algorithm that homogenizes the amplitude of the signal along traces. It is best used to visualize the type of radar facies in between major bounding limits. The AGC gain is a bit more subtle in its effects because it reacts differently depending on the width of the sliding window. It requires individual fitting depending on the frequency used and the objective of the exercise. Whereas the WET and AGC gains do not rely on a physical a priori basis and are related to the signal form only, the SEC gain follows the theoretical amplitude decay of EM waves, without accounting for the specificities of each trace. Relative amplitudes are respected, which enables the perception of major reflections possibly linked with architectural boundaries, without getting bog down by minor reflections that provide information on internal structure. Moreover, a signal that does not respect a theoretical decay will not be accurately amplified. The analyses of the results were performed on images treated with the WET gain, but were interpreted in conjunction with the SEC gain as well.

2.4.3. Penetration depth

Gain is effective as long as the reflected signal overpass the ambient noise signal. In this study, penetration depths for the 250 MHz antenna reach at least 175 ns in two-way travel time (translating into 8-9 m depth). For the 500 MHz antennas, the signal remains coherent down the base of traces, and only the acquisition time (90 ns; 4.5 m) limited the penetration depth. The 800 MHz signal is coherent for around 40 ns (2 m).

2.4.4. Topographic migration

Topographic migration concentrates the energy of reflections at the place and depth of the actual reflectors. It enables the reproduction of the real, natural geometry (dip angle) of stratae that can otherwise be distorted by 10 to 15 % with a standard topographic shift (Lehmann and Green, 2000). Perhaps more interestingly for pyroclastic or debris flow deposits, is the fact that concentrating the energy of reflections also permits the collapsing of diffraction hyperbolae to their apex, which is particularly useful in the case of coarse grained, blocky sediments. Using different EM velocities, diffraction hyperbolae will either become steeper or produce "smileys" for velocities that are too high, and collapse as a point for the right velocity, making their discrimination easy (Fig. 6a-d). However, migration always introduces smearing into the results, so that it may be undesirable for simple interpretation of structures. Moreover, migration needs an accurate velocity model with depth (< 10 % error, Lehmann and Green, 2000) that can only be achieved with systematic CMP profiles.

Migrated profiles from Tungurahua exhibit little difference in dip angles (10 % only corrects a 20º dip into 22º), a lower image sharpness, and correctly collapsed hyperbolae when compared with simple topography shift profiles. Thus the migrated sections have been used as a complement to the simple topographic shift for interpretation, helping to discriminate between hyperbolae generated from massive, coarse grained layers and stacked bedsets of aggrading ash (Fig. 6e).

2.4.5. 3D migration

In comparison with the 2D migration, the 3D migration should improve the images, especially with complex sub-surface geometries, because side reflections will be taken into account. In this study however, 3D migrated images are blunter than the simple topographic migration results (Fig. 5). The exact reasons are not understood, but several parameters remained un-optimized during acquisition. A full 3D acquisition schema requires an interval of a quarter wavelength of the input signal spacing between traces (Grasmueck et al., 2005) in both in-line and cross-line directions of the surface of the 3D cube. This would require one profile every 5 cm (resp. 3 cm) for a mean velocity of 0.1 m/ns and a 500 MHz (resp. 800 MHz) antenna. With a minimum 10 cm step with the 500 and 800 MHz antenna, cross-line aliasing is thus likely to occur. Another factor that may detract from the data quality is, as in the case of 2D migration, an overly simplistic velocity model. Further, a good spatial accuracy is required for the 3D migration (10% of dominant wavelength; Lehmann and Green, 2000; Grasmueck et al., 2002). At the investigation scale, unconstrained paths of antennas during acquisition cannot be avoided and the uncertainties in these frequently overrun the needed accuracy (lateral movements of the antenna, survey lines not perfectly straight, or the measuring wheel not precise enough). The loss of the GPS data during acquisition handicaps the present study. Only few other studies have presented 3D migrated results from GPR surveys, most of them at lower frequencies (Grasmueck et al., 2005; Heincke et al., 2005; McClymont et al., 2008a, 2008b; McClymont et al., 2010). The 3D migration presented here is, to the best of authors' knowledge, a first attempt at such high frequency. It emphasizes a limitation of this processing step, since at such high frequency, the field acquisition with the available equipment cannot reach the necessary precision. Based on the experience from this study, the use of a self-tracking laser theodolite with automatic target recognition capabilities or comparably accurate path tracking method would appear necessary (Lehman and Green, 1999).

2.5. Conclusions

Studies using GPR on volcanic deposits have become routine and demonstrate clearly the utility of the method for pyroclastic deposits. The degree of alteration and the chemistry of the deposits appear to have little influence on the EM wave reflection quality. The large range of antenna frequencies available can cope well with the large grain size range of pyroclastic and debris flow deposits, in order to image most architectural elements. Future studies on coarse grained pyroclastic and debris flow deposits should benefit from having increased imaging quality using migration in the processing step. Many studies seek 3D architectural information for deposits and hence the need for 3D data. GPR is well suited for such purposes and acquisition and processing schemes should further focus on 3D imaging.

On the deposits of the August 2006 dilute pyroclastic density currents at Tungurahua volcano, the good reflective quality yielded the imaging of detailed structures with minimal processing. With the help of migrated data in order to discriminate hyperbolae produced by blocks, the data set can be interpreted with nothing more than a simple topographic shift and a gain function (part 3, this chapter).

The current dataset enabled testing of the application of elaborate processing with the 3D migration. However, the precision required for such a detailed study using a very short wavelength is not achievable yet on topographically uneven relief such as that exhibited in the present setting. 3D acquisition and migration schemes are however promising and future work should be aimed at working with either lower frequencies antennas (larger wavelengths) or very precise tracking devices.

3. The 3D structure of pyroclastic dune bedforms from the August 2006 deposits of Tungurahua volcano, (Ecuador): Part 2, ground penetrating radar results

3.1. Introduction

The ongoing eruption of Tungurahua volcano (Ecuador; Hall et al., 1999) produced pyroclastic density currents (PDCs) in July and August 2006 (Hall et al., 2013). The August deposits, more voluminous and widespread can be classified into valley confined, dense pyroclastic flow deposits, and overbank, cross-stratified, dilute PDC deposits (Douillet et al., 2013a). The cross-stratified deposits outcrop with pristine dune bedform (DB) morphologies at their surface (Douillet et al., 2013b). In order to decipher the formation of these DBs, a ground penetrating radar (GPR) campaign was yielded on the deposits to access their 3D structure (see previous part (chapter 3, part 2)). Here, the interpretation of the data relevant to the DB problem is presented.

3.1.1. Pyroclastic dune bedforms

Firstly recognized in the late 1950s (Richards, 1959), DB cross-stratification formed by dilute PDCs have long been seen as antidunes (Fisher and Waters, 1969, 1970; Schmincke et al., 1973, Brand and Clarke, 2012). Indeed, they can exhibit low angle laminations with a constructional nature, and notably, because the stoss-face can exhibit more deposition than the lee, leading to an overall upstream migration of the crests (regressive bedforms). Such patterns are rarely observed in the sedimentary record and many researchers have suggested that the only way to produce a stoss-aggrading DB was through a stationary gravity wave at the interface of an upper free boundary.

Later, Branney and Kokelaar (2002) emphasized the fundamental influence of the basal boundary zone on sedimentation patterns. Alternative models to the antidune interpretation were suggested that depend on basal processes rather than a whole flow dynamics. Sulpizio and Dellino (2008) and Doronzo (2012) and Andrews and Manga (2012) suggested an “en masse” deposition model for individual laminae forming bedforms. Alternatively, differential draping of landing particles, with the stoss face more exposed than the lee in a net aggrading environment, could produce the intriguing patterns (Douillet et al., 2013b, see also Ponce and Carmona (2011) for turbidites). Wind tunnel measurements showed that, in order to onset saltation, an upstream dipping bed (stoss side) should be exposed to 50% more shearing than a downstream dipping one (lee side; Douillet et al., 2014). This is a simple result of the effects of the slope and could lead to stoss-aggrading DBs with control from the basal boundary. The processes controlling stoss aggradation are thus not well understood, and accurate data are a prerequisite for further advances.

3.1.2. Dune bedforms from the 2006 eruption of Tungurahua

On the 2006 deposits of Tungurahua, DBs deposited from dilute PDCs outcrop directly on the pristine surface and permit the observation of their outer shape and 3D constructional patterns. In proximal zones, dilute PDC deposits outcrop unconfined on a wide area of the upper, steep flanks. In distal zones, where steeply incised valleys confined dense pyroclastic flows, dilute PDC deposits outcrop as isolated ash bodies (100s m extent; up to 10 m thickness) downstream cliffs and on the outer overbank of valley curves. All dilute PDC deposits are shaped by DBs whose size decreases in the down flow direction for each deposition zone individually (from 40 to < 1 m in length; 2 to 0.1 m in thickness, Douillet et al. 2013a). The shape and internal stratification patterns of DBs were found to depend on their location on the flanks as well as within an ash body, and four groups were defined (Fig. 1; Douillet et al. 2013b).

- Elongate DBs are flat and elongate in shape (Fig. 8a). The cross bedding consists of massive layers (several cm thick) with a lensoidal form that stack on the stoss of each other, intercalated with stoss-aggrading bedsets of ash lamination. They outcrop in the proximal zone of unconfined dilute PDCs.

- Transverse DBs have straight crests perpendicular to the flow direction. They are generally steep sided with cross-lamination consisting of stoss-aggrading bedsets of ash sometimes truncated on stoss sides (Fig. 8b). They outcrop all over the ash bodies.

- Lunate DBs have a crescent shape with horns pointing downflow and essentially the same internal structure as transverse (Fig. 8c). They are absent from the upper parts of ash bodies, but outcrop on the middle and lower part together with transverse DBs, and notably, where the influence of two different flow directions is visible.

- 2D DBs have straight crests, but a lateral width way greater than the downflow length and are organized in trains (Fig. 8d).

3.1.3. Nomenclature

The analysis of the GPR profiles is based on the recognition of bounded reflective packages and their classification into reflective architectural elements, following seismic stratigraphy techniques (Catuneanu et al., 2009). By package, we mean any group of reflections that visually shares some homogeneity and can be bounded. Recognition of packages is largely made by recognition of their boundaries (terminations of the reflections), but can also include information on a specific reflector (a marked depositional package), asimilarity in form or stacking pattern (e.g. Neal, 2004; Cassidy et al., 2009; Ettinger et al., 2014).

Terminations are classified into (Mitchum et al., 1977): baselap (downlap and onlap) at the lower boundary; toplap, offlaps and truncations at the upper boundary. A truncation of stratae represents a hiatus and is found on the upper/side boundaries of a package but can be difficult to recognize from offlap and toplaps on a GPR image.

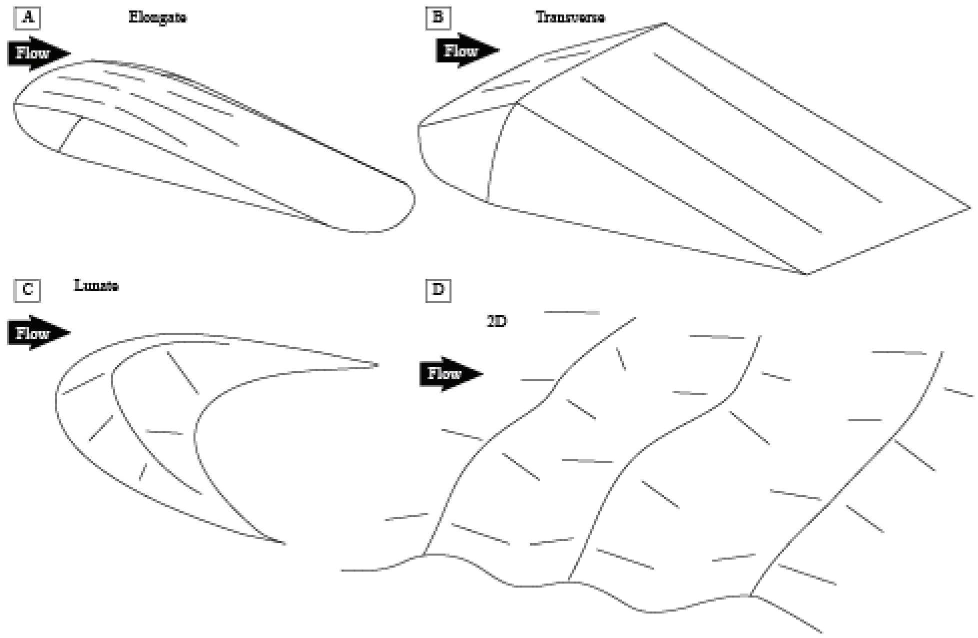

Figure 8 : Sketch of the 4 types of dune bedform morphologies evidenced in Douillet et al. 2013b. A) Elongate, B) Transverse, C) Lunate, D) 2-dimensional.

The GPR survey results are presented for the four types of DB, and for a large bedform that marks the upstream end of a deposition zone.

Architectural shape patterns can be sigmoidal (lensoidal), oblique, or planar, with stoss dip or lee dip, or chaotic.

Stratal stacking patterns define how the architectural patterns are stacked on each other: aggrading (continuous aggradation on both sides of a bedform), which can further be clarified into prograding (more aggradation on lee than stoss) or retrograding (more aggradation on stoss than lee) aggradation; or simply constructional (net deposition – needed for having a deposit!). Furthermore, the inter-reflection relations can be parallel, subparallel, divergent, tangential, or chaotic.

3.2. Data

Individual profiles show numerous, laterally consistent, very high-quality reflections that permit to draw complex sedimentary architectures. The extreme sensitivity of PDC deposits to the GPR method (Cagnoli and Ulrych, 2001c; Kruse et al., 2010; Courtland et al., 2013; Ettinger et al., 2014; previous part (chapter 3, part 2)) is probably linked with the typical consequent grain-size variation between individual laminae that affect the EM impedance.

3.2.1. Quarter pipe onset

The quarter pipe shape that marks the upstream end of the Chontal ash body has been given particular attention with the 250 MHz antenna (Fig. 9 and 10). This intriguing structure contains an evolution from 0 to more than 5.5 m in thickness of cross stratified ash and was previously interpreted as recording a hydraulic jump (see figure 8 in Douillet et al., 2013a).

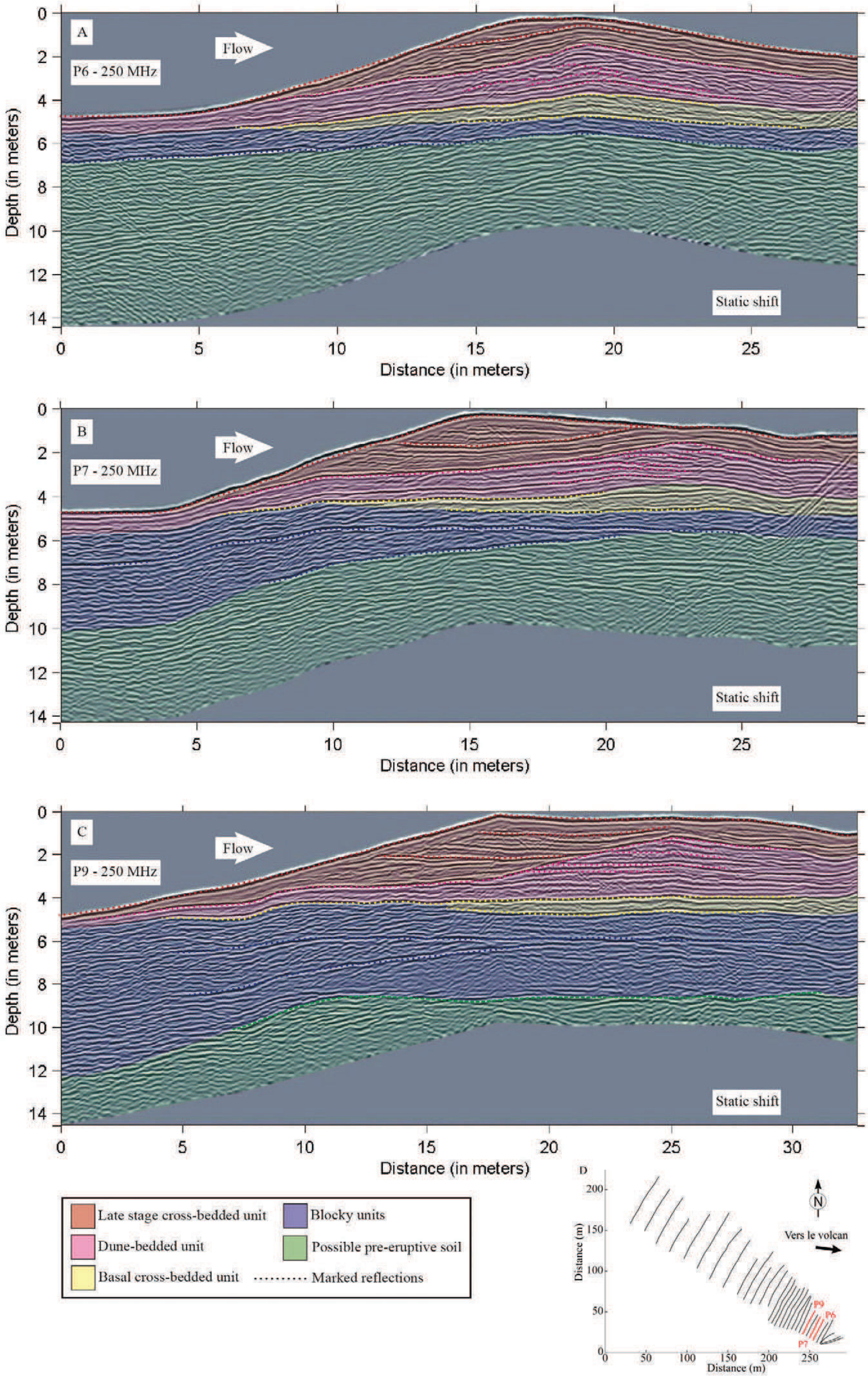

Figure 9 : Three consecutive profiles with the 250 MHz antenna over the quarter pipe shape in Chontal ash body with static shift correction. Main reflectors and units are highlighted. P6 and P7 are 5 m away and P7 and P9 are 10 m away. D) Location of the profiles within the survey.

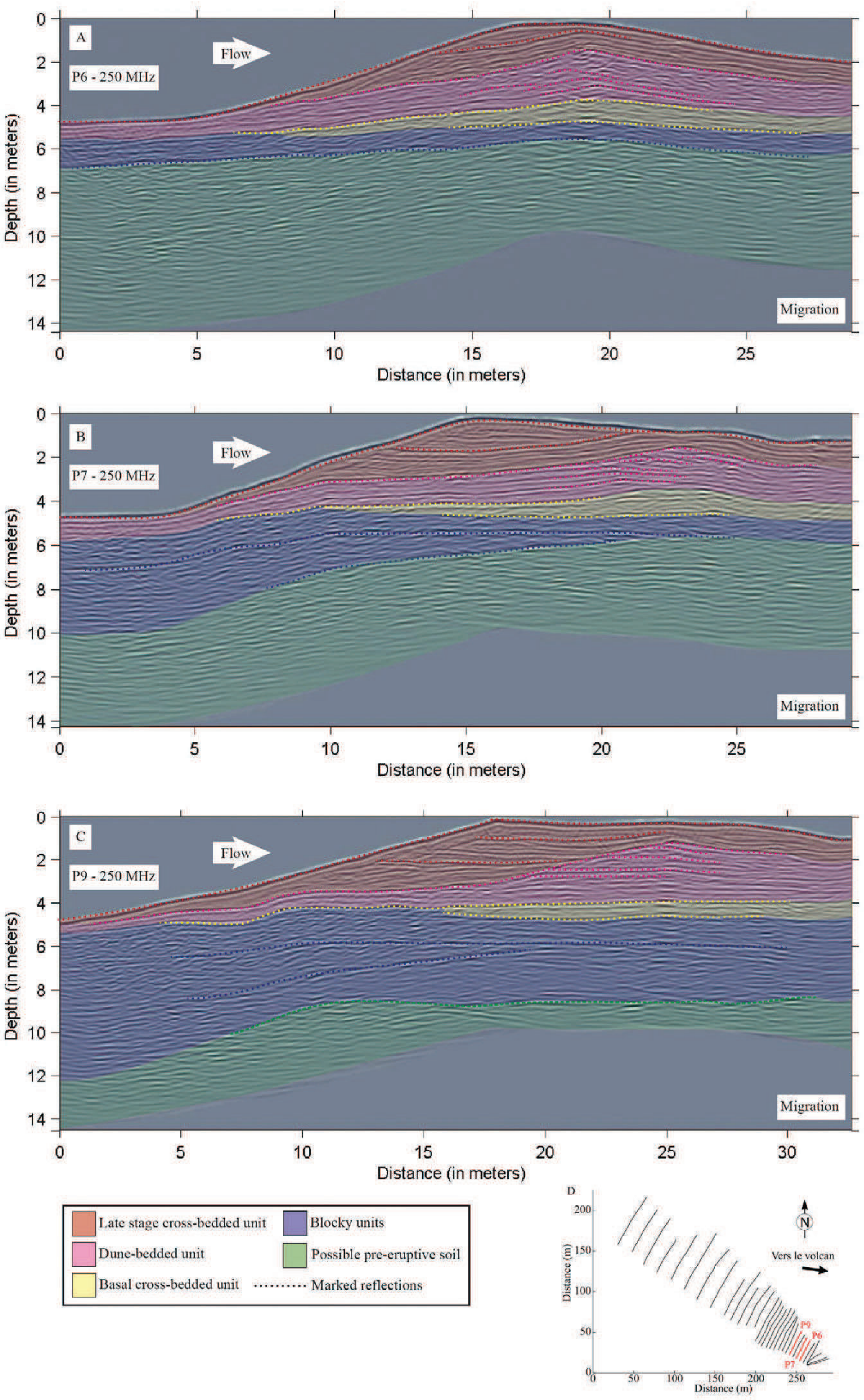

Figure 10 : Similar as figure 9, but processing is done with topographic migration.

3.2.1.1. Units and pre-eruptive surface

Several strong reflections are recognized, that mark changes in the dynamics of the parental flows. The upper part of the bedform is cut in three units that are 1) all cross bedded, 2) show a thickness increase in the downstream direction (wedge shape), 3) are all found in a level above the base of the morphological feature.

The uppermost unit (red) seems to be clearly cross-*laminated* (close stacks of continuous reflections are observed, even on the 500 and 800 MHz profiles), and most of the beds are truncated by the quarter pipe geomorphologic limit.

The second unit (pink) contains cross-reflections and forms a DB. Whereas the red unit shows cross-*laminations*, the pink one can only be interpreted as cross-*bedded*. Indeed, migration results show that many diffraction hyperbolas are present in this unit, representing blocky layers rather than cm-scale laminations.

The third unit (yellow) is not well understood, and too thin for cross-bedding to be well imaged. It may belong to either the pink or blue units, but has a wedge shape. If only dilute PDCs reached the area, the base of the yellow unit could correspond to the pre-eruptive surface. This surface could include burned vegetation (see Fig. 8e in Douillet al., 2013a), some stratified runoff deposits and a base made of blocky deposits. In that case, the upper units may correspond to the different flows evoked in Hall et al. (2013), but nothing permits to confirm this interpretation. The three upper units have a wedge shape, that is sometimes aggrading and sometimes erosive. This supports previous interpretation that they might be the sedimentary record of hydraulic jumps of the dilute PDCs that triggered deposition after overflow.

The lower (blue) unit is made of two or three sub-units. Those sub-units appear messier than the upper ones, with little continuous reflections and a blocky contain is inferred, that is supported by collapsed hyperbolas in the migrated profiles. Whereas the upper one is rather continuous all over the profiles, the second one (only picked on P7-P9) ends up by downstream thinning. This characteristic raises the possibility that the layer corresponds to a final lobe from a dense pyroclastic flow. The basal unit is only found on P9.

On profile P9, a discontinuous line can be drawn between hyperbolas considered from blocks (green). The tendency is also visible in the lower part of P7, but remains unclear. These diffuse, blocky reflections could correspond as well to the pre-eruptive surface (as in Gertisser et al., 2012) containing large blocks or broken trees, but this remains speculative.

3.2.1.2. Lateral variations

Extremely interesting in this outcrop are the small-scale lateral variations found between successive profiles. The paleo-DB in the pink unit exhibits stoss-aggrading patterns in P6. In P7 (5 m further laterally), it contrasts with aggradation but a progressive structure (downstream crest migration) seen on the second profile (P7), whereas P9 (10 m further laterally from P7) even shows a truncated stoss side and lower contain in blocks. This clearly demonstrates the variability in the depositional dynamics of dilute PDCs. Other authors have already described variations in aggradation direction for separate bedforms close to each other, but not for a single bedform (Cole, 1991; Druitt, 1992). Following a “traditional” approach, one would interpret an outcrop through P6 as a supercritical bedform linked with an antidune, an outcrop through P7 as a highly depositional environment, and one through P9 as a subcritical dune. It seems unlikely that a single bedform can be created as an antidune on one of its side, but as a subcritical dune on the other side. We thus interpret this as a reason to disregard stoss-aggradation as a necessary and sufficient argument to interpret antidunes and supercritical bedform, as is usually the case in dilute PDC literature (Schmincke et al., 1973; Brand and Clarke, 2012).

3.2.2. Elongate

In the proximal cross-stratified zone, a DB with typical elongate morphology was chosen for 500 and 800 MHz pseudo 3D profiles. The outer shape shows a smooth crest between gently diping faces on a steep background slope and a surface topographic anomaly with a thickness of c.a. 40 cm (Fig. 11a). The analysis is based on 35 profiles from the 500 MHz antenna with simple topographic shift and WET gain, displayed in Opendtect together with virtual cross lines resulting from interpolation in Opendtect (Fig. 11b-e; see previous part (chapter 3, part 2), for processing steps). Elements cited here have prefix “P” for package, and “L” for layer (see table 4, figure 11).

package	location	top / conformity	top marker color	base: terminations	gpr facies	interpretation
P6	top stoss side	top profile / conform	yellow (base)	L8: onlap	sub-horizontal	runoff stoss fill
P5	crest area	L7: stoss / conform - lee / truncations	dark blue	L6	parallel stoss-aggrading	final differential draping unit eroded on lee
P4	lee side	L6: stoss / conform - lee / diffuse	purple pink	L5	lee beds or backset lensoids	lee-side growth phase
P3	stoss and lee	L5: stoss / conform - lee / toplap	dark red	L4: downlap (also on cross lines)	stoss: aggrading beds / lee: backset lensoids, separated by hyatus.	2 DBs forming in train
L4	stoss and lee	L4: conform downlaps / drapping	green	L4: toplaps -conform	marked reflections on relatively flat bed	pause in flow / base of surface morphology
P2b	stoss side	L3b: conform	dark blue	L2: onlap	sub-horizontal	stoss infill by bedload material
P2	upper lee	L3: stoss / truncation - lee / diffuse	pink	L2: downlaps onlaps	draping / chaotic reflections	growth phase of a proto DB
P1	whole DB	L2: unresolved toplap or truncations	sky blue	L1: tangeantial downlaps	chaotic on stoss, backsets lensoids on upper lee, chaotic and lee beds on lower lee	taken as the lowermost phase, a series of small DBs
P0	-	L1	olive green	-	several coherent phases visible but not followable between profiles	-

Table 4 : Summary of the principal reflections and packages characteristic forming the elongate dune bedform.

3.2.2.1. Similarities with previous description

The DB investigated here by GPR has the typical characteristics previously described. It contains large packages of stoss-aggrading, lensoidal layers (P1, P3 lee part, see table 4 and figure 11b-d), as well as intercalated steeply sided aggrading bedsets (P3 stoss part; P5). However, several patterns were not recognized before.

3.2.2.2. Elongate morphology and runoff deposits

In the DB investigated here, the surface morphology is typical of an elongate type. However, it appears that a large amount of material in the upper part of the stoss side corresponds to a secondary filling of the trough by runoff water transport (P6, Fig. 11b). Whereas this phenomenon was previously considered as minor, it cannot be excluded that the elongate morphologies found in the proximal zones of the cross-stratified deposit are not a bias resulting from larger rework by runoff in this zone. The internal patterns however are representative of the former description.

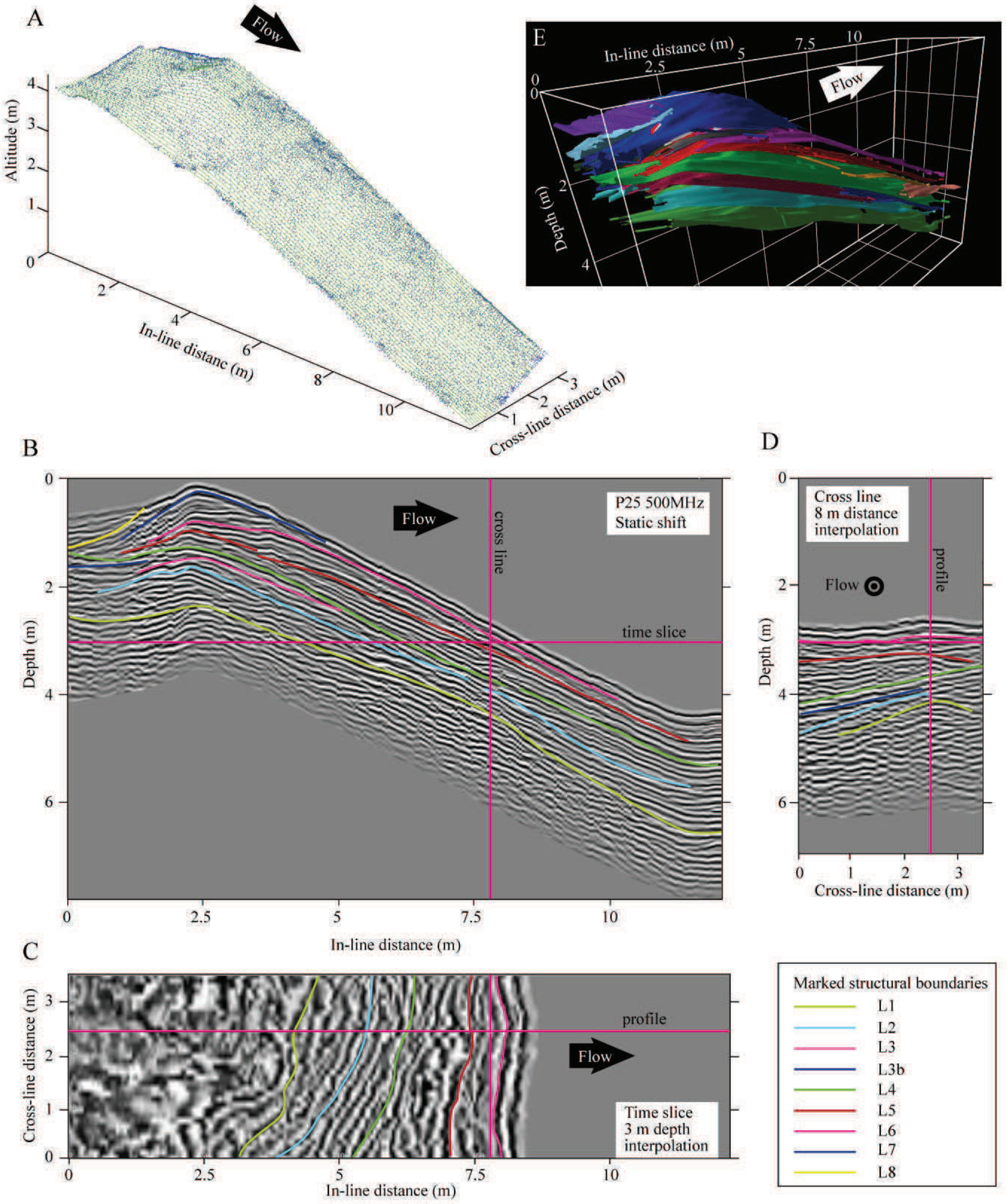

Figure 11 : Elongate survey. A) Topography data extracted from photogrammetry. B) Representative profile, with C) virtual time-slice and D) virtual cross-line. Main boundaries are highlighted, see legend. E) 3D view of the main boundaries picked.

3.2.2.3. Proto-orientation

The bedform is not as well oriented with the surface crest than expected. Indeed, from the virtual time slices interpolated from Opendtect (Fig. 11c), a set of reflections with an angle to the profiles line (taken perpendicular to the crest) is visible (L1, L2, L4). The virtual cross-lines (Fig. 11d) points to the same conclusion, with a prominent proto-DB on the left part (L1-L4), that is later recovered by a package with lensoids in both in-lines and cross-lines to the right (P4, below L5). The 3D structure reconstructed from boundaries picking clearly points toward the same conclusion (Fig. 11e). It seems that the bedform initially developed from the left part, together with the tale of another proto-DB that would lie upstream right of the investigated one (visible on L1 between profiles 1 and 15). Those get covered, but a disequilibrium remains on most boundaries until the final shape is given during formation of P4. Thus, the crest orientations measured in Douillet et al. 2013a and thought to point the flow direction are possibly only representative of the latest stages of the eruption.

3.2.2.4. Pre eruptive surface

L4 is the only (almost) continuous reflection on the whole survey identified and lies at the top of a trough filling layer possibly related to runoff transport (L3b). Both arguments could suggest that L4 marks the pre-eruptive surface. However, the reflector is not particular, and no other insight helps this interpretation.

3.2.2.5. Intricate patterns and boundary control

No planar layer could be identified. Rather, the surface morphology seems to be the result of stacking of several episodes of construction with different tendencies (e.g., P1, P4, P5), but that make only slightly evolve the overall position and shape of the composite structure. The deepest picked reflector (L1) forms a morphology at the place of the actual DB (between profiles 23 and 35). This demonstrates that a DB is stable in position through its whole development. It thus makes little sense to use terms such as “downstream/upstream migrating DB” as it is often encountered in the literature. Rather, one should only refer to the strata stacking patterns that can be lee or stoss-aggrading (alternatively progressive / regressive). Such stability is interpreted as indication that bedform development is controlled by basal boundary irregularities rather than an upper, free flow-boundary or flow dynamics, in agreement with recent studies (Branney and Kokelaar, 2002; Douillet et al., 2013b; Douillet et al., 2014). A dune bedform thus cannot be simply regarded as an isolated system. An input from the upstream and downstream neighbors is present (see lower lee reflections below L2 and L4), and aggradation is not simply triggered on a flat surface but is the result of several episodes with different signature. This is somehow striking in comparison with data from other eruptions (Laacher See, Schmincke et al., 1973; Ubehebe, Crowe and Fisher, 1973), where DB cross-stratification seems to lie directly on a flat bed, but is also observed in other deposits (Purrumbete lake, Jordan et al., 2013).

3.2.3. Transverse

The transverse type of DB was investigated in the lower Achupashal main depositional zone (ash body “III” in Douillet et al. 2013a). This bedform exhibits an extremely steep morphology (35º stoss face and 30º lee face). The still ongoing interpretation is based on 32 profiles with the 800 MHz antenna with static shift topography correction, and readily provides information on this DB (Fig. 12).

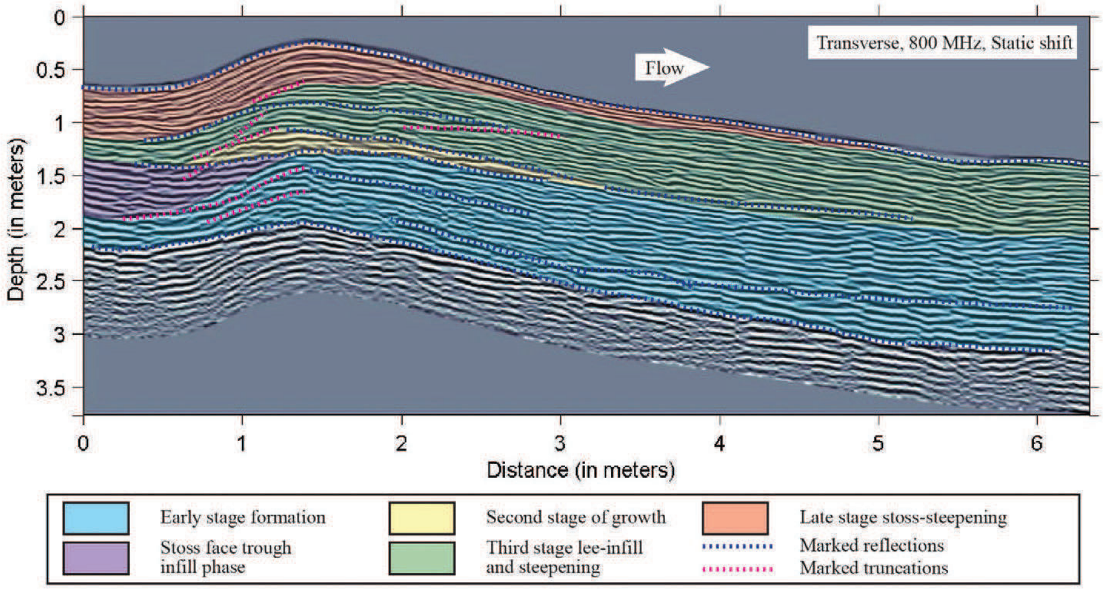

Figure 12 : Representative profile with the 800 MHz antenna over a transverse dune bedform from Achupashal ash body III. Main reflections and interpreted units are highlighted, see legend. The base unit, not highlighted, is interpreted as the possible pre-eruptive soil.

Diffraction hyperbolas are absent, even at high frequency, and thus the structure is thought to comprise only fine-grained material (ash / small lapilli). Several episodes of construction are present and the patterns seem to follow the scheme of Douillet et al. (2013b): construction phases with stoss-aggradation, and episodic truncations on the stoss side only (pink lines in Fig. 12). Additionally, five stages of evolution of the DB can be recognized. A first stage of growth produces the initial bedform from an almost flat substrate (blue). This proto-bedform is then flattened by filling of the trough on the stoss side, and the end of the second phase is again characterized by an almost flat substrate (purple). The third stage is again a phase of growth of a small bedform (yellow) from the almost flat surface, directly followed by a second one (green) and third one (red). The three growth phases are only different in that the yellow phase growth without basal influence, whereas the green phase built on the lee side of the whole bedform, and the red phase steepens the structure by preferential stoss-aggradation. Even more than for the other DBs, this structure shows an extreme stability regarding the position of the crest, highlighting the stability the base surface control on the development.

3.2.4. Lunate

Lunate types of DBs were investigated in a relatively small DB in the Chontal area (figure 8 in Douillet et al., 2013a). Profiles were acquired both with the 500 and 800 MHz antennas and are of high quality, with numerous intricate patterns forming a composite DB (Fig. 13). The interpretation is still ongoing.

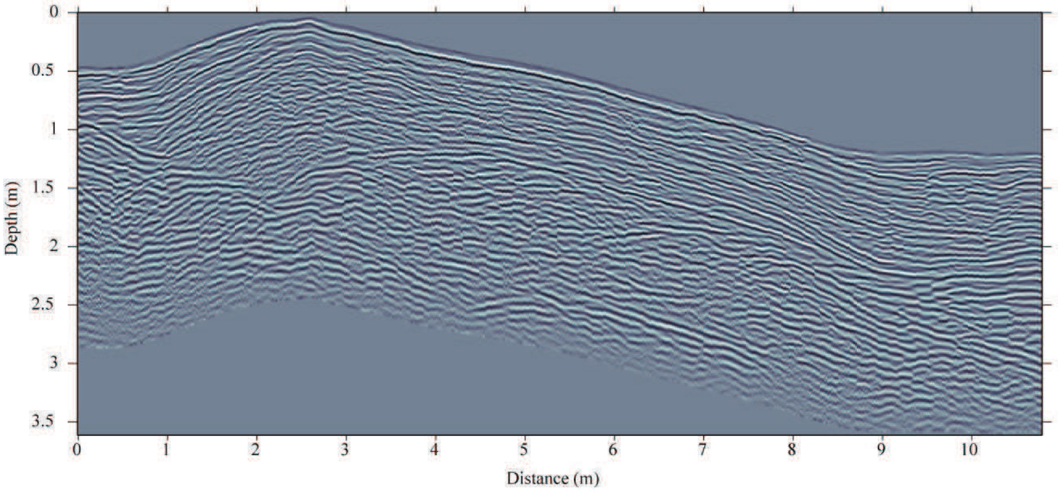

Figure 13 : Representative profile with the 800 MHz over a lunate dune bedform. Interpretation is ongoing, but intricate small scale structures are visible, forming the whole composite dune bedform.

3.2.5. 2D

Due to problems with GPR data, no location of the profiles were possible, neither any topography correction. Profiles were made on two broad, in train, DBs in the Chacauco area as continuous profiles (Fig. 14). The 500 MHz raw profiles do record some continuous reflectors that most probably represent the structure of the two in train DBs but are very noisy. An important part of the noise is due to diffraction hyperbolas that were mostly absent in other DBs investigated, suggesting that the 2D DBs are made of a consequent amount of blocks and coarse material. This coarse material must have been drag down by turbulence from an upstream cliff and cross a river in suspension before deposition.

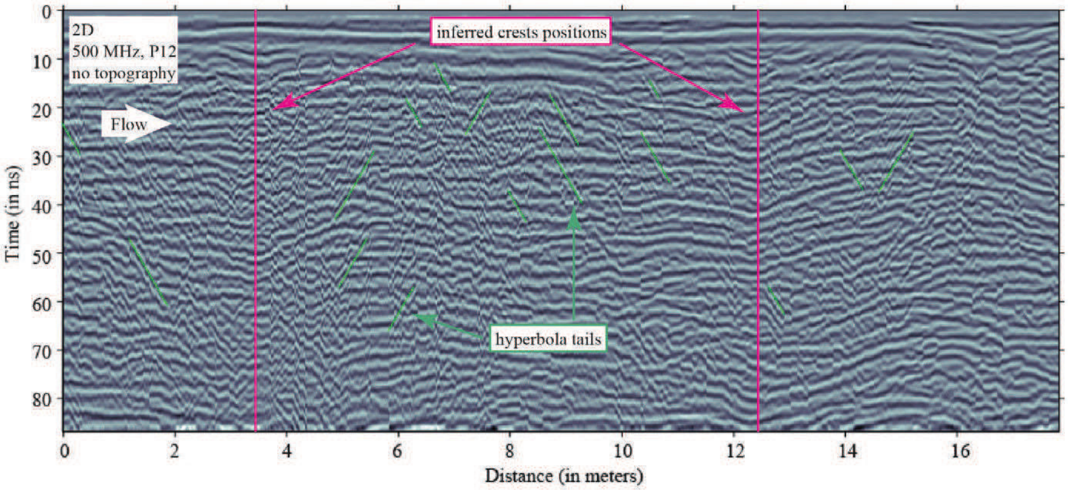

Figure 14 : Profile over a 2D dune bedforms in train. No topography correction. Several coherent reflections are visible and permit to retrieve the position of the crests of dune bedforms (pink). Numerous tails of diffraction hyperbolas are present (green).

3.3. Preliminary conclusions

Dune bedforms formed by dilute pyroclastic density currents from the 2006 eruption of Tungurahua have been imaged with GPR. The 3D variations could be investigated, and show great lateral variability. The root of bedforms cannot be clearly identified and dune bedforms seem to be a stack of several phases of growth and flattening. A dune bedform remains stable in location throughout its history, which suggest that basal boundary instabilities are the main control for their genesis.

CONCLUSION

Le travail de recherche présenté dans ce mémoire s'est concentré sur trois points. Le premier est une part de l'imagerie géoradar qui s'emploie à replacer les réflexions à leur « vraie » position afin de retrouver la géométrie « réelle » du sous-sol : la migration. Nous nous sommes notamment intéressés aux techniques d'intégration de la topographie lors de ce procédé. Cette partie, qui a fait l'objet d'une publication, démontre et décrit la méthode par l'intermédiaire d'un profil synthétique et de données réelles de haute qualité. Cet outil a été confronté aux techniques classiques de correction topographique (static shift suivi d'une migration ou migration suivi d'un static shift). Sa supériorité dans la reconstruction du sous-sol est démontrée, et ce d'autant plus que les variations de topographie sont importantes. L'utilisation de cette méthode est recommandée lorsque les variations du relief sont du même ordre de grandeur que la profondeur de pénétration des données géoradar.

Cependant, la migration ne fonctionne jusqu'à présent qu'avec une vitesse constante. Des variations importantes de vitesses peuvent subvenir dans les milieux prospectés (en présence d'eau par exemple), biaisant la reconstruction. Un algorithme de migration prenant en compte un modèle de vitesse complet plutôt qu'une valeur constante pourrait être d'une grande utilité pour imager les milieux fortement hétérogènes.

Les algorithmes de migration ont également, et malheureusement, leur limitation. Outre les problèmes liés aux vitesses, une quantité de bruit non négligeable peut être introduite dans le profil migré. Ce bruit provient d'artefacts de la migration et se traduit par une perte de définition des profils. Une des causes identifiée (principalement en sismique) résulte de l'aliasing sur l'opérateur. Nous avons, dans notre algorithme de migration, rajouté un filtre pour palier à ce problème. Après explication de l'algorithme, les résultats ont été présentés. Du bruit incohérent est correctement supprimé des données et la continuité des réflexions est améliorée, résultant en une impression de « lissage ». Néanmoins, le pas d'échantillonnage étant relativement petit en géoradar, ce type d'aliasing n'intervient que rarement, et l'utilisation de ce filtre reste marginale à une exception près. Lorsqu'une topographie, localement forte, est présente, les conditions d'aliasing sur l'opérateur peuvent être introduites. Dans ce cas, le filtre anti-aliasing peut avoir une influence non négligeable, et nous préconisons de le tester pour en apprécier les effets.

Dans une dernière partie, nous avons codés un algorithme séparé en deux. La première partie permet le calcul automatique des pentes et la deuxième, la ré-interpolation des traces avec cette info a priori. Deux versions du calcul automatique des pentes (l'une en domaine temporel et l'autre en domaine fréquentiel) ont été testées et celle dans le domaine fréquentiel semble plus robuste. Plusieurs paramètres permettent une utilisation plus ou moins poussée. Lorsque l'utilisation est modérée, une part non négligeable de bruit est supprimée, sans affecter le signal utile. Combinée avec la migration, notamment avant, ou avant et après, une grosse quantité d'artefacts sont éliminés des données. L'algorithme souffre malheureusement d'un temps de calcul énorme (de l'ordre de quelques heures) qui le rend inutilisable sur des grands jeux de données pour un traitement efficace. Optimiser le code serait une obligation pour bénéficier de ces bienfaits.

Les deux sujets suivants sont deux terrains d'étude distincts impliquant le géoradar. Le chapitre deux se focalise sur l'imagerie de faille en Mongolie. Dans un contexte d'étude du risque sismique, deux failles ont été investiguées : la faille d'Emeelt, récemment découverte, et dont les résultats ont fait l'objet d'une publication et la faille de Hustaï. Les résultats présentés ici sont les premiers effectués autour de la capitale Mongole et beaucoup d'efforts restent à fournir pour en apprécier les mécanismes. La méthodologie a été axée sur la combinaison de deux fréquences différentes (50 MHz et 500 MHz) et de tranchées. Bien que les profondeurs de pénétration soient relativement faibles et que les mesures sur la faille d'Emeelt soient de bien meilleure qualité, les conclusions sur l'utilisation des antennes sont similaires. L'antenne de 500 MHz a été utilisée avec une méthodologie pseudo-3D, dont l'objectif est l'imagerie des dépôts sédimentaires à petite échelle (quelques dizaine de mètre de large sur quelques mètres de profondeur). Sa profondeur d'investigation et sa précision (reliée à la longueur d'onde) permettent des comparaisons directes entre les profils géoradar et les tranchées. Ainsi, une zone perturbée, associée à la faille a été détectée dans un cône alluvial et un déplacement dextre, d'amplitude 2 m environ, est mis en évidence dans un paléo-chenal. Aucune information n'a pu être déduite des mesures effectuées sur la faille de Hustaï avec l'antenne de 500 MHz. Le dernier gros séisme pouvant être vieux, les dépôts récents peuvent ne pas avoir été affectés. L'antenne de 50 MHz quant à elle a permis d'enregistrer de long profils 2D, perpendiculaires à la faille. L'observation d'une forte réflexion provenant du plan de faille dans les données nous a donné un accès direct a sa géométrie et son orientation entre 3 et 12 m de profondeur, complétant les données précédentes.

Enfin, le troisième chapitre présente les résultats de mesures géoradar sur les dépôts pyroclastiques de l'éruption d'août 2006 du volcan Tungurahua en équateur. Ce chapitre fait l'objet d'une publication en cours de soumission au moment de la rédaction de ce manuscrit. En premier lieu, une étude bibliographique montre les possibilités offertes par l'utilisation du géoradar sur les dépôts volcanologiques, mais également que les méthodologies utilisées restent souvent basiques. Ce chapitre a principalement une vocation méthodologique. Ainsi nous avons détaillés les traitements effectués, montrant les améliorations apportées et discutant les limitations de chacun des filtres. Des mesures suivant une méthodologie pseudo-3D ont été entreprises avec les antennes 500 MHz et 800 MHz sur des dépôts présentant des dunes. Des représentations et un traitement 3D ont été testés en vain. La distance entre les profils étant trop grand et la précision des traces étant trop faible pour les fréquences employées. Des mesures plus denses, enregistrées avec un matériel plus précis seraient nécessaire pour obtenir de « vraies » image 3D. La campagne de mesure, effectuée avec trois antennes de fréquences différentes (250, 500 et 800 MHz) a permis d'imager plusieurs structures à différentes échelles. Les unités principales ainsi que la stratigraphie interne ont pu être mises en évidence. L'interprétation de ces données est fastidieuse et n'en est encore qu'à ces débuts. Par conséquent les résultats présentés dans ce manuscrit sont à prendre comme des résultats préliminaires. Une étude approndie fera l'objet d'une publication future, actuellement en cours de rédaction.

Références

Abma, R., Bernitsas, N., and Sun, J. 1999. Antialiasing methods in Kirchhoff migration. Geophysics, 64(6), 1783–1792.

Abrams, L.J., and Sigurdsson, H. 2007. Characterization of pyroclastic fall and flow deposits from the 1815 eruption of Tambora Volcano, Indonesia using ground penetrating radar. Journal of Volcanology and Geothermal Research, 161(4), 352-361.

Andrews, B., and Manga, M. 2012. Experimental study of turbulence, sedimentation, and co-ignimbrite mass partitioning in dilute pyroclastic density currents. Journal of Volcanology and Geothermal Research. 225–226:30–44.

Annan, A.P. 1991. Topographic Corrections of GPR data. Sensors and Software Incorporated. Technical Note.

Annan, A.P. 2001. Ground Penetrating Radar Work-shop Notes. Sensors and Software, Incorporated, Mississauga, Ontario.

Annan, A.P. 2002. GPR-History, trends, and future developments. Subsurface sensing technologies and applications, 3(4), 253-270.

Annan, A.P. 2009. Electromagnetic principles of ground penetrating radar (Vol. 1). In Jol, H.M. (ed) Ground Penetrating Radar : Theory and Applications. Elsevier.

Baina, R., Nguyen, S., Noble, M., and Lambaré, G. 2003. Optimal anti-aliasing for ray-based kirchhoff depth migration. Expanded Abstract, 73rd Ann. Internat. Mtg. Soc. Expl. Geophys. Session MIG P, 2.

Baljinnyam, I., Bayasgalan, A., Borisov, B.A., Cisternas, A., Dem'yanovich, M.G., Ganbaatar, L., Kochetkov, V.M., Kurushin, R.A., Molnar, P., Philip, H., and Vashchilov, Y.Y. 1993. Ruptures of major Earthquakes and active deformation in Mongolia and its surroundings. Geological Society of America, 181.

Bano M., Duringer Ph., Ghienne J.F., and Schuster M. 1999. Ground penetrating radar study of dry aeolian environment. 69th SEG meeting, Houston, USA, Expanded Abstracts, 586–589.

Bayasgalan, A., Jackson, J., Ritz, J.-F., and Carretier, S. 1999a. Field examples of strike-slip fault terminations in Mongolia and their tectonic significance. Tectonics, 18, 394-411. doi:10.1029/1999TC900007.

Bayasgalan, A., and Jackson, J. 1999b. A re-assessment of the faulting in the 1967 Mogod earthquake in Mongolia. Geophysical Journal International, 138, 784-800.

Beauprêtre, S., Garambois, S., Manighetti, I., Malavieille, J., Sénéchal, G., Chatton, M., Davies, T., Larroque, C., Rousset, D., Cotte, N., and Romano, C. 2012. Finding the buried record of past earthquakes with GPR based palaeoseismology: a case study on the Hope fault, New Zealand. Geophysical Journal International, 189, 73-100.

Benage, M.C., Dufek, J., Degruyter, W., Geist, D., Harpp, K., and Rader, E. 2014. Tying textures of bread crust bombs to their transport regime and cooling history. Journal of Volcanology and Geothermal Research, 274, 92-107.

Beres, M., Huggenberger, P., Green, A.G., and Horstmeyer, H. 1999. Using two- and three-dimensional georadar methods to characterize glacio fluvial architecture: Sedimentary Geology, 129, 1–24.

Berryhill, J.R., 1979. Wave equation datuming. Geophysics, 44, 1329-1344.

Bevc, D., 1997. Flooding the topography: Wave-equation datuming of land data with rugged acquisition topography. Geophysics 62(5), 1558–1569.

Biondi, B. 2001. Kirchhoff imaging beyond aliasing. Geophysics, 66, 654–666.

Böniger, U., and Tronicke, J. 2010. Integrated data analysis at an archaeological site: A case study using 3D GPR, magnetic, and high-resolution topographic data. Geophysics, 75(4), B169-B176.

Brand, B.D. and Clarke, A.B. 2012. An unusually energetic basaltic phreatomagmatic eruption: using deposit characteristics to constrain dilute pyroclastic density current dynamics. Journal of Volcanology and Geothermal Research. 243–244, 81–90.

Branney, M.J., and Kokelaar, P. 2002. Pyroclastic density currents and the sedimentation of ignimbrites. Geological Society Memoir no 27, London.

Cagnoli, B., and Russell, J. K. 2000. Imaging the subsurface stratigraphy in the Ubehebe hydrovolcanic field (Death Valley, California) using ground penetrating radar. Journal of Volcanology and Geothermal Research, 96(1), 45-56.

Cagnoli, B., and Ulrych, T.J. 2001a. Downflow amplitude decrease of ground penetrating radar reflections in base surge deposits. Journal of Volcanology and Geothermal Research, 105, 25-34.

Cagnoli, B., and Ulrych, T.J. 2001b. Ground penetrating radar images of unexposed climbing dune-forms in the Ubehebe hydrovolcanic field (Death Valley, California). Journal of Volcanology and Geothermal Research, 109, 279-298.

Cagnoli, B., and Ulrych, T.J. 2001c. GPR studies of pyroclastic deposits: Subsurface information where there are no outcrops. The Leading Edge 20.3, 242-248.

Calais, E. Vergnolle, M., Sankov, V., Lukhnev, A., Miroshnitchenko, A., Amarjargal, S., and Déverchère, J. 2003. GPS measurements of crustal deformation in the Baïkal-Mongolia area (1994-2002): Implication for current kinematics of Asia. Journal of Geophysical Research, 108, 2051.

Calais, E., Dong, L., Wang, M., Shen, Z., and Vergnolle, M. 2006. Continental deformation in Asia from a combined GPS solution. Geophysical Research Letters, 33(24).

Carpentier, S.F.A., Green, A.G., Langridge, R., Boschetti, S., Doetsch, J., Abächerli, A. N., Horstmeyer, H., and Finnemore, M. 2012. Flower structures and Riedel shears at a step over zone along the Alpine Fault (New Zealand) inferred from 2-D and 3-D GPR images. Journal of Geophysical Research: Solid Earth (1978–2012), 117(B2).

Carrivick, J.L., Pringle, J.K., Russell, A.J., and Cassidy, N.J. 2007. GPR-derived sedimentary architecture and stratigraphy of outburst flood sedimentation within a bedrock valley system, Hraundalur, Iceland. Journal of Environmental & Engineering Geophysics, 12(1), 127-143.

Cassidy, N.J., Russell, A.J., Marren, P.M., Fay, H., Knudsen, O., Rushmer, E.L., and van Dijk, T.A.G.P. 2003. GPR derived architecture of November 1996 jökulhlaup deposits, Skeidararsandur, Iceland, in Ground Penetrating Radar in Sediments, Bristow, C.S., and Jol, H.M. (eds.), Geological Society of London Special Publications, 211, 153–166.

Cassidy, N.J. 2008. Processing, modelling and analysis. In: Jol H (ed) Ground penetrating radar theory and applications. Elsevier Science and Technology, Amsterdam, 141–176, FIGURE 5.9.

Cassidy, N.J., Calder, E.S., Pavez, A., and Wooller, L. 2009. GPR-derived facies architectures: a new perspective on mapping pyroclastic flow deposits. In: Thordarson, T., Self, S., Larsen, G., Rowland, S., Hoskuldsson, A. (Eds.) Studies in volcanology: the legacy of George Walker. IAVCEI Spec Publ 2, Geological Society of London, 181–210.

Catuneanu, O., Abreu, V., Bhattacharya, J.P., Blum, M.D., Dalrymple, R.W., Eriksson, P.G., Fielding, C.R., Fisher, W.L., Galloway, W.E., Gibling, M.R, Giles, K.A., Holbrook, J.M., Jordan, R., Kendall, C.G.St.C., Macurda, B., Martinsen, O.J., Miall, A.D., Neal, J.E., Nummedal, D., Pomar, L., Posamentier, H.W., Pratt, B.R., Sarg, J.F., Shanley, K.W., Steel, R.J., Strasser, A., Tucker, M.E., and Winker, C. 2009. Towars the standardization of sequence stratigraphy. Earh Science Reviews, 92(1), 1-33.

Chow, J., Chang, S.K., and Yu, H.S. 2006. GPR reflection characteristics and depositional models of mud volcanic sediments - Wushanting mud volcano field, southwestern Taiwan. Journal of Applied Geophysics, 60(3), 179-200.

Christie M., Tsoflias, G.P., Stockli, D.F., and Black R. 2009. Assessing fault displacement and off-fault deformation in an extensional tectonic setting using 3-D ground-penetrating radar imaging. Journal of Applied Geophysics, 68, 9-16.

Claerbout, J.F. 1985. Imaging the Earth's interior, Blackwell Scientific Publications, Oxford.

Claerbout, J.F. 1992. Anti aliasing. Stanford Exploration Project Report 73, 371–389.

Cole, P.D. 1991. Migration direction of sand wave structures in pyroclastic-surge deposits: implications for depositional processes. Geology, 19, 1108–1111.

Corbeanu, R.M., Soegaard, K., Szerbiak, R.B., Thurmond, J.B., McMechan, G.A., Wang, D., Snelgrove, S., Forster, C.B., and Menitove, A. 2001. Detailed internal architecture of a fluvial channel sand stone determined from outcrop, cores, and 3D ground penetrating radar; example from the Middle Cretaceous Ferron Sandstone, east-central Utah: AAPG Bulletin, 85, 1583–1608.

Courtland, L.M., Kruse, S.E., Connor, C.B., Connor, L.J., Savov, I.P., and Martin, K.T. 2012. GPR investigation of tephrafallout, Cerro Negro volcano, Nicaragua: a method for constraining parameters used in tephra sedimentation models. Bulletin of Volcanology, 74(6), 1409-1424.

Courtland, L., Kruse, S., and Connor, C. 2013. Violent Strombolian or not? Using ground-penetrating radar to distinguish deposits of low-and high-energy scoria cone eruptions. Bulletin of volcanology, 75(12), 1-13.

Crowe, B.M., and Fisher, R.V. 1973. Sedimentary structures in base-surge deposits with special reference to cross-bedding, Ubehebe Craters, Death Valley, California. Geological Society of American Bulletin, 84, 663-682.

Daniels, D.J., Gunton, D.J., and Scott, H.F. 1988. Introduction to subsurface radar. IEE Proceedings 135, 278-320.

Davis, J.L., and Annan, A.P. 1989. Ground-penetrating radar for high resolution mapping of soil and rock stratigraphy, Geophysical Prospecting, 37,531–551.

Deparis, J., Garambois, S., and Hantz, D. 2007. On the potential of ground penetrating radar to help rock fall hazard assessment: a case study of a limestone slab, Gorges de la Bourne (French Alps). Engineering Geology, 94, 89–102.

Dentith M., O'Neill A., and Clark D. 2010. Ground penetrating radar as a means of studying palaeofault scarps in a deeply weathered terrain, southwestern Western Australia. Journal of Applied Geophysics, 72, 92–101.

Doronzo, D.M. 2012. Two new end members of pyroclastic density currents: forced convection-dominate dandinertia-dominated. Journal of Volcanology and Geothermal Research, 219-220, 87-91.

Douillet, G.A., Tsang-Hin-Sun, E., Kueppers, U., Letort, J., Pacheco, D.A., Lavallee, Y., Goldstein, F., Hanson, J.B., Bustillos, J., Robin, C., Ramón, P., and Dingwell, D.B. 2013a. Cross-stratified, ash sedimentary wedges deposited from the 2006 dilute pyroclastic density currents at Tungurahua volcano, Ecuador. Bulletin of Volcanology, 75, 765.

Douillet, G.A., Pacheco, D.A.,Kueppers, U., Tsang-Hin-Sun, E., and Dingwell, D.B. 2013b. Dune bedforms produced by the 2006 pyroclastic density currents at Tungurahua volcano, Ecuador. Bulletin of Volcanology, 75, 762.

Douillet, G.A., Rasmussen, K.R., Kueppers, U., Lo Castro, D., Merrison, J., Iversen, J., and Dingwell, D.B. 2014. Saltation threshold for pyroclasts at various bedslopes: wind tunnel experiments. Journal of Volcanology and Geothermal Research, 278, 24-24.

Druitt, T.H. 1992. Emplacement of the 18 May 1980 lateral blast deposit ENE of Mount St. Helens, Washington. Bulletin of Volcanology, 54, 554-572.

Dugarmaa, T., Schlupp, A., Adiya, M., Ankhtsetseg, D., Baasanbat, Ts., Battulga, B., Batsaikhan, Ts., Bayar, G., Bayarsaikhan, Ch., Demberel, S., Erdenezul, D., Mungunsuren, D., Munkhsaikhan, A., Munkhuu, D., Narantsetseg, R., Odonbaatar, Ch., Selenge, L., Tsembel, B., Ulziibat, M., Urtnasan, Kh., Marin, S., Lidin, G., Fouquet, D., and Bayasgalan, A. 2006. Seismic Hazard Assessment of Ulaanbaatar, capital of Mongolia. Seismic micro zoning map. Report of Research Center of Astronomy and Geophysics, 156p.

Dujardin, J-R., and Bano, M. 2013. Topographic migration of GPR data: Examples from Chad and Mongolia. Comptes Rendus Geoscience, 345, 73-80.

Dujardin, J-R., Bano, M., Schlupp, A., Gillard, M., Ferry, M., and Munkhuu, U. 2012. GPR measurements to assess the fault's characteristics in a highly smooth topographic context. EAGE, Near Surface, 18th Meeting of Environmental and Engineering Geophysics, Extended Abstracts, Paris, France.

Ettinger, S., Manville, V., Kruse, S., and Paris, R. 2014. GPR-derived architecture of a lahar-generated fan at Cotopaxi volcano, Ecuador. Geomorphology.

Feng, X., Sato, M., Liu, C., and Zhang, Y. 2009 Profiling the rough surface by migration. IEEE Geoscience and Remote Sensing Letters, 6(2), 258-261.

Ferry, M., Meghraoui, M., Girard, J.-F., Rockwell, T.K., Kozaci, O., Akyuz, S., Barka, A., 2004. Ground-penetrating radar investigations along the North Anatolian fault near Izmit, Turkey: constraints on the right-lateral movement and slip history. Geological Society of America 32, 85-88.

Finizola, A., Ricci, T., Deiana, R., Cabusson, S.B., Rossi, M., Praticelli, N., and Lelli, M. 2010. Adventive hydrothermal circulation on Stromboli volcano (Aeolian Islands, Italy) revealed by geophysical and geochemical approaches: Implications for general fluid flow models on volcanoes. Journal of Volcanology and Geothermal Research, 196(1), 111-119.

Fisher, R.V., and Waters, A.C. 1969. Bedforms in base surge deposits: lunar implications. Science 165, 1349-1352.

Fisher, R.V., and Waters, A.C. 1970. Base surge bedforms in Maar volcanoes. American Journal of Science, 268, 157-180.

Fisher, S.C., Stewart, R.R., and Jolt, H.M. 1992. Processing ground penetrating radar (GPR) data (Vol. 4, pp. 11-1). CREWES Research Report.

Gertisser, R., Cassidy, N.J., Charbonnier, S.J., Nuzzo, L., and Preece, K. 2012. Overbank block-and-ash flow deposits and the impact of valley-derived, unconfinedflows on populated areas at Merapi volcano, Java, Indonesia. Natural hazards, 60(2), 623-648.

Girard, J.F., 2002. Imagerie géoradar et modélisation des diffractions multiples. PhD thesis, Université Louis Pasteur, Strasbourg-I.

Gomez, C., Lavigne, F., Lespinasse, N., Hadmoko, D.S., and Wassmer, P. 2008. Longitudinal structure of pyroclastic-flow deposits, revealed by GPR survey, at Merapi Volcano, Java, Indonesia. Journal of Volcanology and Geothermal Research, 176(4), 439-447.

Gomez, C., Lavigne, F., Hadmoko, D.S., Lespinasse, N., and Wassmer, P. 2009. Block-and-ash flow deposition: a conceptual model from a GPR survey on pyroclastic-flow deposits at Merapi Volcano, Indonesia. Geomorphology, 110(3), 118-127.

Gomez, C., and Lavigne, F. 2010. Transverse architecture of lahar terraces, inferred from radargrams: preliminary results from Semeru Volcano, Indonesia. Earth Surface Processes and Landforms, 35(9), 1116-1121.

Gomez, C., Kataoka, K.S., and Tanaka, K. 2012. Large-scale internal structure of the Sanbongi Fan–Towada Volcano, Japan: Putting the theory to the test, using GPR on volcaniclastic deposits. Journal of Volcanology and Geothermal Research, 229, 44-49.

Gómez-Ortiz, D., Martín-Velázquez, S., Martín-Crespo, T., Márquez, A., Lillo, J., López, I., and Carreño, F. 2006. Characterization of volcanic materials using ground penetrating radar: a case study at Teide volcano (Canary Islands, Spain). Journal of Applied Geophysics, 59(1), 63-78.

Gómez-Ortiz, D., Martín-Velázquez, S., Martín-Crespo, T., Márquez, A., Lillo, J., López, I., Carreno, F., Martin-Gonzalez, F., Herrera, M., and De Pablo, M.A. 2007. Joint application of ground penetrating radar and electrical resistivity imaging to investigate volcanic materials and structures in Tenerife (Canary Islands, Spain). Journal of Applied Geophysics, 62(3), 287-300.

Gómez-Ortiz, D., Martín-Crespo, T., I., Rodríguez, I., Sánchez, M.J., and Montoya, I. 2009. The internal structure of modern barchan dunes of the Ebro River Delta (Spain) from ground penetrating radar. Journal of Applied Geophysics, 68, 159-170.

Grasmueck, M., and Weger, R. 2002. 3D GPR reveals complex internal structure of Pleistocene oolitic sandbar. The Leading Edge, 21(7), 634-639.

Grasmueck, M., Weger, R., and Horstmeyer, H. 2005. Full resolution 3D GPR imaging, Geophysics, 70(1), K12-K19.

Gray, S. 1992. Frequency-selective design of the Kirchhoff migration operator: Geophysical Prospecting, 40, 565–571.

Grimm, R.E., Heggy, E., Clifford, S., Dinwiddie, C., McGinnis, R., and Farrell, D. 2006. Absorption and scattering in ground penetrating radar: Analysis of the Bishop Tuff. Journal of Geophysical Research: Planets (1991–2012), 111(E6).

Gross, R., Holliger, K., Green, A.G., and Begg, J.H. 2000. 3D Ground penetrating radar applied to paleoseismology: examples from the Wellington Fault, New Zealand, in 8th International Conference on Ground Penetrating Radar, Proc. SPIE, Vol. 4084, pp 478-481, edds Noon, D.A., Stickley, G.F. & Longstaff, D., SPIE, Bellingham, WA.

Gross, R., Green, A.G., Holliger, K., Horstmeyer, H., and Baldwin J. 2002. Shallow geometry and displacements on the San Andreas Fault near Point Arena based on trenching and 3D georadar surveying, Geophysical Research Letters, 29(20), 1973-1977.

Gross, R., Green, A., Horstmeyer, H., and Holliger, K. 2003. 3D georadar images of an active fault: efficient data acquisition, processing and interpretation strategies. Subsurface Sensing Technologies and Applications, 4, 19-40.

Gross, R., Green, A.G., Horstmeyer, H., and Begg, J.H. 2004. Location and geometry of the Wellington Fault (New Zealand) defined by detailed three-dimensional georadar data, Journal of Geophysical Research, 109, B05401, doi:10.1029/2003JB002615.

Guillemoteau, J., Bano, M., and Dujardin, J-R. 2012. Influence of grain size, shape and compaction on georadar waves: examples of aeolian dunes. Geophysical Journal International, 190, 1455-1463, doi: 10.1111/j.1365-246X.2012.05577.x.

Hall, M.L., Robin, C., Beate, B., Mothes, P. and Monzier, M. 1999. Tungurahua Volcano, Ecuador: structure, eruptive history and hazards. Journal of Volcanology and Geothermal Research, 91(1), 1-21.

Hall, M.L., Samaniego, P., Le Pennec, J.L., and Johnson, J.B. 2008. Ecuadorian Andes volcanism: a review of Late Pliocene to present activity. Journal of Volcanology and Geothermal Research, 176(1), 1-6.

Hall, M.L., Steele, A. L., Mothes, P.A., and Ruiz, M.C. 2013. Pyroclastic density currents (PDC) of the 16–17 August 2006 eruptions of Tungurahua volcano, Ecuador: Geophysical registry and characteristics. Journal of Volcanology and Geothermal Research, 265, 78-93.

Heggy, E., Clifford, S.M., Grimm, R.E., Dinwiddie, C.L., Wyrick, D.Y., and Hill, B.E. 2006a. Ground-penetrating radar sounding in mafic lava flows: Assessing attenuation and scattering losses in Mars analog volcanic terrains. Journal of Geophysical Research: Planets (1991–2012), 111(E6).

Heggy, E., Clifford, S.M., Grimm, R.E., Dinwiddie, C.L., Stamatakos, J.A., and Gonzalez, S.H. 2006b. Low-frequency radar sounding investigations of the North Amargosa Desert, Nevada: A potential analog of conductive subsurface environments on Mars. Journal of Geophysical Research, 111, E06S03, doi:10.1029/2005JE002523.

Heincke, B., Green, A.G., van der Kruk, J., and Horstmeyer, H. 2005. Acquisition and processing strategies for 3D georadar surveying a region characterized by rugged topography. Geophysics, 70, K53-K61.

Jol, H.M. 1995. Ground penetrating radar antennae frequencies and transmitter powers compared for penetration depth, resolution and reflection continuity. Geophysical Prospecting, 43, 693–709.

Jol, H.M., and Bristow, C.S. 2003. GPR in sediments: advice on data collection, basic processing and interpretation, a good practice guide. Geological Society, London, Special Publications, 211(1), 9-27.

Jol, H.M. 2009. Ground Penetrating Radar Theory and Applications. Elsevier, 08.12.2008 - 544 pp.

Jordan, S.C., Cas, R.A.F., and Hayman, P.C. 2013. The origin of a large (> 3km) maar volcano by coalescence of multiple shallow craters: Lake Purrumbete maar, southeastern Australia. Journal of Volcanology and Geothermal Research, 254, 5-22.

Kelfoun, K., Samaniego, P., Palacios, P., and Barba, D. 2009. Testing the suitability of frictional behaviour for pyroclastic flow simulation by comparison with a well-constrained eruption at Tungurahua volcano (Ecuador). Bulletin of Volcanology, 71(9),1057-1075.

Khan, S.D., Heggy, E., and Fernandez, J. 2007. Mapping exposed and buried lava flows using synthetic aperture and ground-penetrating radar in Craters of the Moon lava field. Geophysics , 72.6: B161-B174.

Khilko, S.D., Kurushin, R.A., Kotchetkov, V.M., Misharina, L.A., Melnikova, V.I., Gileva, N.A., Lastochkin, S.V., Baljinnyam, I., and Monhoo, D. 1985. Strong earthquakes, paleoseismogeological and macroseismic data, in Earthquakes and the Base for Seismic Zoning of Mongolia (in Russian), Trans. Joint Sov.-Mongolian Res. Geol. Sci. Exped., vol 41, Nauka, Moscow.

Koralay, T., Kadioglu, S., and Kadioglu, Y.K. 2007. A new approximation in determination of zonation boundaries of ignimbrite by ground penetrating radar: Kayseri, Central Anatolia, Turkey. Environmental Geology, 52(7), 1387-1397.

Kruse, S., Mora, R., Ramírez, C., and Alvarado, G. 2010. Ground penetrating radar imaging of tephra stratigraphy on Poás and Irazú volcanoes, Costa Rica. Revista Geológica de América Central, 43, 119-136.

Lehmann, F., Mühll, D.V., Van der Veen, M., Wild, P., and Green, A.G. 1998. True topographic 2-D migration of georadar data. SAGEEP11, 107-114.

Lehmann, F., and Green, A.G. 1999. Semi automated georadar data acquisition in three dimensions. Geophysics, 64, 719-731.

Lehmann, F., and Green, A.G. 2000. Topographic migration of georadar data: implications for acquisition and processing. Geophysics, 65 (3), 836-848.

Leparoux, D., Gibert, D., and Cote, Ph. 2001. Adaptation of prestack migration to multi-offset ground-penetrating radar (GPR) data. Geophysical Prospecting, 49(3), 374–386.

Lumley, D.E., Claerbout, J.F., and Bevc, D. 1994. Anti aliased Kirchhoff 3-D migration: 64th Ann. International Meeting, Society of Exploration Geophysics. Expanded Abstracts, 1282–1285.

Malik, J.N., Sahoo, A.K., and Shah, A.A. 2007. Ground penetrating radar investigation along Pinjore Garden Fault: implication toward identification of shallow sub-surface deformation along active fault, NW Himalaya. Current Science, 93(10), 1427-1442.

McClymont, A.F., Green, A.G., Streich, R., Horstmeyer, H., Tronicke, J., Nobes, D.C., Pettinga, J., Campbell, J., and Langridge, R. 2008a. Visualization of active faults using geometric attributes of 3D GPR data: an example from the Alpine Fault Zone, New Zealand. Geophysics, 73, B11-B23.doi:10.1190/1.2825408.

McClymont, A.F., Green, A.G., Villamor, P., Hortsmeyer, H., Grass, C., and Nobes, D.C. 2008b. Characterization of the shallow structures of active fault zones using 3D ground penetrating radar data, Journal og Geophysical Research, 113, B10315, doi:10.1029/2007JB005402.

McClymont, A.F., Villamor, P., and Green, A.G. 2009a. Assessing the contribution of off-fault deformation to slip-rate estimates within the Taupo Rift, New Zealand, using 3-D ground-penetrating radar surveying and trenching. Terra Nova, 21(6), 446-451.

McClymont, A.F., Villamor, P., and Green, A.G. 2009b. Fault displacement accumulation and slip rate variability within the Taupo Rift (New Zealand) based on trench and 3-D ground-penetrating radar data. Tectonics, 28(4).

McClymont, A.F., Green, A.G., Kaiser, A., Horstmeyer, H., and Langridge, R.M. 2010. Shallow fault segmentation of the Alpine fault zone, New Zealand, revealed from 2- and 3-D GPR surveying. Journal of Applied Geophysics, 70(4), 343–354.

Mitchum, R.M.Jr., Vail, P.R., and Thompson III, S. 1977. Seismic stratigraphy and global changes of sea-level, part 2: the depositional sequence as a basic unit for stratigraphic analysis. In: C. E. Payton, Editor, Seismic Stratigraphy — Applications to Hydrocarbon Exploration, Memoir vol. 26, American Association of Petroleum Geologists, 53-62.

Miyamoto, H., Haruyama, J.I., Rokugawa, S., Onishi, K., Toshioka, T., and Koshinuma, J.I. 2003. Acquisition of ground penetrating radar data to detect lava tubes: preliminary results on the Komoriana cave at Fuji volcano in Japan. Bulletin of Engineering Geology and the Environment, 62(4), 281-288.

Miyamoto, H., Haruyamam J., Kobayashi, T., Suzuki, K., Okada, T., Nishibori, T., Showman, A.P., Lorenz, R., Mogi, K., Crown, D.A., Rodriguez, J.A.P., Rokugawa, S., Tokunaga, T., and Masumoto, K. 2005. Mapping the structure and depth of lava tubes using ground penetrating radar, Geophysical Research Letters, 32, L21316, doi:10.1029/2005GL024159.

Munroe, J.S., Doolittle, J.A., Kanevskiy, M.Z., Hinkel, K.M., Nelson, F.E., Jones, B.M., and Kimble, J.M. 2007. Application of ground penetrating radar imagery for three dimensional visualisation of near surface structures in ice rich permafrost, Barrow, Alaska. Permafrost and Periglacial Processes, 18(4), 309-321.

Neal, A. 2004. Ground-penetrating radar and its use in sedimentology: principles, problems and progress, Earth Science Reviews, 66, 261–330.

Nielsen, L., von Brockdorff, A.S., Bjerager, M., and Surlyk, F. 2009. Three dimensional architecture and development of Danian bryozoan mounds at Limhamn, south west Sweden, using ground penetrating radar. Sedimentology, 56(3), 695-708.

Nobes, D.C., Gravley, D.M., Brand, B.D., Bloomberg, S.H., Garden, T.O., and Lindsay, J.M. 2012. Ground penetrating radar imaging of Auckland volcanic surge deposits. In Ground Penetrating Radar (GPR), 2012 14th International Conference on (pp. 653-658). IEEE.

Olhoeft, G.R., Sinex, D.B., Sander, K.A., Lagmanson, M.M., Stillman, D.E., Lewis, S., Clark, B.T., Wallin, E.L., and Kauahikaua, J.P. 2000. Hot and cold lava tube characterization with ground penetrating radar: 8th International Conference on Ground Penetrating Radar, proceedings vol. 4084.

Paillou, P., Grandjean, G., Malézieux, J.M., Ruffié, G., Heggy, E., Piponnier, D., Dubois P., and Achache, J. 2001. Performances of ground penetrating radars in arid volcanic regions: Consequences for Mars subsurface exploration. Geophysical Research Letters, 28(5), 911-914.

Pellicer, X.M., and Gibson, P. 2011. Electrical resistivity and Ground Penetrating Radar for the characterisation of the internal architecture of Quaternary sediments in the Midlands of Ireland. Journal of Applied Geophysics, 75(4), 638-647.

Pettinelli, E., Beaubien, S.E., Lombardi, S., and Annan, A.P. 2008. GPR, TDR, and geochemistry measurements above an active gas vent to studynear-surface gas-migration pathways. Geophysics, 73(1), A11-A15.

Ponce, J.J., and Carmona, N. 2011. Coarse-grained sediment waves in hyperpycnal clinoform systems, Miocene of the Austral foreland basin, Argentina. Geology, 39, 763–766.

Rader, E., Geist, D., Geissman, J., Dufek, J., and Harpp, K. (submitted). Hot clasts and cold blasts: Thermal heterogeneity in boiling-over pyroclastic density currents. Journal of Volcanology and Geothermal Research. 42.

Richards, A.F. 1959. Geology of the Islas Revilla gigedo, Mexico. 1. Birth and development of Volcano Bárcena, Isla San Benedicto. Bulletin of Volcanology, 22(1), 73-12.

Rowell, C.R., Pidlisecky, A., Irving, J.D., and Ferguson, R. J. 2010. Characterization of lava tubes using ground penetrating radar at Craters of the Moon National Monument. USA.CREWES Research Report – Volume 22

Russell, J.K., and Stasiuk, M.V. 1997. Characterization of volcanic deposits with ground-penetrating radar. Bulletin of Volcanology, 58(7), 515-527.

Russell, J.K., and Stasiuk, M.V. 2000. Ground-penetrating radar mapping of Minoan volcanic deposits and the Late Bronze Age palaeotopography. Thera, Greece. Special Publication-Geological Society of London, 171, 105-122.

Rust, A.C., Russell, J.K., and Knight, R.J. 1999. Dielectric constant as a predictor of porosity in dry volcanic rocks. Journal of Volcanology and Geothermal Research, 91(1), 79-96.

Rust, A.C., and Russell, J.K. 2000. Detection of welding in pyroclastic flows with ground penetrating radar: insights from field and forward modeling data. Journal of Volcanology and Geothermal Research, 95(1), 23-34.

Rust, A.C., and Russell, J.K. 2001. Mapping porosity variation in a welded pyroclastic deposit with signal and velocity patterns from ground-penetrating radar surveys. Bulletin of Volcanology, 62(6-7), 457-463.

Samaniego, P., Le Pennec, J.L., Robin, C., and Hidalgo, S. 2010. Petrological analysis of the pre-eruptive magmatic process prior to the 2006 explosive eruptions at Tungurahua volcano (Ecuador).

Journal of Volcanology and Geothermal Research. doi:10.1016/j.jvolgeores.2010.10.010

Schlupp, A. 1996. Néotectonique de la Mongolie occidentale analysée a partir de données de terrain, sismologiques et satellitaires. PhD Thesis, Université Louis Pasteur-Strasbourg I.

Schlupp, A., Ferry, M., Munkhuu, U., Ganbold, B., Adiya, M., Bano, M, Dujardin, J-R., Tsend-Ayush, N., Lkhagvasuren, S., Munschy, M., Fleury, S., Mendbayar, M., Shoovdor, T., Tumen, N-O., Danzansan E., Enkhee B., Batsaikhan T.B., and Sodnomsambuu, D. 2012. Investigation of Active Faults near Ulaanbaataar. Implication for Seismic Hazard Assesment. Extended Abstract, 9th General Assembly of Asian Seismological Commission, September 2012 Ulaanbaatar, 265-267.

Schmincke, H.U., Fisher, R.V., and Waters, A.C. 1973. Antidunes and chute-and-pool structures in the base surge deposits of the Laacher See area, Germany. Sedimentology, 20, 553-574.

Schneider, W.A. 1978. Integral formulation for migration in two and three dimensions. Geophysics, 43(1), 49–76.

Sheriff, R.E., and Geldart, L.P. 1995. Exploration Seismology. Cambridge University Press.

Shtivelman, V., and Canning, A. 1988. Datum correction by wave-equation extrapolation. Geophysics, 53(10), (octobre 1): 1311 -1322. doi:10.1190/1.1442409.

Starheim, C.C., Gomez, C., Harrison, J., Kain, C., Brewer, N.J., Owen, K., Hadmoko, D. S., Purdie, H., Zawar-Reza, P., Owens, I., Wassmer, P., and Lavigne, F. 2013. Complex internal architecture of a debris-flow deposit revealed using ground-penetrating radar, Cass, New Zealand. New Zealand Geographer, 69(1), 26-38.

Stasiuk, M.V., and Russell, J.K. 1994. Preliminary studies of Recent volcanic deposits in southwestern British Columbia using ground penetrating radar. In Current Research 1994-A; Geological Survey of Canada, 151-157.

Sulpizio, R., and Dellino, P. 2008. Sedimentology, depositional mechanisms and pulsating behaviour of pyroclastic density currents. In: Gottsman J, Marti J (eds). Calderas volcanism: analysis, modelling and response. Developments in Volcanology, 10, 57–96.

Tapponnier, P., and Molnar, P. 1979. Active faulting and cenozoic tectonics of the Tien Shan, Mongolia, and Baykal Regions. Journal of Geophysical Research: Solid Earth, 84, 3425-3459. doi: 10.1029/JB084iB07p03425.

Tronicke, J., Vilamor, P., and Green, A.G. 2004. Estimating vertical displacement within the NgakuruGraben, New Zealand, using 2D and 3D georadar. 10th International Conference on Ground Penetrating Radar, June 21-24, Delft, the Netherlands.

Van Dam, R.L. 2012. Landform characterization using geophysics - Recent advances, applications, and emerging tools. Geomorphology, 137(1), 57-73

Vergnolle, M., Calais, E., and Dong, L. 2007. Dynamics of continental deformation in Asia. Journal of Geophysical Research: Solid Earth (1978–2012), 112(B11).

Wang, W., Gerrard, C., and Ren, J. 2003. Amplitude Preserving Antialiasing In Kirchhoff Migration. In 2004 SEG Annual Meeting. Society of Exploration Geophysicists.

Widess, M.B. 1973. How thin is a thin bed? Geophysics, 38, 1176–1180.

Wiggins, J.W. 1984. Kirchhoff integral extrapolation and migration of nonplanar data. Geophysics, 49(8), 1239-1248.

Yalçiner, C.Ç., Altunel, E., Bano M., Meghraoui M., Karabacak V., and Serdar H., A. 2012. Application of GPR to normal faults in the Büyük MenderesGraben, Western Turkey. Journal of Geodynamics, http://dx.doi.org/10.1016/j.jog.2012.05.011.

Yilmaz, Ö. 2001. Seismic data analysis. Tulsa, OK., 2nd ed., Society of Exploration Geophysicists.

Zeng, X., McMechan, G.A., Janok, P., Bhattacharya, J.P., Aiken, C.L.V., Xu, X., William S., Hammon, W.S., and Corbeanu, R.M. 2004. 3D imaging of a reservoir analogue in point bar deposits in the Ferron Sandstone, Utah, using ground-penetrating radar. Geophysical Prospecting, 52, 151–163.

Zeng, H. 2009. How thin is a thin bed? An alternative perspective. Leading Edge, October, 1192–1137.

ANNEXES

C. R. Geoscience 345 (2013) 73–80

Contents lists available at SciVerse ScienceDirect

Comptes Rendus Geoscience

www.sciencedirect.com

Internal geophysics

Topographic migration of GPR data: Examples from Chad and Mongolia

Migration topographique des données géoradar : exemples du Tchad et de la Mongolie

Jean-Rémi Dujardin, Maksim Bano *

Institut de physique du globe de Strasbourg, CNRS–UDS UMR 7516 CNRS, université de Strasbourg/EOST), 1, rue Blessig, 67084 Strasbourg cedex, France

ARTICLE INFO

Article history:
Received 14 July 2012
Accepted after revision 10 January 2013
Available online 17 March 2013

Presented by Ghislain de Marsily

Keywords:
Ground-Penetrating Radar (GPR)
Static corrections
Diffraction hyperbola
Topographic Kirchhoff migration

Mots clés :
Géoradar
Corrections statiques
Hyperboles de diffraction
Migration topographique de Kirchhoff

ABSTRACT

Most ground-penetrating radar (GPR) measurements are performed on nearly flat areas. If strongly dipping reflections and/or diffractions are present in the GPR data, a classical migration-processing step is needed in order to determine the geometries of shallow structures. Nevertheless, a standard migration routine is not suitable for GPR data collected on areas showing a variable and large topographic relief. To take into account topographic variations, the GPR data are, in general, corrected by applying static shifts instead of using an appropriate topographic migration that would place the reflectors at their correct locations with the right dip angle. In this article, we present an overview of Kirchhoff's migration and show the importance of topographic migration in the case where the depth of the target structures is of the same order as the relief variations. Examples of synthetic and real GPR data are shown to illustrate the efficiency of the topographic migration.

RÉSUMÉ

La plupart des mesures géoradar sont effectuées sur des zones relativement planes. Lorsque des réflexions à fort pendage et/ou des diffractions sont présentes dans les données, un algorithme de migration classique est nécessaire pour retrouver les géométries des structures souterraines. Cependant, une migration standard n'est pas adaptée aux données géoradar enregistrées sur des zones présentant de fortes variations du relief. Pour prendre en compte les variations de la topographie, une correction statique est généralement appliquée aux données géoradar. Une migration topographique serait plus appropriée pour replacer les réflecteurs à leur vraie position, avec leur vrai pendage. Dans cet article, nous présentons une vue d'ensemble de la migration de Kirchhoff et montrons l'importance de la migration topographique dans le cas où la profondeur des structures et les variations du relief sont du même ordre de grandeur. Des exemples, basés sur des données radar synthétiques et réelles, permettent d'illustrer l'efficacité de la méthode.

1. Introduction

The ground-penetrating radar reflection (GPR) technique, a geophysical method based on high frequency (10–2300 MHz) electromagnetic (EM) wave propagation, can provide very detailed and continuous images of the subsurface. One of the goals of GPR measurements is to determine the geometries of fine structures by imaging the

---

* Corresponding author.
E-mail addresses: jrdujardin@unistra.fr (J.-R. Dujardin), maksim.bano@unistra.fr, maksim.bano@eost.u-strasbg.fr (M. Bano).

1631-0713/$ – see front matter © 2013 Académie des sciences. Published by Elsevier Masson SAS. All rights reserved.
http://dx.doi.org/10.1016/j.crte.2013.01.003

shallow subsurface. In general, the GPR measurements are performed on nearly flat surfaces and in this case, if highly dipping reflections and/or diffractions are present in the data, a standard migration is needed in order to precisely determine the geometries of shallow structures (Feng et al., 2009; Zeng et al., 2004).

For a variable topographic relief, a standard processing procedure includes the application of static shifts (Annan, 1991; Sheriff and Geldart, 1995) followed by a classical migration commonly performed with a flat datum plane. Nevertheless, this processing technique does not give good results for large topographic variations. In addition, the inadequacy of conventional elevation static corrections to take into consideration a gentle to rugged topographic relief was shown to be a particular problem (Lehmann and Green, 2000). To obtain reliable images from GPR data acquired on areas showing irregular topography, a special processing that takes topography into account may be required. Although the relief variation, in seismic acquisition, is small compared to the investigation depth, various migration methods with topography have been developed for seismic data (Berryhill, 1979; Bevc, 1997; Shtivelman and Canning, 1988; Wiggins, 1984). These migration techniques could be of a more important use in GPR data than in seismic, as the target structures have often the same order of depth as the topographic relief variations.

Lehmann and Green (2000) adapted a topographic migration for GPR data based on the Kirchhoff algorithm proposed by Wiggins (1984) for the seismic data collected in mountainous areas. According to these authors, the topographic migration should be considered when the surface slope exceeds 10%. This migration method has been successfully used, in 3D, by McClymont et al. (2008) for the GPR data acquired on active fault areas showing a rugged topography.

In this article, we first present an overview of Kirchhoff's topographic migration algorithm and demonstrate the diffraction equation used in this method as presented by Lehmann et al. (1998). To show the efficiency of the method, we first use synthetic data from a single diffraction point model, and compare the migration results with flat datum and topography, respectively. Then, we present two different examples of real GPR data recorded in areas presenting local and large topographic variations as well as a mean slope of less than 10%. The first example is from a dry sand dune of the Chadian desert, presenting a high velocity medium with local topographic variations, while the second one is from Mongolia, presenting a topographic slope of 10%. Finally, we show and compare the results of GPR profiles processed with static shift followed by migration, migration followed by static shift and topographic migration, and discuss the superiority of the later one even in the cases where the topographic slope is lower than 10%.

2. The Kirchhoff topographic migration

2.1. The Kirchhoff migration

Let us consider a simple 2D geological model (x–z plane) composed of a diffraction point (diffractor) placed on a perfectly resistive medium with a constant EM velocity. The coordinates of this diffractor are x_d and z_d, respectively (Fig. 1a). We assume a zero-offset survey with transmitting and receiving antennas that move on a flat horizontal surface at $z = 0$ (dashed line in Fig. 1a). In this case, the result of the zero-offset GPR profile in time (x–t plane) will be a diffraction hyperbola (shown by the dashed line in Fig. 1b) and the electric field variation can be described by a scalar wave propagation equation, which is similar to the acoustic wave equation (Leparoux et al., 2001).

The goal of the migration is to find the geological model (in the x–z plane) from the zero-offset GPR profile (in the x–t plane). For a resistive medium (high-frequency approximation), we can use Kirchhoff's method that gives the wave field at the location of the diffractor (x_d, z_d) from the zero-offset wave field measured at the surface $z = 0$ (Feng et al., 2009; Schneider, 1978). Practically, the Kirchhoff migration will calculate the diffraction hyperbola (migration template) for each point of the GPR profile and, by

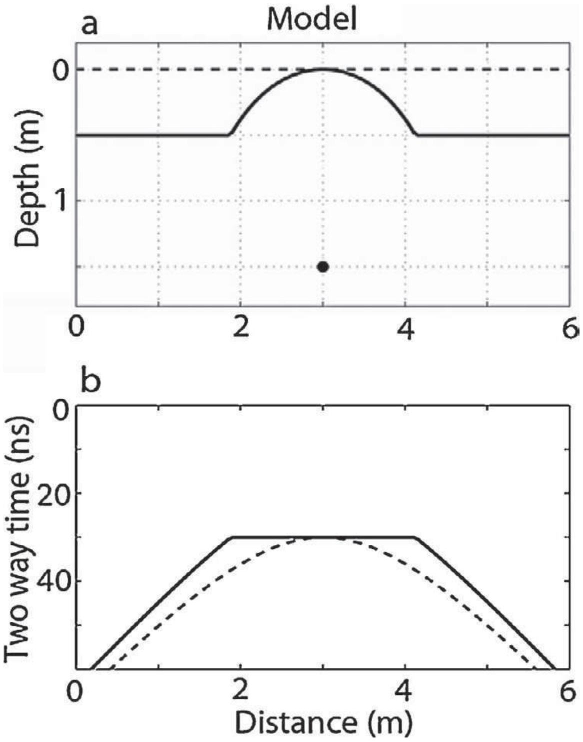

Fig. 1. a) Geological model composed of a diffraction point (black dot) placed on (x_d, z_d). The dashed line represents the flat datum plane located at $z_0 = 0$, while the thick one shows the acquisition surface with topography; b) zero-offset ground-penetrating radar profiles obtained by moving the antennas on both surfaces. The dashed line (a diffraction hyperbola) corresponds to the acquisition on the flat datum plane (dashed line in Fig. 1a), while the thick line represents the case where the acquisition is performed on the surface with topography (thick line in Fig. 1a). Note the difference between the two observed curves.

Fig. 1. a) Modèle géologique composé d'un point diffractant (point noir), placé en (x_d, z_d). La ligne pointillée représente la surface plane théorique, située en $z_0 = 0$. La ligne épaisse représente la surface d'acquisition réelle. b) profil géoradar à offset nul, obtenu en déplaçant les antennes sur les deux surfaces. La ligne pointillée (hyperbole de diffraction) correspond à l'acquisition sur la surface plane théorique (ligne pointillée, Fig. 1a). La ligne épaisse représente l'acquisition sur la surface avec topographie (ligne épaisse, Fig. 1a). Noter la différence entre les deux résultats.

adding the amplitudes along the template, will place it at the top of the template in the migrated profile (Claerbout, 1985; Yilmaz, 2001). Migrating each of these points for a given velocity will focus the amplitudes at their correct positions and the reflector is imaged with its true position and dip angle.

2.2. *Effect of the topography*

When GPR measurements are performed over a surface with topography, the migration template is no longer a diffraction hyperbola; instead, it will be a distorted diffraction curve. This is shown in Fig. 1 where the topography is chosen to be a circle whose centre is on the diffraction point (x_d, z_d), and on both sides of which the topography is flat (see the thick line in Fig. 1a). The distance between the diffraction point and the antennas (in zero offset), moving on the surface along the circle, is constant. Therefore, the migration template, shown by the thick line in Fig. 1b, will be flat on the top, and on both sides it will be represented by two flanks of a diffraction hyperbola. In this case, the imaging result of the classical Kirchhoff migration with a flat datum plane will be spurious (Fig. 4). For this reason, we absolutely need to take into account the topography of the GPR acquisition surface.

2.3. *Migration with topography*

For the standard Kirchhoff migration, at a location *x* on the surface $z = 0$ (i.e. the antennas move on the flat datum plane), the two-way travel time *t(x)* along the grey line path in Fig. 2 is given by:

$$t(x) = \sqrt{{t_0}^2 + \frac{4(x - x_d)^2}{V^2}} \tag{1}$$

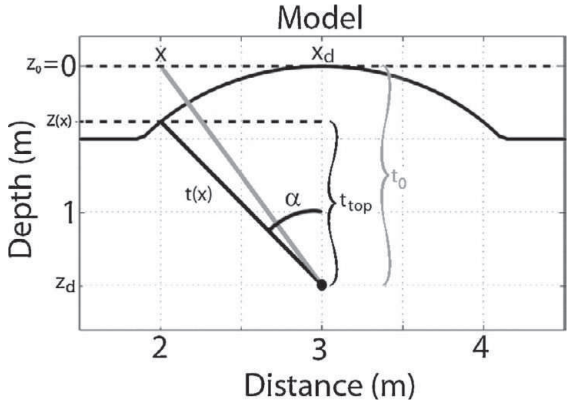

Fig. 2. Schematic presentation showing the topographic correction for the Kirchhoff migration. For a given position *x* at the surface $z_0 = 0$, we take into account the topography $z(x)$ instead of considering the flat datum plane (dashed line at $z_0 = 0$). The travel time $t(x)$ is now calculated along the thick line path rather than along the grey line one.

Fig. 2. Schéma illustrant la correction topographique pour la migration de Kirchhoff. Pour une position *x* donnée sur la surface $z_0 = 0$, la topographie $z(x)$ est utilisée au lieu de considérer la surface plane théorique (ligne pointillée à $z_0 = 0$). Le temps de trajet $t(x)$ est alors calculé le long de la ligne noire plutôt que de la ligne grise.

where $t_0 = 2z_d/V$ is the two-way travel time above the diffraction point (black dot in Fig. 2), x_d is the horizontal position of the diffraction point, z_d is the depth of the diffraction point from the flat datum surface (Fig. 2), and *V* is the EM wave velocity. This is the equation of a diffraction hyperbola (or migration template) which is used in the standard Kirchhoff migration scheme with a flat datum plane.

Correcting for the topography means to choose for the migration template the thick line of Fig. 1b, instead of using the dashed one, which is exactly a diffraction hyperbola. This will allow the template to follow exactly the real travel path of the GPR data. Indeed, for the same *x* location (Fig. 2), the *z* position of the antennas (moving on the rugged surface) has been changed and the two-way travel time $t(x)$ is now calculated along the thick line path in Fig. 2 to obtain:

$$t(x) = \sqrt{{t_{top}}^2 + \frac{4(x - x_d)^2}{V^2}} \tag{2}$$

with:

$$t_{top} = t_0 - \frac{2(z(x) - z_0)}{V} \tag{3}$$

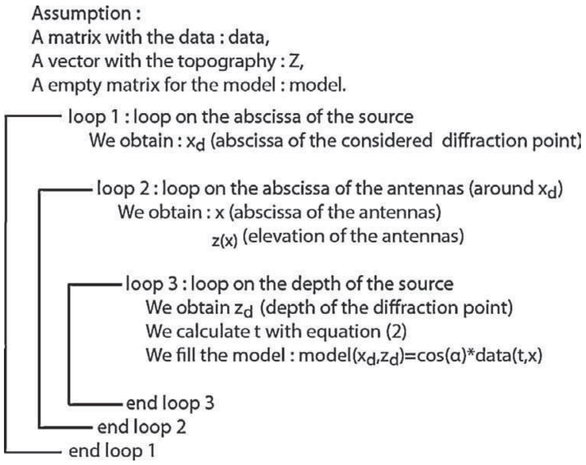

```
Assumption :
A matrix with the data : data,
A vector with the topography : Z,
A empty matrix for the model : model.

loop 1 : loop on the abscissa of the source
    We obtain : $x_d$ (abscissa of the considered diffraction point)
    loop 2 : loop on the abscissa of the antennas (around $x_d$)
        We obtain : x (abscissa of the antennas)
                    z(x) (elevation of the antennas)
        loop 3 : loop on the depth of the source
            We obtain $z_d$ (depth of the diffraction point)
            We calculate t with equation (2)
            We fill the model : model($x_d$,$z_d$)=cos(α)*data(t,x)
        end loop 3
    end loop 2
end loop 1
```

Fig. 3. Diagram showing the different steps of the Kirchhoff topographic algorithm. The names of the variables are the same as the ones used in equations (1) to (4) and Fig. 2. A first matrix with the data (data), a vector **Z** with the topography, and an empty matrix for the model (model) are required. The algorithm starts with a first loop on the x position of the diffraction point (x_d). We move around the x_d position to get *x* and $z(x)$ (position of the antenna) in a second loop. The third loop is running on the depth location of the diffraction point (z_d). Finally, we calculate the two-way travel time between the antennas location (x, $z(x)$) and the diffraction location (x_d, z_d) using equation (2) to fill the model.

Fig. 3. Schéma représentant les différentes étapes de l'algorithme de la migration de Kirchhoff. Les noms des variables sont les mêmes que ceux utilisés dans les équations (1) à (4) et la Fig. 2. Une première matrice avec les données (data), un vecteur **Z** comprenant la topographie, et une matrice vide pour le modèle (model) sont requis. L'algorithme commence par une première boucle sur l'abscisse du point diffractant (x_d). Dans une seconde boucle, la position des antennes est déplacée autour de la position x_d pour obtenir *x* et $z(x)$ (position des antennes). La troisième boucle incrémente sur la profondeur du point diffractant considéré (z_d). Le temps de trajet aller-retour entre la position des antennes (x, $z(x)$) et la position du point diffractant (x_d, z_d) est calculé via l'équation (2) pour remplir la matrice modèle (model).

where *z(x)* is the topography of the acquisition surface shown by the thick line in Fig. 2. Substituting equation (3) into equation (2), we obtain:

$$t(x) = \sqrt{{t_0}^2 + 4\frac{(x - x_d)^2 (z(x) - z_0)^2}{V^2} - 4\frac{t_0 (z(x) - z_0)}{V}} \qquad (4)$$

This equation is the same as the one given without any demonstration by Lehmann et al. (1998) in the case of a 2D migration. Fig. 3 presents an overview of the different steps to compute the topographic migration. We have used the same notations as in equations (1) to (4).

In Fig. 4 we compare the results of the classical migration with flat datum plane, the classical migration after static shift and the topographic Kirchhoff migration. Fig. 4b displays the synthetic radargram computed with the model of Fig. 4a. This radargram is obtained by using a second order Ricker source having a dominant frequency of 500 MHz, located over a homogeneous medium with a velocity of 0.1 m/ns. The distance between traces is 2 cm.

Fig. 4c shows the classical migration of the zero-offset GPR synthetic data of Fig. 4b. One can see a flat horizontal 2-m-wide layer located at a depth of 1.5 m, as well as a bright spot in the middle of the section at a depth of around 1 m (Fig. 4c). The imaging result is very poor and might lead to a misinterpretation of the data. The actual classical procedure is a static shift followed by a classical migration. Fig. 4d shows the synthetic data after the static shift, and Fig. 4e displays the migration after the static shift. The result seems to be better than the one of Fig. 4c. In Fig. 4e

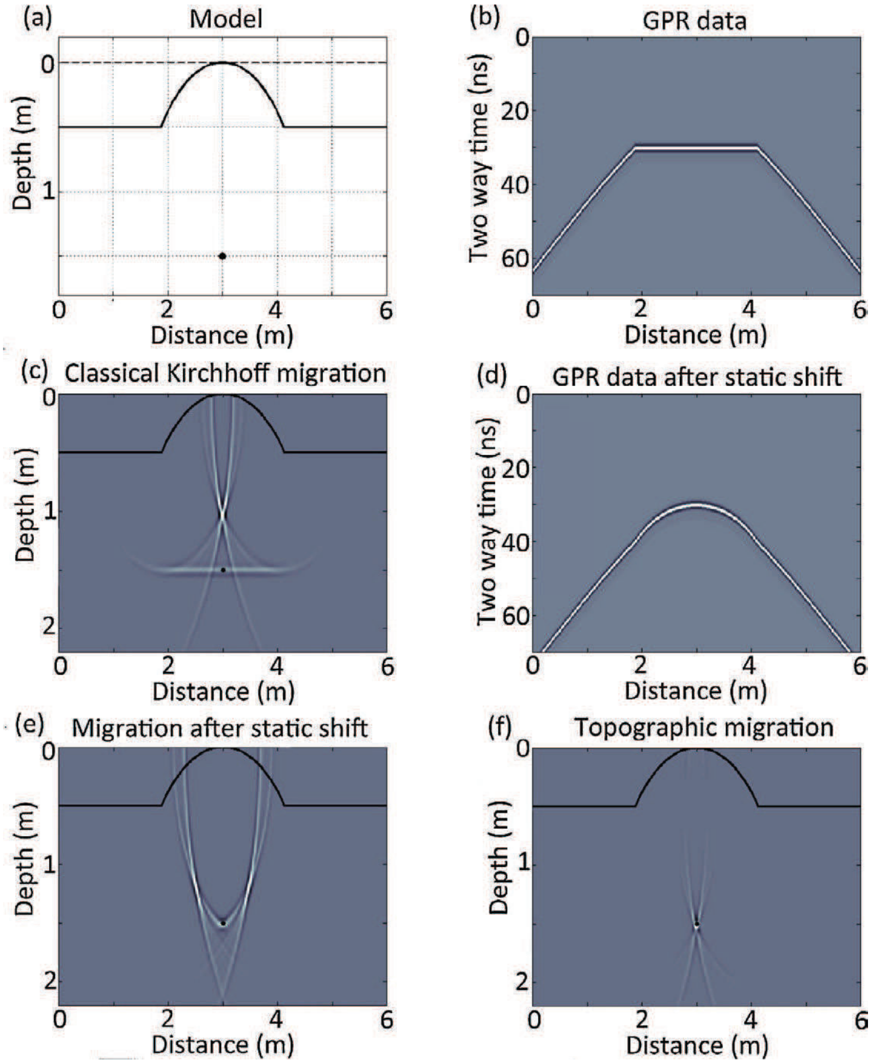

Fig. 4. a) Diffraction point model, with topography (thick line); b) zero-offset ground-penetrating radar data corresponding to a survey over this area. Note the distorted diffraction curve (migration template); c) classical Kirchhoff migration with a flat surface at $z = 0$; d) GPR data after the static shift, e) classical Kirchhoff migration after static shift; f) The result of the topographic migration; the thick line on Fig. c, e and f corresponds to the real topography.

Fig. 4. a) Modèle du point diffractant avec la topographie (ligne noire continue) ; b) données géoradar à offset nul correspondant à un levé sur la zone. À noter : la distorsion de la courbe de diffraction (maquette de migration) ; c) migration de Kirchhoff classique avec une surface plane à $z = 0$; d) données géoradar après corrections statiques ; e) migration de Kirchhoff classique après corrections statiques ; f) migration avec topographie. La ligne noire continue en c, e et f correspond à la vraie topographie.

we observe not only a bright spot at the correct depth of 1.5 m, but also two strong spots located on both sides of the diffraction point (around a depth of 1.2 m). In Fig. 4f, we present the result of the topographic migration appropriately weighted by an amplitude factor proportional to $\cos(\alpha) = t_{\text{top}}/t(x)$ which also depends on the topography (Fig. 2). The amplitude factor is added to take into account the directivity factor that describes the angle dependence of amplitudes and is given by the cosine of the angle between the propagation direction and the vertical axis (Claerbout, 1985; Yilmaz, 2001). The data are well imaged and, as expected, are focused on a single bright spot located at its real depth of 1.5 m (Fig. 4f).

3. Real ground-penetrating radar data examples

3.1. The Chad Dunes

The first example is a GPR profile collected over an aeolian dry dune in the Chadian desert (Bano et al., 1999). The goal of this survey was to image the interior and the base of the dunes to better understand sedimentological processes. The GPR profile has been obtained using a 450-MHz shielded antenna. The acquisition mode was a constant offset of 0.25 m, the antennas were moved by 0.125 m steps with a stack of 64 to improve the signal-to-noise ratio.

A standard processing (with in-house interactive GPR software) has been applied and the resulting profile is displayed in Fig. 5a. The following processing sequence was used: constant shift to adjust the time zero followed by normal move-out corrections; running average (DC) filter to remove the low frequency; flat reflections filter to remove some clutter noise (continuous flat reflections) caused by multiple reflections between shielded antennas and the ground surface; a band-pass filter and finally a time-varying gain function. The same standard processing is applied to all GPR data presented in this section.

The GPR profile of Fig. 5a shows complex geometries, with imbricate reflections corresponding to different deposit phases. The undulating reflection indicated by four white arrows in this figure represents the base of the dune, which in fact is nearly flat and consists of pebbles (> 2.0 mm in diameter). This reflection stems from the contact between the aeolian sands near the surface and deeper lake deposits consisting of an unconsolidated silty sandstone layer of very fine to medium grain size. In order to apply the topographic static shift and/or migration, we need to know the velocity of the GPR waves. In Fig. 5a, we also observe a nice 10-m-wide (80 traces) diffraction hyperbola situated just under the base of the dune (see black circle). After analyzing this diffraction, with different velocities, we found that it can be fitted very well with a constant velocity model of 0.18 m/ns. This value represents an average velocity from the surface of the dune to the diffraction point and it is in good agreement with values found in the literature for dry sands (Gómez-Ortiz et al., 2009; Guillemoteau et al., 2012).

Fig. 5b shows the same GPR profile as in Fig. 5a, but when a standard migration followed by topographic corrections is performed, using a velocity of 0.18 m/ns. The topography shows a local variation of about 30% (at profile coordinate 38 m, black arrow in Fig. 5b) and its global variation of about 5 m (5%) is comparable to the investigation depth. The diffraction hyperbola is well collapsed (at profile coordinate 25 m, black circle) and the reflection from the base of the dune is roughly flattened. Below the area of high topographic gradient (38 m horizontally), we observe a very bad feature (black arrow). The whole area looks blurred, and reflectors are losing consistency. The results of the standard migration followed by topographic corrections are bad.

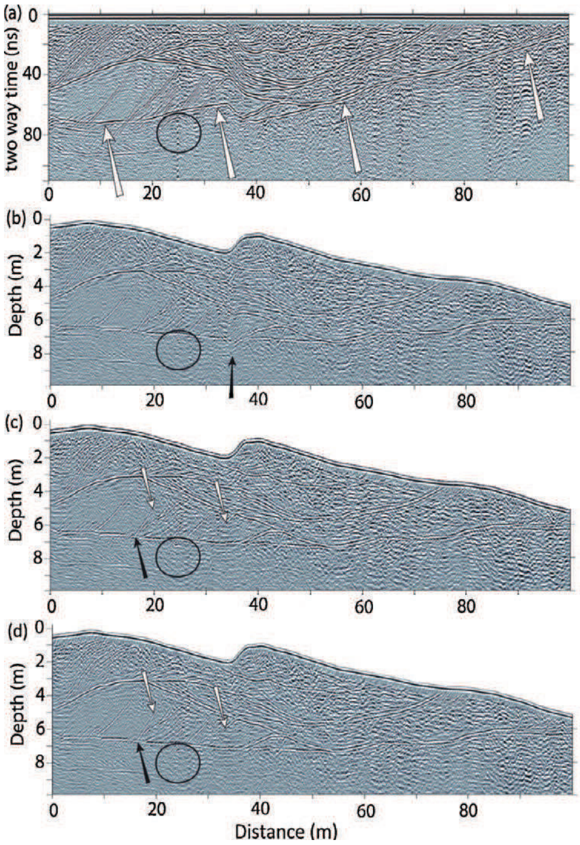

Fig. 5. Ground-penetrating radar profile acquired over a Chadian dry dune with a 450-MHz antenna. a) After the standard processing described in the text. b) after a standard migration followed by a static shift, with a velocity of 0.18 m/ns. This same velocity has been used for all following migrations and topographic corrections; c) after static shift followed by standard migration and d) after Kirchhoff's topographic migration.

Fig. 5. Profil géoradar enregistré sur une dune de sable sec, dans le désert du Tchad, avec une antenne de 450 MHz. a) Après le traitement classique décrit dans le texte ; b) après migration classique suivie d'une correction statique, avec une vitesse de 0,18 m/ns. Cette vitesse a été utilisée pour toutes les migrations et les corrections statiques qui suivent ; c) après corrections statiques, suivies par une migration classique ; d) après migration topographique de Kirchhoff.

Fig. 5c presents the profile after a static shift followed by a standard migration. The migration hyperbola (black circle) is slightly over-migrated. The bad feature indicated by the black arrow in Fig. 5b is corrected. The reflectors are now consistent and the dipping reflector shown by the black arrow (Fig. 5c) has been moved up-dip.

Fig. 5d presents the topographic migration with the same velocity (0.18 m/ns, as in both previous cases) and a specific migration template 13 m wide (100 traces) has been chosen, which is slightly larger than the width of the observed hyperbola (10 m) on the profile. The base of the dune is flattened and the diffraction at 25 m is now correctly focused on a single point inside the black circle, which justifies our choice of 0.18 m/ns for the GPR velocity. The dipping reflector shown by the black arrow has undergone a vertical and horizontal shift of 1.1 and 3.8 m, respectively. It starts at the base of the dune and goes up-dip rightwards as expected (on the non-migrated section of Fig. 5a, these reflections were crossing the base of the dune).

The measured dips on the topographic migrated section of the same reflectors (shown by white arrows) are slightly larger than the dips measured in Fig. 5c (static shift followed by standard migration). Their values are now 26.5° and 19.5° on the topographic migrated section, instead of 25° and 17.7° in Fig. 5c. Although the global topographic variation of the profile does not exceed 5%, the result of the topographic migration is slightly better than the result of the static shift followed by the standard migration. Remember here that the later routine over-migrates the data at large depth (case of the diffraction under the base of the dune).

Fig. 6 shows a portion of the profile of Fig. 5d with topographic migration for different velocities ranging from 0.16 m/ns (left) to 0.20 m/ns (right) with a 0.1 m/ns increment. The hyperbola is not collapsed for the two first figures, while it is over-migrated for the last two ones. The middle figure shows the migrated image with the correct velocity of 0.18 m/ns. The depths and the dips of the reflectors are also changed. The depth of the diffracting point is ranging from 6.5 m (for a velocity of 0.16 m/ns) to 7.8 m (for a velocity of 0.20 m/ns). Therefore, a change of around 5% in the velocity causes a change in depth of nearly 0.3 m (for a depth of around 7 m). The dip of the reflector indicated by the arrow is ranging from 22.6° (velocity of 0.16 m/ns) to 29.9° (velocity of 0.20 m/ns). The dip increases by roughly 2° per 0.01 m/ns velocity increase. To have a correct migration, we conclude that the precision in the estimation of the velocity should be better than 5% of the true velocity.

3.2. Example of a fault in Mongolia

In 2010, we conducted a GPR campaign in Mongolia, 80 km to the west of the capital Ulaanbaatar. The context of this study was seismic hazard. Fig. 7 shows a GPR profile obtained with an unshielded 50 MHz Rough Terrain Antenna (RTA). The profile is more than 200 m long and is perpendicular to the Hustay Fault. This is in a context of a very low slip rate (most likely less than 1 mm per year), and the fault geomorphology has been smoothed during a long period of erosion. Therefore displacements in the topography are not observable. However, in the field, evidences of the fault plane are still visible. Most of the profiles acquired in this area display a strong reflection, which corresponds to the fault plane. These profiles give complementary information such as the dip of the structure and the exact location of the fault near the surface to help design the layout of future palaeoseismic campaigns. The acquisition mode was a constant offset of 4.1 m; traces have been recorded every 0.2 m with a stack of 16 to improve signal-to-noise ratio.

The processing used to obtain Fig. 7a is similar to the one used in the case of the Chadian GPR data. A velocity analysis, which is not presented here, has been done over the surveying area by analysing diffraction hyperbolae present in the GPR data. A mean velocity of 0.12 m/ns has been determined for the whole area. As in the previous example, the topographic variation of 20 m (slope less than 10%) is comparable to the investigation depth. Figs. 7b, c and d respectively display the data after standard migration followed by static shift, static shift followed by standard migration, and topographic migration. The diffraction hyperbola indicated by the black circle is well focused in Fig. 7b and d, and appears slightly over-migrated in Fig. 7c (as in the case of the Chad dune). The dipping reflector (fault plane) indicated by the white arrow now displays a constant slope down to a depth of 24 m in

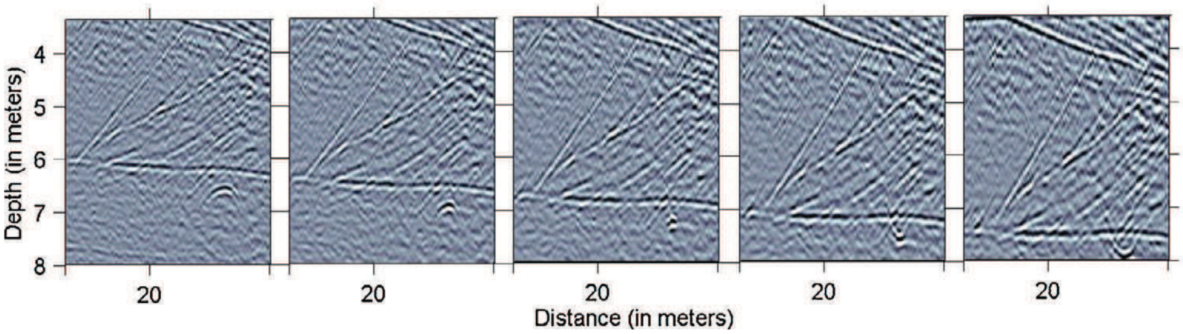

Fig. 6. Detailed area of the base of the dune showing the topographic migration of the diffraction curve (under the base of the dune) for different velocities ranging from 0.16 m/ns (on the left) to 0.20 m/ns (on the right) with a 0.01 m/ns increment. The figure in the middle shows the correct topographic migration with V = 0.18 m/ns.

Fig. 6. Zoom sur la base de la dune, montrant la migration topographique de l'hyperbole de diffraction (sous la base de la dune) pour différentes vitesses allant de 0,16 m/ns (à gauche) à 0,2 m/ns (à droite), avec un incrément de 0,01 m/ns. La figure du milieu montre la migration topographique correcte avec une vitesse de 0,18 m/ns.

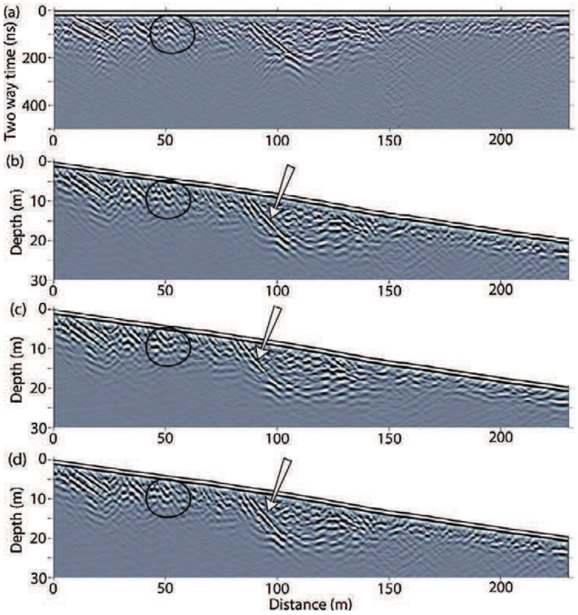

Fig. 7. Ground-penetrating radar profile obtained in Mongolia with an unshielded 50 MHz Rough Terrain Antenna. a) Standard processing (see the text); b: with standard migration followed by static shift; c) with static shift followed by standard migration and d) with topographic migration. Static corrections and migration are performed with a constant 0.12 m/ns velocity.

Fig. 7. Profil géoradar obtenu en Mongolie avec une antenne non blindée de 50 MHz. a) Après traitement standard des données (voir dans le texte) ; b) après migration standard suivie par une correction statique ; c) après correction statique suivie par une migration classique et d) après migration topographique. Les corrections statiques et les migrations ont été faites avec une vitesse constante de 0,12 m/ns.

Fig. 7b and d. However, on the section of Fig. 7c, the reflector is attenuated at a depth of 17 m and has lost its continuity. Its dip angle is changing from 32.2° (migration and static shift) to 34° (static shift and migration and migration with topography). The main observation is the location of the reflector, which is very similar in the cases of Fig. 7b and d, while in Fig. 7c the reflector has been shifted (5.5 m horizontally and 2.6 m vertically) and is reaching the surface. In this case, the migration followed by static shift seems to give more convincing results than the static shift followed by migration (which is the opposite of what was observed in the Chadian dune example). From this result, we conclude that topographic migration should be considered at any location where the subsurface shows steep dip angle structures (exceeding 30°), even in the case where the surface slope is less than 10%.

As in the previous case, we performed a velocity sensitivity analysis by using a topographic migration of the fault plane reflection with different velocities ranging from 0.1 m/ns to 0.14 m/ns with a 0.01 m/ns step. After topographic migrations, the slope of this reflector is varying from 28.9° to 39.5° and increases by roughly 2.65° for a 0.01-m/ns increase in the velocity. In this case, for a correct topographic migration, the estimation of the velocity should be better than 8%.

4. Conclusion

In the presence of relief variations of the same order as the investigation depth of GPR data, a topographic migration is necessary to correctly locate the dipping reflectors and focus the diffractions. The topographic migration presented in this article is based on Kirchhoff's algorithm similar to the method proposed by Lehmann and Green (2000). The application may be more useful for GPR data than for seismic data, as the topographic variations are comparable to the depth of the target structures. We demonstrate the template migration equation, as a function of the topography, along which the amplitudes are added together to give a single point on the migrated section.

By comparing processed sections obtained from GPR data measured over media of high EM velocity (dry sand) having large local topographic variations within a global topographic slope of 5%, we show that reflectors obtained by standard processing (static shift corrections followed by migration) have dip angles that deviate from the angles in a topographically migrated profile by 1 to 2 degrees. Their locations are also changing by a few meters, even for reflectors close to the surface. Thus, for high velocity media with large local topographic variations, even in the case where the global surface slope does not exceed 5%, the application of the topographic migration is necessary and efficient. We also show that topographic migration should be considered at any location where the subsurface shows steeply dipping structures (> 30°), even for surface topographic slopes of less than 10%. Finally, we have shown that the precision in the velocity estimation should be from 5 to 10% of the true velocity, in order to have a correct topographic migration.

Acknowledgement

We thank the reviewers of the initial draft of this article, C. Çağlar Yalciner, S. Garambois, and F. Rejiba for their help in improving the manuscript.

References

Annan, A.P., 1991. Topographic Corrections of GPR data. Sensors&Software Inc. Technical Note.

Bano, M., Duringer, P., Ghienne, J.F., Schuster, M., 1999. Ground penetrating radar study of dry aeolian environment. 69th SEG meeting, Houston, USA, Expanded Abstracts. pp. 586–589.

Berryhill, J.R., 1979. Wave equation datuming. Geophysics 44, 1329–1344.

Bevc, D., 1997. Flooding the topography: wave-equation datuming of land data with rugged acquisition topography. Geophysics 62 (5), 1558–1569.

Claerbout, J.F., 1985. Imaging the Earth's Interior. Blackwell Scientific Publications, Oxford.

Feng, X., Sato, M., Liu, C., Zhang, Y., 2009. Profiling the rough surface by migration. IEEE Geosci. Remote S. Lett. 6 (2), 258–261.

Gómez-Ortiz, D., Martín-Crespo, T.I., Rodríguez, I., Sánchez, M.J., Montoya, I., 2009. The internal structure of modern barchan dunes of the Ebro River Delta (Spain) from ground penetrating radar. J. Geophys. 68, 159–170.

Guillemoteau, J., Bano, M., Dujardin, J.R., 2012. Influence of grain size, shape and compaction on georadar waves: examples of aeolian dunes. Geophys. J. Int. 190, 1455–1463.

Lehmann, F., Green, A.G., 2000. Topographic migration of georadar data: implications for acquisition and processing. Geophysics 65 (3), 836–848.

Lehmann, F., Mühll, D.V., Van der Veen, M., Wild, P., Green, A.G., 1998. True Topographic 2-D Migration of Georadar Data. SAGEEP11 107–114.

Leparoux, D., Gibert, D., Cote, P., 2001. Adaptation of prestack migration to multi-offset ground-penetrating radar (GPR) data. Geophys. Prospect. 49 (3), 374–386.

McClymont, A.F., Green, A.G., Streich, R., Horstmeyer, H., Tronicke, J., Nobes, D., Pettinga, D., Campbell, J., Langridge, R., 2008. Visualization of active faults using geometric attributes of 3D GPR data: An example from the Alpine Fault Zone, New Zealand. Geophysics 73 (2), B11–B23, http://dx.doi.org/10.1190/1.2825408.

Schneider, W.A., 1978. Integral formulation for migration in two and three dimensions. Geophysics 43 (1), 49–76.

Sheriff, R.E., Geldart, L.P., 1995. Exploration Seismology. Cambridge University Press.

Shtivelman, V., Canning, A., 1988. Datum correction by wave-equation extrapolation. Geophysics 53 (10), 1311–1322, http://dx.doi.org/10.1190/1.1442409.

Wiggins, J.W., 1984. Kirchhoff integral extrapolation and migration of nonplanar data. Geophysics 49 (8), 1239–1248.

Yilmaz, Ö., 2001. Seismic Data Analysis, 2nd ed. Society of Exploration Geophysicists, Tulsa, OK.

Zeng, X., McMechan, G.A., Janok, P., Bhattacharya, J.P., Aiken, C.L.V., Xu, X., William, S., Hammon, W.S., Corbeanu, R.M., 2004. 3D imaging of a reservoir analogue in point bar deposits in the Ferron Sandstone, Utah, using ground-penetrating radar. Geophys. Prospect. 52, 151–163.

Geophysical Journal International

Geophys. J. Int. (2014) doi: 10.1093/gji/ggu130

Geophysical Journal International Advance Access published April 30, 2014

GPR measurements to assess the Emeelt active fault's characteristics in a highly smooth topographic context, Mongolia

Jean-Rémi Dujardin,[1] Maksim Bano,[1] Antoine Schlupp,[1] Matthieu Ferry,[2] Ulziibat Munkhuu,[3] Nyambayar Tsend-Ayush[3] and Bayarsaikhan Enkhee[3]

[1] *Institut de Physique du Globe de Strasbourg, CNRS UMR 7516, Université de Strasbourg, Strasbourg, France. E-mail:* jrdujardin@unistra.fr
[2] *University of Montpellier 2, Géosciences, Montpellier, France*
[3] *Research Center of Astronomy and Geophysics, Mongolian Academy of Sciences, Ulaanbaatar, Mongolia*

Accepted 2014 April 2. Received 2014 April 2; in original form 2013 August 9

SUMMARY

To estimate the seismic hazard, the geometry (dip, length and orientation) and the dynamics (type of displacements and amplitude) of the faults in the area of interest need to be understood. In this paper, in addition to geomorphologic observations, we present the results of two ground penetrating radar (GPR) campaigns conducted in 2010 and 2011 along the Emeelt fault in the vicinity of Ulaanbaatar, capital of Mongolia, located in an intracontinental region with low deformation rate that induces long recurrence time between large earthquakes. As the geomorphology induced by the fault activity has been highly smoothed by erosion processes since the last event, the fault location and geometry is difficult to determine precisely. However, by using GPR first, a non-destructive and fast investigation, the fault and the sedimentary deposits near the surface can be characterized and the results can be used for the choice of trench location. GPR was performed with a 50 MHz antenna over 2-D lines and with a 500 MHz antenna for pseudo-3-D surveys. The 500 MHz GPR profiles show a good consistency with the trench observations, dug next to the pseudo-3-D surveys. The 3-D 500 MHz GPR imaging of a palaeochannel crossed by the fault allowed us to estimate its lateral displacement to be about 2 m. This is consistent with a right lateral strike-slip displacement induced by an earthquake around magnitude 7 or several around magnitude 6. The 2-D 50 MHz profiles, recorded perpendicular to the fault, show a strong reflection dipping to the NE, which corresponds to the fault plane. Those profiles provided complementary information on the fault such as its location at shallow depth, its dip angle (from 23° to 35°) and define its lateral extension.

Key words: Geomorphology; Palaeoseismology; Fractures and faults; Asia.

1 INTRODUCTION

Central Asia is known for its high level of seismic hazards, especially Mongolia, which has been one of the most seismically active intracontinental regions in the world with four large earthquakes (magnitude around 8) along its active faults in the western part of the country during the last century (Khilko *et al.* 1985). The deformation in Mongolia is located between compressive structures related to the collision and penetration of the Indian plate into the Eurasian plate and extensive structures in the north of the country related with the Baykal rift (Tapponnier & Molnar 1979; Baljinnyam *et al.* 1993; Schlupp 1996; Bayasgalan & Jackson 1999).

The seismic activity observed in the vicinity of Ulaanbaatar (UB), capital of Mongolia, is relatively low compared to the activity observed in western Mongolia. Nevertheless, since 2005, the seismic activity around UB not only has increased, but is also organized (see Fig. 1) at the west of UB along two perpendicular directions, which determine two active faults: Emeelt fault, discovered in 2008 (NNW-SSE direction, 25-km-long minimum and situated about 10 km W of UB) and Hustai fault (WSW–ENE direction, 80 km long, with its NE tip at less than 20 km west of UB); their length and morphology indicate that they can produce earthquakes of magnitude 6.5–7.5 (Schlupp *et al.* 2012). Most of the Mongolian population (1.2 million over 3 million) is concentrated at UB, which is the main political and economical centre of the country. Hence, the study of seismic hazard and the estimation of the probability of future destructive earthquakes are of primary importance for the country (Dugarmaa *et al.* 2006). Since the last large earthquake, the faults geomorphology has been highly smoothed by erosional processes and the exact location of the fault plane surface rupture is thus hidden within a several metre wide strip.

The GPR method has been proven to give good and useful results to characterize faults by identifying offsets of radar reflections (Malik *et al.* 2007; Christie *et al.* 2009; Yalçiner *et al.* 2013) and

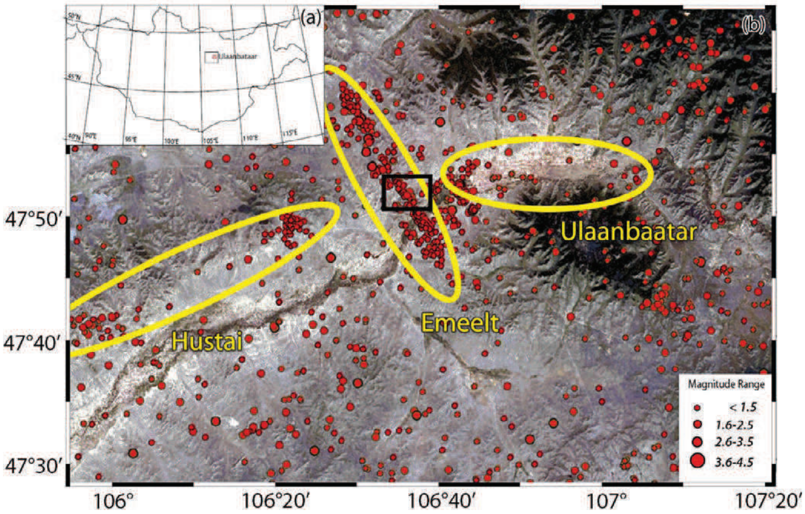

Figure 1. (a) Map of Mongolia with location of the capital, Ulaanbaatar. (b) Zoom over the area of Ulaanbaatar. Yellow lines surround the two main active faults (Emeelt and Hustaï) and Ulaanbaatar urban area. Red dots represent the seismicity since 2005 (after NDC data, RCAG). Note the strong alignment of the seismicity defining the Emeelt fault.

buried fluvial channel deposits (Ferry *et al.* 2004). Many studies have shown that pseudo-3-D and 3-D GPR allow a better and reliable interpretation than 2-D GPR profiles (e.g. Gross *et al.* 2000, 2002, 2003, 2004; Tronicke *et al.* 2004; McClymont *et al.* 2008b). Beauprêtre *et al.* (2012) used a pseudo-3-D survey in order to image a buried channel network, which allows the reconstruction of the past slip history. McClymont *et al.* (2008a) have used geometric attributes of 3-D GPR data to improve the visualization of active faults. Dentith *et al.* (2010) compared GPR data with trench results in order to study palaeofault scarps in the case of deeply weathered terrains. The concept of radar facies developed and mainly used in sedimentology (Neal 2004; Pellicer & Gibson 2011) is now widely considered in active tectonic context (e.g. McClymont *et al.* 2008a, 2010).

Nevertheless, none of these studies were performed on active fault zones showing low slip rate. It is the first time that we use GPR to explore and reveal the buried traces of an active fault in such a context. Our study is focused on the Emeelt fault (Fig. 1), which is associated to an intracontinental context, with moderate deformation very likely much less than 1 mm yr^{-1} (Calais *et al.* 2003, 2006; Vergnolle *et al.* 2007). After some preliminary geomorphologic observations and a trench dug in 2009, two GPR campaigns were conducted in 2010 and 2011. Pseudo-3-D profiles were recorded with a 500 MHz antenna over an alluvial fan and a palaeochannel crossed by the fault, to look for the displacement and/or the deformation of reflections and horizons. In addition, several long 50 MHz 2-D lines (about 200 m long) were realized perpendicular to the fault in a much wider area. The objective of these profiles was to look for the geometry and lateral extension of the fault at greater depth and to verify the presence of other branches.

2 CONTEXT AND PURPOSE

The geomorphologic features shown by the picture in Fig. 3 are clearly visible on the satellite view (Fig. 2). The scarp generated by the fault is clearly seen. The trace left by the fault on the surface (black arrows, Fig. 2) is a couple of metre wide. It has a N143° direction and can be followed about 10 km on the satellite image (Fig. 2, from Google Earth). If we include the seismic activity, we can consider its length to be 25 km minimum. From the picture (Fig. 3), we observe a valley in the centre that is surrounded by two hills on both sides. The scarps separate those hills and the valley. This specific geometry recalls a collapsed basin such as a normal graben system (in an extensional tectonic context) or a reverse graben (in a compressional tectonic context) or even in a transtensional context. However, due to the low slip rate (less than 1 mm yr^{-1}) and the long recurrence time, the fault scarp has been heavily smoothed by erosional processes, hiding the precise location of the fault on the surface. In addition, no clues on the direction of the fault dip are yet observed. However, recent deposits recognized in the area allow possible dating in palaeoseismology. Thus, a first trench (referred to as trench T1) was dug in 2009 on the edge of an actual alluvial fan (Fig. 2c). GPR surveys were performed only in 2010 near the trench to, on the one hand, compare both data sets and connect GPR facies with geological units and, on the other hand, identify the fault rupture at depth. Furthermore, we investigated a palaeochannel, by combining the trenches and GPR results, to estimate the cumulative displacement along the fault. A second trace, parallel to the first one, is observed on a smaller area (white arrows, Figs 2 and 3). Both traces show a similar signature on the surface, and raise the question of a possible second branch.

3 DATA ACQUISITION AND PROCESSING

3.1 Methodology of GPR acquisition

Ground penetrating radar (GPR) is a geophysical method based on the propagation, reflection and scattering of high-frequency (from 10 MHz to 2 GHz) electromagnetic (EM) waves in the Earth (Daniels *et al.* 1988; Jol 2009). For non-magnetic rocks, it allows imaging of the electric and dielectric contrasts of the shallow subsurface. The depth of investigation depends on the EM attenuation of the medium and the frequency used. The lower the frequency, the greater the penetration depth, which varies from a few centimetres in conductive materials up to 50 m for low conductivity (less than 1 mS m^{-1}) media (Davis & Annan 1989; Jol 2009). The vertical resolution depends on the velocity of EM waves and the frequency

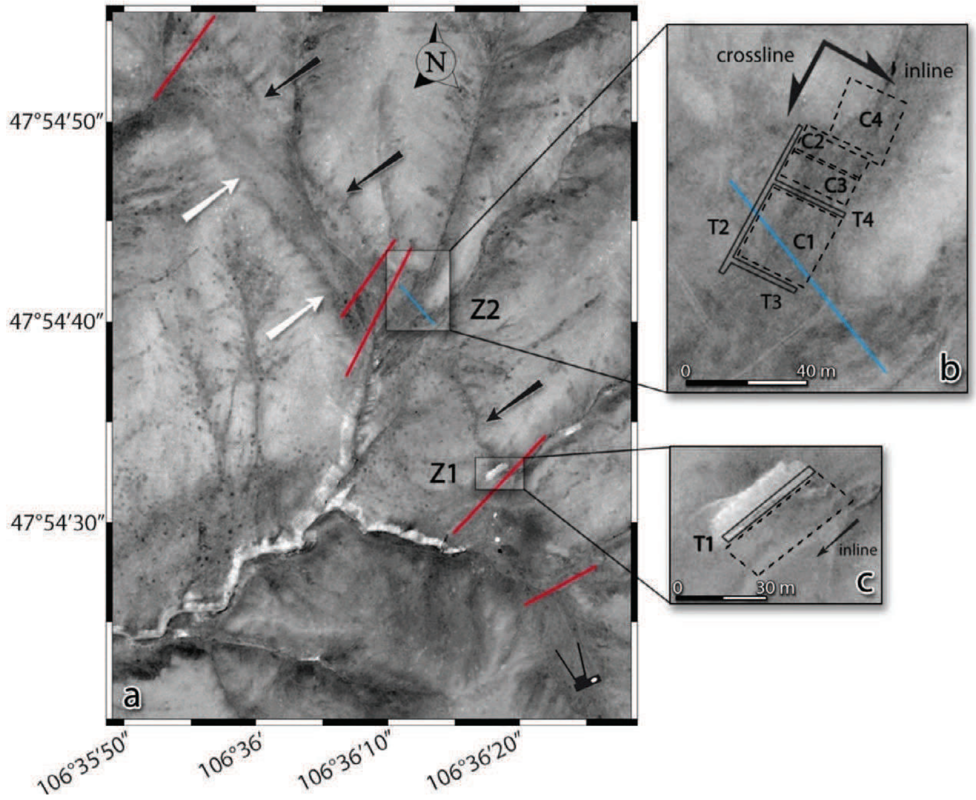

Figure 2. Aerial view of the studied area (satellite image digital globe, Google Earth 2009). Red lines indicate the location of the 50 MHz profiles (RTA). Black arrows highlight the fault trace and white arrows highlight a morphological scarp at the opposite side of the basin. Camera pictogram indicates the viewpoint of the Fig. 3. (b) and (c) Zoom of areas Z1 and Z2. Trench locations are in black and the border of pseudo-3-D 500 MHz GPR cubes are with black dashed lines. The C1 and C2 cubes were recorded in 2010, while the C3 and C4 cubes were recorded in 2011 (see the text for more details). The blue line in Z2 area represents the 500 MHz profile shown in Fig. 6.

Figure 3. Picture of the survey area (see Fig. 2 for location). Black arrows highlight the Emeelt fault scarp and white arrows show another morphological scarp. The trenches are visible on the right side.

of the antennae used. Following the λ/4 criterion (Widess 1973; Jol 1995; Zeng 2009), it varies from 70 to 5 cm for frequencies of 50–500 MHz and velocities of 0.1–0.14 m ns^{-1}. In general, features such as sedimentary structures, lithological boundaries, fractures and/or faults are clearly visible with GPR (Gross *et al.* 2004; Neal 2004; Deparis *et al.* 2007; McClymont *et al.* 2010), even when these features differ only by small changes in the nature, size, shape, orientation and packing of grains (Guillemoteau *et al.* 2012).

After the geomorphologic recognition of the Emeelt fault and a preliminary trench (T1) realized in 2009 (Fig. 2), we decided to use GPR measurements to investigate subsurface deposits potentially affected by the fault on a wider area. The GPR observations should help us to decide location of future trenches. Our first objective was to study an alluvial fan situated close to the trench T1 (referred to as Z1 area) for three reasons. First, the sedimentary deposits provide a stratigraphy that, if offset by the fault, can give us information on the geometry and dynamic of the fault, such as the dip, amplitude and direction of displacement with a non-destructive method. Secondly, sediments are usually favourable to EM propagation and thirdly, the proximity of the trench will allow us to perform a direct comparison of both data sets (geology and GPR). In this survey, we used a 500 MHz antenna to get detailed features at shallow depth and to have a depth of penetration and a wavelength consistent with the trench observations. We recorded 25 profiles of 40 m long on both sides of the trench T1 and parallel to it with the aim to cut through the fault. The space between profiles was 1 m and the recoding step

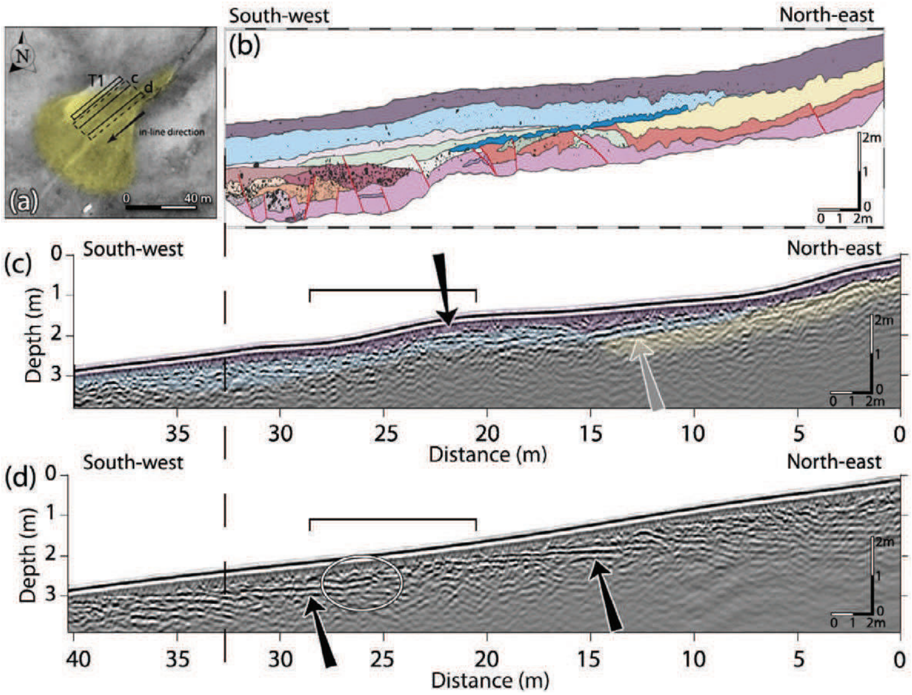

Figure 4. (a) Same as Fig. 2(c) with the location of the GPR profiles (c and d) and the alluvial fan in yellow. (b) Log of the southern wall of trench T1 situated in Z1 area and dug in 2009. (c) and (d) 500 MHz GPR profiles. The profiles and the log are equally scaled; the vertical exaggeration is 1.9. Red lines in the log represent ruptures dipping mostly to the north–east from 20° to subvertical. The three first units, purple, blue and yellow in (b) are superimposed on the profile (c) for comparison. Black arrows show horizontal reflections and grey arrow shows dipping reflection (contact between blue and yellow units). Horizontal black brackets show the position of the fault scarp at the surface.

was 0.03 m. Only 15 profiles situated south of the trench show interesting results and two of them are presented and discussed later on (Fig. 4).

About 300 m north of Z1 area, the morphology shows two small streams crossing the fault and evidence of recent sedimentary deposits (Fig. 2). To check for the presence of hidden palaeochannels filled by sediments and cut by the fault, we recorded 11 profiles across and perpendicular to both streams using the 500 MHz antenna. The profiles were 80 m long with a recording step of 0.03 m. The profiles show a clear palaeochannel under the northernmost stream, well imaged by GPR (blue line in Figs 2b and 6). Consequently, we decided to perform the pseudo-3-D GPR survey in this area crossed by the fault (Z2 area). We opened simultaneously, due to field constraints, three trenches (T2, T3 and T4) in Z2 area; one across the fault (T2) and two parallel to it (T3 and T4). Their location and geometry are shown in Fig. 2(b). The GPR survey was separated in four distinct pseudocubes, denoted 1–4. Cubes C1 and C2 were recorded in 2010, while complementary cubes C3 and C4 were recorded in 2011. An overlap of five profiles was performed between the cubes C2 and C3 in order to assess the reliability of GPR data recorded at two different periods (2010 and 2011). The main objective of this survey was to image the palaeochannel in 3-D in order to characterize any horizontal/vertical displacement caused by the fault. The pseudo-3-D approach has become a common procedure and has successfully been used in the case of active fault studies (e.g. Malik *et al.* 2007; Beauprêtre *et al.* 2012). A full 3-D acquisition schema requires an interval of a quarter wavelength grid spacing (Grasmueck *et al.* 2005) in both inline and cross-line directions of the 3-D cube. This would require one profile every 5 cm (for a mean velocity of 0.1 m ns^{-1}) with a 500 MHz antenna. The number of profiles would then be multiplied by five compared to our current survey. As a result, and due to time constraints on the field, we have chosen the pseudo-3-D approach rather than a full 3-D schema.

The profiles were parallel to the fault direction and spaced each 25 cm (see Table 1 for more details about the acquisition geometry). In addition, long 2-D lines were recorded with a 50 MHz rough terrain antenna (RTA). The acquisition geometry is shown in Table 2. The purpose of those lines was to provide additional information such as the geometry and behaviour of the fault at greater depth, the lateral extension of the fault and to test the hypothesis of a second branch in the area of investigation, which could take place along the second scarp.

The topography of all GPR profiles was recorded using differential GPS. The GPS antenna was mounted on a backpack carried by an operator who was following GPR paths. The recording step of the GPS was set to twenty centimetres. Saw-tooth effects were observed on the topographic profiles due to the small movements

Table 1. Details of the pseudo-3-D surveys.

	C1 (2010)	C2 (2010)	C2 (2011)	C3 (2011)
Size (inline × cross-line)	25 m × 26.5 m	24 m × 10 m	24 m × 9.5 m	20 m × 22 m
Number of inlines	107	41	38	45
Space between inlines	25 cm	25 cm	25 cm	50 cm
Number of cross-lines	26	25	9	
Space between cross-lines	1 m	1 m	3 m	

Table 2. Details of the acquisition parameters.

Frequency	50 MHz	500 MHz (Z1)	500 MHz (Z2)
Antenna separation	4.2 m	0.18 m	0.18 m
Step Interval	0.2 m	0.02 m	0.03 m
Samples	512	528	528
Stacks	16	16	16
Time window (ns)	535	82	82

of the operator while he was walking. In order to get rid of these undesirable effects, a high degree polynomial curve fitting for the data was used, instead of using raw topographic profiles.

3.2 Methodology of GPR processing

The processing of all GPR profiles has been performed with in-house software (Girard 2002) written in Matlab. We used a common flow procedure involving a constant shift to adjust the time zero; a dc filter to remove the low frequencies; a flat reflections filter to remove some clutter noise (ringing caused by multiple reflections between shielded antennae and the ground surface); a time varying gain function and finally a bandpass filter (elliptic-tapered filter). The time varying gain function is a smoothed version of the trace envelope calculated by Hilbert transform. Bandpass filters are of 20–150 and 100–800 MHz for the 50 and 500 MHz antennae, respectively. A velocity analysis, which is not presented here, has been done over the surveying area by analyzing diffraction hyperbolae present in the GPR data. It gives a mean velocity of 0.135 and 0.095 m ns^{-1} for the data collected in 2010 and 2011, respectively. These values are constant and consistent for both frequencies (500 and 50 MHz antennae). The difference in velocity is explained by the unusual humid period during the survey in 2011 compared to the 2010 dry summer. Afterwards, a Kirchhoff migration, which accounts for the topography (Lehmann & Green 2000; Heincke *et al.* 2005; Dujardin & Bano 2013), has been applied before loading the data into seismic interpretation software (OpendTect). The topographic migration of each profile has been performed with a constant velocity.

4 GPR IMAGING RESULTS AND INTERPRETATION

4.1 500 MHz antenna, Z1 area, description of the profiles

The filtered radar sections were visually analysed for data interpretation, and two of them are presented in Fig. 4. They are equally scaled and are presented with a vertical exaggeration of 1.9. Their locations are shown in Fig. 4(a). The investigated alluvial fan is highlighted in yellow in Fig. 4(a). The beginning of the profiles is on the NE to be in agreement with the map. The *x*-axis is also from NE to SW to stay consistent with the recording path of the GPR. For the interpretation, we used a combination of reflections picking with radar facies recognition. Four facies, used in the interpretation, are presented in Fig. 5. Despite the very low penetration depth of the profiles (up to 1.5 m), special features are observed and are related to the local geology. They give us information that helps to understand the fault behaviour. The first facies is visible on both the profiles, it is either horizontal (pointed by black arrows) or with a slight dip in the direction of the topographic slope (grey arrow). Horizontal ones are related to the inner stratigraphy of the alluvial fan and were slowly deposited probably during rainfall or snow thaw. The dipping one is only observed in the first profile and is aligned with the uphill topography. This reflection is interpreted as palaeotopography before being wrapped up by the recent alluvial fan. Looking at the location of the profiles (Figs 2 and 4a), we note that profile (c) is on the edge of the fan, whereas profile (d) is much more on its central part. The sediment cover, undoubtedly greater in the central part of the alluvial fan (combined with the low penetration depth), results in the disappearance in the GPR profiles of the dipping reflection, which are either deeper or eroded. The third facies, the discontinuous-chaotic background, is observed on profile (d) at the beginning and the end. It also appears in-between the horizontal reflections (profile (c): from 23 m to the end; profile (d): from 20 to 25 m). On profile (d), a special feature has to be noted: at the meeting point of facies 1 and 3, horizontal reflections are bent upward (circle in Fig. 4d). This curvature can be due to the warping of the reflectors during the last fault rupture.

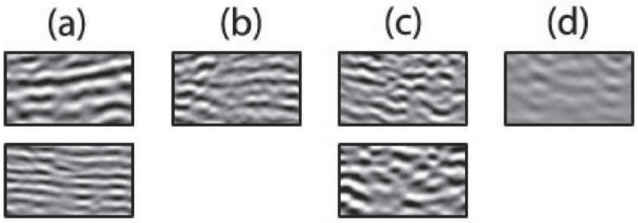

Figure 5. Facies used in the interpretation of the 500 MHz data. (a) Facies having subhorizontal to slightly dipping reflections with a clear lateral continuity. (b) Subhorizontal to slightly dipping reflections with a moderate lateral continuity. (c) Chaotic background with no lateral continuity. (d) Strongly attenuated signal.

4.2 Comparison with the trench

Trench T1 was dug in 2009 on the edge of an actual alluvial fan (Fig. 2c), just before the GPR survey. It is around 2 m deep and displays mainly typical alteration from dry and cold climate. In the first metre, we find clay and silty material, which can be responsible for the low depth of penetration the GPR signal. On the south wall of the trench, a network of synthetic and antithetic ruptures and displacing deposits has been mapped (see red lines). The dip of these ruptures ranges from 20° to subvertical and most of them are dipping toward the north–east. The upper units of the trench (purple, blue and yellow) have been reported on profile (c) to allow comparison. Although the profile is 5.5 m away from the trench, interfaces between units are relatable to particular reflections in the GPR profile. The dipping reflection (grey arrow) is then well aligned with the top of the yellow unit and on the left is following the bottom of the light blue one. The interface between the purple and the blue units is rather flat and fits the observed horizontal reflections (from 16 to 13 m). This is relatable to both reflections indicated by black arrows on profile (d) of Fig. 4. The chaotic background in the middle of the profiles (24–29 m on profile (c) and 20–25 m on profile (d)) corresponds to the location where the purple–blue interface is dipping. However, due to the low penetration of the 500 MHz antenna, it is not possible to link the deeper units and ruptures with the GPR data.

To sum up, two different types of reflections were observed (the dipping one and the horizontal ones), and a chaotic facies is breaking off their continuity. The dipping reflection observed on the first profile is related with a previous palaeosurface, wrapped up by the alluvial fan sediments. The horizontal reflections, overlapping the dipping one on the right, are related to the inner sedimentation of the fan. However, in the middle, a chaotic facies is observed and

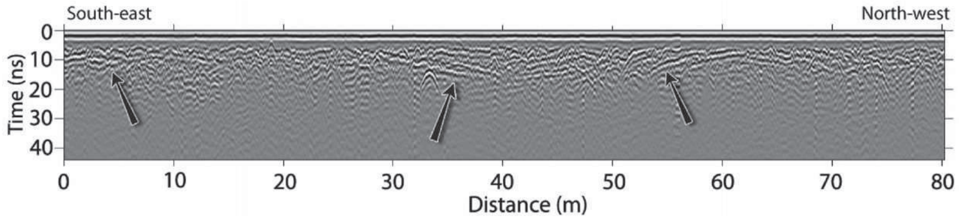

Figure 6. Example of a 500 MHz profile crossing palaeochannels and recorded in 2010 to verify the presence of the palaeochannel in the GPR data before the precise work on 'cubes'. Its location is displayed in Fig. 2 (blue line). Black arrows highlight dipping reflections (with facies, Fig. 5a), which are related to the flanks of the channels.

interpreted in terms of crushed or disorganized material destroying the continuity of the layers. The location of it, in the fault zone (black brackets, Figs 4c and d), is considered to be the result of the movement of the fault underneath. The horizontal reflections are bent where they meet the chaotic facies. As the fault seems to have an important strike-slip component, we cannot use these observations as a measure of displacement but only as a deformation zone.

4.3 500 MHz antenna, Z2 area, pseudo-3-D cubes

4.3.1 Description of the profiles

On the north of the Z1 area, we recorded 11 profiles of 80 m long across the two streams to verify the presence of the palaeochannel in the GPR data and to help choose a location for the precise 3-D work. One of these profiles is presented in Fig. 6. The dipping reflections showing moderate continuity are indicated by black arrows. The middle and the right ones clearly define the flanks of a palaeochannel. Subhorizontal reflections with moderate continuity and many diffraction hyperbolas lie in-between and are related to the sedimentary filling of the channel and the presence of many rocks. On the left side, another dipping reflection is observed. It is related to the edge of a second palaeochannel crossed by the profile. From those results, we decided to investigate the first channel in depth with the pseudo-3-D surveys (Dujardin *et al.* 2012). The acquisition geometry is presented in Table 2.

A selection of five profiles, extracted from the pseudo-3-D cubes, equally scaled and with a vertical exaggeration of 1.4 is displayed in Fig. 7. The depth axes of the profiles are related to the most

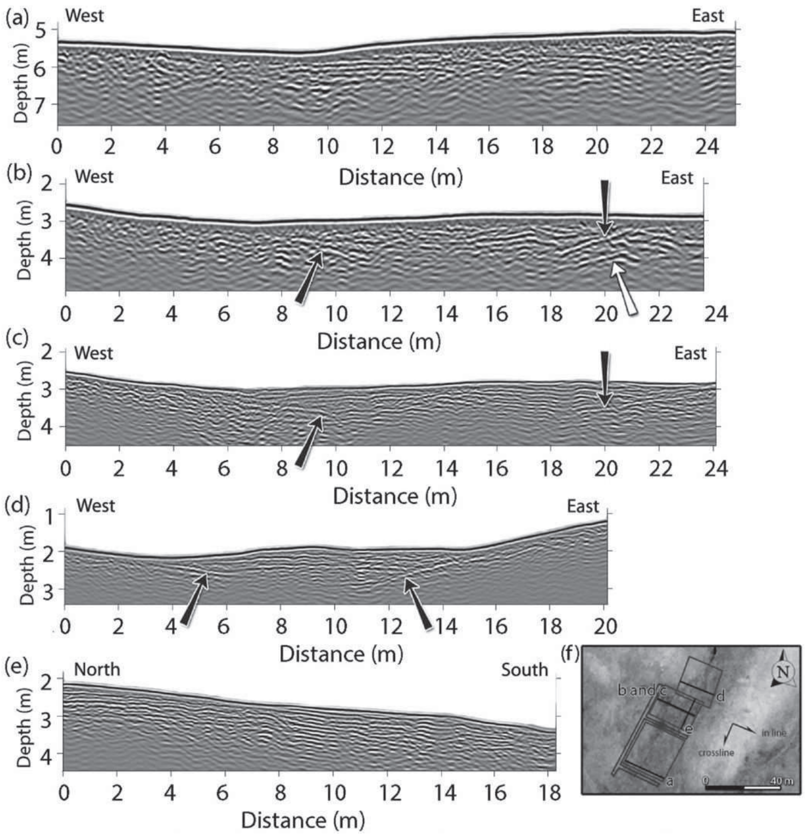

Figure 7. Selection of 500 MHz profiles from the pseudo-3-D cubes in Z2 area (profiles (a)–(e) in Fig. 7f), respectively. They are equally scaled and the vertical exaggeration is 1.4. Although the depth of penetration is low (from 1 to 1.5 m), many reflections, organized in two groups, are observed. The dipping reflections are related to the flanks of the channel (black arrows), while the horizontal reflections, confined between the flanks, are related to the sedimentary filling of the channel. Note on profile (b) a second deeper flank (grey arrow) probably due to interlocked channels. Profiles (b) and (c) are the same (b was recorded in 2010 and c in 2011), and display very consistent image. Note the much smaller wavelength in (c) due to the lower velocity in 2011 (soil more humid). Profile (e) is a cross-line showing only subhorizontal reflections dipping slightly downstream, which are related to the sedimentary filling.

elevated point for the four GPR cubes; thus, the zero does not appear in the presented profiles. As observed in the map (Fig. 7f), profiles (a)–(d) are inline profiles (from downstream to upstream). Profile (e) is a cross-line profile. Profiles (a) and (b) were recorded in 2010, and profiles (c), (d) and (e) in 2011. GPR sections (c) and (b) are both presenting the same profile, but recorded at different periods (2010 and 2011, respectively). They allow a comparison between the 2010 and the 2011 surveys. The location of the actual stream is at the lowest point of the topography in the profiles (between 6 and 10 m in profiles (a)–(c)). Once again, for the interpretation, we use the combination of reflection picking with facies recognition as presented in Fig. 5. The first facies (having subhorizontal to slightly dipping reflections) show strong continuity and are observed in the central part of each profile. Their edges are highlighted by dipping reflections (black arrows) towards the centre of the profiles except for profile (a). The dipping reflections are the signature of the flanks of the channel. On profile (b), a second, deeper reflection is observed (grey arrow). This feature is probably due to interlocked channels. Horizontal reflections are related to the sedimentation within the channel. Facies having subhorizontal reflections with moderate continuity and facies showing chaotic background with no lateral continuity are interlocked in between (profile (a): 14–18 m; profile (b): 11–14 m; profile (c): 13–15 m) and on the extremities of the profiles (profile (a): before 9 m and after 21 m; profile (b): before 8 m; profile (c): before 7 m). On profile (d), the extremities are characterized by a strong attenuation of the GPR signal corresponding to the bedrock in which the channel has been incised and filled. EM waves are then attenuated by a different lithology. The last profile (e) presents a cross-line from north to south; it shows many continuous reflections subparallel to the topography and consistent with the first facies. They are the GPR response of the sedimentary deposition in the direction of the flow. Cross-line profiles are of great importance in the later interpretation as they allow a strong connection with inline profiles.

4.3.2 Comparison of the 2010 and 2011 data

The 2010 and 2011 profiles were then compared to check for their consistency. In 2011, the weather was very wet with heavy rainfall. This translated into a soil much more humid and a decrease in the EM wave velocity from 0.135 m ns^{-1} in 2010 to 0.095 m ns^{-1} in 2011. Profile (c) is the repetition of profile (b) (Fig. 7). The most striking feature is the difference in the wavelength, a direct consequence of the change in the velocity. The first facies is recognized in both profiles. In profile (b), it is restricted between 14 and 20 m, with the chaotic facies lying from 9 to 14 m. In profile (c), the first facies is observed in the whole channel and the dipping reflection on the left, related to the flank of the channel, is better resolved until the surface. On the right, the deeper flank is not observed on profile (c). The electrical conductivity of the ground is higher due to the increased water content and the depth of penetration has decreased, masking the deeper flank on the 2011 data. It is not possible to connect specific reflection in both profiles, but the location of the facies is in good agreement and the channel flanks are very similar in both the profiles.

4.3.3 Comparison between profiles and trenches

Fig. 8(a) presents a photomosaic from the north wall of trench T4. White wires in vertical and horizontal directions highlight the 1 m spacing gridding of the trench. The profile shown in Fig. 8(b) is the northern most profile of the cube C1 and is 2.5 m away from the trench T4 wall. The photomosaic and the GPR profile have the same scale, and there is no vertical exaggeration. Three main units were identified in the trench and highlighted here by brown, yellow and orange colours. The brown unit is a homogeneous silty–sandy material with some gravel scattered inside it. In some areas, gravels are gathered in thin horizontal layers, highlighted by red lines. It corresponds to the filling of the channel. The two next units are characterized by yellowish coarser material. The first one (the yellow unit) is a layer of around 50 cm thick with centimetric stones. The last unit (orange one) is very similar to the yellow unit, but with many scattered centimetric stones. The consistency between the GPR profile and the photomosaic becomes evident when we superimposed the interpretation of the trench on the profile. Boundaries of the units match reflections observed in the GPR profiles. The gravel lens (red lines) is almost perfectly aligned with a reflection in the GPR profile. The left flank of the channel (limit between the yellow and the orange unit) is as well matching a reflection and the yellow unit corresponds to an attenuated signal. On the east side, the units interfaces seem to match with dipping reflections but with a lateral offset that can be explained by the distance

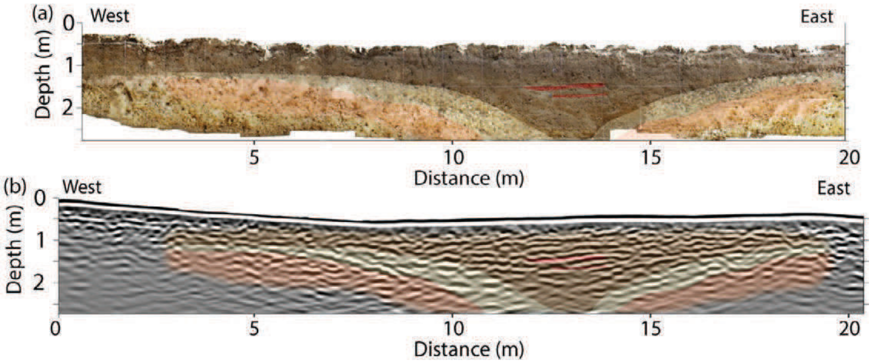

Figure 8. (a) Photomosaic of the north wall of T4 trench and (b) northernmost profile of cube C1, 2.5 m away from the trench wall (see location at Fig. 2). Three main different units were identified in the trench highlighted here by brown, yellow and orange colours. They are superimposed on the trench and the profile for comparison. The brown is a thin brownish unit filling the channel, the yellow is a yellowish coarse deposits unit (centimetric sized) and the orange is a yellowish unit with fine material. Within the brown unit, a gravel lens is observed and highlighted by the red lines. A good consistency is observed between the GPR data and the trench. The gravel lens (red lines) is almost perfectly aligned with a reflection in the GPR profile. The left flank of the channel (limit between the yellow and the orange unit) is as well matching a reflection and the yellow unit corresponds to an attenuated signal. On the east side, the units interfaces seem to match with dipping reflections but with a lateral offset that can be explained by the distance between the trench and the GPR profile (2.5 m).

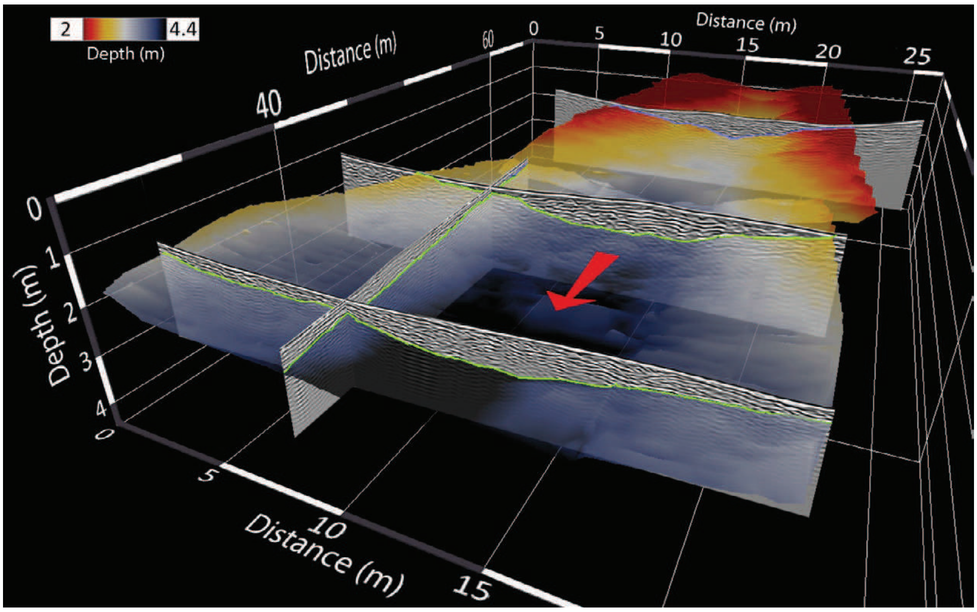

Figure 9. Four GPR profiles with the palaeochannel picked in green. The 3-D surface (in colours) of the palaeochannel was deduced from the picking on all the profiles of the cube C2, C3 and C4. The red arrow shows the palaeoflow direction.

between the trench and the GPR profile (2.5 m). It is worthwhile to do the comparison for two reasons: first, it confirms our interpretation and secondly, it allows the connection of GPR facies with a specific lithology. Thus, first and second facies (Fig. 5) are linked to the brownish, massive unit of silty sands where gravel-sized lenses are found sporadically. Third facies is linked to a coarser-grained material (centimetric size stones) showing no evidence of layering.

4.3.4 Picking of the palaeochannel

After processing, all the profiles were merged in one single survey and loaded into seismic interpretation software (Opendtect) which allows 3-D representations, depth slices and horizon picking. We tried depth slices representation and attribute analysis to improve the quality of the interpretation, but the results were disappointing due to the space between the profiles. Horizon picking was much more time-consuming but gave much more interesting results. Owing to the strong disparity of the reflections, which did not allow a semi-automatic picking, we picked the channel's flanks manually. During this step, cross-line profiles were of great importance as they permit a strong correlation of the reflections from one profile to the next one. The result of the manual picking is the 3-D surface presented in Fig. 9 in relation with GPR profiles (three inlines and one cross-line). The depth (from the most elevated point in the topography) is presented by colour scale. Green lines on the profiles represent the picking, thus the intersection between the surface and the profiles. The red arrow indicates the flow direction. The displayed surface is obtained by interpolating the picked profiles taken from cubes C2, C3 and C4. Afterwards, the main slope of the channel was subtracted to provide a better interpretability of the data. The removal of the main slope straightens the channel, and the geometry of the flanks is greatly enhanced. The result is superimposed on the aerial view (Fig. 13). The channel appears very heterogeneous and many bumps are observed at its bottom. The penetration depth, from 1.5 to 2 m, is often lower than the depth of the channel. Thus, the bumps are related either to a mispicking of the base of the channel or to the collapse of a flank during storm weather. The SE flank is fairly straight on its upper part and starts enlarging at around 27 m distance from the south–east corner of cube C1 (scale on Fig. 13a). This enlargement is linked to the arrival in the sedimentary basin. The NW flank is as well fairly straight in its deepest part except for the shift at around 49 m distance with right lateral amplitude of about 2 m (black arrow, Fig. 13).

4.4 RTA (50 MHz antenna)

RTA profiles (50 MHz) were interpreted in a similar way as the 500 MHz profiles. They were visually analysed and interpreted using a combination of GPR facies with reflection picking. The four facies used in the interpretation are shown in Fig. 10. They represent reflections parallel to the topography with strong and moderate continuity, facies with chaotic reflections, and finally, facies strongly attenuated. All the RTA profiles presented in Fig. 11 were equally scaled with a vertical exaggeration of 1.8. The *x*-axis is from right to left to match the direction of the profiles on the map (Figs 2 and 11f). Black lines on the map are the intersection of the fault scarps with the profiles. Their locations are reported on the profiles

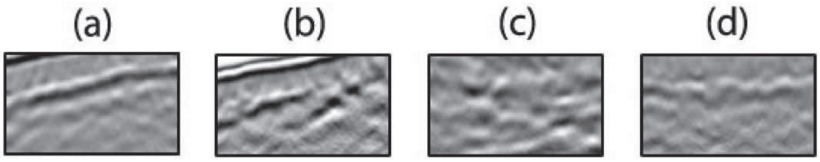

Figure 10. Four facies (extracted from the GPR images) used in the interpretation of the 50 MHz GPR profiles. (a) Reflections showing clear lateral continuity; (b) reflections showing moderate lateral continuity; (c) chaotic background and (d) strongly attenuated signals.

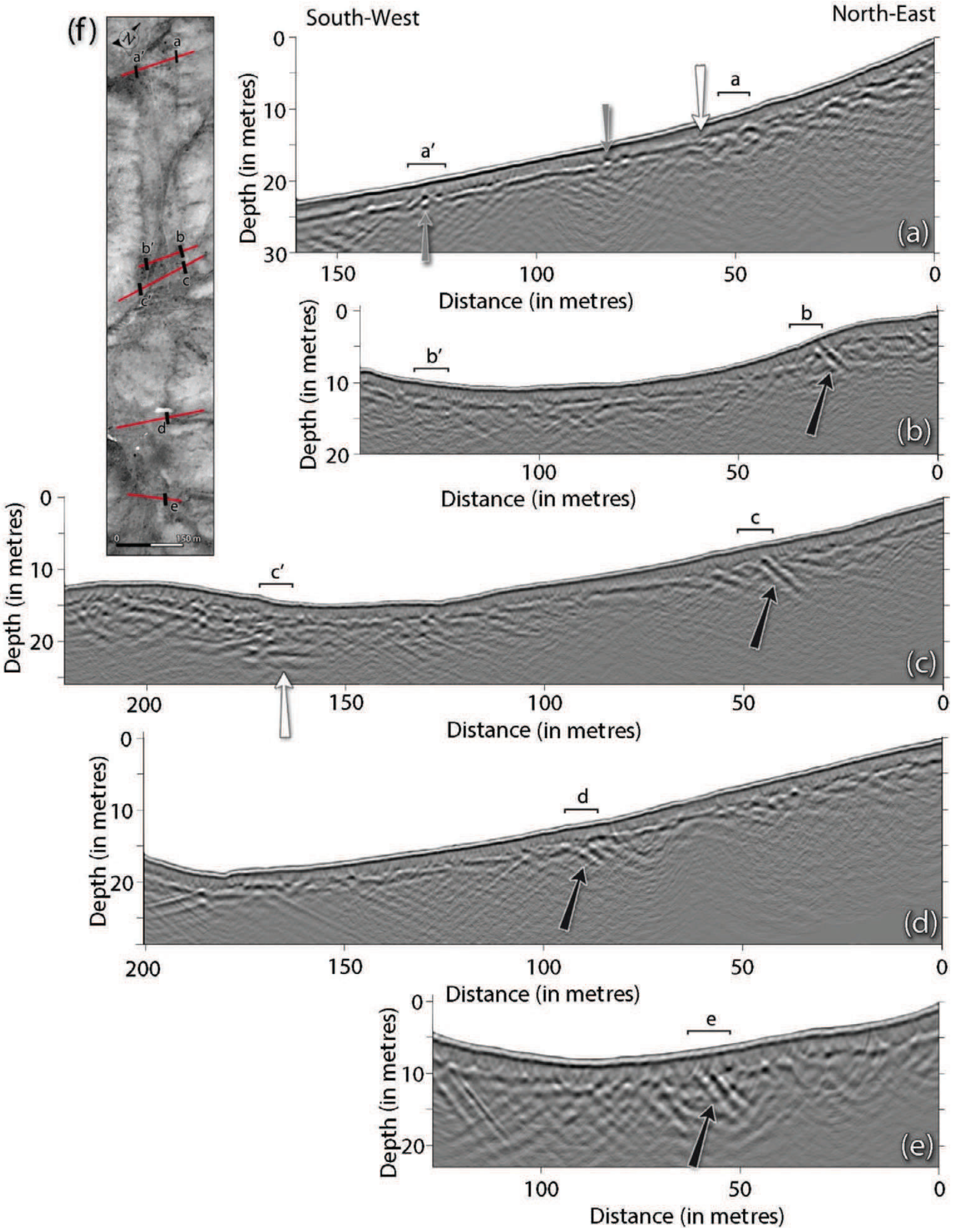

Figure 11. 50 MHz GPR profiles (RTA). All the profiles are equally scaled with a vertical exaggeration of 1.8. Location of profiles (from top to bottom) is shown by red lines on the map (Fig. 11f). Letters (a)–(e) show the place where morphological scarps are observed on the surface. Black arrows show the reflections from the fault plane and the change in the GPR facies that highlight the location and geometry of the fault (see the text for more details).

with the brackets. Despite the low penetration depth (10 m in the best case), much information is recovered from those profiles. First, a strong north–east dipping reflection was observed in almost every profile (indicated by black arrows). This feature is interpreted as a direct reflection from the fault plane, it gives access to the dipping direction (north–east), its dip and the exact location of the fault (from near the surface up to 10 m depth). The dip ranges from 27° in the north (profiles b and c), to 23° (profile d) increasing up to 35° in the south (profile e). Those reflections are exactly located under the brackets, which mean that the rupture reaches the surface. On profile (a), the reflection is not observed. However, a strong separation (white arrow) between the chaotic facies (at NE) and

Downloaded from http://gji.oxfordjournals.org/ May 1, 2014

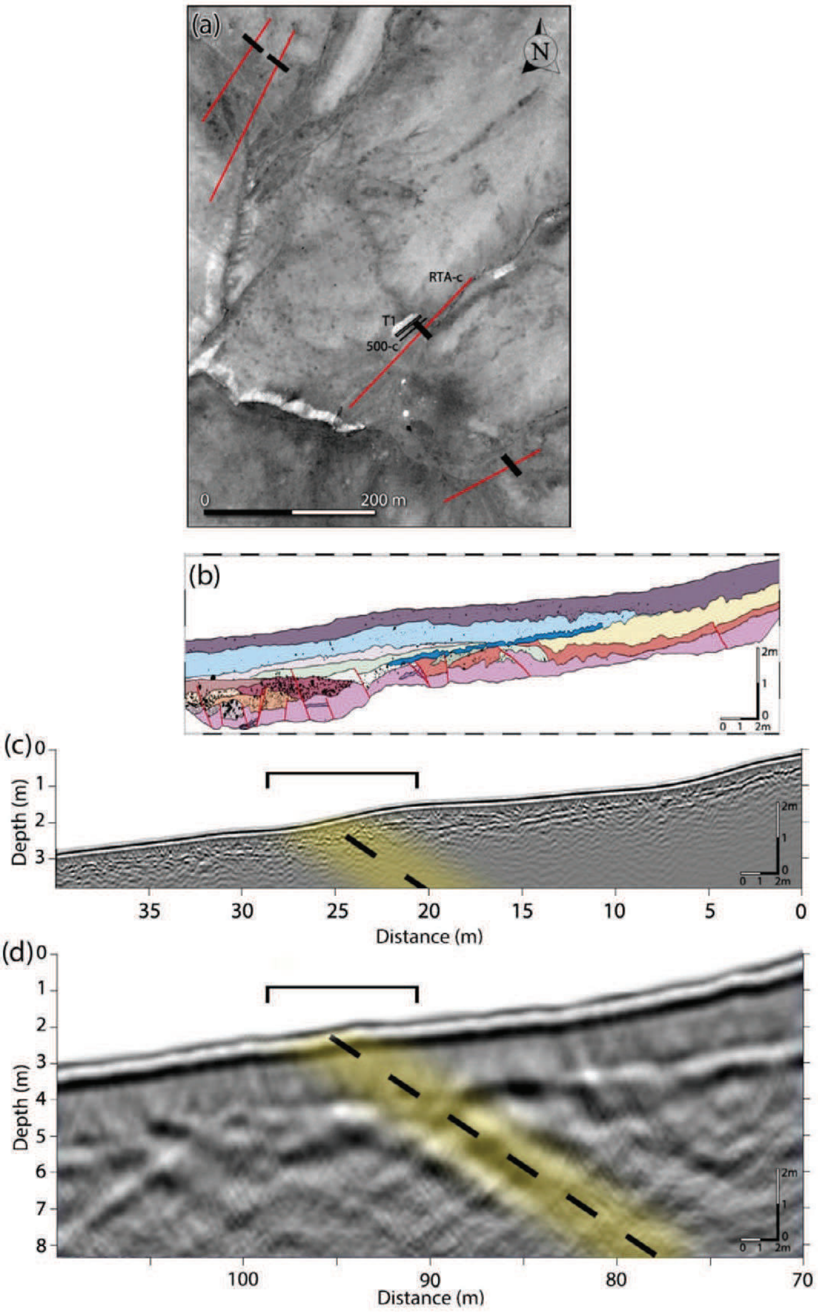

Figure 12. Synthesis figure of area Z1. (a) Map, displaying the RTA profiles (red lines) with the location of the fault at surface (black lines perpendicular to the profiles). Trench T1 and the 500 MHz profile are drawn in black. (b) Trench T1, (c) 500 MHz profile from Z1 (Fig. 4c) and (d) RTA profile (Fig. 11d). They are all equally scaled and the vertical exaggeration is 1.9. Black brackets at the top of the profiles show the location of the scarp as observed on the field and satellite image. The dashed line, surrounded by yellow zone, highlights the fault as observed in the RTA profile. It is reported as well on the 500 MHz profile and corresponds to a chaotic facies between clear horizontal reflections.

the reflection with clear continuity (at SW) is observed at the base of the scarp. Discontinuities in the reflections (pointed by grey arrows) are the results of the collapse of diffraction hyperbolae after migration. Reflections, showing a clear continuity, are also present in other profiles, especially in their central part (in the valley) and in profiles (c) and (d), in their upper part as well. Around the fault reflections, a chaotic facies is always observed on a width of around 30–40 m.

On the other side of the valley, neither reflections nor a change in facies are observed on profiles (a) and (b) where they cross the second scarps. However, profile (c) displays an abrupt variation as well with a change in the penetration depth (white arrow). Reflections with lateral continuity on the right are contrasting with a chaotic background on the left. This sharp contact is in good agreement with the location of the geomorphologic scarp but is not enough to conclude on its origin.

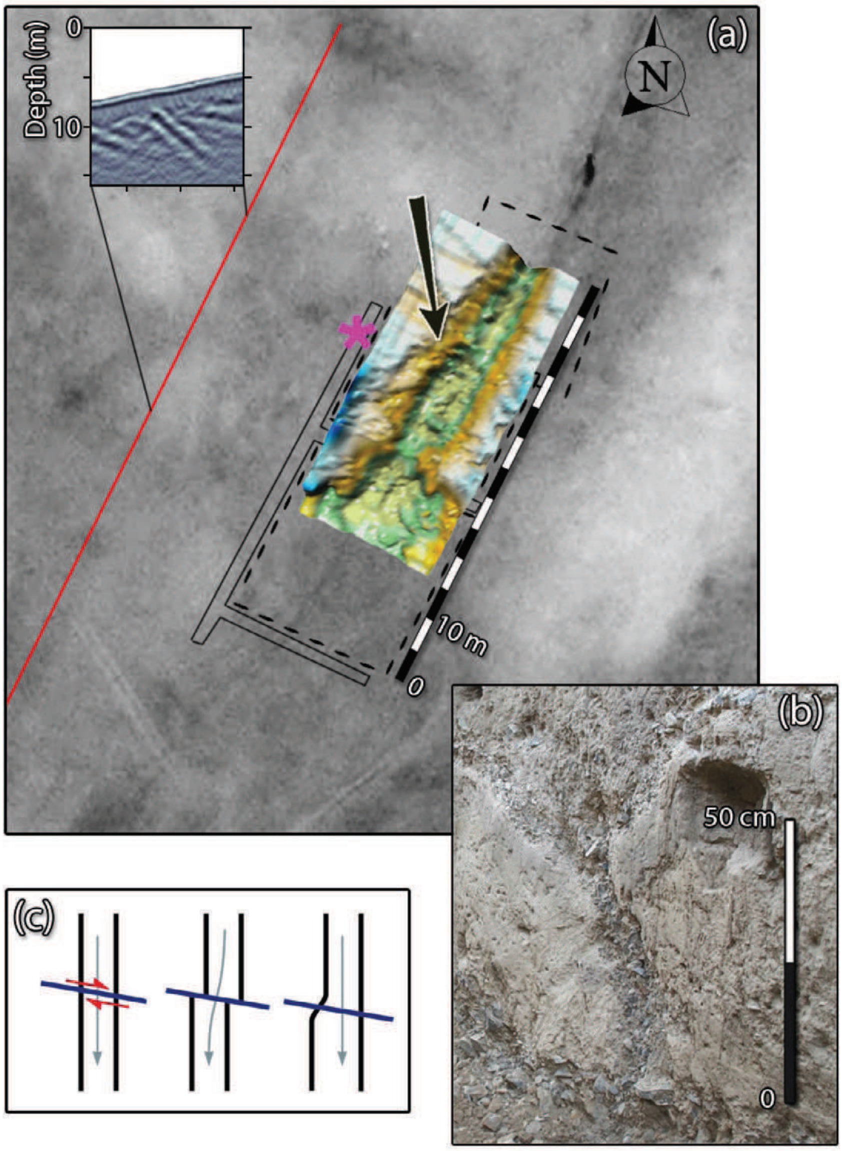

Figure 13. (a) Interpretation map of Z2 area. The interpolated 3-D surface of the channel (after subtraction of its main slope) is superimposed on the satellite image. An offset of 2 m horizontally is observed on the NW flank of the channel (see black arrow), which is consistent with a right lateral strike-slip. The pink asterisk shows the location of picture (b) in the trench where an evidence of the fault is observed. The closest RTA profile (upper left corner) shows the record and the location of the fault plane in depth. (c) Illustration of the evolution of the channel flanks due to the right lateral strike-slip. The down left flank is preserved while the down right flank is eroded after the shift. The filling of the palaeochannel fossilizes the palaeomorphology.

5 DISCUSSION

In addition to geomorphology and trench observations, the GPR images obtained by using 500 and 50 MHz antennae give us important information about the Emeelt fault, which was discovered in 2008 (Schlupp *et al.* 2012).

The GPR profiles across the fault with the 50 MHz antenna show the structure between 3 and 12 m depth. The location of the fault is consistent with the surface observations. The strong reflection, observed on all the profiles and related to the fault plane, confirmed the stability of the fault geometry in depth along the structure over about 2 km. This reflection is probably due to the contact between base rock on top and sedimentary deposits underneath. It gives us a good estimation of the near surface slope of the fault (23°–35° to the NNE) in addition to the observations done at the bottom of the trench T1 (in area Z1) at depth between 1.5 and 2.5 m but showing steeper angle, mainly from 30° to 45° (Fig. 4b and 12b). The picture in Fig. 13(b) has been taken inside the trench T2 (area Z2), at the position of the pink asterisk. It shows evidence of the fault within a gravel layer with a dip towards the NNE. This dip direction was also determined at the surface as the fault trace moves upstream when crossing a local valley.

The 500 MHz profiles across the fault, imaging a small alluvial fan (Z1 area), highlight a chaotic facies, interpreted in terms of crushed or disorganized material destroying the continuity of the layers, and located in the fault zone but no 'fault reflection' has been observed with this antenna (Figs 4b and d). However, the 'fault reflection' observed in the 50 MHz profile crossing the area is totally consistent with the location of this chaotic facies (Figs 12c and d). The locally apparent vertical offsets of reflections on some of these profiles cannot be directly related to a vertical component of the slip. First, it is impossible to associate the reflections observed on each side of the fault zone because of the shallow penetration of 500 MHz signal and the very few subhorizontal reflections. On the other hand, the right lateral component can bring itself apparent vertical offsets in a context of interlocked alluvial deposits. However, a vertical component is suspected by the morphology and the dip of the fault near the surface but its amplitude cannot be quantified by our data.

On Z2 area, we observed a deep palaeochannel with a few 500 MHz profiles (down to about 2.5 m depth) fossilized by the filling material and crossing the fault. As we suspected a horizontal slip component from the linearity of the seismicity and the fault morphology, we decided to map the channel flanks across the fault by a pseudo-3-D approach with numerous 500 MHz inline and cross-line profiles that were acquired during 2010 and 2011 summers. A right lateral offset of about 2 m was imaged on the right downstream flank; it was preserved on the downstream right flank, while it has been eroded on the downstream left flank (schema, Fig. 13c). Afterwards, the filling of the palaeochannel fossilizes the palaeomorphology.

This horizontal displacement could have been produced by one event (at least of $M_w = 7$) as it is observed for the Mogod earthquake (in 1967, about 280 km west of UB) of $M_w = 7.1$ with a mean horizontal slip of 1.5 m (Baljinnyam *et al.* 1993; Bayasgalan *et al.* 1999) or by several of $M_w \geq 6$. In the 3-D channel reconstruction, we did not observe any clear vertical offset. Nevertheless, it does not prove its absence as the bottom of the channel was locally difficult to follow due the low penetration depth, which was more or less of same depth as the bottom of the channel.

6 CONCLUSION

This work is a part of numerous studies on the characterization of active faults near the capital of Mongolia, UB. For the first time, we used GPR to explore and reveal the buried traces of a newly discovered active fault in area showing low slip rate. It is a challenge as we are in a context where the geomorphologic features have been heavily smoothed since the last event due to erosion processes combined with a very long return period probably of several thousands of years. Despite the low penetration depth of the GPR (up to 12 m for the 50 MHz antenna and 1.5 m for the 500 MHz antenna), it clearly provided several important pieces of information that improve our understanding of the Emeelt fault geometry and horizontal displacement. The combination of 500 with 50 MHz antennae produces two complementary and consistent data sets as they allow the imaging of different structures.

A good consistency is observed between the 500 MHz GPR profiles and trench results. Pseudo-3-D profiles, recorded with a 500 MHz antenna over a palaeochannel crossing the fault, provided information about the lateral displacement of 2 m caused by the fault. It could be associated with an earthquake with magnitude M_w of about 7 or several with magnitude $M_w \geq 6$.

The 50 MHz GPR profiles show a direct reflection, coming from the fault plane, giving access to the location, the dip angle and direction of the fault. The dip is towards NNE and it ranges from 23° in the north to 35° in the south part of fault segment investigated. In contrast, the linearity of the actual seismicity indicates a near vertical fault plane. To clarify that point, we need to investigate more in depth the active structure, by combining GPR with high-resolution seismic profiles and very precise 3-D relocation of the seismicity.

ACKNOWLEDGEMENTS

The authors thank the Editor, Prof. Randy Keller and two anonymous reviewers for their constructive comments and helpful suggestions, which considerably improved the quality of the manuscript. The DGB Earth Sciences society made their Interpretation Software OpendTect freely available to academic research. The GPR campaigns conducted in 2010 and 2011 were funded by EOST and RCAG, respectively. Many thanks to Sarantsetseg Lkhagvasuren and two students, Battsetseg Byambakhorol and Batdorj Nyamdavaa, who participated in the acquisition of the GPR data.

REFERENCES

Baljinnyam, I. *et al.*, 1993. *Ruptures of Major Earthquakes and Active Deformation in Mongolia and Its Surroundings,* Memoir 181, Geological Society of America.

Bayasgalan, A. & Jackson, J., 1999. A re-assessment of the faulting in the 1967 Mogod earthquake in Mongolia, *Geophys. J. Int.,* **138,** 784–800.

Bayasgalan, A., Jackson, J., Ritz, J.-F. & Carretier, S., 1999. Field examples of strike-slip fault terminations in Mongolia and their tectonic significance, *Tectonics,* **18,** 394–411.

Beauprêtre, S. *et al.*, 2012. Finding the buried record of past earthquakes with GPR based palaeoseismology: a case study on the Hope fault, New Zealand, *Geophys. J. Int.*, **189,** 73–100.

Calais, E., Vergnolle, M., Sankov, V., Lukhnev, A., Miroshnitchenko, A., Amarjargal, S. & Déverchère, J., 2003. GPS measurements of crustal deformation in the Baïkal-Mongolia area (1994–2002): implication for current kinematics of Asia, *J. geophys. Res.,* **108,** 2051, doi:10.1029/2002JB002373.

Calais, E., Dong, L., Wang, M., Shen, Z. & Vergnolle, M., 2006. Continental deformation in Asia from a combined GPS solution, *Geophys. Res. Lett.,* **33**(24), doi: 10.1029/2006GL028433.

Christie, M., Tsoflias, G.P., Stockli, D.F. & Black, R., 2009. Assessing fault displacement and off-fault deformation in an extensional tectonic setting using 3-D ground-penetrating radar imaging, *J. appl. Geophys.,* **68,** 9–16.

Daniels, D.J., Gunton, D.J. & Scott, H.F., 1988. Introduction to subsurface radar, *IEE Proc.,* **135,** 278–320.

Davis, J.L. & Annan, A.P., 1989. Ground-penetrating radar for high resolution mapping of soil and rock stratigraphy, *Geophys. Prospect.,* **37,** 531–551.

Dentith, M., O'Neill, A. & Clark, D., 2010. Ground penetrating radar as a means of studying palaeofault scarps in a deeply weathered terrain, southwestern Western Australia, *J. appl. Geophys.,* **72,** 92–101.

Deparis, J., Garambois, S. & Hantz, D., 2007. On the potential of ground penetrating radar to help rock fall hazard assessment: a case study of a limestone slab, Gorges de la Bourne (French Alps), *Eng. Geol.,* **94,** 89–102.

Dujardin, J.-R. & Bano, M., 2013. Topographic migration of GPR data: examples from Chad and Mongolia, *C. R. Geosci.,* **345,** 73–80.

Dugarmaa, T. *et al.*, 2006. Seismic hazard assessment of Ulaanbaatar, capital of MONGOLIA. Seismic micro zoning map, *Report of Research Center of Astronomy and Geophysics,* 156 p.

Dujardin, J.-R., Bano, M., Schlupp, A., Gillard, M., Ferry, M. & Munkhuu, U., 2012. GPR measurements to assess the fault's characteristics in a highly smooth topographic context. EAGE, near surface, in *Proceedings of the 18th Meeting of Environmental and Engineering Geophysics,* Extended Abstracts, Paris, France.

Ferry, M., Meghraoui, M., Girard, J.-F., Rockwell, T.K., Kozaci, O., Akyuz, S. & Barka, A., 2004. Ground-penetrating radar investigations along the North Anatolian fault near Izmit, Turkey: constraints on the right-lateral movement and slip history, *Geol. Soc. Am.,* **32,** 85–88.

Girard, J.F., 2002. *Imagerie géoradar et modélisation des diffractions multiples, PhD thesis*, Université Louis Pasteur, Strasbourg-I.

Grasmueck, M., Weger, R. & Horstmeyer, H., 2005. Full resolution 3D GPR imaging, *Geophysics,* **70**(1), K12–K19.

Gross, R., Holliger, K., Green, A.G. & Begg, J.H., 2000. 3D ground penetrating radar applied to paleoseismology: examples from the Wellington Fault, New Zealand, in *Proceedings of the 8th International Conference on Ground Penetrating Radar, Proc. SPIE,* Vol. **4084,** eds Noon, D.A., Stickley, G.F. & Longstaff, D., SPIE, Bellingham, WA, pp. 478–481.

Gross, R., Green, A.G., Holliger, K., Horstmeyer, H. & Baldwin, J., 2002. Shallow geometry and displacements on the San Andreas Fault near point arena based on trenching and 3D georadar surveying, *Geophys. Res. Lett.,* **29**(20), 1973–1977.

Gross, R., Green, A., Horstmeyer, H. & Holliger, K., 2003. 3D georadar images of an active fault: efficient data acquisition, processing and interpretation strategies, *Subsurf. Sens. Technol. Appl.,* **4,** 19–40.

Gross, R., Green, A.G., Horstmeyer, H. & Begg, J.H., 2004. Location and geometry of the Wellington Fault (New Zealand) defined by detailed three-dimensional georadar data, *J. geophys. Res.,* **109,** B05401, doi:10.1029/2003JB002615.

Guillemoteau, J., Bano, M. & Dujardin, J.-R., 2012. Influence of grain size, shape and compaction on georadar waves: examples of aeolian dunes, *Geophys. J. Int.,* **190,** 1455–1463.

Heincke, B., Green, A.G., van der Kruk, J. & Horstmeyer, H., 2005. Acquisition and processing strategies for 3D georadar surveying a region characterized by rugged topography, *Geophysics,* **70,** K53–K61.

Jol, H.M., 1995. Ground penetrating radar antennae frequencies and transmitter powers compared for penetration depth, resolution and reflection continuity, *Geophys. Prospect.,* **43,** 693–709.

Jol, H.M., 2009. *Ground Penetrating Radar: Theory and Applications,* Elsevier Science, 525 pp.

Khilko, S.D. *et al.*, 1985. Strong earthquakes, paleoseismogeological and macroseismic data, in *Earthquakes and the Base for Seismic Zoning of Mongolia* (in Russian), Trans. Joint Sov.-Mongolian Res. Geol. Sci. Exped., vol **41,** Nauka.

Lehmann, F. & Green, A.G., 2000. Topographic migration of georadar data: implications for acquisition and processing, *Geophysics,* **65**(3), 836–848.

Malik, J.N., Sahoo, A.K. & Shah, A.A, 2007. Ground penetrating radar investigation along Pinjore Garden Fault: implication toward identification of shallow sub-surface deformation along active fault, NW Himalaya, *Curr. Sci.,* **93**(10), 1427–1442.

McClymont, A.F. *et al.*, 2008a. Visualization of active faults using geometric attributes of 3D GPR data: an example from the Alpine Fault Zone, New Zealand, *Geophysics,* **73,** B11–B23.

McClymont, A.F., Green, A.G., Villamor, P., Hortsmeyer, H., Grass, C. & Nobes, D.C., 2008b. Characterization of the shallow structures of active fault zones using 3D ground penetrating radar data, *J. geophys. Res.,* **113,** B10315, doi:10.1029/2007JB005402.

McClymont, A.F., Green, A.G., Kaiser, A., Horstmeyer, H. & Langridge, R.M., 2010. Shallow fault segmentation of the Alpine fault zone, New Zealand, revealed from 2- and 3-D GPR surveying, *J. appl. Geophys.,* **70**(4), 343–354.

Neal, A., 2004. Ground-penetrating radar and its use in sedimentology: principles, problems and progress, *Earth Sci. Rev.,* **66,** 261–330.

Pellicer, X.M. & Gibson, P., 2011. Electrical resistivity and ground penetrating radar for the characterisation of the internal architecture of Quaternary sediments in the Midlands of Ireland, *J. appl. Geophys.,* **75**(4), 638–647.

Schlupp, A., 1996. *Néotectonique de la Mongolie occidentale analysée a partir de données de terrain, sismologiques et satellitaires, PhD thesis*, Université Louis Pasteur-Strasbourg I.

Schlupp, A. *et al.*, 2012. Investigation of active faults near Ulaanbaataar. Implication for seismic hazard assesment, in *Proceedings of the 9th General Assembly of Asian Seismological Commission,* Extended Abstract, Ulaanbaatar, pp. 265–267.

Tapponnier, P. & Molnar, P., 1979. Active faulting and cenozoic tectonics of the Tien Shan, Mongolia, and Baykal Regions, *J. geophys. Res: Solid Earth,* **84,** 3425–3459.

Tronicke, J., Vilamor, P. & Green, A.G., 2004. Estimating vertical displacement within the NgakuruGraben, New Zealand, using 2D and 3D georadar, in *Proceedings of the 10th International Conference on Ground Penetrating Radar,* Delft, the Netherlands.

Vergnolle, M., Calais, E. & Dong, L., 2007. Dynamics of continental deformation in Asia, *J. geophys. Res: Solid Earth,* **112**(B11), doi:10.1029/2006JB004807.

Widess, M.B., 1973. How thin is a thin bed?, *Geophysics,* **38,** 1176–1180.

Yalçiner, C.Ç., Altunel, E., Bano, M., Meghraoui, M., Karabacak, V. & Serdar, H.A., 2013. Application of GPR to normal faults in the Büyük MenderesGraben, Western Turkey, *J. Geodyn.,* **65,** 218–227.

Zeng, H., 2009. How thin is a thin bed? An alternative perspective, *Leading Edge,* **28,** 1192–1137.

UNIVERSITÉ DE STRASBOURG

Imagerie géoradar (GPR) en milieu hétérogène

EOST
Ecole et Observatoire
des Sciences de la Terre

Résumé

Le géoradar est une méthode électromagnétique haute fréquence (>10 MHz) utilisé pour caractériser les premiers mètres du sous-sol.

Lors de la présence d'une topographie, les données géoradar sont déformées en conséquence. Afin de retrouver la vraie géométrie des réflecteurs, nous avons codés un algorithme de migration prenant en compte la topographie. La méthode est démontrée grâce à un modèle synthétique simple, puis testée avec succès sur des données réelles.

Les algorithmes de migration apportent cependant du bruit dans les données. Pour pallier à ce problème, deux méthodes ont été mises en place : la première, inhérente à la migration, permet de réduire l'aliasing dit sur l'opérateur. La deuxième est un filtre ré-interpolant les traces en se basant sur un profil de pendage. Les deux méthodes suppriment un bruit incohérent des données mais dégradent les profils lorsqu'utilisées abusivement.

Dans un deuxième chapitre, nous avons appliqués avec succès le géoradar dans un contexte de paléo-sismologie en Mongolie. L'utilisation conjointe de deux fréquences (50 et 500 MHz) ainsi que des comparaisons avec des tranchées a permis d'obtenir des informations complémentaires sur les géométries et les déplacements potentiels le long de deux failles.

Dans un dernier chapitre, nous avons appliqués les mesures géoradar sur les dépôts pyroclastiques du volcan Tungurahua en Equateur. A nouveau, l'utilisation jointe de différentes fréquences (250, 500 et 800 MHz) nous permet d'imager efficacement les dépôts. Les unités principales sont mises en évidence avec l'antenne de 250 MHz et les architectures des dépôts sont observables avec les antennes de 500 et 800 MHz.

Mots clés : géoradar, migration topographique, paléo-sismologie, dépôts pyroclastiques

Abstract

Georadar is a high frequency (>10MHz) electromagnetic method used to prospect near surface.

When a topography is present, GPR images are distorted. To restore the true geometry of reflexions, we coded an migration algorithm which takes the topography into account. The method is first demonstrate on a simple synthetic model, and then succesfully applied on real data.

However, migration algorithms bring noise to the data. Two methods have then been tested to avoid and remove it. The first one is inherent to the migration algorithm and reduce what is called operator's aliasing. The second one is a filter re-interpolating traces based on a profile containing the slope. Both methods remove inconsistent noise when used with caution, but decrease their quality when used with excess: reflexions presenting dip are the first to be deteriorated, as well as reflexions below strong topography.

In a second chapter, we successfully used GPR in a paleo-sismology context in Mongolia. The use of two frequencies (50 and 500 MHz) as well as comparison with trenches bring complementaries informations on the geometry and possible offset along two faults.

In the last chapter, GPR was tested over pyroclastic deposits from the Tungurahua volcano in Ecuador. Again, the combination of several frequencies (250, 500 and 800 MHz) has proven its efficiency. Main units were obvious with the 250 MHz antenna while the inner architecture of deposits was visible with the 500 and 800 MHz antenna.

Keywords: georadar, topographic migration, paleosismology, pyroclastic deposits